Jets and Fragmentation

Dissertation

der Mathematisch-Naturwissenschaftlichen Fakultät
der Eberhard Karls Universität Tübingen
zur Erlangung des Grades eines
Doktors der Naturwissenschaften
(Dr. rer. nat.)

vorgelegt von
Tom Kaufmann
aus Reutlingen

Tübingen
2017

Gedruckt mit Genehmigung der Mathematisch-Naturwissenschaftlichen Fakultät der Eberhard Karls Universität Tübingen.

Tag der mündlichen Qualifikation:	19.10.2017
Dekan:	Prof. Dr. Wolfgang Rosenstiel
1. Berichterstatter:	Prof. Dr. Werner Vogelsang
2. Berichterstatter:	Prof. Dr. Thomas Gutsche

Summary

The main focus of this PhD thesis is on final state physics at particle colliders. In particular, two different inclusive final state observables are considered: hadronic jets and identified hadrons originating from a fragmentation process. Said inclusive final states may also be combined into a novel class of semi-inclusive observables: in-jet fragmentation processes. All of these final states are of major importance in the era of high energy particle colliders like the famous Large Hadron Collider (LHC).

In this thesis we work within the framework of perturbative Quantum Chromodynamics (pQCD) and present analytical next-to-leading order (NLO) calculations for final state hadronic jets and, for the first time, for observed hadrons inside fully reconstructed jets in an inclusive setup. Afterwards, we utilize this calculation to perform a global extraction of D^*-meson fragmentation functions including recent D^*-in-jet data from the ATLAS collaboration. Finally, we explore two closely related topics: photon-in-jet production and fragmentation functions beyond fixed order accuracy.

To be more precise, we start by presenting a NLO calculation for the inclusive production of jets at hadron colliders. The calculation of the partonic cross sections is performed analytically within the so-called narrow jet approximation, where the jet is assumed to be rather collimated. In said calculation we address two novelties: the formulation of jet cross sections in a convenient form using appropriate jet functions and the first NLO implementation of a newly proposed jet algorithm which is based on maximizing an appropriate function of the jet's energy and momentum. The formulation of jet cross sections in terms of jet functions has been established in the framework of soft collinear effective theory (SCET) for electron-positron annihilation and for exclusive jet production. We present a consistent formulation within the standard framework of pQCD for inclusive jet production in hadronic collisions. The so obtained structure not only facilitates the implementation of new jet algorithms, but also allows for an interesting physical interpretation in close analogy to inclusive hadron production.

After having established the formulation of jet cross sections in terms of jet functions, we study the production of identified hadrons inside jets. Again, we use the narrow jet approximation to formulate the partonic cross sections analytically in terms of suitable sets of semi-inclusive jet functions. The first set describes the formation of the jet and the second set parametrizes the formation of a specific parton inside the jet. Said parton eventually undergoes the complicated and not yet completely understood process of hadronization to form the observed final state hadron. In the factorized pQCD framework, hadronization is parametrized by non-perturbative functions, so-called fragmentation functions. We demonstrate the importance of this process for studies of fragmentation functions. At leading order (LO) the cross section directly probes the fragmentation functions in a similar way as single-inclusive annihilation (SIA) does. Moreover, due to the hadronic initial state, the process gives valuable constraints on the elusive gluon-to-hadron fragmentation function.

Recently, first data for observed hadrons inside jets were presented by the ATLAS collaboration. These D^*-in-jet data are not well described with the D^*-fragmentation functions available in literature. Thus, we perform a global NLO analysis of D^*-fragmentation functions, including data for single-inclusive hadron production in electron-positron annihilation and hadronic collisions, and, for the first time, hadron-in-jet data. We find a consistent set of fragmentation functions which yields a satisfying description of all the available data. This extraction is possible due to the analytical calculation of the hadron-in-jet cross section which is a prerequisite for an efficient numerical implementation.

Moreover, we present results for two topics which are closely related to the work described above. Motivated by the success of in-jet fragmentation in the extraction of parton-to-hadron fragmentation functions, we extend the framework to photon-in jet production and present the NLO calculation necessary to include this process into future extractions of parton-to-photon fragmentation functions. We make use of the same techniques developed for the hadron-in-jet calculation and present analytical expressions in terms of (photonic) jet functions within the narrow jet approximation.

Finally, we study fragmentation functions beyond fixed order accuracy by including small-z resummations. These resummations account for the singular behavior of the time-like evolution kernels and the coefficient functions by summing up the divergent terms to all orders in perturbation theory. Since the corresponding resummed expressions are not available for other processes, we restrict our analysis to SIA. While the inclusion of such resummations is needed for a reasonable formulation of integrated observables, we find that for phenomenological studies of differential observables in the kinematical regimes accessible by today's experiments already next-to-next-to-leading order (NNLO) results yield a satisfying description of data. The resummed expressions only show negligible differences compared to NNLO ones well within the experimental uncertainties.

Zusammenfassung

Die Physik an Teilchenbeschleunigern ist Gegenstand der Forschung im Rahmen dieser Doktorarbeit. Genauer gesagt, werden verschiedene hadronische Endzustände untersucht: Jets sowie identifizierte Hadronen, die aus einem Fragmentationsprozess entstanden sind. Diese inklusiven Endzustände können auch zu einer neuen Klasse von semi-inklusiven Observablen zusammengefügt werden: den Fragmentationsprozessen innerhalb eines Jets. Alle diese Observablen sind von großer Bedeutung in der Ära der Hochenergieteilchenbeschleuniger, wie zum Beispiel dem LHC.
In dieser Dissertation arbeiten wir im Framework der störungstheoretischen Quanten Chromodynamik (pQCD). Wir präsentieren analytische Rechnungen in nächst-zu-führender Ordnung (NLO) für hadronische Jets. Zum ersten Mal wird auch eine analytische NLO Rechnung für beobachtete Hadronen im Inneren von vollständig rekonstruierten Jets durchgeführt. Danach verwenden wir diese Rechnung, um eine globale Extraktion von Fragmentationsfunktionen für D^*-Mesonen durchzuführen. Dazu bedienen wir uns den kürzlich veröffentlichten D^*-in-Jet-Daten der ATLAS Kollaboration. Am Ende der Arbeit betrachten wir noch zwei Themen, welche mit den bisher erwähnten eng verwandt sind: die Produktion von Photonen in einem Jet und resummierte Fragmentationsfunktionen.

Etwas ausführlicher gesagt, beginnen wir mit einer NLO Rechnung für inklusive Jetproduktion in hadronischen Kollisionen. Die Berechnung der partonischen Wirkungsquerschnitte wird analytisch durchgeführt. Dies geschieht im Rahmen der sogenannten “narrow jet approximation” (NJA). In dieser Näherung wird angenommen, dass der Jet relativ stark kollimiert ist. In unserer Rechnung widmen wir uns zweierlei Neuheiten: einerseits der eleganten und praktischen Formulierung von Jetwirkungsquerschnitten mithilfe von entsprechenden Jetfunktionen, andererseits der ersten NLO Implementierung eines neuen Jetalgorithmus. Dieser neue Algorithmus basiert auf der Maximierung einer geeigneten Funktion der Jetenergie und des Jetimpulses. Die Formulierung von Jetwirkungsquerschnitten mithilfe von Jetfunktionen wurde im Rahmen der “soft collinear effective theory” (SCET) für Elektron-Positron-Annihilation etabliert, allerdings ausschließlich für exklusive Jetproduktion. Wir präsentieren eine konsistente Formulierung für inklusive Jetproduktion in hadronischen Kollisionen. Dies geschieht im Rahmen der pQCD. Die durch die Formulierung mit Jetfunktionen gewonnene Struktur vereinfacht nicht nur die Implementierung neuer Jetalgorithmen, sondern sie erlaubt auch eine interessante physikalische Interpretation: die gefundenen Jetfunktionen treten in enger Analogie zu den Fragmentationsfunktionen der inklusiven Hadronenproduktion auf.
Nachdem wir die Formulierung von Jetwirkungsquerschnitten mittels Jetfunktionen etabliert haben, wenden wir uns der Produktion von identifizierten Hadronen im Inneren von Jets zu. Wir verwenden wieder die NJA um die partonischen Wirkungsquerschnitte analytisch zu formulieren. Diesmal geschieht dies unter Verwendung zweierlei Arten von geeigneten semi-inklusiven Jetfunktionen. Die erste Art beschreibt die Entstehung des Jets. Die zweite Art parametrisiert die Entstehung eines spezifischen Partons innerhalb des Jets. Dieses Parton

durchläuft schließlich den komplizierten und noch nicht ganz verstandenen Prozess der Hadronisierung. Dadurch wird das beobachtete Hadron im Endzustand erzeugt. Im Rahmen der faktorisierten pQCD wird die Hadronisierung durch nicht-störungstheoretische Funktionen beschrieben; diese werden Fragmentationsfunktionen genannt. Wir zeigen, wie wichtig Hadron-in-Jet-Produktion ist, um neue Informationen über Fragmentationsfunktionen zu gewinnen. In führender Ordnung (LO) sondiert der Wirkungsquerschnitt nämlich direkt die Fragmentationsfunktionen. Dies geschieht in einer ähnlichen Art und Weise wie bei "single-inclusive annihilation" (SIA).

Kürzlich wurden erste Daten für beobachtete D^*-Mesonen innerhalb eines Jets von der ATLAS Kollaboration veröffentlicht. Diese Daten können mit den D^*-Fragmentationsfunktionen, die in der Literatur verfügbar sind, nicht zufriedenstellend beschrieben werden. Um zu überprüfen ob das ein Problem der Daten oder der Fragmentationsfunktionen ist, führen wir eine globale NLO Analyse von D^*-Fragmentationsfunktionen durch. Wir verwenden dazu Daten inklusiver Hadronenproduktion in Elektron-Positron-Annihilation sowie in hadronischen Kollisionen. Darüber hinaus verwenden wir auch zum ersten Mal Hadron-in-Jet-Daten für eine solche globale Analyse. Damit finden wir ein konsistentes Set von Fragmentationsfunktionen. Es liefert eine befriedigende Beschreibung aller verfügbaren Daten. Die Extraktion ist dank der analytischen Berechnung des Hadron-in-Jet-Wirkungsquerschnitts möglich. Analytische Rechnungen sind dabei eine Voraussetzung für effizienten numerischen Code.

Darüber hinaus präsentieren wir Ergebnisse zu zwei Themengebieten, welche mit den bisher beschriebenen eng verwandt sind. Motiviert durch den Erfolg der In-Jet-Fragmentation hinsichtlich der Extraktion von Parton-zu-Hadron-Fragmentationsfunktionen erweitern wir dieses Framework hin zur Photon-in-Jet-Produktion. Wir präsentieren die NLO Rechnung, welche notwendig ist um diesen Prozess in zukünftige Extraktionen von Parton-zu-Photon-Fragmentationsfunktionen miteinzubeziehen. Dazu verwenden wir die selben Techniken, die für die Hadron-in-Jet Rechnung entwickelt wurden. Dadurch gelingt es uns, analytische Ausdrücke zu formulieren. Dies geschieht mittels (photonischer) Jetfunktionen im Rahmen der NJA.

Zum Schluss präsentieren wir noch eine Analyse von Fragmentationsfunktionen, die über die gewöhnliche störungstheoretische Entwicklung hinaus geht. Dazu beziehen wir sogenannte "small-z" Resummationen mit ein. Diese Resummationen tragen dem singulären Verhalten der zeitartigen Evolutionskerne und der Koeffizientenfunktionen Rechnung. Indem man die divergenten Terme zu allen Ordnungen der Störungstheorie aufsummiert, können endliche Ergebnisse gewonnen werden. Die entsprechenden resummierten Ausdrücke sind in der Literatur allerdings nur für SIA vorhanden, weshalb unsere Analyse auf diesen Prozess beschränkt ist. Für eine sinnvolle Formulierung von integrierten Observablen sind solche resummierten Ausdrücke unbedingt notwendig. Wir haben jedoch herausgefunden, dass für phänomenologische Studien von differentiellen Observablen bereits Ergebnisse in nächst-zu-nächst-zu-führender Ordnung (NNLO) ausreichen. Zumindest im kinematischen Bereich, der heutzutage für Experimente zugänglich ist, genügt eine NNLO Rechnung für die zufriedenstellende Beschreibung der vorhandenen Daten. Die resummierten Ergebnisse zeigen nur vernachlässigbare Unterschiede im Vergleich zu NNLO Ergebnissen. Diese Unterschiede sind dabei weit innerhalb der experimentellen Unsicherheiten.

List of Publications

Journal papers

[I] Daniele P. Anderle, Tom Kaufmann, Felix Ringer, Marco Stratmann, Ivan Vitev,
"Using hadron-in-jet data in a global analysis of D^* fragmentation functions",
Phys. Rev. D**96** 034028 (2017)

[II] Daniele P. Anderle, Tom Kaufmann, Felix Ringer, Marco Stratmann,
"Fragmentation Functions Beyond Fixed Order Accuracy",
Phys. Rev. D**95** 054003 (2017)

[III] Tom Kaufmann, Asmita Mukherjee, Werner Vogelsang,
"Access to Photon Fragmentation Functions in Hadronic Jet Production",
Phys. Rev. D**93** 114021 (2016)

[IV] Tom Kaufmann, Asmita Mukherjee, Werner Vogelsang,
"Hadron Fragmentation Inside Jets in Hadronic Collisions",
Phys. Rev. D**92** 054015 (2015)

[V] Tom Kaufmann, Asmita Mukherjee, Werner Vogelsang,
"Next-to-leading Order Calculation for Jets Defined by a Maximized Jet Function",
Phys. Rev. D**91** 034001 (2015)

Conference Proceedings

[VI] Tom Kaufmann, Asmita Mukherjee, Werner Vogelsang,
"Recent developments on parton-to-photon fragmentation functions",
`arXiv:1708.06683`, to appear in the proceedings to the PHOTON 2017 conference.

[VII] Daniele P. Anderle, Tom Kaufmann, Felix Ringer, Marco Stratmann,
"Fragmentation functions at NNLO and their small-z logarithmic corrections",
Proceedings, Parton Radiation and Fragmentation from LHC to FCC-ee, pages 37-43, 2017

[VIII] Daniele P. Anderle, Tom Kaufmann, Felix Ringer, Marco Stratmann,
"Fragmentation Functions beyond Next-To-Leading Order",
PoS DIS2016 063 (2016)

Contents

Introduction

"What is the world made of?" This demanding question is what led mankind from philosophical considerations several thousand years ago to these days, where we have a well established theory based on empirical science which contains all our present knowledge on the answer of this question: The Standard Model of Particle Physics.

The outset of this journey in the history of particle physics may be dated back to the ancient Greek times, where philosophers introduced the concept of fundamental building blocks which make up everything around us. These microscopic objects were named atoms (from the Greek word "atomos" which means indivisible). However, in that time, the way of thinking about these fundamental objects was driven by philosophical and theological reasoning. It took quite a while until the methods of empirical science were used to investigate the building blocks of nature. In 19th century, scientists made first progress in understanding matter. The first milestone in particle physics was the discovery of the first subatomic particle, the electron, by J.J. Thompson in 1897 [1]. Only a few years later, H. Geiger, E. Marsden and E. Rutherford [2, 3] discovered in their famous scattering experiments around 1909 that the atom consists of a tiny, but very massive, positively charged nucleus which is surrounded by negatively charged electrons. Furthermore, Rutherford revealed in 1919 that the nucleus of nitrogen contains nuclei of hydrogen [4]. Hence, the hydrogen nucleus, which he later on named proton, seemed to be a building block of the nucleus of other atoms. Finally, J. Chadwick, a student of Rutherford, discovered the neutron as part of the nucleus in 1932 [5, 6]. This finding completed the picture of the atom, where the tiny but massive nucleus consists of protons and neutrons and is surrounded by very light electrons.

Beside the experimental progress, much theoretical effort is gone into understanding the building blocks of nature. The advent of quantum mechanics at the beginning of the 20th century helped a lot in understanding the nature of atoms. Especially the simplest atom, hydrogen, was extensively studied in the framework of quantum mechanics. This led to numerous predictions and explanations of experimental findings. However, for several decades an underlying theory to describe the rich field of phenomenology in nuclear physics was missing. Instead, models were used to give a phenomenological description of nuclear interactions. Progress was made, when it was realized that nucleons themselves have an inner structure and are not the fundamental particles by themselves. The recognition that nucleons are complex bound states of quarks and gluons finally paved the way to a fundamental theory of the interactions of nucleons: Quantum Chromodynamics (QCD), a quantum field theory which describes the strong interaction. Together with Quantum Electrodynamics (QED), describing the electroweak interaction, these two theories encode our present knowledge of the basic building blocks and forces in nature: The Standard Model of Particle Physics (SM). Today, we assume that the fundamental particles of nature are the fermionic quarks and leptons which interact through the exchange of gauge bosons. The SM thus describes three out of the four fundamental forces in physics: the strong, the weak and the electromagnetic interactions. Only gravity still stands separated from the other three, although much theoretical effort has been and still is being put into the unification of the SM and gravity. The SM is one of the most successful theories in the history of physics. Theoretical predictions are confirmed by astoundingly precise experimental measurements, like the anomalous magnetic dipole moment of the electron "$g-2$", to name only one example. However, even if there are many satisfying results, a lot of unanswered questions and issues with the SM remain. Certain experimental observations indicate physics beyond the SM (BSM). One example are the cosmological observations [7–9] that only about $\sim 5\%$ of the energy content of the universe is contributed by ordinary matter described by the SM, while $\sim 23\%$ are attributed to so-called dark matter and the remaining $\sim 72\%$ come from the completely unknown dark energy. But also for particles which are part of the SM there exist observations that cannot be explained by the SM itself: The phenomena of neutrino oscillations require at least two out of the three known neutrino species to have a non-zero mass. However, in the SM it is not possible to have massive neutrinos. Given these open issues, it is clear that searches for BSM physics have become very important in the last decades. The combined effort in understanding the SM and its predictions at very high accuracy on the one hand side, and the search for new physics on the other side, has led to the development of the world's most sophisticated experimental setups: particle colliders together with giant detectors located at the collision points.

The main focus of this thesis is on the QCD sector of the SM. QCD is a non-abelian gauge theory describing the interaction between spin-1/2 quarks and spin-1 gluons. While in the abelian case of QED the photon is electrically neutral and thus has no self-interaction, the gluons interact among themselves. They carry the charge of the strong interaction which is the so-called "color-charge". Another important difference compared to QED is, that the fundamental particles described by the theory (the quarks and gluons) do not exist as free particles. In nature, they are always confined into color-neutral bound states, called hadrons. The most prominent examples are the proton and the neutron. This main feature of QCD, the "confinement" is still not understood theoretically and subject of present research. Another crucial feature of QCD is "asymptotic freedom" [10, 11] that is the interaction between quarks and gluons becomes weak at high energies. This energy dependence of the coupling strength of the strong interaction allows utilizing the well known techniques of perturbation theory at high energies. Thus it is obvious that the experimental tool of choice to investigate the inner structure of hadrons are particle colliders which work at high energies.

The first remarkable success in discovering the hadron structure were deep inelastic scattering (DIS) experiments carried out at SLAC in 1968 [12, 13] which revealed that the nucleon is build up by point-like particles, named partons, which eventually turned out to be the quarks and gluons. In the following decades, many dedicated high energy collider experiments were set up, each revealing important new knowledge on the nature of elementary particles. PETRA and HERA at DESY helped discovering the gluon in 1979 [14–16] and understanding the proton structure, respectively. SPS at CERN discovered the massive gauge bosons of the electroweak interaction in 1983 [17–20] and LEP at CERN performed numerous precision experiments on the SM and provided an enormous amount of data on hadron production in electron-positron annihilation in the 1990s. The Tevatron at Fermilab proved the existence of the top quark in 1995 [21, 22]. Today, experiments like RHIC at BNL, KEKB at KEK, PEP-II at SLAC, or the most prominent one, LHC at CERN, aim to further extend our knowledge on the structure of hadrons. On the other hand, all of these experiments are also trying to find evidence for BSM physics.

As already mentioned above, theoretical calculations which are needed to understand the experimental outcome, are possible due to the fact that asymptotic freedom ensures a coupling strength which allows for perturbative calculations at collider energies. Another key concept to describe hadronic processes within the framework of perturbative QCD (which is a theory for the interaction of quarks and gluons) is factorization [23–32]. Factorization theorems allow for the separation of long-distance non-perturbative effects from the short-distance hard process of parton scattering. In a typical hadronic scattering process, the distribution of partons inside the hadrons is encoded in the so-called parton distribution functions (PDFs). In a leading order picture in the infinite-momentum frame, the PDFs may be interpreted as probability densities to find a certain parton inside the parent hadron which carries some longitudinal momentum fraction of the hadron. These initial state partons then undergo the hard scattering process and produce partons in the final state. However, it is not possible to observe the final state quark or gluon directly, as they are not colorless objects. Each final state parton undergoes a complicated and not completely understood process of hadronization. In the factorized framework, this hadronization process is parametrized with another set of non-perturbative functions, the so-called fragmentation functions (FFs).

While the perturbative hard scattering cross sections may be computed in perturbative QCD, the non-perturbative ingredients cannot be calculated from first principles. They have to be extracted from experimental data. This is done by several collaborations which have developed sophisticated methods over the last decades. The main idea is based on the assumption that PDFs and FFs are universal, i.e. process independent functions. Hence, they may be extracted from certain reference processes and used for the calculation of other processes. The textbook example for the reference process to gain information on PDFs is DIS, $ep \to e'X$. In the final state, only the electron is observed, which is a very clean signal, while in the initial state the proton needs to be described with PDFs. At leading order (LO) in perturbation theory, the cross section is directly proportional to the PDFs, which makes this process valuable for gaining information on PDFs. Another example of a clean final state is jet production. A jet is defined as collimated hadronic energy in a certain solid angle. Since only the energy is observed and not the individual hadrons contributing to a jet, there is no need for FFs. The only non-perturbative functions entering this process are the PDFs for initial state hadrons. In a similar way, clean reference processes for the extraction of FFs do not have PDF contamination in the initial state. Hence, the prime example is hadron production in semi-inclusive annihilation (SIA), $e^+e^- \to hX$.

However, it was noticed that using only such “simple” and clean processes is not enough to obtain precise information on FFs and PDFs. The simple processes are not able to disentangle different flavor contributions or to give information on the gluon FFs or PDFs. Thus, more elaborate processes have to be used in addition to the clean processes mentioned above. This turns the extraction of PDFs and FFs into global QCD analyses.

The precise knowledge of PDFs and FFs is crucial for making predictions for current collider experiments. Since several experiments are searching for BSM physics by looking for very small deviations from data compared to SM calculations, said calculations have to be very precise. Theorists try to include higher and higher orders in perturbation theory or electroweak corrections to QCD processes. However, the non-perturbative functions still account for a large amount of the theoretical uncertainties of phenomenological calculations. While the PDFs are rather well constrained and usually have an uncertainty of a few percent, the FFs often have uncertainties exceeding ten percent. Thus, a better understanding of the non-perturbative functions is not only interesting by itself and to gain more insight into the structure of the nucleon and the process of hadronization, but it is also crucial for precision tests of the SM and the search of new physics beyond the SM.

This thesis is focused on jets and fragmentation processes. We study several processes which hopefully will help for a better determination of non-perturbative functions in the near future. As mentioned above, jet cross sections are an important ingredient to global PDF analyses. Furthermore, jets are copiously produced in hadronic collisions and hence are an important background signal for basically all observables at hadron colliders. However, a jet is not intrinsically well defined. One has to specify what is meant by "collimated hadronic energy in a certain solid angle". This is done by the jet algorithm. Several jet algorithms exist with different advantages and disadvantages. Today, most experiments work with the anti-k_T algorithm [33]. However, it is important to further study different and new jet algorithms to see if they come with more advantages compared to the ones which are frequently used. In 2014 a new jet algorithm, based on maximizing a suitable function of the jet's energy and momentum, was proposed by H. Georgi [34]. We perform a first analytical NLO calculation of single-inclusive jet production using this newly developed jet algorithm to define the jets in Chap. 2. Moreover, we present an elegant formulation of jet cross sections in terms of jet functions which show close analogy to fragmentation functions, but are calculable in perturbation theory.

In Chap. 3 we then present an observable which combines jets and fragmentation into one process: in-jet fragmentation. Hence, the final state is characterized by an identified hadron inside a fully reconstructed jet. This class of processes was first developed in the framework of soft-collinear effective theory (SCET) for e^+e^- collisions and in an exclusive setup for pp collisions [35–39]. Our calculation is the first analytical NLO calculation of the partonic cross sections for an inclusive measurement in pp collisions. We found out that this process offers valuable complementary information on parton-to-hadron fragmentation functions, especially for the gluon. We expect our calculation to be included in global FF analyses for identified light hadrons as soon as corresponding data are available. To this date, experimental results for identified hadrons inside jets are measured by the ATLAS collaboration for D^* mesons [40] as well as prompt and non-prompt J/ψ production in jets [41] from LHCb. D^* mesons are heavy charmed mesons for which the usual massless framework is only applicable at sufficiently high transverse momenta of the observed D^* meson. Otherwise, mass effects will become non-negligible. With this caveat we present a global NLO extraction of D^* FFs from SIA, inclusive pp and hadron-in-jet data in Chap. 4.

After having realized the enormous potential of in-jet fragmentation processes concerning the access to fragmentation functions, we perform a similar calculation for photon-in-jet production in Chap. 5. The parton-to-photon FFs are relatively unknown and only two extractions have been made in the mid-90s. The main issue is the lack of precise data: Photon production in single-inclusive annihilation is dominated by the fragmentation contribution, however only sparse data with large uncertainties exist. In contrast, quite some data exist for hadro-production of photons from several fixed target experiments and also from the PHENIX collaboration at RHIC. However, it turns out that these processes are quite insensitive to (especially the gluon) fragmentation functions. Thus, we suggest the process of

photon-in-jet production to be used in future FF extractions. We show in Chap. 5 that this process is very sensitive to the FFs, as the direct component is not present at LO. We also perform a detailed background analysis for the dominant π^0 background which is present in any measurement with observed final state photons.
Finally, we study one aspect of FFs beyond fixed order accuracy. Fixed order analyses of FFs always have a limited range of validity in the longitudinal momentum fraction z transferred from the fragmenting parton to the hadron. This is mainly due to the singular behavior of fixed order expressions in the large- and small-z region. For $z \to 0$, the singular behavior is caused by two additional powers of $\log^{2k}(z)$ that arise in each fixed order of the strong coupling constant α_s^k. The well established procedure to deal with such logarithms at the edge of phase space is resummation. Small-z resummed results for the coefficient functions of SIA and also for the time-like evolution kernels can be found at next-to-next-to-leading logarithmic (NNLL) accuracy in literature [42, 43]. In Chap. 6 we study the relevance of these resummations for phenomenological applications in kinematical regimes relevant for today's experiments. We perform an extraction of small-z resummed FFs at NNLO+NNLL accuracy and find only moderate effects compared to fixed-order NNLO FFs.

Before presenting the topics discussed above, we invite the reader to a short introduction on the basic theoretical methods used in this thesis: In Chap. 1 we start by introducing the Lagrangian density of QCD and recalling the main features of pQCD like the running of the strong coupling, infrared safety, factorization and evolution. Afterwards, an overview of parton-to-hadron and parton-to-photon fragmentation functions is presented. Finally, we summarize the basic theoretical concepts of jet physics before presenting the explicit NLO calculation for single-inclusive jet production in Chap. 2.

Chapter 1

Theoretical Framework and Basic Concepts

1.1 Quantum Chromodynamics

In the 1950's and 60's the field of particle physics was quite chaotic. Many high energy experiments around the world frequently discovered new strongly interacting hadrons. The situation was comparable to chemistry before Mendeleev (1869) and Meyer (1870) brought order into the known chemical elements by introducing the periodic table of elements. Around 1960 physicists aimed for structure within the variety observed hadrons. A first attempt in understanding the particle zoo was the "eightfold way" by Gell-Mann [44] and Ne'eman [45] in 1961. Thereafter, in 1964, Gell-Mann [46] and Zweig [47] came up with the concept of quarks. The idea was that fundamental particles were quarks, spin 1/2 point-like particles, rather than hadrons themselves. Instead, hadrons were regarded as bound states formed by quarks. They could either be built from three quarks (baryons) or by an quark antiquark pair (mesons). This model explained in a natural way the organization of hadrons in the eightfold way. With structure, predictive power came back and the Ω^--baryon was proposed and later on found by experimentalists at the Brookhaven National Laboratory [48]. However, most particle physicists of that time did not actually believe in the existence of quarks as physical particles. First direct evidence that quarks actually exist was found in deep inelastic scattering (DIS) experiments at the Stanford Linear Accelerator Center in 1968 [12, 13]. However, it took nearly 30 years until the last quark, the so called top quark, was discovered at Fermilab in 1995 [21, 22]. Even if the quark model had its first success, there were a lot of unanswered problems, e.g. the statistics problem with the Δ^{++}-baryon or the question why there are only qqq or $q\bar{q}$ bound states and none of all the other possible combinations of quarks and antiquarks. The statistics problem was explained by the introduction of color in 1965 [49]. The concept of color was confirmed by other experimental evidence, like the $\pi^0 \to \gamma\gamma$ decay rate or the ratio of produced hadrons to produced muons in e^+e^- collisions.

Already in 1954, Yang and Mills presented a Lagrangian density which is invariant under local $SU(N)$ gauge transformations [50]. Their concept was extended and color was used as a starting point for a gauge theory by Fritzsch, Gell-Mann and Leutwyler in 1973 [51]. This was the birth of Quantum Chromodynamics (QCD). In the same year, Gross and Wilczek [10], and Politzer [11] discovered the asymptotic freedom of QCD, i.e. the interaction between quarks and gluons becomes weak at high energies.

1.1.1 Lagrangian of QCD

After experimental evidence for the existence of quarks was found in DIS experiments, a gauge theory of strong interaction was developed. Here, we only give a very brief summary of the main aspects in the construction of an appropriate Lagrangian density. For further details, we refer to any standard textbook on QCD, e.g. [52–54]. We start with the quark content of QCD which is expressed in analogy to the electron content of QED as

$$\mathcal{L}_{\text{quark}} = \sum_f \bar{q}_f (i\not{\mathcal{D}} - m_f) q_f \,, \tag{1.1}$$

where the sum runs over the N_f quark flavors and m_f is the mass of the quark with flavor f. It is known from experiments that the physical world is independent of the three color degrees of freedom, meaning that observables are independent of the explicit color configurations of the elementary particles. Demanding this condition at every point separately leads to a local $SU(3)$ symmetry. Mathematically speaking, the Lagrange density has to be invariant under local $SU(3)$ transformations $U(x)$ which may be expressed as

$$U(x) \equiv e^{i\alpha_a(x)T_a} \,, \qquad a \in \{1 \dots 8\} \,. \tag{1.2}$$

This unitary operator is defined by the $N^2 - 1 = 8$ generators T_a of $SU(N = 3)$. A common choice is $T_a \equiv \lambda_a/2$ with the Gell-Mann matrices $\lambda_a \in \mathbb{C}^{3\times 3}$ [55]. The unitarity of $U(x)$ implies that the generators are traceless. Furthermore, they obey the commutation relations

$$\left[T^a, T^b\right] = i f^{abc} T^c \qquad \Leftrightarrow \qquad i f^{abc} = 2\,\mathrm{Tr}\left(\left[T^a, T^b\right] T^c\right) \,. \tag{1.3}$$

which, as indicated, define the so-called (antisymmetric) structure constants f^{abc}. The quark fields transform under this $SU(3)$ rotation as

$$\begin{aligned} q_f(x) &\rightarrow q'_f(x) = U(x) q_f(x) \,, \\ \bar{q}_f(x) &\rightarrow \bar{q}'_f(x) = \bar{q}_f(x) U^\dagger(x) \,. \end{aligned} \tag{1.4}$$

Due to the unitarity of $U(x)$, the mass term in Eq. (1.1) is trivially invariant with respect to this transformation. More work has to be done for the kinetic term. To ensure invariance as well, one has to introduce a new vector gauge field A^a_μ in the definition of the covariant derivative

$$\mathcal{D}_\mu = \partial_\mu - i g_s A^a_\mu T_a \,, \tag{1.5}$$

where the coupling strength of QCD is denoted by g_s. This gauge field A^a_μ represents the gluon degrees of freedom. In analogy to QED, a kinetic term for the gauge fields is obtained by constructing the field strength tensor $G^a_{\mu\nu}$, which is defined by the commutator of two covariant derivatives,

$$\left[\mathcal{D}_\mu, \mathcal{D}_\nu\right] q_f(x) \equiv i g_s T_a G^a_{\mu\nu} q_f(x) \,. \tag{1.6}$$

Hence,

$$G^a_{\mu\nu} = \partial_\mu A^a_\nu - \partial_\nu A^a_\mu - g_s f_{abc} A^b_\mu A^c_\nu \,. \tag{1.7}$$

The last term in Eq. (1.7) describes the self interaction of the gluon field. It is present due to the fact that QCD is a non-abelian gauge theory. This term is the main difference compared to the Lagrangian density of QED. The kinetic term for the gluon field may be written as

$$\mathcal{L}_{\text{gluon}} = -\frac{1}{4} G^a_{\mu\nu} G^{\mu\nu}_a \,. \tag{1.8}$$

As it contains two field strength tensors this part gives rise to terms which are cubic and quartic in the gauge field A^a_μ. This yields a three and four gluon vertex which makes QCD calculations much more sophisticated than the QED pendants. We note that including a mass for the gluon is not possible in a gauge invariant way. For example, a typical mass term

$$\propto m^2 A^a_\mu A^\mu_a \tag{1.9}$$

is not gauge invariant.
Combining the results for the quark and the gluon content, one obtains a classical Lagrangian density containing mass, kinetic and interaction terms

$$\mathcal{L}_{\text{class}} = \mathcal{L}_{\text{quark}} + \mathcal{L}_{\text{gluon}} \tag{1.10}$$

To obtain a quantization of the theory, the path integral formalism is conveniently used [56–58]. When using this formalism, the gauge has to be fixed. For covariant gauges, the condition $\partial_\mu A^\mu_a = 0$ is implemented by adding the gauge fixing term

$$\mathcal{L}_{\text{gauge}} = -\frac{1}{2\xi}(\partial_\mu A^\mu_a)^2 \,. \tag{1.11}$$

The arbitrary gauge parameter ξ defines the gauge. Prominent choices are Feynman gauge $\xi = 1$, Landau gauge $\xi \to 0$ and Unitary gauge $\xi \to \infty$.

If the gauge is fixed in the way described above, one has to add another term to the Lagrangian density involving scalar Grassmann fields. Following Fermi statistics, these fields η^a are unphysical. They are known as Faddeev-Popov ghosts [59]. Besides helping to deal with mathematical issues in the path integral quantization they rule out unphysical degrees of freedom of the gluon fields. The ghost term is given by

$$\mathcal{L}_{\text{ghost}} = \partial_\mu \bar{\eta}^a \mathcal{D}^\mu_{ab} \eta^b \,, \tag{1.12}$$

where the covariant derivative in the adjoint representation reads $\mathcal{D}^\mu_{ab} = \partial^\mu \delta_{ab} - g_s f^{abc} A^\mu_c$.

Combining everything above, one is ready to write down the complete Lagrangian density of QCD

$$\mathcal{L}_{\text{QCD}} \quad = \quad \mathcal{L}_{\text{class}} + \mathcal{L}_{\text{gauge}} + \mathcal{L}_{\text{ghost}} \,. \tag{1.13}$$

The Feynman rules of QCD derived from the Lagrangian density (1.13) may be found in any standard text book on QCD (see e.g. [52–54]) and we refrain from listing them here.

We finally note, that it is also possible to choose non-covariant gauges [60], for instance Coulomb or axial gauges. For the latter ones, the condition $n^\mu A^a_\mu = 0$, for a fixed gauge vector n^μ, may be implemented by the gauge fixing term

$$\mathcal{L}_{\text{gauge}} = -\frac{1}{2\xi}(n_\mu A^\mu_a)^2 \,. \tag{1.14}$$

If $n^2 < 0$ the gauge is called a pure axial gauge, while $n^2 = 0$ is named light-cone gauge and $n^2 > 0$ is referred to as temporal gauge. Compared to covariant gauges, axial gauges have the advantage of being ghost-less, i.e. there is no need to introduce the unphysical ghost fields. This is why they are sometimes referred to as "physical gauges". The price to pay is that the gluon propagator takes a more complicated form and loop integrations have to be performed very carefully [60].

1.1.2 The Running Coupling

As will be discussed below, physical observables are formulated in terms of squared matrix elements. Hence, they always come with an even power of g_s. Thus, it is convenient to consider expressions in terms of the strong coupling

$$\alpha_s \equiv \frac{g_s^2}{4\pi}\,, \tag{1.15}$$

rather than in terms of g_s. Obviously, α_s is defined in complete analogy to the fine structure constant in QED,

$$\alpha \equiv \frac{e^2}{4\pi}\,, \tag{1.16}$$

where e is the elementary charge. Moreover, in literature and during this work, expressions are sometimes formulated in terms of

$$a_s \equiv \frac{\alpha_s}{4\pi} = \left(\frac{g_s}{4\pi}\right)^2 \tag{1.17}$$

rather than the strong coupling itself.

If one calculates a quantity using a perturbative expansion in α_s one encounters ultraviolet divergencies caused by loop diagrams. This is not a specific QCD issue, but also occurs, for example, in QED. Ultraviolet divergencies are handled with a standard procedure called renormalization, which we address to some extend in Sec. 1.1.3. The important point in the process of renormalization is the introduction of an arbitrary mass scale μ_R. By demanding that a physical observable must not have any dependence on this scale, one obtains a so-called renormalization group equation (RGE). The RGE is a differential equation describing the dependence of α_s on the scale μ_R

$$\mu_R^2 \frac{d\alpha_s(\mu_R^2)}{d\mu_R^2} = \beta(\alpha_s) \equiv -\alpha_s^2 \sum_{k=0}^{\infty} b_k \alpha_s^k\,. \tag{1.18}$$

Note that sometimes in literature and also in this thesis coefficients β_k are used instead of b_k. They are related by

$$\beta_k = b_k (4\pi)^{k+1}\,. \tag{1.19}$$

The function introduced in Eq. (1.18) is known as the beta function of QCD. The coefficients b_k of its expansion can be calculated in perturbation theory. To this day, $\beta(\alpha_s)$ is known up to next-to-next-to-next-to-leading order (N^{3}LO), i.e. b_3 [61–63]. The first coefficients of the expansion read

$$\begin{aligned} b_0 &= \frac{11C_A - 2N_f}{12\pi}\,, \\ b_1 &= \frac{17C_A^2 - 5C_A N_f - 3C_F N_f}{24\pi^2}\,, \end{aligned} \tag{1.20}$$

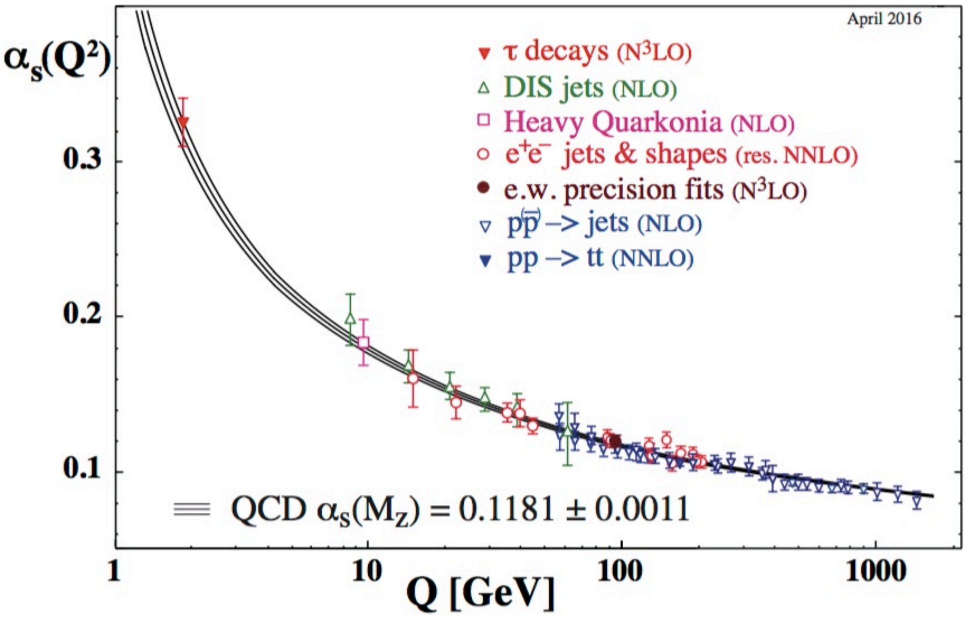

Figure 1.1: The strong coupling constant from theory and experiment. The non-perturbative input is extracted at the Z-boson mass, $\mu_0 = M_Z$. Figure taken from the "Review of Particle Physics (2016)" [64].

where $C_A = 3$ and $C_F = 4/3$ are the usual $SU(3)$ Casimir operators. It is worth mentioning that the coefficients $b_{k\geq 2}$ are renormalization scheme dependent. The fact that α_s becomes small for high energies, which is called asymptotic freedom, originates from the negative QCD beta function. As can be seen in Eq. (1.20), this remains true as long as there are no more than 16 quark flavors, i.e. $N_f \leq 16$.

At leading order, the RGE (1.18) can be solved analytically,

$$\alpha_s(\mu_R^2) = \frac{\alpha_s(\mu_0^2)}{1 + b_0 \alpha_s(\mu_0^2) \log\left(\frac{\mu_R^2}{\mu_0^2}\right)} . \tag{1.21}$$

Beyond the leading order, it is possible to derive an implicit equation for α_s which may be solved approximately, see e.g. [52]. Thus, one is able to compute α_s at a given scale in perturbation theory if the value of the strong coupling constant is known at some reference scale μ_0. $\alpha_s(\mu_0)$ is a first example of a "non-perturbative" input which has to be determined from experiments. In practical applications, α_s is often determined by simply solving the differential equation (1.18) numerically, for example by using Runge-Kutta methods.
Fig. 1.1 shows a prediction of α_s together with several experimental data points. From there it can be seen that $\alpha_s < 1$ for sufficiently large energies and thus, in principle, allows to define a perturbative series in α_s.
However, it is known that the coefficients of a perturbative series in QCD diverge [65, 66]. To be more precise, let us consider a physical quantity, described as a series $f = \sum_{n=0}^{\infty} f_n \alpha_s^n$.

In QCD, the coefficients f_n show factorial growth, $f_n \sim K n! a^n n^b$, with some constants K, a and b [65]. The series would equal the quantity f only for $\alpha_s = 0$. For $\alpha_s \to 0$ the series can in the best case scenario be asymptotic to f. In general, a series is called asymptotic if

$$\left| f - \sum_{n=0}^{N} f_n \alpha_s^n \right| \leq C_{N+1} \alpha_s^{N+1} \tag{1.22}$$

for $N \in \mathbb{N}$ and some constant C. An asymptotic series does not uniquely define f. However, if α_s is sufficiently small, the series may give a well-approximated answer. It is one of the main assumptions of pQCD, which has not been strictly proven yet, that perturbative series are asymptotic.

Another crucial ingredient for pQCD calculations is the incoherence of long- and short-distance effects. Thus, one has to consider observables that either are insensitive to long-distance physics or for which the long- and short-distance physics can be separated in a systematic way. These considerations give rise to two essential concepts of pQCD, namely infrared safety and factorization, which will be discussed in Sec. 1.2. While factorization is proven for a variety of inclusive processes [23–32] it can only be assumed for other processes. However, the impressive success of pQCD calculations in describing the experimental data makes people very confident that the assumptions mentioned above will eventually turn out to be true.

1.1.3 Perturbative QCD

The running of the strong coupling constant basically divides QCD into two regions: the low energy regime and the high energy regime. Although the transition is smooth between the two regions, an energy scale around $1 - 5$ GeV roughly separates the two. The low energy regime is arguably less understood and there are many open issues which are subject to current research. To name only some of them, much effort is put into the investigation of confinement, quark masses, and the non-trivial structure of the QCD vacuum. As analytical pQCD calculations are not reliable for low energies, other methods have to be used, for example lattice calculations, chiral effective theory or various model approaches [67]. However, the focus of this thesis is on the high energy regime which we will address in detail from now on.

In the high energy regime, where the coupling constant of QCD is sufficiently small, we may calculate observables using perturbation theory, if we accept the assumptions mentioned at the end of Sec. 1.1.2. Our main interest lies on scattering processes. Basically all observables for this type of processes are formulated in terms of (differential) cross sections. A cross section of a specific process is proportional to the probability of said process to happen. As extensively discussed in any standard textbook on quantum field theory (see e.g. [52–54]), the probability of a scattering process from an initial state $|i\rangle$ into a final state $|f\rangle$ is given by $\mathcal{P}_{i\to f} \propto |\langle f|\hat{S} - \mathbb{1}|i\rangle|^2$. It is related to the interaction Lagrangian $\mathcal{L}_I$ via the "scattering operator" (also called S-matrix)

$$\hat{S} \equiv \mathcal{T} \exp\left[i \int d^4x \, \mathcal{L}_I \right] . \tag{1.23}$$

Here, $\mathcal{T}$ denotes the usual time-ordering operator. Assuming $|i\rangle$ and $|f\rangle$ to be momentum eigenstates, the matrix element can be expressed as [54]

$$\langle f|\hat{S} - \mathbb{1}|i\rangle = i(2\pi)^4\delta^4\left(\sum p_i - \sum p_f\right)\mathcal{M}_{i\to f}\,, \tag{1.24}$$

where the invariant matrix element $\mathcal{M}_{i\to f}$ describes the interaction of quarks and gluons. It can be expressed by a series expansion in α_s. These invariant matrix elements can be visualized by Feynman diagrams which follow from the Feynman rules that are derived from the Lagrangian. Each pictorial Feynman diagram represents a strict mathematical expression which can be evaluated according to the Feynman rules. Formally, Eq. (1.24) is obtained from the "Lehmann-Symanzik-Zimmermann" (LSZ) reduction formula [68].
In this thesis, we are mainly interested in cross sections describing a $2 \to n$ scattering process. The cross section is obtained by integrating the matrix element squared over the respective n-body final state phase space Φ_n,

$$\sigma^{2\to n} = \frac{1}{F(p_1,p_2)}\int d\Phi_n\,|\mathcal{M}_{i\to f}|^2\,, \tag{1.25}$$

where the flux-factor $F(p_1,p_2)$ depends on the momenta of the two initial state particles. Accordingly, a differential cross section is obtained if one does not integrate out the full phase space, but keeps it differential in the desired variables. As mentioned above, $\mathcal{M}_{i\to f}$ and thus the cross section is expressed as a series in α_s. The first non-vanishing order defines the leading order (LO), followed by the next-to-leading order (NLO), the next-to-next-to-leading order (NNLO), and so forth.

Equation (1.25) serves as a working formula for pQCD calculations. First, one has to find all relevant Feynman diagrams for the process of interest. They are obtained basically from combinatorial considerations which become numerous and complicated for higher order calculations. Then, one has to compute the matrix elements squared using the Feynman rules. Also the appropriate (differential) phase space has to be calculated. In the end, the matrix element is integrated over the phase space to obtain the final result. Beyond the leading order, however, calculations suffer from several technical problems. One big issue is the appearance of all kinds of singularities. As it turns out (see e.g. [52–54]), they are only present in the intermediate steps of a calculation while the final result for a well defined observable turns out to be finite. In a massless pQCD approach, the singularities emerge from three sources:

Soft or infrared divergencies emerge when a parent parton emits a parton with vanishing four-momentum. This may be seen, for example, in Fig. 1.2a. The propagator of the intermediate parton with momentum $q = k_1 + k_2$ contains a term $\propto 1/q^2$ which may be expressed as

$$\frac{1}{q^2} = \frac{1}{(k_1+k_2)^2} = \frac{1}{2E_1E_2(1-\cos\theta_{12})}\,, \tag{1.26}$$

where E_1 and E_2 are the energies of the partons with four-momentum k_1 and k_2, respectively, and θ_{12} is the angle between their corresponding three momenta. It is clear, that this propagator will diverge if $E_1 \to 0$ or $E_2 \to 0$, i.e. if one of the daughter partons becomes soft.

- **Collinear divergencies** appear when a parent parton splits collinearly into two daughter partons. This may also be seen in Fig. 1.2a and Eq. (1.26), respectively. The propagator not only diverges in the soft limit, but also when $\cos\theta_{12} \to 1$, i.e. $\theta_{12} \to 0$.

- **Ultraviolet divergencies** are caused by loop integrals which appear e.g. in virtual corrections to a diagram. As an example we show a virtual correction to the quark propagator in Fig. 1.2b. Since we do not observe the virtual gluon, we have to integrate over all possible loop momenta l. This gives an integral of the form

  $$I = \int \frac{d^4 l}{(2\pi)^4} \frac{n(l)}{l^2 (l-p)^2}\,, \tag{1.27}$$

  where the numerator factor $n(l)$ is polynomial in l and contains all trivial factors. Naive power counting reveals that this diagram has a superficial degree of divergence of

  $$D = 4 \cdot (\#\text{loops}) - 2 \cdot (\#\text{inner lines}) = 4 \cdot 1 - 2 \cdot 2 = 0\,. \tag{1.28}$$

  The fact that $D \geq 0$ indicates that this diagram might be divergent for $l \to \infty$, which may be confirmed by an explicit calculation, see e.g. [69].

Details on the occurrence of soft and collinear divergencies as well as their disappearance in final results will be discussed in Sec. 1.2. The ultraviolet divergencies are removed by a procedure called renormalization. The basic idea is to find a way of regulating the divergencies by making them manifest. The regularization frequently used today is the so-called dimensional regularization [70–73]. One uses the number of dimensions as a regularization parameter by performing calculations in $n = 4 - 2\varepsilon$ dimensions. This is motivated by the observation that divergent integrals in 4 dimensions may be convergent in less than 4 dimensions. Calculations in non-integer dimensions are performed by means of analytical continuation. First, integrals are solved in n dimensions, where n is assumed to be integer. The result is then formulated in terms of functions which allow for analytical continuation

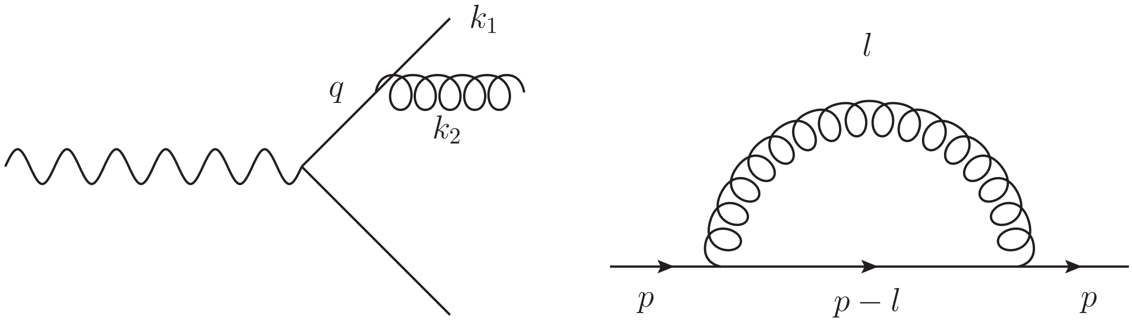

(a) Gluon radiation **(b)** Loop diagram

Figure 1.2: Two example diagrams which cause divergencies. On the left, we have a gluon radiation diagram which may cause a soft and/or collinear divergency. On the right, we have a loop diagram which causes an ultraviolet divergency due to the integration over the unobserved loop momentum. See discussion in text.

(e.g. the Euler Gamma and Beta functions) so that in the end the dimension n can be real as well.

In dimensional regularization, the divergencies mentioned above manifest themselves in $1/\varepsilon^k,\ k \in \mathbb{N}$ singularities. To obtain a renormalized theory, one adds a finite number of terms at any order in perturbation theory, so-called "counter-terms". This basically gives a redefinition of all fields and parameters (couplings, masses, etc.). During the redefinition, the singularities are removed into the former unrenormalized (also called "bare") quantities. One has the freedom to remove not only the poles, but also finite terms into the bare quantities. The explicit prescription of this removal is defined by the renormalization scheme. Removing only the poles in ε is known as the minimal subtraction (MS) scheme [74]. As the poles appearing in dimensional regularization usually are accompanied by the terms

$$\frac{1}{\varepsilon} + \log 4\pi - \gamma_E\,, \tag{1.29}$$

with the Euler-Mascheroni constant γ_E, it is common to remove these finite terms together with the singularity. This is called the modified minimal subtraction ($\overline{\text{MS}}$) scheme [75, 76]. The $\overline{\text{MS}}$ scheme is among the most popular schemes in pQCD calculations and also used throughout this thesis if not stated otherwise. A side effect of the renormalization procedure is the introduction of a new (and arbitrary) scale μ_R, because the requirement of a dimensionless action $S = \int d^n x\, \mathcal{L}(x)$ demands the replacement $g_s \to \tilde{g}_s = \mu_R^{\varepsilon}\, g_s$ [77, 78].

1.2 Infrared Safety and Factorization

As described in Sec. 1.1.2, the incoherence of short- and long-distance physics leads to the basic concepts of infrared safety and factorization. In this section we will discuss these concepts in some detail. A formal definition of an infrared safe quantity may be found, for instance, in [79, 80]. We look at an explicit example, and, following the notation in Refs. [79, 80], express an observable in terms of the cross sections

$$\frac{d\sigma[n]}{d\Omega_2 dE_3 d\Omega_3 \cdots dE_n d\Omega_n}\,. \tag{1.30}$$

They describe the production of n hadrons in e^+e^- annihilation. We denote the energy and the solid angle of the jth hadron with E_j and Ω_j, respectively. Some inclusive measurement $\mathcal{I}$ shall be given in terms of symmetric functions $\mathcal{S}_n$ as

$$\begin{aligned}\mathcal{I} \;=\;& \frac{1}{2!}\int d\Omega_2 \frac{d\sigma[2]}{d\Omega_2}\mathcal{S}_2(p_1^\mu, p_2^\mu)\\ &+\frac{1}{3!}\int d\Omega_2 dE_3 d\Omega_3 \frac{d\sigma[3]}{d\Omega_2 dE_3 d\Omega_3}\mathcal{S}_3(p_1^\mu, p_2^\mu, p_3^\mu)\\ &+\cdots\,.\end{aligned} \tag{1.31}$$

To obtain an infrared safe measurement, the functions $\mathcal{S}_n$ have to satisfy

$$\mathcal{S}_{n+1}(p_1^\mu, \ldots, (1-\lambda)p_n^\mu, \lambda p_n^\mu) = \mathcal{S}_n(p_1^\mu, \ldots, p_n^\mu) \tag{1.32}$$

for $0 \le \lambda \le 1$. The physical picture of Eq. (1.32) is that our observable should not be sensitive to radiation with vanishing momentum (soft radiation) which is described by $\lambda = 0$

or $\lambda = 1$. Furthermore, the measurement should be insensitive to the splitting of a particle into two collinear ones ($0 < \lambda < 1$). Of course, the same is true vice versa, i.e. absorption of a soft particle or recombination of two collinear ones.
A simple example for an infrared safe measurement is the total cross section. Here we have

$$\mathcal{S}_n(p_1^\mu, \ldots, p_n^\mu) = 1 \qquad \forall n\,. \tag{1.33}$$

This trivially satisfies the condition (1.32). Other, less trivial, examples are "thrust" or n jet events. Jets will be discussed to some extend in Sec. 1.4.
While calculating the observable $\mathcal{I}$, infrared safety manifests itself in the cancellation of singularities. The divergent contributions emerge from configurations which are either simultaneously soft and collinear (giving rise to $1/\varepsilon^2$ poles) or simple $1/\varepsilon$ soft poles. The cancellation happens between virtual and real contributions when all matrix elements squared are added. This is guaranteed for infrared safe QCD observables by the Kinoshita-Lee-Nauenberg theorem [81, 82].
As a last remark, we note that although infrared safe observables are free of explicit divergencies, the cancellation of singularities leaves behind large logarithmic terms originating from the edge of phase space. Only in fully inclusive observables such logarithms are not present.

From the list of divergencies in Sec. 1.1.3 we have not talked about collinear divergencies yet. By renormalization and the cancellation of soft singularities, we gain control over UV and IR divergencies. The remaining collinear divergencies are removed by a procedure called factorization [23–32]. We want to discuss the concept of factorization with an explicit example: single-inclusive pion production in electron positron annihilation, $e^+e^- \to \gamma \to \pi X$, mediated through a photon, where X is some unobserved hadronic final state. This process is often referred to as semi-inclusive annihilation (SIA) in literature. We note that SIA is, of course, also possible with a Z boson as an intermediate particle. However, this may easily be included in the calculation by substituting the fractional quark charges e_q by the electroweak quark charges $\hat{e}_q$ which are listed, for example, in appendix A of [83].

We are interested in the cross section differential in the scaling variable

$$z \equiv \frac{2P_\pi \cdot q}{Q^2}\,, \tag{1.34}$$

where P_π and q are the four momenta of the observed pion and time-like photon, respectively, and $Q^2 \equiv q^2 > 0$. As q^2 is positive, SIA is often referred to as "time-like" process. Following the notation of [84] we express the cross section in terms of a transverse (T) and a longitudinal (L) cross section

$$\frac{d\sigma^\pi}{dz} = \sum_{k=T,L} \frac{d\sigma_k^\pi}{dz}\,. \tag{1.35}$$

Furthermore, we define the (structure) functions

$$F_k^\pi(z, Q^2) = \frac{1}{\sigma_{\text{tot}}^{(0)}(Q^2)} \frac{d\sigma_k^\pi}{dz}\,, \qquad k = T, L \tag{1.36}$$

where

$$\sigma^{(0)}_{\text{tot}}(Q^2) = \frac{4\pi\alpha^2}{3Q^2} N_c \sum_q e_q^2 \tag{1.37}$$

is the leading order cross section for the production of a $q\bar{q}$ pair summed over all flavors. It is not possible to calculate the production of hadrons from first principles. QCD gives us a theoretical framework at the level of quarks and gluons. Thus, we may calculate the production of a parton in e^+e^- annihilation in the framework of pQCD. These partonic results are then convoluted with non-perturbative functions which describe the transition of a given parton into a specific hadron. Hence, the functions defined in Eq. 1.36 are given by

$$\begin{aligned} F_k^\pi(z, Q^2) &= \sum_{p=q,\bar{q},g} \int_z^1 \frac{dx}{x} \tilde{D}_p^\pi\left(\frac{z}{x}\right) \tilde{\mathcal{F}}_{k,p}(x, Q^2, \varepsilon) && (1.38) \\ &\equiv \sum_{p=q,\bar{q},g} \left[\tilde{D}_p^\pi \otimes \tilde{\mathcal{F}}_{k,p}\right](z, Q^2, \varepsilon) \,. && (1.39) \end{aligned}$$

In the second line, we have defined a convolution $\otimes$ of two functions $g(x,\dots)$ and $f(x,\dots)$ with respect to their first argument as

$$[f \otimes g](z,\dots) \equiv \int_z^1 \frac{dx}{x} f\left(\frac{z}{x},\dots\right) g(x,\dots) \,. \tag{1.40}$$

For later reference, we note that this convolution may equivalently be written as

$$[f \otimes g](z) = \int_0^1 dx \int_0^1 dy\, f(x)\, g(y)\, \delta(z - xy) \,, \tag{1.41}$$

which sometimes turns out to be more useful than the definition in Eq. (1.40). The functions $\tilde{\mathcal{F}}_{k,p}(x, Q^2, \varepsilon)$ are the partonic analogues to the $F_k^\pi(z, Q^2)$. They are calculated as a perturbative series within the framework of pQCD from Feynman diagrams. The corresponding diagrams up to next-to-leading order are shown in Fig. 1.3. The partonic functions depend on the partonic scaling variable

$$x \equiv \frac{2k_p \cdot q}{Q^2} \,, \tag{1.42}$$

where k_p is the four momentum of the respective parton. Furthermore, as we use dimensional regularization, they carry an ε dependence. When performing the explicit calculation (see [85–87] for the calculation at next-to-leading order and [84] for next-to-next-to-leading order results) one encounters all the ε poles described in Sec. 1.1.3. The IR singularities cancel in the sum of real and virtual diagrams and the UV poles are removed by renormalization. The remaining $1/\varepsilon$ poles originate from collinear configurations. They are finally removed by factorizing them into the "bare" parton-to-pion fragmentation functions $\tilde{D}_p^\pi$. This is achieved by expressing

$$\begin{aligned} \tilde{\mathcal{F}}_{k,q} &= \Gamma_{qq} \otimes \mathbb{C}_{k,q} + \Gamma_{qg} \otimes \mathbb{C}_{k,g} \,, \\ \tilde{\mathcal{F}}_{k,g} &= \Gamma_{gq} \otimes \mathbb{C}_{k,q} + \Gamma_{gg} \otimes \mathbb{C}_{k,g} \,. && (1.43) \end{aligned}$$

with the transition functions Γ_{ij} which contain all collinear divergencies and the finite, ε independent coefficient functions $\mathbb{C}_{k,p}$. As we will show in Sec. 1.3.2 the transition functions

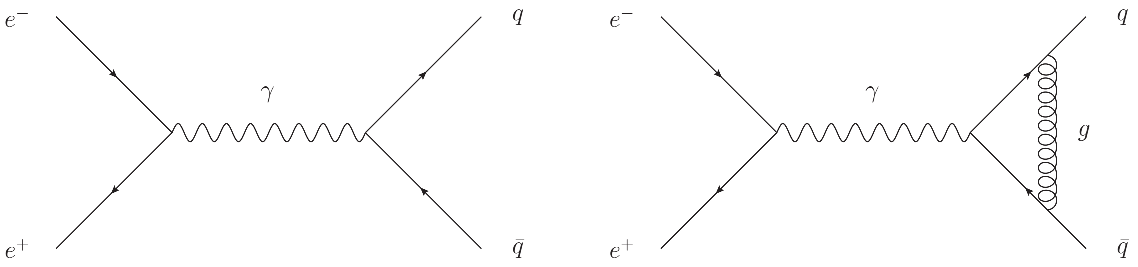

(a) LO **(b)** Virtual correction

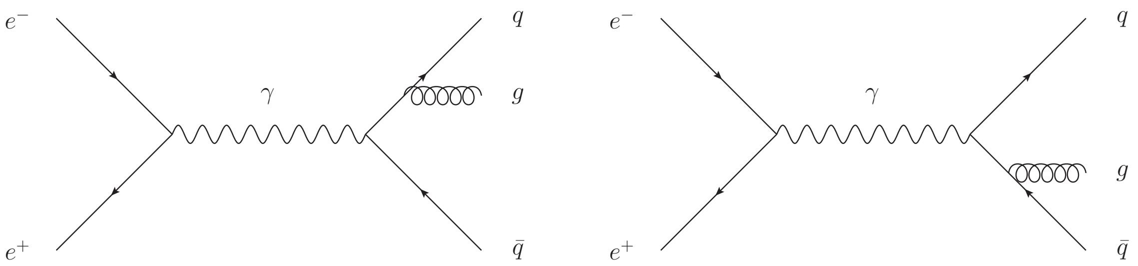

(c) Real correction **(d)** Real correction

Figure 1.3: The LO Feynman diagram for $e^+e^- \to q\bar{q}$ together with real and virtual NLO corrections.

may, in principle, be calculated order by order in a_s. We now insert Eq. (1.43) into (1.38) and the collinear divergencies are absorbed by the bare parton-to-pion fragmentation functions by defining the finite parton-to-pion fragmentation functions

$$\begin{aligned} D_q^\pi &\equiv \Gamma_{qq} \otimes \tilde{D}_q^\pi + \Gamma_{gq} \otimes \tilde{D}_g \\ D_g^\pi &\equiv \Gamma_{qg} \otimes \tilde{D}_q^\pi + \Gamma_{gg} \otimes \tilde{D}_g \,. \end{aligned} \tag{1.44}$$

This finally gives

$$F_k^\pi(z, Q^2) = \sum_{p=q,\bar{q},g} \int_z^1 \frac{dx}{x} D_p^\pi \left(\frac{z}{x}, \mu_f^2 \right) \mathbb{C}_{k,p} \left(x, \frac{Q^2}{\mu_f^2} \right) . \tag{1.45}$$

In the end, we are able to calculate our observable as a convolution of two finite quantities. Note, that the finite parton-to-pion fragmentation functions became dependent on the factorization scale μ_f. This is the scale at which the factorization is performed. The finite parton-to-hadron fragmentation functions are simply referred to as fragmentation functions (FFs). Similar to what is done in the renormalization procedure, one has the freedom to factorize finite parts into the bare quantities as well. Usually, one again removes the $(\log 4\pi - \gamma_E)$ terms which always come together with the $1/\varepsilon$ poles when using dimensional regularization. This $\overline{\text{MS}}$ factorization scheme is used during this thesis if not stated otherwise.

In this example, we have seen the basic techniques to obtain collinear finite observables by factorizing the poles into bare quantities. Of course, the method outlined above is not restricted to this explicit example. The calculation of structure functions for kaons, protons

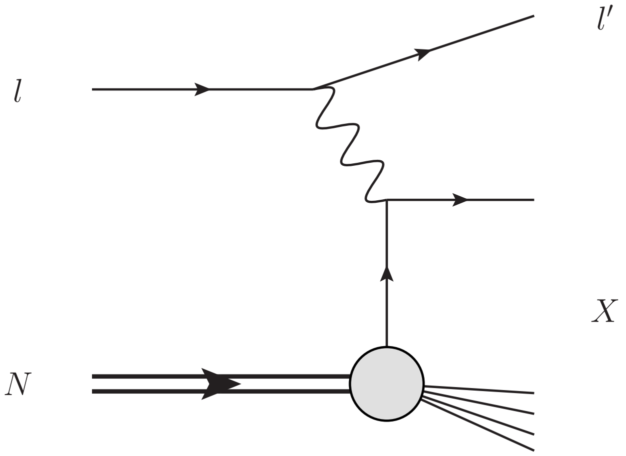

Figure 1.4: Schematic leading order diagram of the DIS process $lN \to l'X$.

or other light hadron species may be performed in a completely analogue way. The only ingredient needed are the respective parton-to-hadron fragmentation functions, while the coefficient functions are always the same.

Moreover, collinear configurations also appear in the initial state. The space-like analogue to the example presented above is the deep-inelastic scattering (DIS) process $lN \to l'X$, where l is a lepton which scatters off a nucleon N to produce an observed lepton l' and some unobserved remainder X in the final state. This process is schematically shown in Fig. 1.4. In this case, the collinear singularities are absorbed into bare initial state parton densities to obtain the finite parton distribution functions (PDFs). Similar to SIA, the observables of interest are the so-called inclusive longitudinal (L) and transverse (T) structure functions $F^{\mathrm{DIS}}_{k=T,L}$. In a factorized form, they read

$$F_k^{\mathrm{DIS}}(x_b, Q^2) = \sum_{p=q,\bar{q},g} \int_{x_b}^{1} \frac{d\xi}{\xi} f_p^N\left(\frac{x_b}{\xi}, \mu_f^2\right) \mathbb{C}^{\mathrm{DIS}}_{k,p}\left(\xi, \frac{Q^2}{\mu_f^2}\right) . \tag{1.46}$$

Here,

$$x_b = \frac{Q^2}{2P_N \cdot q} , \tag{1.47}$$

with P_N and q being the four momenta of the initial state nucleon and the virtual vector boson, respectively. Moreover, we have $Q^2 \equiv -q^2 > 0$. Hence, DIS is usually called a “space-like” process in contrast to the time-like SIA process. The coefficient functions $\mathbb{C}^{\mathrm{DIS}}_{k,p}$ are known up to next-to-next-to-leading order [88–90].

The concept of factorization is widely used, because without the separation of long- and short-distance physics it would not be possible to make predictions using perturbation theory. The two processes discussed so far may schematically be written in a factorized form as

$$\begin{aligned} d\sigma^{\mathrm{SIA}} &= d\hat{\sigma}^{\mathrm{SIA}} \otimes \mathrm{FF} , \\ d\sigma^{\mathrm{DIS}} &= \mathrm{PDF} \otimes d\hat{\sigma}^{\mathrm{DIS}} , \end{aligned} \tag{1.48}$$

where the hat on $d\hat{\sigma}$ indicates a quantity which may be calculated in perturbation theory, usually called "partonic cross section". However, factorized expressions may be more complicated, for example, semi-inclusive deep inelastic scattering (SIDIS) in which compared to DIS an additional hadron is observed in the final state. Hence, the factorized cross section schematically reads

$$d\sigma^{\rm SIDIS} = {\rm PDF} \otimes d\hat{\sigma}^{\rm SIDIS} \otimes {\rm FF}\,. \tag{1.49}$$

In the case of *pp* collisions, one has two initial state hadrons and therefore two PDFs in the factorized expression. For example for the Drell-Yan (DY) process $pp \to \mu^+\mu^-X$ or for jet cross sections $pp \to {\rm jet}X$ one finds

$$\begin{aligned} d\sigma^{\rm DY} &= {\rm PDF}_1 \otimes {\rm PDF}_2 \otimes d\hat{\sigma}^{\rm DY}\,, \\ d\sigma^{\rm jet} &= {\rm PDF}_1 \otimes {\rm PDF}_2 \otimes d\hat{\sigma}^{\rm jet}\,. \end{aligned} \tag{1.50}$$

Finally, one could observe an identified hadron in *pp* collisions, $pp \to hX$, described by

$$d\sigma^{\rm pph} = {\rm PDF}_1 \otimes {\rm PDF}_2 \otimes d\hat{\sigma}^{\rm pph} \otimes {\rm FF}\,. \tag{1.51}$$

Both, FFs and PDFs are non-perturbative objects which have to be determined by experiments. In the following Sec. 1.3 we will discuss the extraction from data and related topics in detail.

Since *pp* initiated processes play an important role in Chaps. 2 - 5, we want to mention some further details concerning this class of processes. Even if the schematic structure of the cross sections is similar to processes with initial state leptons, the explicit expressions are more complicated. We refrain from showing the explicit cross section formulas here, since they are given in Eq. (2.1) for single-inclusive hadron production and in Eq. (2.18) for inclusive jet production in *pp* collisions. We only discuss the main aspects of *pp* initiated cross sections here. The complicated structure has two main origins. On the one hand side, more convolution integrals and more non-perturbative functions are present. On the other hand, numerous different channels exist in the partonic cross sections. While there is only one partonic channel at LO in SIA (namely $e^+e^- \to qX$) one has ten LO channels for inclusive observables in *pp* collisions [91]:

$$\begin{aligned} qq' &\to qX\,, \\ q\bar{q}' &\to qX\,, \\ q\bar{q} &\to q'X\,, \\ qq &\to qX\,, \\ q\bar{q} &\to qX\,, \\ q\bar{q} &\to gX\,, \\ qg &\to qX\,, \\ qg &\to gX\,, \\ gg &\to gX\,, \\ gg &\to qX\,. \end{aligned} \tag{1.52}$$

At higher orders in perturbation theory this becomes more and more complicated since further new channels appear compared to SIA. This is why analytic results for QCD inclusive partonic cross sections are available only up to NLO (see, for instance, Ref. [91]), while expressions for SIA can be found up to NNLO in literature [84].

We have already noticed that in the process of factorization the non-perturbative functions as well as the partonic cross sections became scale dependent. However, this scale dependence is unphysical and only present in fixed order results. If one would be able to sum up all orders in perturbation theory, the cross section would not depend on the scale anymore. In general, the residual scale dependence is reduced order by order when PDFs, FFs and partonic cross sections are combined. Even if full results beyond NLO (partially already NNLO) are not available yet, there is another way to systematically reduce the scale dependence. The techniques of resummation allow for a systematical approach to sum up dominant logarithmic terms to all orders in perturbation theory. Resummed results are available for jet production [92] as well as for single-inclusive particle production [93]. Since resummed expressions contain the dominant parts of higher order corrections, the scale dependence of resummed cross sections is usually reduced compared to fixed order results. In Sec. 6.1.2 we present a detailed discussion concerning the basic ideas of resummations for a specific class of logarithms, so-called "small-z logarithms".

1.3 FFs and PDFs

This section is dedicated to the non-perturbative functions introduced in Sec. 1.2 above. There, FFs and PDFs were needed to get rid of collinear singularities. We start with a brief historical overview on FFs [94].

Already in 1972, Feynman [95] wrote about the idea of fragmentation functions $D_i^h(z)$ which describe the transition of a parton i into a hadron h where the observed hadron has longitudinal momentum fraction z with respect to the parton, $p_h = zp_i$. This idea grew towards a more sophisticated model during the 70's [96–98]. The FFs were thought of as universal objects in the sense that they are process independent. Furthermore, the scale dependence was investigated in detail [86, 99, 100]. These considerations led to the evolution equations for FFs, which are the time-like counterparts of the well-known equations pertinent to the scale evolution of PDFs, the so-called "Dokshitzer-Gribov-Lipatov-Altarelli-Parisi" (DGLAP) equations [101–105]. The dependence of the gluon and N_f quark and antiquark FFs on the factorization scale is governed by a set of $2N_f + 1$ integro-differential equations

$$\begin{aligned}
\frac{\partial}{\partial \log \mu^2} D_i^h(z, \mu^2) &= \sum_j \int_z^1 \frac{dx}{x} P_{ji}^T \left(\frac{z}{x}, \mu^2\right) D_j^h \left(x, \mu^2\right) \\
&\equiv \sum_j \left[P_{ji}^T \otimes D_j^h\right](z, \mu^2) \, . \qquad (1.53)
\end{aligned}$$

In Eq. (1.53) we have introduced the time-like splitting functions P_{ji}^T, often also called time-like evolution kernels, which are calculable in perturbation theory. The evolution equations, their ingredients, the solutions as well as several technical aspects will be discussed in more detail in Sec. 1.3.2. For now, it is enough to recognize that the scale dependence of FFs (and also PDFs) is described by evolution equations and thus may in principle be calculated using perturbation theory.

1.3.1 Formal Definition of FFs

After the groundbreaking work, people started to settle the framework of fragmentation functions on a field theoretical basis by giving a precise field theoretical definition of these objects. In that sense, the fragmentation functions are understood as the objects that connect gluon or quark lines to hadrons in the final state. They are defined as connected matrix elements of non-local operators [106–110]. Note that this formal definition is parton model inspired and everything what follows is expressed in terms of bare quantities. We follow the notation of [111] for the field theoretic definitions of FFs. We denote the four momenta of the observed hadron and the initiating parton with P_h and k, respectively. We use light-cone coordinates and work in a reference frame where the hadron has no transverse momentum, i.e.

$$P_h = (P_h^+, P_h^-, \vec{0}_T) \qquad \text{and} \qquad k = (k^+, k^-, \vec{k}_T)\,. \tag{1.54}$$

When working in light-cone coordinates it is convenient to define the two light-like vectors

$$n \equiv (0, 1, \vec{0}_T) \qquad \text{and} \qquad \bar{n} \equiv (1, 0, \vec{0}_T)\,. \tag{1.55}$$

They satisfy $n^2 = \bar{n}^2 = 0$ and $n{\cdot}\bar{n} = 1$. Hence, one can obtain the plus and minus components of a generic 4-vector a by $a^+ = n \cdot a$ and $a^- = \bar{n} \cdot a$, respectively.

The FFs are specified through bilocal light-cone correlators. The fragmentation correlator for a quark with flavor q fragmenting into a hadron h is a (4×4) matrix in Dirac space and reads [108, 110]

$$\begin{aligned} \Delta^{h/q}(z; P_h, S_h) \;=\; & \sum\!\!\!\!\!\!\!\int_X \int \frac{d\xi^+}{2\pi} e^{ik^-\xi^+} \left\langle 0 \,\middle|\, \mathcal{W}(\infty^+, \xi^+) q(\xi^+, 0^-, \vec{0}_T) \,\middle|\, P_h, S_h; X \right\rangle \\ & \times \left\langle P_h, S_h; X \,\middle|\, \bar{q}(0^+, 0^-, \vec{0}_T) \mathcal{W}(0^+, \infty^+) \,\middle|\, 0 \right\rangle \end{aligned} \tag{1.56}$$

with

$$\sum\!\!\!\!\!\!\!\int_X \equiv \sum_X \int \frac{d^3\vec{P}_X}{(2\pi)^3 2P_X^0}\,. \tag{1.57}$$

The argument z is the longitudinal momentum fraction which is transferred from the parton to the hardon along the minus direction, $P_h^- = zk^-$, and the quark field operator is denoted by q. In Eq. (1.56) we had to introduce “Wilson lines” to ensure color gauge invariance of the correlator. A Wilson line connects two points a and b and is defined as a path ordered exponential

$$[a^+, a^-, \vec{a}_T; b^+, b^-, \vec{b}_T] \equiv \mathcal{P} \exp\left[-ig_s \int_a^b ds_\mu A_a^\mu(s) T^a\right]\,, \tag{1.58}$$

where the integral runs along a straight line. Hence, the Wilson lines appearing in Eq. (1.56) are defined as

$$\mathcal{W}(a^+, b^+) \equiv [a^+, 0^-, \vec{0}_T; b^+, 0^-, \vec{0}_T]\,. \tag{1.59}$$

Following [112], we define the the trace of $\Delta^{h/q}$ with an arbitrary Dirac matrix Γ,

$$\Delta^{h/q[\Gamma]}(z; P_h, S_h) \equiv \frac{1}{4z} \operatorname{Tr}\left[\Delta^{h/q}(z; P_h, S_h)\Gamma\right]\,. \tag{1.60}$$

Using this notation, the leading-twist (twist-2) fragmentation function, which is what we simply call FF, is given by [108, 110–112]

$$\begin{aligned} D_q^h(z) &= z^2 \Delta^{h/q[\gamma^-]}(z;P_h,S_h) \\ &= \frac{z}{4} \sum\!\!\!\!\!\!\!\!\int_X \int \frac{d\xi^+}{2\pi} e^{ik^-\xi^+}\, \mathrm{Tr}\Big[\Big\langle 0 \Big| \mathcal{W}(\infty^+,\xi^+) q(\xi^+,0^-,\vec{0}_T) \Big| P_h,S_h;X \Big\rangle \\ &\quad \times \Big\langle P_h,S_h;X \Big| \bar{q}(0^+,0^-,\vec{0}_T) \mathcal{W}(0^+,\infty^+) \Big| 0 \Big\rangle \gamma^- \Big] . \end{aligned} \tag{1.61}$$

We note that the extraction of other types of FFs, like polarized or higher twist FFs, is possible by taking the trace with other Dirac matrices. However, these objects do not play any role in this thesis and we refer to [111] for a detailed review on all kinds of fragmentation functions.

For antiquarks, the correlator reads [111–113]

$$\begin{aligned} \bar{\Delta}^{h/q}(z;P_h,S_h) &= \sum\!\!\!\!\!\!\!\!\int_X \int \frac{d\xi^+}{2\pi} e^{ik^-\xi^+} \Big\langle 0 \Big| \mathcal{W}(\infty^+,\xi^+) \bar{q}(\xi^+,0^-,\vec{0}_T) \Big| P_h,S_h;X \Big\rangle \\ &\quad \times \Big\langle P_h,S_h;X \Big| q(0^+,0^-,\vec{0}_T) \mathcal{W}(0^+,\infty^+) \Big| 0 \Big\rangle . \end{aligned} \tag{1.62}$$

In [111–113] it is found that

$$\bar{\Delta}^{h/q[\gamma^-]} = \Delta^{h/\bar{q}[\gamma^-]} , \tag{1.63}$$

where $\Delta^{h/\bar{q}}$ contains charge conjugated quark fields in contrast to Eq. (1.56). Thus, the FF for antiquarks is given in complete analogy to quarks by

$$D_{\bar{q}}^h(z) = z^2 \Delta^{h/\bar{q}[\gamma^-]}(z;P_h,S_h) . \tag{1.64}$$

As a last point towards a formal definition of FFs we address the gluon-to-hadron FF. It can be defined in terms of the gluon-gluon fragmentation correlator [108, 110, 111, 114]

$$\begin{aligned} \Delta^{h/g,ij}(z;P_h,S_h) &= \sum\!\!\!\!\!\!\!\!\int_X \int \frac{d\xi^+}{2\pi} e^{ik^-\xi^+} \Big\langle 0 \Big| \mathcal{W}_{ba}(\infty^+,\xi^+) G_a^{-i}(\xi^+,0^-,\vec{0}_T) \Big| P_h,S_h;X \Big\rangle \\ &\quad \times \Big\langle P_h,S_h;X \Big| G_c^{-j}(0^+,0^-,\vec{0}_T) \mathcal{W}_{cb}(0^+,\infty^+) \Big| 0 \Big\rangle . \end{aligned} \tag{1.65}$$

Here, $G_a^{\mu\nu}$ is the gluon field strength tensor defined in Eq. (1.7) and the Wilson lines are in the adjoint representation. Finally, the gluon-to-hadron FF is specified by [108, 110, 111, 114]

$$D_g^h(z) = -\frac{z^2}{2P_h^-} g_T^{ij} \Delta^{h/g,ij}(z;P_h,S_h) \tag{1.66}$$

where $g_T^{\mu\nu} \equiv g^{\mu\nu} - n^\mu \bar{n}^\nu - n^\nu \bar{n}^\mu$ with the vectors n and $\bar{n}$ defined in Eq. (1.55). We note that the scale dependence of fragmentation functions, discussed in detail in the next section, enters when the bare quantities in Eqs. (1.61) and (1.66) are being renormalized. The renormalized fragmentation functions finally are scale and scheme dependent.

It is worth mentioning that the FFs satisfy the momentum sum rule [108],

$$\sum_h \int_0^1 dz\, z D^h_{q/g}(z,\mu) = 1\,, \tag{1.67}$$

where the sum runs over all hadrons. This sum rule simply expresses the conservation of the longitudinal momentum of the parton, i.e. that all the longitudinal parton momentum has to be transferred into hadrons. This very intuitive sum rule may also be derived in a field theoretical context [108, 115]. However, it is of rather academic interest, as it does not give a constraint which may be used in practical extractions of FFs, as the sum over *all* hadrons cannot be performed in a reasonable way and fixed order FFs show divergent behavior for $z \to 0$, see Chap. 6 for further details.

1.3.2 Evolution

In this section, which is based on Sec. II D of our publication [116] (which in turn closely follows Refs. [117, 118]), we want to give some detailed insight into the evolution of FFs and PDFs. As already mentioned in Sec. 1.3, the dependence of the gluon and N_f quark and antiquark FFs on the factorization scale μ_F is governed by the set of $2N_f + 1$ integro-differential equations

$$\frac{\partial}{\partial \log \mu^2} D^h_i(z,\mu^2) = \sum_j \left[P^T_{ji} \otimes D^h_j\right](z,\mu^2)\,, \tag{1.68}$$

with $i, j = q, \bar{q}, g$. For simplicity, we have set the renormalization scale equal to the factorization scale, $\mu_R = \mu_F \equiv \mu$. The $i \to j$ time-like splitting functions $P^T_{ji}(z,\mu^2)$ obey a perturbative expansion in α_s,

$$P^T_{ji} = \frac{\alpha_s}{2\pi} P^{T,(0)}_{ji} + \left(\frac{\alpha_s}{2\pi}\right)^2 P^{T,(1)}_{ji} + \left(\frac{\alpha_s}{2\pi}\right)^3 P^{T,(2)}_{ji} + \dots\,, \tag{1.69}$$

where here and in what follows we suppress the arguments z and μ^2 for the sake of readability. The LO splitting functions are identical for the time-like and the space-like case and are given by

$$\begin{aligned}
P^{(0)}_{qq}(z) &= C_F \left[\frac{1+z^2}{(1-z)_+} + \frac{3}{2}\delta(1-z)\right]\,, \\
P^{(0)}_{gq}(z) &= C_F\, \frac{1+(1-z)^2}{z}\,, \\
P^{(0)}_{gg}(z) &= 2C_A \frac{(1-z+z^2)^2}{z(1-z)_+} + \frac{\beta_0}{2}\delta(1-z)\,, \\
P^{(0)}_{qg}(z) &= \frac{1}{2}\left(z^2 + (1-z)^2\right)\,,
\end{aligned} \tag{1.70}$$

with $\beta_0 \equiv \frac{11}{3}C_A - \frac{2}{3}N_f$. Beyond the leading order, the space-like splitting functions differ from the time-like ones. As discussed extensively in [117], up to a minor missing part in the off-diagonal splitting kernel $P_{qg}^{T,(2)}$, the expansion (1.69) is known up to NNLO accuracy [119–121], i.e., $\mathcal{O}(\alpha_s^3)$. This remaining uncertainty, which stems from adopting analytic continuation ($\mathcal{AC}$) relations on the known NNLO space-like results, is presumably numerically irrelevant for all phenomenological applications; see Ref. [122] for the status of an ongoing direct calculation of the three-loop time-like kernels.

Instead of directly solving the $2N_f+1$ coupled integro-differential equations in (1.68) it turns out to be convenient to define the flavor singlet

$$D_{\Sigma}^{h} \equiv \sum_{q}^{N_f} (D_q^h + D_{\bar{q}}^h)\,. \tag{1.71}$$

For the singlet sector, Eq. (1.68) translates into two coupled integro-differential equations, which read

$$\frac{\partial}{\partial \log \mu^2} \begin{pmatrix} D_{\Sigma}^h \\ D_g^h \end{pmatrix} = \begin{pmatrix} P_{qq}^T & 2N_f P_{gq}^T \\ \frac{1}{2N_f} P_{qg}^T & P_{gg}^T \end{pmatrix} \otimes \begin{pmatrix} D_{\Sigma}^h \\ D_g^h \end{pmatrix}. \tag{1.72}$$

The remaining $2N_f-1$ equations can be fully decoupled by choosing the following, convenient non-singlet (NS) combinations of FFs:

$$D_{\mathrm{NS},l}^{h,\pm} \equiv \sum_{i=1}^{k} (D_{q_i}^h \pm D_{\bar{q}_i}^h) - k(D_{q_k}^h \pm D_{\bar{q}_k}^h)\,, \tag{1.73}$$

$$D_{\mathrm{NS},v}^{h} \equiv \sum_{q}^{N_f} (D_q^h - D_{\bar{q}}^h)\,. \tag{1.74}$$

In Eq. (1.73), we have $l = k^2-1$, $k = 2,\ldots,N_f$, and the subscripts i,k were introduced to distinguish different quark flavors. Each combination in Eq. (1.73) and (1.74) evolves independently with the following NS splitting functions [119–121]

$$P_{\mathrm{NS}}^{T,\pm} = P_{qq}^{T,v} \pm P_{q\bar{q}}^{T,v}\,, \tag{1.75}$$

$$P_{\mathrm{NS}}^{T,v} = P_{\mathrm{NS}}^{T,-} + P_{\mathrm{NS}}^{T,s}\,, \tag{1.76}$$

respectively, and one has the following relation for P_{qq}^T that enters in Eq. (1.72)

$$P_{qq}^T = P_{\mathrm{NS}}^{T,+} + P^{T,ps}\,. \tag{1.77}$$

Similar to the space-like case, one finds $P_{q\bar{q}}^{T,v} = P_{\mathrm{NS}}^{T,s} = P^{T,ps} = 0$ and $P_{\mathrm{NS}}^{T,s} = 0$ at LO and NLO, respectively. Hence, three NS quark combinations that evolve differently first appear at NNLO accuracy [119–121]. After the evolution is performed, i.e. the singlet and the $(2N_f-1)$ non-singlet equations are solved, the individual D_q^h and $D_{\bar{q}}^h$ can be recovered from Eqs. (1.71), (1.73), and (1.74). Likewise, any combination relevant for a cross section calculation can be computed, such as those used in the factorized expression for SIA given in Eq. (1.45).

It is most convenient to solve the set of evolution equations in Mellin N space. In general, the pair of Mellin integral and inverse transforms of a function $f(z)$ and $f(N)$ are defined by

$$f(N) = \int_0^1 dz\, z^{N-1} f(z) \equiv \mathcal{M}[f(z)] \tag{1.78}$$

and

$$f(z) = \frac{1}{2\pi i} \int_{\mathcal{C}_N} dN\, z^{-N}\, f(N)\,, \tag{1.79}$$

respectively, where $\mathcal{C}_N$ denotes a suitable contour in the complex Mellin N plane that guarantees fast convergence in numerical applications, see Refs. [116, 118, 123, 124] for a comprehensive discussion of technical details and subtleties. The main reason to perform this transformation is that convolutions as defined in Eq. (1.41) turn into simple products in Mellin moment space,

$$\begin{aligned} \mathcal{M}\Big[[f \otimes g](z)\Big] &= \int_0^1 dz\, z^{N-1} \int_0^1 dx \int_0^1 dy\, f(x)\, g(y)\, \delta(z - xy) \\ &= \int_0^1 dx\, x^{N-1} f(x) \int_0^1 dy\, y^{N-1} g(y) \\ &= f(N) \cdot g(N)\,. \end{aligned} \tag{1.80}$$

Hence, one can rewrite all evolution equations as ordinary differential equations. Schematically, one finds with a_s defined in Eq. (1.17)

$$\frac{\partial \boldsymbol{D}^h(N, a_s)}{\partial a_s} = -\frac{1}{a_s}\Big[\boldsymbol{R}_0(N) + \sum_{k=1}^{\infty} a_s^k \boldsymbol{R}_k(N)\Big]\boldsymbol{D}^h(N, a_s)\,, \tag{1.81}$$

where the characters in boldface indicate that we are dealing in general with 2 × 2 matrix-valued equations, cf. Eq. (1.72). For the NS combinations (1.73) and (1.74), Eq. (1.81) reduces to a set of independent partial differential equations, which are straightforward to solve, and we do not discuss them here.

The $\boldsymbol{R}_k$ in (1.81) are defined recursively by

$$\boldsymbol{R}_0 \equiv \frac{1}{\beta_0} \widetilde{\boldsymbol{P}}^{T,(0)}\ , \quad \boldsymbol{R}_k \equiv \frac{1}{\beta_0} \widetilde{\boldsymbol{P}}^{T,(k)} - \sum_{i=1}^{k} b_i \boldsymbol{R}_{k-i}\ , \tag{1.82}$$

where $\widetilde{\boldsymbol{P}}^{T,(k)}(N)$ is the k-th term in the perturbative expansion of the 2 × 2 matrix of the N-moments of the singlet splitting functions

$$\widetilde{\boldsymbol{P}}^{T}(N) = \begin{pmatrix} P_{qq}^T(N) & 2N_f P_{gq}^T(N) \\ \frac{1}{2N_f} P_{qg}^T(N) & P_{gg}^T(N) \end{pmatrix}. \tag{1.83}$$

Note that here and in Eq. (1.72), the normalizations of the off-diagonal entries of the matrix $\widetilde{\boldsymbol{P}}^{T}$ differ sometimes in literature, because they depend on the definition of the singlet (1.71). Sometimes, the singlet is defined with an extra factor $1/N_f$ which eventually will change the off-diagonal entries in Eq. 1.83. In addition, we have introduced $b_i \equiv \beta_i/\beta_0$, where the β_i (defined in Eq. (1.19)) denote the expansion coefficients of the QCD β-function; see Refs. [61–63] for the explicit expressions up to N^{3}LO, i.e. β_3 which is the current state of the art.

Due to the matrix-valued nature of Eq. (1.81), a unique closed solution beyond the lowest order approximation can only be written as an expansion around the LO solution,

$(a_s/a_0)^{-\boldsymbol{R}_0(N)}\boldsymbol{D}^h(N,a_0)$. Here, a_0 is the value of a_s at the initial scale μ_0, where the non-perturbative input $\boldsymbol{D}^h(N,a_0)$ is specified from a fit to data. More explicitly, this expansion reads

$$\begin{aligned}\boldsymbol{D}^h(N,a_s) &= \left[1+\sum_{k=1}^{\infty} a_s^k\,\boldsymbol{U}_k(N)\right]\left(\frac{a_s}{a_0}\right)^{-\boldsymbol{R}_0(N)} \\ &\quad\times\left[1+\sum_{k=1}^{\infty} a_s^k\,\boldsymbol{U}_k(N)\right]^{-1}\boldsymbol{D}^h(N,a_0)\,. \end{aligned}\tag{1.84}$$

The evolution matrices $\boldsymbol{U}_k$ are again defined recursively by the commutation relations

$$[\boldsymbol{U}_k,\boldsymbol{R}_0] = \boldsymbol{R}_k + \sum_{i=1}^{k-1}\boldsymbol{R}_{k-1}\boldsymbol{U}_i + k\boldsymbol{U}_k\,. \tag{1.85}$$

When examining Eq. (1.84) more closely, it turns out that a fixed-order solution at N^{m}LO accuracy is not unambiguously defined. A certain degree of freedom still remains in choosing the details on how to truncate the series at order m. For example, suppose the perturbatively calculable quantities $\widetilde{\boldsymbol{P}}^{T,(k)}$ and β_k are available up to a certain order $k=m$. One possibility is to expand Eq. (1.84) in a_s and strictly keep only terms up to a_s^m. This defines what is usually called the *truncated solution* in Mellin moment space.

However, given the iterative nature of the $\boldsymbol{R}_k$ in Eq. (1.82), one may alternatively calculate the $\boldsymbol{R}_k$ and, hence, the $\boldsymbol{U}_k$ in Eq. (1.85) for any $k>m$ from the known results for $\widetilde{\boldsymbol{P}}^{T,(k)}$ and β_k up to $k=m$. Any higher order $\widetilde{\boldsymbol{P}}^{T,(k>m)}$ and $\beta_{k>m}$ are simply set to zero. Taking into account all the thus constructed $\boldsymbol{U}_k$ in Eq. (1.84) defines the so-called *iterated solution.* This solution is important as it mimics the results that are obtained when solving Eq. (1.68) directly in z-space by some iterative, numerical methods. It should be stressed that both choices are equally valid as they only differ by terms that are of order $\mathcal{O}(a_s^{m+1})$ and thus beyond the perturbative accuracy under consideration. After having solved the evolution equations in Mellin space, one needs to perform the inverse Mellin transformation (1.79) to obtain the fragmentation functions in z-space.

Equipped with the concept of evolution, we are also able to derive an equation which, if solved order by order, provides us with the transition functions introduced in Sec. 1.2. Starting from Eq. (1.68) and neglecting the arguments z and μ^2 for the sake of readability, we have in matrix notation [125]

$$\begin{aligned}\boldsymbol{P}^T\otimes\boldsymbol{D}^h &= \frac{\partial}{\partial\log\mu^2}\boldsymbol{D}^h \\ &= \frac{\partial\boldsymbol{\Gamma}}{\partial\log\mu^2}\otimes\tilde{\boldsymbol{D}}^h \\ &= \frac{\partial\boldsymbol{\Gamma}}{\partial\log\mu^2}\otimes\boldsymbol{\Gamma}^{-1}\otimes\boldsymbol{D}^h\,. \end{aligned}\tag{1.86}$$

Hence, by comparing the first and last expressions and rewriting the derivative with respect to $\log\mu^2$ in terms of the derivative with respect to a_s, we arrive at [42]

$$\beta_d(a_s)\frac{\partial\boldsymbol{\Gamma}}{\partial a_s}\otimes\boldsymbol{\Gamma}^{-1} = \boldsymbol{P}^T \tag{1.87}$$

with the d-dimensional beta function of QCD, $\beta_d(a_s) = -\varepsilon a_s - a_s^2 \sum_{i=0}^{\infty} \beta_i a_s^i$. Equation (1.86) implicitly defines the transition functions. They may be determined by solving this equation order by order in a_s.

Finally, a short comment on the evolution of PDFs is in order. The methodology for solving the space-like evolution equations (1.89) is completely analogous to the time-like case. One only has to replace P_{ji}^T by P_{ij}^S and D_i^h by f_i^H. A detailed outline for the space-like case may for example be found in [118].

1.3.3 Extraction from Data

In the previous sections, we have found field theoretic definitions for the non-perturbative FFs and we have studied their evolution to some extend. In a similar way it is possible to define PDFs in a field theoretic way and to solve their evolution equations. However, since the focus of this thesis is on fragmentation, we refrain from listing the details here and refer to the literature (see e.g. [108, 126]).

Having well defined objects, we are now ready to address the question how to extract these non-perturbative functions from experiments. The two main features which make extraction from data possible are universality and evolution. One cannot calculate FFs from first principles, however, we know that due to universality the FFs should be the same in SIA, SIDIS, $pp \to hX$, or any other process involving one identified (massless) hadron in the final state. On the other hand, evolution tells us the FFs at any scale μ, given the FFs at a reference scale μ_0. To extract information about the FFs from data, one usually performs a fit of a specified functional form for the input distribution at a reference scale μ_0. The most used functional form is

$$D_i^h(z, \mu_0) = z^{\alpha_i}(1-z)^{\beta_i} f(z, 1-z; \{\gamma_i\}) \tag{1.88}$$

with some parameters α_i and β_i, and f being a function of z and/or $1-z$ which in general depends on a further set of parameters $\{\gamma_i\}$, see Eqs. (4.13) and (6.71) for some explicit examples of input parametrizations. One then has to evolve this input parametrization to the corresponding energy scale given by a certain data set and compute the observable in terms of the evolved FFs. This has to be compared to data and the best set of the parameters for the input distributions has to be determined (usually done by a χ^2 optimization, see Sec. 4.2.4 for further details). This procedure has been performed first for SIA at next-to-leading order (see e.g. [83, 127–129]) for observed pions and kaons but also for heavier particles like protons or the Λ^0.

Historically, the next step was utilizing universality to determine the FFs from "global" analyses, where several different processes were used. This is important to obtain more information on the FFs compared to SIA. For example, the gluon FF enters in SIA only at next-to-leading order indirectly or via evolution while in $pp \to hX$ it is present already at leading order. Another drawback of SIA is that the quark and antiquark FFs always come together as $D_q + D_{\bar{q}}$ as can be seen from Eq. (1.45). SIDIS overcomes this problem, giving the opportunity to disentangle quark and antiquark contributions. Global analyses at NLO were performed, for example, in [130–134]. Recently, even a next-to-next-to-leading order study for the pion FF was presented, however, due to the missing NNLO cross sections for other processes, only for SIA [117].

These analyses rely on several ingredients. Obviously, experimental data have to be available with sufficiently high precision. From a theoretical point of view, the cross sections for the respective observables have to be calculated in perturbation theory. Nowadays, NLO calculations are the standard accuracy, however, for several processes besides SIA, NNLO results are in progress or already partially available [124]. Since the full fixed order results are not known yet, it is possible to use soft gluon resummed results expanded to NNLO accuracy, see for example [135–137]. Furthermore, one needs to know the evolution kernels, i.e. the time-like splitting functions, to the same order in perturbation theory as the cross sections. This is important to obtain a consistent analysis. They are known up to NNLO [119–121].

Everything described above is done in a similar way also for PDFs. In contrast to the time-like evolution (1.53), the PDFs obey space-like DGLAP evolution,

$$\frac{\partial}{\partial \log \mu^2} f_i^H(x,\mu^2) = \sum_j \left[P_{ij}^S \otimes f_j^H \right] (x,\mu^2) \,, \tag{1.89}$$

where P_{ij}^S are the space-like splitting functions which also are known up to NNLO [138, 139]. They differ from their time-like counterparts beyond the leading order. The extraction of PDFs works pretty much the same as for FFs. Only the processes of interest are different. The cleanest access is given in DIS. Moreover, there are a lot of processes initiated by two hadrons and hence with two PDFs in the initial state. Of special interest are processes with a "clean" final state, i.e. leptons or jets. Thus, the Drell-Yan process, vector boson production and jet cross sections are used to extract information on PDFs. It can also be helpful to consider an asymmetric initial state by considering $p\bar{p}$ collisions instead of pp collisions. In contrast to FFs, NNLO already became the standard accuracy for PDFs. Recent extractions from global analyses may be found for example in [140–142].

As a final remark, we want to emphasize one important difference between FFs and PDFs. Since for FFs an identified hadron is observed in the final state (see, for example, Eq. (1.61)) a local operator product expansion (OPE) does not exist. This is different for the fully inclusive PDF case where an OPE applies. Since the OPE is a prerequisite for the computation of PDFs within the framework of moment based lattice QCD, it is thus not possible to use this method to compute FFs from first principles [130]. We note that recently a lattice method was proposed which is not restricted to certain integer moments and PDFs are extracted from lattice QCD in x-space [143, 144]. To the best of our knowledge, the application of this method to the time-like case of FFs has not yet been studied. Hence, information about FFs can only be obtained by such QCD analyses described in this section, while for PDFs the lattice approach offers alternative ways of investigating the structure of the nucleon.

1.3.4 Photonic Distributions

Probably less known compared to their hadronic counterparts, are the photonic distributions, i.e. the parton-to-photon fragmentation functions D_i^γ and their space-like counterparts, the parton distribution functions of the photon f_i^γ. As before, we focus on the time-like sector in this thesis. For more information on the f_i^γ, see, for example, Refs. [145, 146] and references therein. Note, that also photon PDFs exist, i.e. the distribution of photons inside a hadron f_γ^H, see, for instance, Ref. [147] and references therein.

The parton-to-photon FFs $D_i^\gamma(z,\mu^2)$ describe the non-perturbative transition of a parton i into a photon γ. For better understanding of the need of their existence, we follow our publications [148, 149] and take a closer look on photon production cross sections. As was discussed a long time ago [150], in perturbative high-p_T processes there are two production mechanisms for photons. The photon may be directly produced in the hard scattering process through its "point-like" QED coupling to a quark. Such contributions are usually referred to as "direct". On the other hand, photons may also emerge in jet fragmentation, when a quark, antiquark, or gluon emerging from a QCD hard-scattering process fragments into a photon plus a number of hadrons. The need for introducing such a "photon fragmentation" contribution is physically motivated by the fact that the photon may result, for example, from conversion of a high-p_T ρ meson. Furthermore, at higher orders, the perturbative direct component contains divergencies from configurations where the photon and a (massless) final-state quark become collinear. These are long-distance contributions that naturally signify the need for non-perturbative fragmentation functions into which they can be absorbed. Schematically, photon production cross sections may be written in a factorized form as

$$d\sigma^\gamma = d\hat{\sigma}^\gamma + \sum_c d\hat{\sigma}^c \otimes D_c^\gamma \,, \tag{1.90}$$

where the sum runs over all partons (quarks, antiquarks and gluons). Note, that for processes with initial state hadrons, the partonic cross sections in Eq. (1.90) have to be further convoluted with the respective PDFs; see, for example, Eq. (5.1). In general, the parton-to-photon fragmentation functions depend on the longitudinal momentum fraction z which is transferred to the photon and on the factorization scale μ: $D_c^\gamma \equiv D_c^\gamma(z,\mu^2)$. The non-perturbative functions D_c^γ are assumed to be universal und thus may in principle be extracted in the same manner as the parton-to-hadron FFs D_c^h via fits to experimental data. While there has been much progress on parton-to-hadron FFs in the last years [116, 117, 132, 134, 151, 152], there have been no new extractions of parton-to-photon FFs for about two decades, and our knowledge of these functions has remained relatively poor. This is mostly due to the fact that the largest data set comes from *single-inclusive* photon data in hadronic collisions, for which the dominant contribution comes from the direct (i.e. non-fragmentation) part. For the reaction $e^+e^- \to \gamma X$ fragmentation yields the dominant contribution; however, here only a very sparse data set exists, and the amount of photon data and their precision does not match that of hadron production data. The two most recent sets of photon FFs available are the "Glück-Reya-Vogt" (GRV) set [153] and the "Bourhis-Fontannaz-Guillet" (BFG) set [154]. The latter is based on the somewhat older "Aurenche-Chiappetta-Fontannaz-Guillet-Pilon" (ACFGP) set [155]. We note, that the BFG set actually consists of two sets of FFs, which mainly differ in the gluon-to-photon fragmentation function.

Besides universality, another key ingredient to extractions of FFs is evolution. The presence of the direct part affects the evolution equations for photonic distributions. Following [153, 154], the DGLAP-like evolution equations may be written as

$$\frac{d}{d\log\mu^2} D_i^\gamma(z,\mu^2) = \sum_j P_{ji}(z,\mu^2) \otimes D_j^\gamma(z,\mu^2) \,, \tag{1.91}$$

where i, j run over all parton flavors including the photon itself, i.e. $i, j \in \{q_{i,j}, \bar{q}_{i,j}, g, \gamma\}$, so that we also have a photon-to-photon FF D_γ^γ and photon splitting functions. The symbol $\otimes$ denotes the standard convolution integral. The evolution kernels, also called time-like splitting functions, are double series in the electromagnetic coupling α and the strong coupling α_s,

$$P_{ij}(z, \mu^2) = \sum_{m,n} \left(\frac{\alpha(\mu^2)}{2\pi}\right)^m \left(\frac{\alpha_s(\mu^2)}{2\pi}\right)^n P_{ij}^{(m,n)}(z)\,. \tag{1.92}$$

Usually, only the leading order in the electromagnetic coupling is considered, so that

$$D_\gamma^\gamma(z, \mu^2) = \delta(1 - z)\,. \tag{1.93}$$

Furthermore, the running of α is neglected. The evolution equations then reduce to the frequently used inhomogeneous evolution equations

$$\frac{d}{d \log \mu^2} D_i^\gamma(z, \mu^2) = k_i^\gamma(z, \mu^2) + \sum_j P_{ji}(z, \mu^2) \otimes D_j^\gamma(z, \mu^2)\,, \tag{1.94}$$

where now just $i, j \in \{q_{i,j}, \bar{q}_{i,j}, g\}$. The inhomogeneous term is given by

$$k_i^\gamma(z, \mu^2) = \frac{\alpha}{2\pi} \sum_n \left(\frac{\alpha_s(\mu^2)}{2\pi}\right)^n P_{\gamma i}^{(1,n)}(z)\,. \tag{1.95}$$

Like for hadron FFs, these evolution equations are solved most conveniently in Mellin-N space where the convolutions turn into simple products, see Eq. (1.80). Furthermore, they usually are decomposed into the standard singlet and non-singlet combinations, see, for instance, [153, 154]. The full solution of the evolution equations (1.94) is given by the sum of a particular solution to the inhomogeneous equation, which can be computed in perturbation theory, and a general solution to the homogeneous equation, which contains the non-perturbative component. Schematically, we have

$$D_i^\gamma = D_i^{\gamma,\mathrm{inhom}} + D_i^{\gamma,\mathrm{hom}}\,. \tag{1.96}$$

While the first part in Eq. (1.96) is perturbative, the second non-perturbative part has to be extracted from experiment or modeled. Ideally, one would prefer to extract this part from a clean reference process without contamination of other non-perturbative functions (like PDFs), i.e. from single-inclusive annihilation (SIA) $e^+e^- \to \gamma X$. However, only a very limited amount of data are available for this process, which furthermore have rather large uncertainties [156]. In view of this, the two most recent extractions of FFs have resorted to the vector meson dominance (VMD) model, for which one assumes that the fragmentation process is dominated by conversion of vector mesons. Thus, the ansatz

$$D_i^{\gamma,\mathrm{hom}}(z, \mu_0^2) = \alpha \sum_{v=\rho,\omega,\phi,\ldots} C_v D_i^v(z, \mu_0^2) \tag{1.97}$$

is used at the initial scale for the evolution, along with a vanishing inhomogeneous piece at the initial scale. Here, the sum runs over all vector mesons under consideration and the D_i^v are the fragmentation functions into the corresponding vector mesons. As the FFs for the latter are rather poorly known as well, the GRV set adopts pion FFs for them instead. The

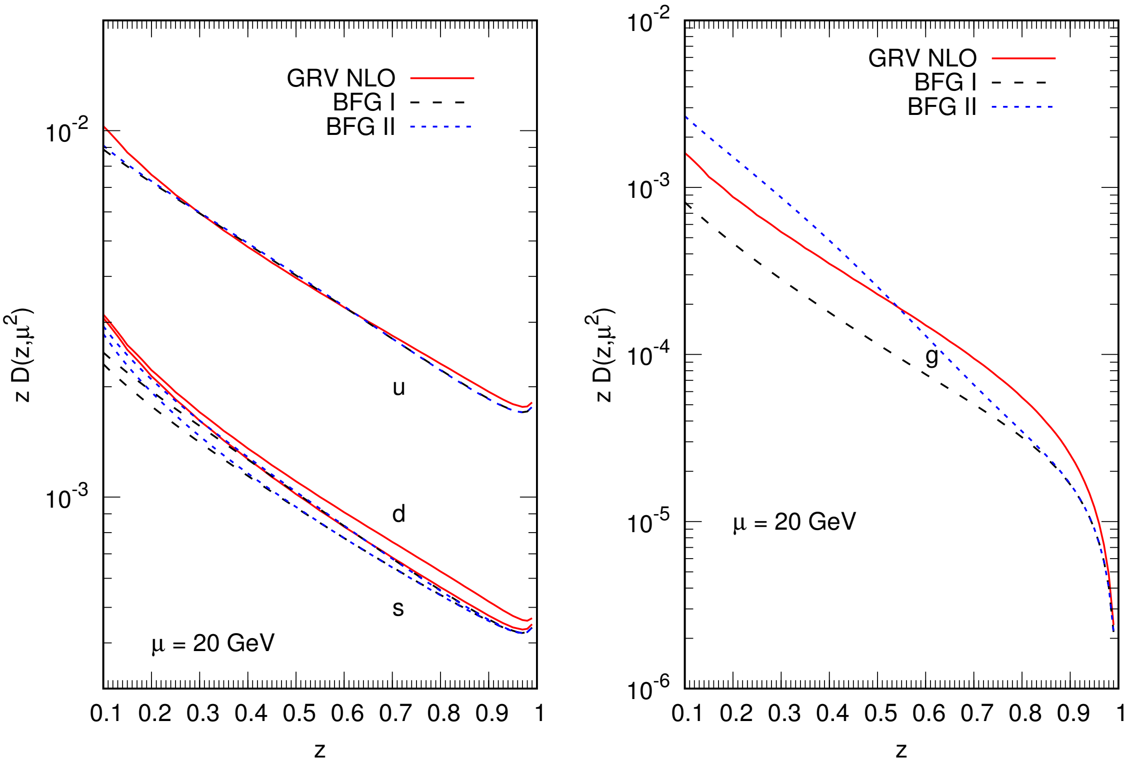

(a) Quark FFs **(b)** Gluon FFs

Figure 1.5: Comparison of the different FF parametrizations [153, 154]. In subfig. (a) and (b) we show $zD_i^{\gamma}(z,\mu^2 = (20\,\mathrm{GeV})^2)$ for $i = u, d, s$ and $i = g$, respectively.

BFG set uses ρ data from ALEPH [157] and HRS [158] to constrain their VMD ansatz. We note that the recent paper [159] presented a detailed Monte-Carlo event generator study of the inclusive hadro-production of photons and vector mesons. By adding the p_T spectra of the light vector mesons (ρ, ω, ϕ), weighted with α divided by the individual vector-meson decay constants, one obtains a fairly good description of inclusive photon data in the low-p_T region, which is the kinematic regime where the fragmentation process dominates over the direct part [160]. This observation supports the VMD ansatz for the non-perturbative part of photon FFs.

It is interesting to compare the different FF sets that are available [160, 161]. In Fig. 1.5 we show $zD_i^{\gamma}(z,\mu^2 = (20\,\mathrm{GeV})^2)$ for $i = u, d, s, g$, as given by the GRV and the two BFG sets. While the quark FFs are rather similar, the gluon FF is quite different in each of the three sets. SIA data would not be expected to help discriminate among the various D_i^g as the gluon FF enters only at NLO or via evolution. In order to see whether single-inclusive photon production in hadronic collisions, $pp \to \gamma X$, is more promising, we compare in Fig. 1.6 the theoretical cross section at NLO (using the code of Ref. [162]) with data from PHENIX [163–165]. As can be seen, the different FF sets yield very similar results. Compared to the experimental uncertainties, the difference in the FF sets is negligible. Even though the gluon FF is very different and channels with *initial* gluons dominate, the

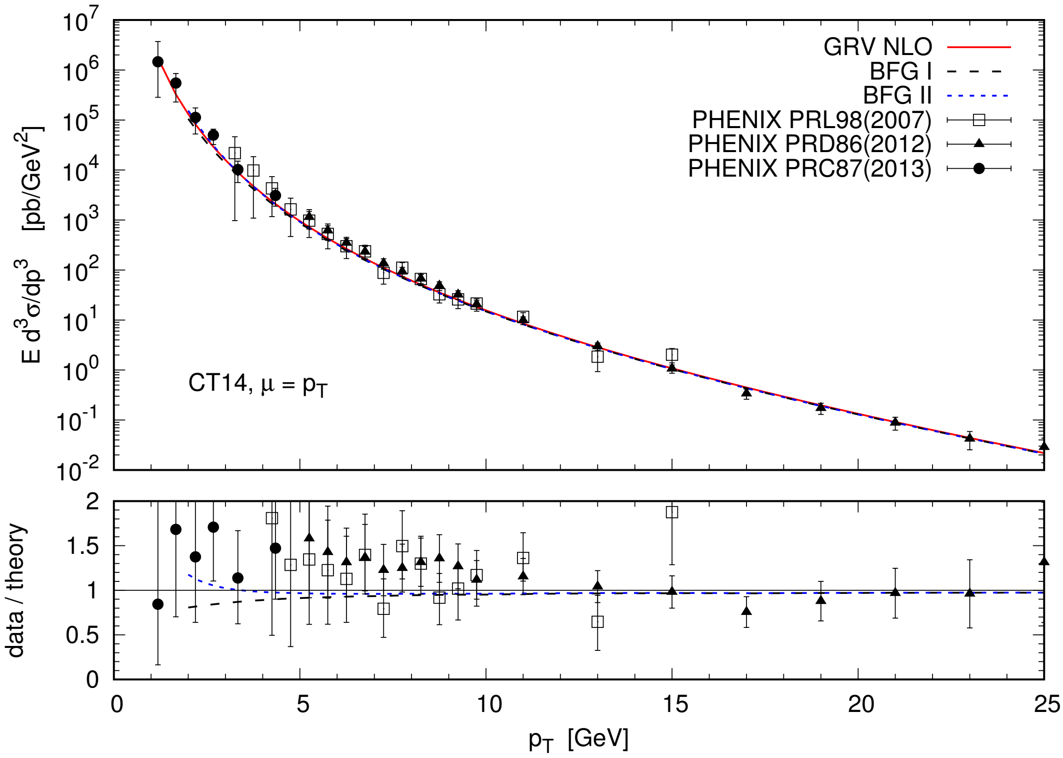

Figure 1.6: Comparison to PHENIX data [163–165]. In the lower panel we show the ratio of the data and the two BFG sets with respect to the GRV set.

inclusive photon production is apparently not really sensitive to the gluon FF. We note that this observation has been made in previous literature for various collider and fixed target settings; see, for instance, [160, 161, 166, 167]. We stress that the fact that the presently available sets of photon FFs yield similar cross section predictions does not imply that the fragmentation contribution to photon production is under satisfactory control. For instance, there is arguably a much larger uncertainty in the u-quark FF than suggested by the curves shown in Fig. 1.5.

These observations also have ramifications for photon signals in pA and, especially, AA collisions. For the latter, photons are used in studies of the quark-gluon plasma (QGP). While photons produced directly in the collision will traverse the medium with only little attenuation, the fragmentation photons will originate from partons that suffered energy loss in the medium. To assess this effect properly, good understanding of the “vacuum” photon fragmentation functions is essential.

We finally note that in pp collider experiments usually a photon isolation cut is introduced in order to suppress the large background from $\pi^0 \to \gamma\gamma$ decay. The idea is to center a cone around the final state photon and to demand that the hadronic energy fraction inside this cone be less than a certain amount ε. Such isolation cuts also suppress the photon fragmentation contribution [168, 169], since they confine the fragmentation contribution to large values of z. This, however, introduces further uncertainties since the FFs are completely unconstrained in the region of large z and since this region is much harder to treat theoretically. For instance, large logarithmic $\log(1-z)$ contributions arise here in the evolution kernels and partonic cross sections [170]. This especially affects the inhomogeneous part which does not vanish for $z \to 1$ [153]. Moreover, the isolation procedure also introduces logarithmic contributions in the energy fraction $\log \varepsilon$ [170] and the cone opening [171, 172].

We emphasize, that any experimental observable that can provide direct information on photon fragmentation at high z will provide valuable insights into these questions. For this reason, we investigate the semi-inclusive process $pp \to (\text{jet}\,\gamma)X$, for which the photon is observed inside a fully reconstructed jet and is part of the jet, in Chap. 5. There, we show that the process $pp \to (\text{jet}\,\gamma)X$ offers much potential for providing valuable new information on parton-to-photon FFs.

1.4 Jets

After having discussed the non-perturbative fragmentation functions needed for the description of identified final state hadrons, we now turn to another class of hadronic observables which, however, can be described without non-perturbative functions in the final state: Jets. Jet physics is a frequently studied field of QCD. In hadron collisions, jets are copiously produced and hence, they contribute in a significant way to most measurements at hadron colliders. Moreover, jets offer a rich field of phenomenology: Jet cross sections are useful in the determination of unpolarized and polarized PDFs [173–175], for the extraction of α_s [176–179], and even for studies on new physics beyond the Standard Model [180, 181]. When talking about a jet, we mean collimated hadronic energy in a certain solid angle. This is a very pictorial and intuitiv definition. However, one needs a formal definition which satisfies both theoretical and experimental needs. First attempts were made in the SNOWMASS accords [182], where people formulated basic requirements for a formal jet definition:

1. Simple to implement in an experimental analysis,

2. simple to implement in the theoretical calculation,

3. defined at any order of perturbation theory,

4. yields finite cross section at any order of perturbation theory,

5. yields a cross section that is relatively insensitive to hadronization.

Form a theoretical point of view, one might want to add infrared and collinear safety as well as invariance under boosts [183]. The efforts in finding a suitable jet definition led to several types of jet algorithms.

Before presenting an explicit NLO calculation of single-inclusive jet production in Chap. 2, we first give a summary of the most commonly used jet algorithms.

Cone Algorithms

Several cone algorithms with subtle differences in the specification of the jet variables exist and a lot of effort on numerical speed was made in their implementation [184]. A common choice is to define a jet as a deposition of total transverse hadronic energy E_T^{jet} of all final-state hadrons that satisfy

$$(\eta^{\text{jet}} - \eta^i)^2 + (\phi^{\text{jet}} - \phi^i)^2 \leq R_{\text{cone}}^2 . \tag{1.98}$$

Hence, a jet is formed by associating together entities (partons or particles, respectively) which are moving inside a geometrical cone and the jet four-momentum is the sum of of the four-momenta of all entities inside the cone. This cone is given in the two dimensional $\eta \times \phi$ space, where ϕ is the usual azimuthal angle and the pseudo rapidity η is defined as

$$\eta \equiv -\log \tan \frac{\theta}{2} , \tag{1.99}$$

with θ being the angle with respect to the beam axis. The jet variables read

$$\begin{aligned} E_T^{\text{jet}} &= \sum_i E_T^i , \\ \eta^{\text{jet}} &= -\log \tan \frac{\theta^{\text{jet}}}{2} = \frac{\sum_i E_T^i \eta^i}{E_T^{\text{jet}}} , \\ \phi^{\text{jet}} &= \frac{\sum_i E_T^i \phi^i}{E_T^{\text{jet}}} . \end{aligned} \tag{1.100}$$

There are various ways to implement this jet definition in a calculation. If one is interested in a widely analytical calculation, the narrow jet approximation (NJA) is used [174]. In this approximation, one assumes the jet to be relatively narrow, i.e. contributions of order $\mathcal{O}(R_{\text{cone}}^2)$ are neglected in the partonic cross section. At NLO, one has at most three partons in the final state. As at least one has to take the recoil, at most two of them can form a jet. Thus, the condition (1.98) is employed as a phase space restriction on the angle θ_j between partons j and the jet axis. This angle is limited to $\theta_j \leq \delta$, where the choice $\delta = R_{\text{cone}} / \cosh \eta^{\text{jet}}$ [185] ensures the NJA definition to be equivalent to (1.98).

On the other hand, if one uses parton shower techniques or one performs an experimental data analysis, one has to deal with numerous final state partons or particles. Then, iterative algorithms are mostly used to find jets. After having chosen some initial jet candidate (usually the most energetic entities) to define a jet axis, all entities satisfying Eq. (1.98) are combined to a jet. Then, the new jet axis is calculated according to (1.100). This procedure is iterated until the jet axis is stable in the sense that it does not change from one iteration to another. If the final state consists of two or more jets, one has to take care of overlapping cones by defining a suitable split and merge criterion.

However, there is a big issue about these seeded iterative algorithms. They turn out to be infrared unsafe. Additional soft radiation or collinear splittings may cause different jets in the end, which is exactly the behavior an infrared safe observable should not have. See Fig. 1.7 for an example of how soft radiation may spoil an infrared unsafe jet algorithm. Thus, various attempts were made to improve these iterative cone algorithms [183, 186, 187]. However, it turned out that these improvements did not actually solve the problem of infrared unsafety but shifted the problems to higher orders in perturbation theory.

A solution to the problem is to abolish the idea of iterative methods and to simply solve the mathematical problem (1.98). However, for a large number of particles, a naive implementation is unusable due to runtime reasons: for N final state particles, the naive solution

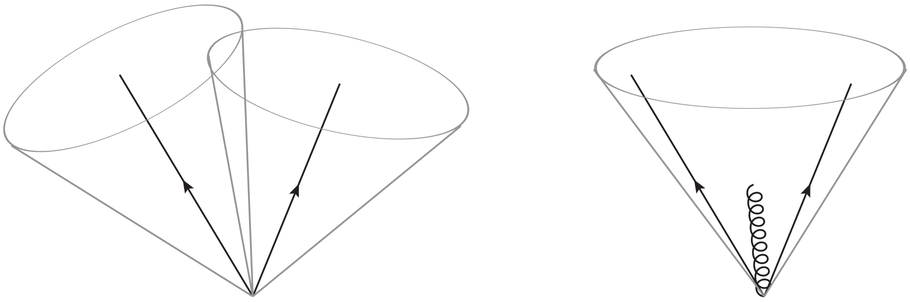

Figure 1.7: This sketch illustrates the way soft radiation may spoil an infrared unsafe jet algorithm. The soft gluon may cause a different number of jets constructed by the algorithm. This sketch is inspired by a similar figure in Ref. [188].

has algorithmic complexity $\mathcal{O}(N2^N)$. Fortunately, an improved implementation exists which reduces the complexity to $\mathcal{O}(N^2 \log N)$: the "Seedless Infrared Safe Cone Algorithm" (SISCone) [189]. This is the only infrared safe cone type implementation so far.

k_T Algorithms

The k_T algorithms are a class of successive recombination algorithms. For their definition, one introduces two distances [33]: d_{ij}, the distance between two entities (particles or jets) i and j, and d_{iB}, the distance between entity i and the beam,

$$d_{ij} = \min\left((k_T^i)^{2p}, (k_T^j)^{2p}\right) \frac{\Delta_{ij}^2}{R_{k_T}^2}, \tag{1.101}$$

$$d_{iB} = (k_T^i)^{2p}. \tag{1.102}$$

Here, $\Delta_{ij}^2 \equiv (\eta^i - \eta^j)^2 + (\phi^i - \phi^j)^2$, k_T^i is the transverse momentum of entity i with respect to the beam direction, and $p \in \mathbb{R}$ is a parameter which specifies the type of the k_T algorithm. It can be shown that there are only three relevant choices of p which show qualitatively different behavior [33]: $p > 0$, $p < 0$ and $p = 0$. Each of these classes is represented by the following prominent choices: "the" k_T algorithm ($p = 1$) [190, 191], the Cambrigde-Aachen algorithm ($p = 0$) [192] and the anti-k_T algorithm ($p = -1$) [33]. Moreover, the parameter R_{k_T} specifies the "size" of the jet.

Particles or partons, respectively, are part of a jet if their distance to the jet is smaller than the distance to the beam, i.e. $d_{i,\text{jet}} < d_{iB}$. Similar to the cone algorithm, one can use the NJA to perform an analytical jet calculation [175]. In that case, Eqs. (1.101) and (1.102) yield the phase space restriction and terms of order $\mathcal{O}(R_{k_T}^2)$ are neglected in the partonic cross section. On the other hand, utilizing the algorithm after parton showering or in data analyses for a large number of final state entities is done by the following algorithm. Starting with a list of all final state entities, the algorithm computes the distances (1.101) and (1.102) for all of them. After this initialization, the minimum distance is computed for each entity. If the minimum is d_{iB}, the entity is called a jet and removed from the list. Else, if the minimum is d_{ij}, the entities i and j are removed from the list and merged into an entity l by adding their 4-momenta, $p_l^\mu = p_i^\mu + p_j^\mu$. Finally, l is reinserted into the list. This procedure

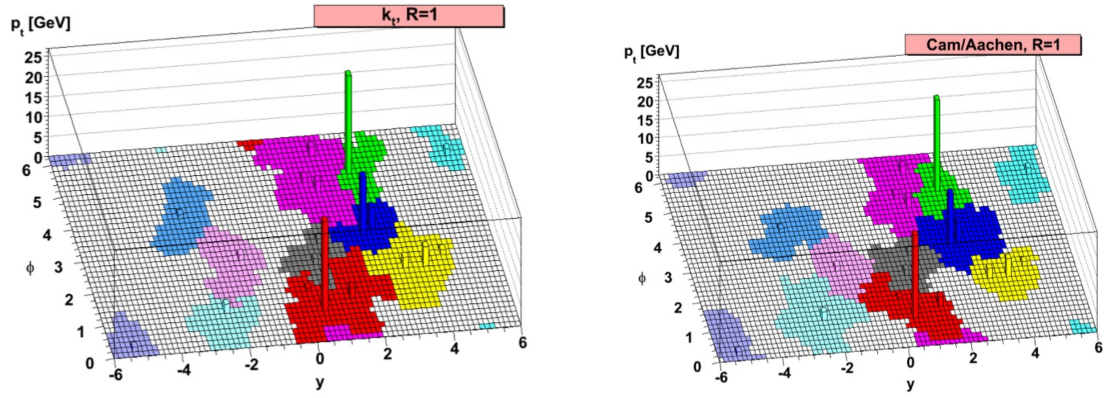

(a) k_T algorithm

(b) Cambridge-Aachen algorithm

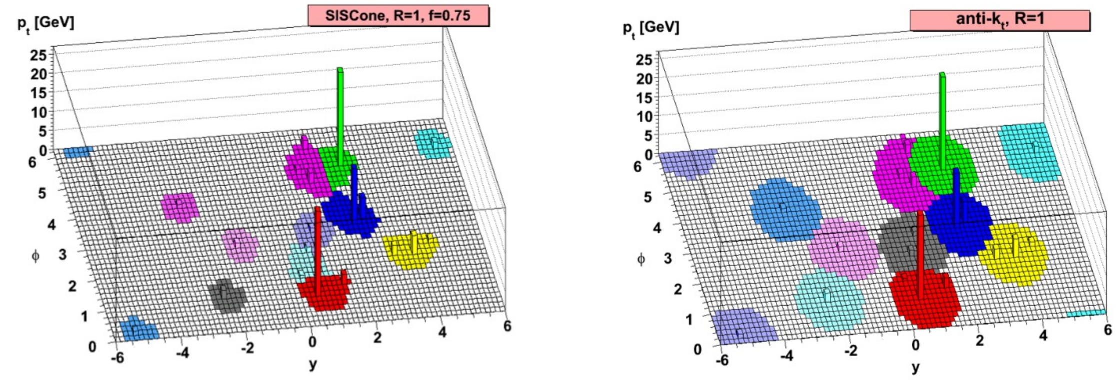

(c) SISCone algorithm

(d) Anti-k_T algorithm

Figure 1.8: Jet clustering with four different jet algorithms starting from the same generated parton-level sample with randomly distributed soft entities. The entities are located in the $\phi \times y$ plane, where y is the rapidity. The figures show the transverse momentum p_T of the entities in GeV as a function of their position in angular space. The colored areas are the jets as identified by the algorithms. Figures taken from [33].

is repeated until the list is empty.

It is quite instructive to compare the different k_T algorithms and the SIScone algorithm by running them on the same event. This has be done in [33] and the resulting plots are shown in Fig. 1.8. One of the reasons for preferring the anti-k_T algorithm over the other k_T algorithms are the nicely shaped jets produced by this algorithm. This may be understood from the nature of the anti-k_T algorithm. With $p = -1$ in Eq. (1.101) the distance d_{ij} becomes large between two soft (i.e. low k_T) objects. Thus, having a hard object surrounded by soft ones, the minimum distance of all the soft objects will be the distance to the hard object. This eventually leads to fact that soft particles will prefer to cluster with the hard one over clustering among themselves. For this reason, a hard entity which is surrounded by only soft ones within a distance of $2R_{k_T}$ will cluster all soft particles within a circle of

radius R_{k_T}. This gives a perfectly conical jet.
On the other hand, the k_T algorithm and the Cambridge/Aachen algorithm tend to cluster soft particles among themselves before associating them to the harder ones. This leads to the irregularly shaped objects in Fig. 1.8.
In comparison to the cone algorithm, it is worth mentioning that there is no need to define a split and merge criterion, as the recombinative nature of the k_T algorithms cannot produce overlapping jets. This can be seen in the two jets near $y = 2$ and $\phi = 5$ in Fig. 1.8. The cone algorithm found two overlapping jets. The chosen split and merge criterion splits the overlapping region along a straight line between the two jets. With the anti-k_T algorithm, however, all the soft particles surrounding the harder event get clustered among this one, leaving behind a crescent-like shape for the softer jet.

The J_{E_T} Algorithm

We follow the introduction of our publication [193] and present a rather new algorithm for defining jets that was proposed by Georgi in 2014 [34]. It is based on the idea of assembling jets by maximizing a suitable function of the four-momenta of final-state particles. Defining the total four-momentum of a given subset of the final-state particles as

$$P_{\text{set}} \equiv \sum_{i \,\in\, \text{set}} p_i \,, \tag{1.103}$$

this function may in its simplest form be defined as

$$J(P_{\text{set}}) \equiv E_T^{\text{set}} - \beta \, \frac{m_{\text{set}}^2}{E_T^{\text{set}}} \,, \tag{1.104}$$

where $m_{\text{set}}^2 \equiv (P_{\text{set}})^2$. This definition corresponds to the one originally given in [34], except that we have followed Ref. [194] to use the total *transverse* energy,

$$E_T^{\text{set}} \equiv \sqrt{(P_{\text{set}}^x)^2 + (P_{\text{set}}^y)^2 + m_{\text{set}}^2} \,, \tag{1.105}$$

of the particles rather than just their energy, the former being boost-invariant and hence more appropriate for the application to hadronic scattering. In this version, the algorithm has been termed "J_{E_T} algorithm" in [194]. The parameter $\beta > 1$ is fixed and specifies the algorithm. The idea behind maximizing J in Eq. (1.104) is that it forces particles to be arranged in collimated jets: if the invariant mass m_{set} of the set is large, the set will not produce a global maximum of J. So only high-E_T^{set}, low-mass, sets give rise to jets. A reconstructed jet thus maximizes the function J with the value

$$J(P_{\text{jet}}) \equiv E_T^{\text{jet}} - \beta \frac{m_{\text{J}}^2}{E_T^{\text{jet}}} \,, \tag{1.106}$$

P_{jet} and E_T^{jet} being the four-momentum and transverse energy of the jet, respectively, and m_{J} its invariant mass. The algorithm is iterative; once a jet has been found, its particles are removed from the list of particles in the event, and the algorithm is applied to the remaining ones. We note that variants of the function J may be introduced, which may potentially improve the applicability in actual experimental jet analyses. For instance, one can define a class of J_{E_T} algorithms by considering weighted functions [194, 195]

$$J^{(n)}(P_{\rm set}) \;\equiv\; (E_T^{\rm set})^n \left(1 - \beta \frac{m_{\rm set}^2}{(E_T^{\rm set})^2}\right) \tag{1.107}$$

for the maximization procedure, where the case $n = 1$ corresponds to (1.104), i.e. $J^{(1)} = J$. Other choices are conceivable. For instance, one could define

$$\tilde{J}^{(k)}(P_{\rm set}) \;\equiv\; E_T^{\rm set} \left[1 - \beta \left(\frac{m_{\rm set}}{E_T^{\rm set}}\right)^{2k}\right] \qquad \text{with} \qquad k > 0\,, \tag{1.108}$$

which increases or decreases the "penalty" for sets with large $m_{\rm set}$. Although infrared-safe at NLO, this choice modifies the infrared structure of the cross section by changing the threshold logarithms, which is not desirable. We also note that related ideas for defining jets were introduced earlier in the context of the "N-jettiness" observable [196], although there the focus was on defining an exclusive N-jet cross section.

Chapter 2

NLO Calculation for Jets defined by a Maximized Jet Function

In this chapter, which is based on our publications [193, 197], we present a next-to-leading order QCD calculation for the single-inclusive production of collimated jets at hadron colliders. We mainly focus on jets defined by maximizing a suitable jet function that depends on the momenta of final-state particles in the event. A jet algorithm of this type was initially proposed by H. Georgi and subsequently further developed into the class of "J_{E_T} algorithms". We have described this class of algorithms in Sec. 1.4 to some extend. Our calculation establishes the infrared safety of the algorithms at next-to-leading order. Following the work in [174, 175], we will derive analytical results for the partonic NLO cross sections by assuming that the jets are rather collimated. This is an approximation that was termed "Narrow Jet Approximation" (NJA) in [175]. In the context of the novel jet algorithms defined by Eqs. (1.104) and (1.107) it means that β is chosen to be rather large, $\beta \gg 1$. In fact, as we shall see, β very closely corresponds to $1/R^2$ where R is the jet parameter in the more standard jet definitions, i.e. the cone opening R_{cone} in cone algorithms or the "distance" parameter R_{k_T} in (anti-)k_T algorithms. In perturbation theory, the NLO jet cross section for the new algorithms will exhibit a form $\mathcal{A}\log(1/\beta)+\mathcal{B}+\mathcal{O}(1/\beta^2)$. The coefficients $\mathcal{A}$ and $\mathcal{B}$ are determined analytically in our NJA approach. As was shown in [174, 175], for the standard jet algorithms the NJA is very accurate even at relatively large $R \sim 0.7$. For our present study, this implies that our calculations will be accurate even for values of β rather close to unity. We discuss similarities and differences with respect to jets defined by cone or (anti-)k_T algorithms and present numerical results for the Tevatron and the LHC.

The remainder of this chapter is organized as follows: In Sec. 2.1 we present our framework for the calculation of NLO jet cross sections in the NJA. We show how to express these cross section in an elegant way by introducing appropriate jet functions. Due to the close analogy of said jet functions and fragmentation functions, we first revisit single-inclusive hadron production in Sec. 2.1.1. After defining the jet functions in Sec. 2.1.2 we show how this method may be applied to the commonly used cone and k_T algorithms in Sec. 2.1.3. After all these preparations, we present the technical details and analytical results of our calculation of single-inclusive jet cross sections in the NJA for the new algorithms in Sec. 2.2. Section 2.3 contains a few simple phenomenological results where we also compare to results for the more standard algorithms. Section 2.4 contains our conclusions.

2.1 Jet Production at Next-to-Leading Order in the NJA

2.1.1 Single-inclusive Hadron Production in Hadronic Collisions

Our formalism to describe single-inclusive jet production in hadronic collisions is best developed by first considering the process $H_1H_2 \to hX$, where a hadron h is observed at large transverse momentum p_T, but no requirement of a reconstructed hadronic jet is made. This is of course a standard reaction, for which the NLO corrections have been known for a long time [91, 198]. The factorized cross section at given hadron p_T and rapidity η reads

$$\begin{aligned}\frac{d\sigma^{H_1H_2\to hX}}{dp_T d\eta} &= \frac{2p_T}{S}\sum_{abc}\int_{x_a^{\min}}^1 \frac{dx_a}{x_a} f_a^{H_1}(x_a,\mu_F)\int_{x_b^{\min}}^1 \frac{dx_b}{x_b} f_b^{H_2}(x_b,\mu_F)\\ &\quad\times\int_{z_c^{\min}}^1 \frac{dz_c}{z_c^2}\,\frac{d\hat{\sigma}_{ab}^c(\hat{s},\hat{p}_T,\hat{\eta},\mu_F,\mu_F',\mu_R)}{v dv dw}\, D_c^h(z_c,\mu_F')\,, \qquad (2.1)\end{aligned}$$

with the usual parton distribution functions f_a^H, the fragmentation functions D_c^h, and the hard-scattering cross sections $d\hat{\sigma}_{ab}^c$ for the partonic processes $ab \to cX'$, X' denoting an unobserved partonic final state. Defining

$$V \equiv 1 - \frac{p_T}{\sqrt{S}}\, e^{-\eta}\,, \quad W \equiv \frac{p_T^2}{SV(1-V)}\,, \qquad (2.2)$$

with $\sqrt{S}$ the hadronic c.m.s. energy, we have

$$x_a^{\min} = W\,, \quad x_b^{\min} = \frac{1-V}{1-VW/x_a}\,, \quad z_c^{\min} = \frac{1-V}{x_b} + \frac{VW}{x_a}\,. \qquad (2.3)$$

The $d\hat{\sigma}_{ab}^c$ are functions of the partonic c.m.s. energy $\hat{s} = x_a x_b S$, the partonic transverse momentum $\hat{p}_T = p_T/z_c$ and the partonic rapidity $\hat{\eta} = \eta - \frac{1}{2}\log(x_a/x_b)$. Since only $\hat{p}_T$ depends on z_c, the last integral in Eq. (2.1) takes the form of a convolution. The variables v and w in (2.1) are the partonic counterparts of V and W:

$$v \equiv 1 - \frac{\hat{p}_T \mathrm{e}^{-\hat{\eta}}}{\sqrt{\hat{s}}}\,, \quad w \equiv \frac{\hat{p}_T^2}{\hat{s}v(1-v)}\,. \qquad (2.4)$$

One customarily expresses $\hat{p}_T$ and $\hat{\eta}$ by v and w:

$$\hat{p}_T^2 = \hat{s}vw(1-v)\;\;,\quad \hat{\eta} = \frac{1}{2}\log\left(\frac{vw}{1-v}\right)\,. \qquad (2.5)$$

Finally, the various functions in Eq. (2.1) are tied together by their dependence on the initial- and final-state factorization scales, μ_F and μ_F', respectively, and the renormalization scale μ_R.

The partonic hard-scattering cross sections may be evaluated in QCD perturbation theory. We write the perturbative expansion to NLO as

$$\frac{d\hat{\sigma}_{ab}^c}{dvdw} = \frac{d\hat{\sigma}_{ab}^{c,(0)}}{dv}\,\delta(1-w) + \frac{\alpha_s(\mu_R)}{2\pi}\,\frac{d\hat{\sigma}_{ab}^{c,(1)}}{dvdw} + \mathcal{O}(\alpha_s^2(\mu_R))\,, \qquad (2.6)$$

where we have used that $w = 1$ for leading-order (LO) kinematics (since the unobserved partonic final state X' consists of a single parton), equivalent to $2\hat{p}_T\cosh(\hat{\eta})/\sqrt{\hat{s}} = 1$. The NLO terms $d\hat{\sigma}_{ab}^{c,(1)}$ have been presented in Refs. [91, 198].

2.1.2 Translation to single-inclusive jet cross section via jet functions

As shown in Refs. [174, 175, 199, 200], one can transform the cross section for single-inclusive hadron production to a single-inclusive jet one. References [174, 175, 199, 200] explicitly constructed this translation at NLO. We may write the jet cross section as

$$\begin{aligned}\frac{d\sigma^{H_1H_2\to\mathrm{jet}X}}{dp_T^{\mathrm{jet}}d\eta^{\mathrm{jet}}} &= \frac{2p_T^{\mathrm{jet}}}{S}\sum_{ab}\int_{x_a^{\min}}^1\frac{dx_a}{x_a}f_a^{H_1}(x_a,\mu_F)\int_{x_b^{\min}}^1\frac{dx_b}{x_b}f_b^{H_2}(x_b,\mu_F)\\ &\quad\times\frac{d\hat{\sigma}_{ab}^{\mathrm{jet,algo}}(\hat{s},p_T^{\mathrm{jet}},\hat{\eta},\mu_F,\mu_R,\mathcal{R})}{vdvdw}\,,\end{aligned}\tag{2.7}$$

where p_T^{jet} and η^{jet} are the jet's transverse momentum and rapidity, and $\mathcal{R}$ denotes a parameter specifying the jet algorithm. We note that we always define the four-momentum of the jet as the sum of four-momenta of the partons that form the jet. This so-called "E recombination scheme" (see, for example [183] and references therein) is the most popular choice nowadays. For the jet cross section we still have

$$x_a^{\min}=W\,,\quad x_b^{\min}=\frac{1-V}{1-VW/x_a}\,,\tag{2.8}$$

as in (2.3), but with V and W now defined by

$$V\equiv1-\frac{p_T^{\mathrm{jet}}}{\sqrt{S}}e^{-\eta^{\mathrm{jet}}}\,,\quad W\equiv\frac{(p_T^{\mathrm{jet}})^2}{SV(1-V)}\,.\tag{2.9}$$

Likewise, v and w are as in (2.4) but with $\hat{p}_T\to p_T^{\mathrm{jet}}$. Furthermore, in analogy with the inclusive-hadron case, $\hat{\eta}=\eta^{\mathrm{jet}}-\frac{1}{2}\log(x_a/x_b)$. We note that the partonic cross sections $d\hat{\sigma}_{ab}^{\mathrm{jet,algo}}$ relevant for jet production depend on the algorithm used to define the jet. They do not carry any dependence on a final-state factorization scale.
In order to go from the inclusive-parton cross sections $d\hat{\sigma}_{ab}^{c}$ to the jet ones $d\hat{\sigma}_{ab}^{\mathrm{jet}}$, the idea is to apply proper correction terms to the former. The $d\hat{\sigma}_{ab}^{c}$ have been integrated over the full phase space of all final-state partons other than c. Therefore, they contain contributions where a second parton in the final state is so close to parton c that the two should jointly form the jet for a given jet definition. One can correct for this by subtracting such contributions from $d\hat{\sigma}_{ab}^{c}$ and adding a piece where they actually do form the jet together. At NLO, where there can be three partons c,d,e in the final state, one has after suitable summation over all possible configurations:

$$\begin{aligned}d\hat{\sigma}_{ab}^{\mathrm{jet}} &= \left[d\hat{\sigma}_{ab}^{c}-d\hat{\sigma}_{ab}^{c(d)}-d\hat{\sigma}_{ab}^{c(e)}\right]+\left[d\hat{\sigma}_{ab}^{d}-d\hat{\sigma}_{ab}^{d(c)}-d\hat{\sigma}_{ab}^{d(e)}\right]+\left[d\hat{\sigma}_{ab}^{e}-d\hat{\sigma}_{ab}^{e(c)}-d\hat{\sigma}_{ab}^{e(d)}\right]\\ &\quad+d\hat{\sigma}_{ab}^{cd}+d\hat{\sigma}_{ab}^{ce}+d\hat{\sigma}_{ab}^{de}\,.\end{aligned}\tag{2.10}$$

Here $d\hat{\sigma}_{ab}^{j(k)}$ is the cross section where parton j produces the jet, but parton k is so close that it should be part of the jet, and $d\hat{\sigma}_{ab}^{jk}$ is the cross section when both partons j and k jointly form the jet. The decomposition (2.10) is completely general to NLO. It may be applied for any jet algorithm, as long as the algorithm is infrared-safe. A property of the $d\hat{\sigma}_{ab}^{\mathrm{jet}}$ is that all dependence on the final-state factorization scale μ_F', which was initially present in the $d\hat{\sigma}^{j}_{ab}$, must cancel. This cancellation comes about in (2.10) because the $d\hat{\sigma}^{jk}_{ab}$ possess final-state collinear singularities that require factorization. This introduces dependence on μ'_F in exactly the right way as to compensate the μ'_F-dependence of the $d\hat{\sigma}^{j}_{ab}$.

In the NJA, the correction terms $d\hat{\sigma}^{j(k)}_{ab}$ and $d\hat{\sigma}^{jk}_{ab}$ may be computed analytically. At NLO, they both receive contributions from real-emission 2 → 3 diagrams only. For the NJA one assumes that the observed jet is rather collimated. This in essence allows to treat the two outgoing partons j and k as collinear. We start with the computation of the $d\hat{\sigma}^{jk}_{ab}$. Usually, the partonic cross section is considered differential in the variables

$$v = 1 + \frac{t}{s}\ , \quad w = \frac{-u}{s+t}\ , \tag{2.11}$$

where the partonic Mandelstam variables are defined by

$$s \equiv (p_a + p_b)^2, \quad t \equiv (p_a - P_{\rm jet})^2, \quad u \equiv (p_b - P_{\rm jet})^2, \tag{2.12}$$

with the momenta p_a, p_b of the incoming partons and the jet momentum $P_{\rm jet}$. However, for our purposes it turns out to be more convenient to work with the variables,

$$v \quad \text{and} \quad z \equiv 1 - v + vw\ , \tag{2.13}$$

instead. As was shown in [174, 175], in the NJA $d\hat{\sigma}^{jk}_{ab}$ is given by

$$\frac{d\hat{\sigma}^{jk}_{ab}}{dv dw} = \frac{\alpha_s}{2\pi}\mathcal{N}_{ab\to K}(v,w,\varepsilon)\, v\delta(1-z)\int_0^1 d\zeta\, \zeta^{-\varepsilon}(1-\zeta)^{-\varepsilon}\tilde{P}^{<}_{jK}(\zeta)\int_0^{(m^{\rm algo}_{\rm J,max})^2(\zeta)}\frac{dm_{\rm J}^2}{m_{\rm J}^2}\, m_{\rm J}^{-2\varepsilon}, \tag{2.14}$$

where we have used dimensional regularization with $D = 4 - 2\varepsilon$ space-time dimensions. Equation (2.14) is derived from the fact that the leading contributions in the NJA come from a parton K splitting into partons j and k “almost” collinearly in the final state. We therefore have an underlying Born process $ab \to KX$ (with some unobserved recoil final state X), whose d-dimensional cross section is contained in the “normalization factor” $\mathcal{N}_{ab\to K}$, along with some trivial factors. The integrand then contains the D-dimensional splitting functions $\tilde{P}^{<}_{jK}(z)$, where the superscript “$<$” indicates that the splitting function is strictly at $z < 1$, that is, without its $\delta(1-z)$ contribution that is present when $j = K$ (see [174, 175]). These splitting functions are obtained in the following way: Dropping the δ-function contributions and ignoring the “plus”-distributions in (1.70), we obtain the splitting functions $P^{<}_{ij}(z)$ at $z < 1$. For our calculations, we actually need these functions computed in dimensional regularization in $D = 4 - 2\varepsilon$ dimensions, where they are denoted as $\tilde{P}^{<}_{ij}(z)$. We have

$$\tilde{P}^{<}_{ij}(z) = P^{<}_{ij}(z) + \varepsilon P^{(\varepsilon)}_{ij}(z)\,. \tag{2.15}$$

The functions $\tilde{P}^{<}_{ij}(z)$ are given by

$$\begin{aligned}
\tilde{P}^{<}_{qq}(z) &= C_F\left[\frac{1+z^2}{1-z}-\varepsilon(1-z)\right], \\
\tilde{P}^{<}_{qg}(z) &= \frac{1}{2}\left[z^2+(1-z)^2-2\varepsilon z(1-z)\right], \\
\tilde{P}^{<}_{gq}(z) &= C_F\left[\frac{1+(1-z)^2}{z}-\varepsilon z\right], \\
\tilde{P}^{<}_{gg}(z) &= 2C_A\frac{(1-z+z^2)^2}{z(1-z)},
\end{aligned} \tag{2.16}$$

where $C_A = 3$ and $C_F = 4/3$. The argument ζ of the splitting functions in Eq. (2.14) is the fraction of the intermediate particle's momentum (equal to the jet momentum) transferred in the splitting. The second integral in (2.14) runs over the pair mass of partons j and k, which for the contribution $d\hat{\sigma}^{jk}_{ab}$ is identical to the jet mass m_{J}. The explicit factor m_{J}^2 in the denominator represents the propagator of the splitting parton K. The integral over the pair mass of partons j and k runs between zero and an upper limit $m^{\text{algo}}_{\text{J,max}}$. In the NJA, where the two partons are assumed to be almost collinear, $m^{\text{algo}}_{\text{J,max}}$ is formally taken to be relatively small, which justifies the approximations made in deriving Eq. (2.14). Note that powers of m_{J}^2 have been neglected wherever possible, which makes the integral over m_{J}^2 trivial. As indicated, the value of $m^{\text{algo}}_{\text{J,max}}$ depends on the jet algorithm chosen.

We now turn to the terms $d\hat{\sigma}^{j(k)}_{ab}, d\hat{\sigma}^{k(j)}_{ab}$ in (2.10). These are defined in such a way that they subtract the contribution where parton j forms the jet, but parton k is so close that it should normally be included in the jet (or vice versa). It is useful to introduce the pair mass m of partons j and k. Note that this is not the jet mass since for $d\hat{\sigma}^{j(k)}_{ab}$ only parton j forms the jet. In terms of m we find from Eq. (13) of Ref. [174]

$$\frac{d\hat{\sigma}^{j(k)}_{ab}}{dvdw} = \frac{\alpha_s}{2\pi}\mathcal{N}_{ab\to K}(v,w,\varepsilon)\,v\,[z(1-z)]^{-\varepsilon}\tilde{P}^{<}_{jK}(z)\int_0^{(m^{\text{algo}}_{\max})^2(z)}\frac{dm^2}{m^2}\,m^{-2\varepsilon}, \tag{2.17}$$

where $z = 1-v+vw$ is the relevant variable for the splitting $K \to jk$. Again, implementation of the jet algorithm boils down to the determination of the upper limit on the m^2 integration.

By close inspection of Eqs. (2.10), (2.14) and (2.17), we have found that in the NJA the jet cross section may be cast into a form that makes use of the *single-inclusive parton* production cross sections $d\hat{\sigma}^c_{ab}$:

$$\begin{aligned}
\frac{d\sigma^{H_1H_2\to\text{jet}X}}{dp_T^{\text{jet}}d\eta^{\text{jet}}} &= \frac{2p_T^{\text{jet}}}{S}\sum_{abc}\int_{x_a^{\min}}^1\frac{dx_a}{x_a}f_a^{H_1}(x_a,\mu_F)\int_{x_b^{\min}}^1\frac{dx_b}{x_b}f_b^{H_2}(x_b,\mu_F) \\
&\times\int_{z_c^{\min}}^1\frac{dz_c}{z_c^2}\,\frac{d\hat{\sigma}^c_{ab}(\hat{s},\hat{p}_T,\hat{\eta},\mu_F,\mu'_F,\mu_R)}{vdvdw}\,\mathcal{J}_c^{\text{algo}}\left(z_c,\frac{\mathcal{R}p_T^{\text{jet}}}{\mu'_F},\mu_R\right),
\end{aligned} \tag{2.18}$$

with *inclusive jet functions* $\mathcal{J}_q^{\rm algo}$ and $\mathcal{J}_g^{\rm algo}$. We have $\hat{p}_T = p_T^{\rm jet}/z_c$, and $x_a^{\rm min}, x_b^{\rm min}, z_c^{\rm min}$ and v, w are now as in (2.3) and (2.4), respectively. Equation (2.18) thus states that one can go directly from the cross section for single-hadron production to that for jet production by replacing the fragmentation functions D_c^h in (2.1) by the jet functions $\mathcal{J}_c^{\rm algo}$. The latter are such that any dependence on μ_F' disappears from the cross section. They depend on the jet algorithm and hence on a generic jet parameter $\mathcal{R}$. We emphasize, that these inclusive jet functions are not to be confused with the function used to define the class of J_{E_T} algorithms!

Similar to the partonic cross sections in Eq. (2.6), the jet functions obey a perturbative expansion which reads

$$\mathcal{J}_c^{\rm algo}\left(z, \lambda, \mu_R\right) = \delta(1-z) + \frac{\alpha_s(\mu_R)}{2\pi}\mathcal{J}_c^{\rm algo,(1)}\left(z, \lambda\right) + \mathcal{O}(\alpha_s^2(\mu_R))\,. \tag{2.19}$$

Equation (2.18) evidently exhibits a factorized structure in the final state for the jet cross section in the NJA. Its physical interpretation is essentially that the hard scattering produces a parton c that "fragments" into the observed jet via the jet function $\mathcal{J}_c^{\rm algo}$, the jet carrying the fraction z_c of the produced parton's momentum. At NLO, the factorization is in fact rather trivial. To get a clear sense of it, it is instructive to see how one recovers (2.7),(2.10) from (2.18). To this end, we combine (2.6) and (2.19) and expand to first order in the strong coupling. The products of the $d\hat{\sigma}_{ab}^c$ with the LO $\delta(1-z)$ terms in $\mathcal{J}_c^{\rm algo}$ just reproduce the single-inclusive parton cross sections at $\hat{p}_T = p_T^{\rm jet}$, i.e. the terms $d\hat{\sigma}_{ab}^c, d\hat{\sigma}_{ab}^d, d\hat{\sigma}_{ab}^e$ in (2.10). The only other terms surviving in the expansion to $\mathcal{O}(\alpha_s)$ are the products of the LO terms $\delta(1-w)\, d\hat{\sigma}_{ab}^{c,(0)}/dv$ of (2.6) with the $\mathcal{O}(\alpha_s)$ terms in the jet functions. Hence, we construct the $\mathcal{O}(\alpha_s)$ part of the jet functions in such a way that these terms precisely give the remaining contributions $d\hat{\sigma}_{ab}^{cd} - d\hat{\sigma}_{ab}^{c(d)} - d\hat{\sigma}_{ab}^{d(c)}$ (plus the other combinations) in (2.10). Because of the convolution in z_c in (2.18), the $\delta(1-w)$-function in the Born cross section actually fixes z_c to the value $z_c = 2p_T^{\rm jet}\cosh(\hat{\eta})/\sqrt{\hat{s}}$. Based on our NLO calculation, we evidently cannot prove the factorization shown in (2.18) to beyond this order. We note, however, that similar factorization formulas have been derived using Soft Collinear Effective Theory (SCET) techniques [201–203], for the case of jet observables in e^+e^- annihilation. In particular, functions closely related to our inclusive jet functions $\mathcal{J}_{q,g}^{\rm algo}$ may be found in Ref. [201], where they are termed "unmeasured" quark (or gluon) jet functions. However, the observable considered in Ref. [201] is of a more exclusive type. Inclusive calculations for jets in hadronic collisions within the framework of SCET may be found, for instance, in Refs. [204–206]. We shall return to comparisons with SCET results below.

To explicitly construct the jet functions for a given jet algorithm we look again at Eqs. (2.14) and (2.17) and perform the mass integrations. The common factor $v\mathcal{N}_{ab\to K}(v, w, \varepsilon)$ includes the partonic born cross section and thus is part of $d\hat{\sigma}_{ab}^c$ in Eq. (2.18) as described above. Thus, we write

$$\begin{aligned}\frac{d\hat{\sigma}_{ab}^{jk}}{dv dw} &= \frac{\alpha_s}{2\pi}\mathcal{N}_{ab\to K}(v, w, \varepsilon)\, v\left(-\frac{1}{\varepsilon}\right)\delta(1-z)\int_0^1 d\zeta\,\zeta^{-\varepsilon}(1-\zeta)^{-\varepsilon}\tilde{P}_{jK}^{<}(\zeta)\left[(m_{\rm J,max}^{\rm algo})^2(\zeta)\right]^{-\varepsilon} \\ &\equiv v\,\mathcal{N}_{ab\to K}(v, w, \varepsilon)\times\frac{\alpha_s}{2\pi}\,d\tilde{\sigma}_{jk}\end{aligned} \tag{2.20}$$

and

$$\begin{aligned}\frac{d\hat{\sigma}_{ab}^{j(k)}}{dv dw} &= \frac{\alpha_s}{2\pi}\mathcal{N}_{ab\to K}(v,w,\varepsilon)\, v\left(-\frac{1}{\varepsilon}\right)\,[z(1-z)]^{-\varepsilon}\tilde{P}_{jK}^{<}(z)\left[(m_{\max}^{\rm algo})^2(z)\right]^{-\varepsilon} \\ &\equiv v\,\mathcal{N}_{ab\to K}(v,w,\varepsilon)\times\frac{\alpha_s}{2\pi}\,d\tilde{\sigma}_{j(k)} \qquad (2.21)\end{aligned}$$

Now the $\mathcal{O}(\alpha_s)$ part of jet functions describing the perturbative transition of a quark or gluon into a jet is given by

$$\begin{aligned}\mathcal{J}_q^{(1)}(z,\lambda) &= d\tilde{\sigma}_{qg} - d\tilde{\sigma}_{q(g)} - d\tilde{\sigma}_{g(q)} - d\sigma_q^{\rm coll}\,, \\ \mathcal{J}_g^{(1)}(z,\lambda) &= \frac{1}{2}d\tilde{\sigma}_{gg} - d\tilde{\sigma}_{g(g)} + n_f d\tilde{\sigma}_{q\bar{q}} - n_f d\tilde{\sigma}_{q(\bar{q})} - n_f d\tilde{\sigma}_{\bar{q}(q)} - d\sigma_g^{\rm coll}\,, \qquad (2.22)\end{aligned}$$

where $d\sigma_i^{\rm coll}$ are appropriate collinear subtraction terms, see, for instance Eq. (16) in [174]. When evaluating Eqs. (2.20) and (2.21) double and single poles in ε appear. The $1/\varepsilon^2$ terms cancel between the $d\tilde{\sigma}_{jk}$ and $d\tilde{\sigma}_{j(k)}$ in the combinations given in Eq. (2.22). The $1/\varepsilon$ singularities take exactly the form of the collinear subtraction terms and since we have to subtract these configurations as discussed in the text above, these terms cancel as well. Only finite terms remain which define our jet functions.

2.1.3 Jet Functions for Cone and k_T Algorithms

Before presenting the results for the newly developed class of J_{E_T} jet algorithms, we first revisit inclusive jet production in the NJA for the standard cone and k_T algorithms as presented in [174, 175]. When talking about the standard cone algorithm, we have in mind primarily the "Seedless Infrared Safe Cone" (SISCone) algorithm introduced in Ref. [189] which represents the only cone-based jet definition known to be strictly infrared-safe. However, for single-inclusive jet cross sections, the lack of infrared-safety of other cone-type algorithms occurs first at next-to-next-to-leading order in perturbation theory and hence is not an issue here. Compared to the calculations in [174, 175], we formulate everything in terms of jet functions within the framework outlined in the previous section. All we have to do is to find the correct limits of the mass integrations, $(m_{\rm J,max}^{\rm algo})^2(\zeta)$ and $(m_{\max}^{\rm algo})^2(z)$. From [175] we have

$$\begin{aligned}(m_{\rm J,max}^{k_T})^2(\zeta) &= (p_T^{\rm jet})^2 R_{k_T}^2\zeta(1-\zeta)\,, \\ (m_{\rm J,max}^{\rm cone})^2(\zeta) &= (p_T^{\rm jet})^2 R_{\rm cone}^2 \min\left(\frac{\zeta}{1-\zeta},\frac{1-\zeta}{\zeta}\right)\,. \qquad (2.23)\end{aligned}$$

To obtain the mass limits relevant for the $d\tilde{\sigma}_{j(k)}$, we have to find the configurations where parton k is so close to parton j that they should form the jet together, but actually only j is forming the jet. This is a very similar situation as for the $d\tilde{\sigma}_{jk}$. However, instead of integrating over the momentum fraction ζ, the momentum fraction is fixed to z. Thus, we have to replace $\zeta \to z$. Furthermore, while the jet is composed by partons j and k together in $d\tilde{\sigma}_{jk}$ (i.e. $E_{\rm jet} = E_j + E_k$) and the momentum fraction ζ was defined by $E_j = \zeta E_{\rm jet}$, we now have $E_j = E_{\rm jet}$ since only parton j is forming the jet. To correct for this, we have to replace $E_{\rm jet} \to E_{\rm jet}/z$ in Eq. (2.23) which effectively can be achieved by dividing the right hand sides in Eq. (2.23) by z^2. All in all, we obtain

$$\begin{aligned}
(m_{\rm max}^{k_T})^2(z) &= (p_T^{\rm jet})^2 R_{k_T}^2 \frac{(1-z)}{z}\,, \\
(m_{\rm max}^{\rm cone})^2(z) &= (p_T^{\rm jet})^2 R_{\rm cone}^2 \frac{1}{z^2} \min\left(\frac{z}{1-z}, \frac{1-z}{z}\right).
\end{aligned} \tag{2.24}$$

Once the mass limits are found, the calculation of the jet functions is quite straightforward. The poles generated by expression (2.21) may be extracted in the standard way. If $\tilde{P}_{jK}^{<}$ is a non-diagonal splitting function one may simply expand in ε. If it is a diagonal one, it has a term $C_j/(1-z)$ (where $C_q = C_F$ and $C_g = 2C_A$) that gives rise to a double pole. To see this, we use the identity

$$C_j(1-z)^{-1-2\varepsilon} = C_j\left[-\frac{1}{2\varepsilon}\delta(1-z) + \frac{1}{(1-z)_+} - 2\varepsilon\left(\frac{\log(1-z)}{1-z}\right)_+ + \mathcal{O}(\varepsilon^2)\right], \tag{2.25}$$

where the "plus"-distribution is defined as usual by

$$\int_0^1 dz\, f(z)[g(z)]_+ \equiv \int_0^1 dz\,(f(z)-f(1))g(z)\,. \tag{2.26}$$

After having replaced all appearing $(1-z)^{-1-2\varepsilon}$ according to Eq. (2.25), we may safely expand in ε. The first term of Eq. (2.25) together with the overall $1/\varepsilon$ yields the double pole.

All in all, we obtain by combining the appropriate $d\tilde{\sigma}_{jk}$ and $d\tilde{\sigma}_{j(k)}$ according to Eq. (2.22) the jet functions

$$\begin{aligned}
\mathcal{J}_q^{\rm algo}(z,\lambda,\mu_R) &= \delta(1-z) - \frac{\alpha_s(\mu_R)}{2\pi}\Bigg[2C_F(1+z^2)\left(\frac{\log(1-z)}{1-z}\right)_+ + P_{qq}(z)\log\left(\lambda^2\right) \\
&\qquad + \delta(1-z) I_q^{\rm algo} + \mathcal{I}_q^{\rm algo}(z) + C_F(1-z)\Bigg] \\
&\qquad - \frac{\alpha_s(\mu_R)}{2\pi}\Big[P_{gq}(z)\log\left(\lambda^2(1-z)^2\right) + C_F\, z\Big]\,, \\
\mathcal{J}_g^{\rm algo}(z,\lambda,\mu_R) &= \delta(1-z) - \frac{\alpha_s(\mu_R)}{2\pi}\Bigg[\frac{4C_A(1-z+z^2)^2}{z}\left(\frac{\log(1-z)}{1-z}\right)_+ \\
&\qquad + P_{gg}(z)\log\left(\lambda^2\right) + \delta(1-z) I_g^{\rm algo} + \mathcal{I}_g^{\rm algo}(z)\Bigg] \\
&\qquad - \frac{\alpha_s(\mu_R)}{2\pi}\, 2N_f\Big[P_{qg}(z)\log\left(\lambda^2(1-z)^2\right) + z(1-z)\Big]\,,
\end{aligned} \tag{2.27}$$

where $C_F = 4/3$, $C_A = 3$ and N_f is the number of active flavors. In Eq. (2.27) we have used the standard LO splitting functions, see Eq. (1.70). The dependence on the jet algorithm is reflected in the terms $I_q^{\rm algo}$ and $I_g^{\rm algo}$, which are just numbers, and the z dependent functions $\mathcal{I}_q^{\rm algo}(z)$ and $\mathcal{I}_g^{\rm algo}(z)$. For cone algorithms we have

$$\begin{aligned}
I_q^{\rm cone} &= C_F\left(-\frac{7}{2}+\frac{\pi^2}{3}-3\log 2\right)\,,\\
I_g^{\rm cone} &= C_A\left(-\frac{137}{36}+\frac{\pi^2}{3}-\frac{11}{3}\log 2\right)+\frac{N_f}{2}\left(\frac{23}{18}+\frac{4}{3}\log 2\right)\,,\\
\mathcal{I}_q^{\rm cone}(z) &= -2\left[P_{qq}(z)+P_{gq}(z)\right]\left[\log(z)\Theta\left(z>\frac{1}{2}\right)+\log(1-z)\Theta\left(z<\frac{1}{2}\right)\right]\,,\\
\mathcal{I}_g^{\rm cone}(z) &= -2\left[P_{gg}(z)+2N_f P_{qg}(z)\right]\left[\log(z)\Theta\left(z>\frac{1}{2}\right)+\log(1-z)\Theta\left(z<\frac{1}{2}\right)\right]\,,
\end{aligned} \tag{2.28}$$

while for the (anti-)k_t algorithms

$$\begin{aligned}
I_q^{k_t} &= C_F\left(-\frac{13}{2}+\frac{2\pi^2}{3}\right)\,,\\
I_g^{k_t} &= C_A\left(-\frac{67}{9}+\frac{2\pi^2}{3}\right)+\frac{23}{18}N_f\,,\\
\mathcal{I}_q^{k_T}(z) &= 0\,,\\
\mathcal{I}_g^{k_T}(z) &= 0\,.
\end{aligned} \tag{2.29}$$

We finally note, that these results are consistent with Refs. [204–206] where calculations are performed within the framework of SCET. Moreover, the authors of Ref. [206] propose a momentum sum rule for jet functions,

$$\int_0^1 dz\; z\,\mathcal{J}_c^{\rm algo}(z, z\lambda, \mu_R) = 1\,. \tag{2.30}$$

This sum rule is similar to the momentum sum rule for fragmentation functions in Eq. (1.67). It basically reflects conservation of longitudinal momentum. The existence of such a sum rule is consistent with the interpretation of the jet functions in the sense that these functions describe the formation of a *jet* from an initiating parton analogously to FFs describing the formation of a *hadron* from an initiating parton. The difference compared to the FF case is that the jet functions are calculable within perturbation theory and that there is no need to include a sum over all hadron species. It is said hadronic sum and the singular behavior for $z \to 0$, which make the momentum sum rule for FFs unusable in practical applications. However, in the case of inclusive jet production, there is no hadronic sum and the expressions are integrable for $z \in [0,1]$. Hence, the sum rule offers a powerful check of the calculation. Indeed, we have verified by an explicit calculation that the jet functions (2.27) satisfy the sum rule (2.30).

2.2 Jet Functions for J_{E_T} Algorithms

We will now apply the NJA to the jet definition obtained by maximizing the function $J^{(n)}$ introduced by Eq. (1.107). We can straightforwardly derive the mass limits for this class of J_{E_T} algorithms. For $d\tilde{\sigma}_{jk}$, we just need to make sure that the two partons j and k really jointly form the jet. This requires that the value of the $J^{(n)}$ function constructed from the two partons together is larger than the value of $J^{(n)}$ for each parton individually, or

$$(E_T^{\rm jet})^n \left(1 - \beta \frac{m_{\rm J}^2}{(E_T^{\rm jet})^2}\right) \geq \max\left((E_T^j)^n, (E_T^k)^n\right) \ , \tag{2.31}$$

which implies

$$m_{\rm J}^2 \leq \frac{(E_T^{\rm jet})^2}{\beta}\left(1 - \frac{\max\left((E_T^j)^n, (E_T^k)^n\right)}{(E_T^{\rm jet})^n}\right) . \tag{2.32}$$

From this it is evident that the NJA corresponds to the limit of large β. We note that in the NJA we may replace the transverse energies by the transverse momenta (denoted by $p_T^{\rm jet}$ and p_T^j, p_T^k for the jet and the partons, respectively), since corrections introduced by this will always be suppressed by an additional power of $1/\beta$. Using the relations $p_T^j = \zeta p_T^{\rm jet}$, $p_T^k = (1-\zeta)p_T^{\rm jet}$ appropriate for the splitting described above, Eq. (2.32) finally gives

$$m_{\rm J}^2 \leq \frac{(p_T^{\rm jet})^2}{\beta} \min\left(1 - (1-\zeta)^n, 1 - \zeta^n\right) \equiv \left(m_{\rm J,max}^{J_{E_T}}\right)^2 (\zeta) \ . \tag{2.33}$$

The right-hand-side is precisely the $(m_{\rm J,max}^{J_{E_T}})^2$ we need. Inserting this mass limit into (2.14) we arrive at

$$d\tilde{\sigma}_{jk} \ = \ \delta(1-z)\left(-\frac{1}{\varepsilon}\right)\left(\frac{(p_T^{\rm jet})^2}{\beta}\right)^{-\varepsilon} I_{jK}^{(n)} \ , \tag{2.34}$$

where

$$I_{jK}^{(n)} \equiv \left[\int_0^{1/2} d\zeta \ \left(1-(1-\zeta)^n\right)^{-\varepsilon} + \int_{1/2}^1 d\zeta \ \left(1-\zeta^n\right)^{-\varepsilon}\right] \zeta^{-\varepsilon}(1-\zeta)^{-\varepsilon} \, \tilde{P}_{jK}^{<}(\zeta) \, . \tag{2.35}$$

Evaluation of these integrals for general n is tedious. In any case, we are only interested in the cases $n = 1$ and $n = 2$ here, for which the integrals may be easily computed in closed form. For $n = 1$, expanding to $\mathcal{O}(\varepsilon)$ because of the overall $1/\varepsilon$-pole in (2.34), we find:

$$\begin{aligned}
I_{qq}^{(1)} \ &= \ C_F\left[-\frac{1}{\varepsilon} - \frac{3}{2} + \varepsilon\left(-5 + \frac{\pi^2}{2} - \frac{3}{2}\log 2\right)\right] \ = \ I_{gq}^{(1)} \ , \\
I_{qg}^{(1)} \ &= \ \frac{1}{2}\left[\frac{2}{3} + \varepsilon\left(\frac{23}{12} + \frac{2}{3}\log 2\right)\right] \ , \\
I_{gg}^{(1)} \ &= \ 2C_A\left[-\frac{1}{\varepsilon} - \frac{11}{6} + \varepsilon\left(-\frac{45}{8} + \frac{\pi^2}{2} - \frac{11}{6}\log 2\right)\right] \ ,
\end{aligned} \tag{2.36}$$

while for $n=2$

$$\begin{aligned}
I_{qq}^{(2)} &= C_F\left[-\frac{1}{\varepsilon}-\frac{3}{2}+\log 2+\frac{\varepsilon}{2}\left(-13+\pi^2+18\log 2+\log^2 2-9\log 3+2\,\mathrm{Li}_2\left(\frac{1}{4}\right)\right)\right] \ , \\
I_{gq}^{(2)} &= I_{qq}^{(2)} \ , \\
I_{qg}^{(2)} &= \frac{1}{2}\left[\frac{2}{3}+\varepsilon\left(\frac{67}{18}-12\log 2+6\log 3\right)\right] \ , \\
I_{gg}^{(2)} &= 2C_A\left[-\frac{1}{\varepsilon}-\frac{11}{6}+\log 2\right. \\
&\qquad \left.+\frac{\varepsilon}{2}\left(-\frac{289}{18}+\pi^2+30\log 2+\log^2 2-15\log 3+2\,\mathrm{Li}_2\left(\frac{1}{4}\right)\right)\right] \ ,
\end{aligned} \tag{2.37}$$

with the value $\mathrm{Li}_2(1/4)=0.267653\ldots$ of the Dilogarithm function. Note that these integrals differ from the corresponding ones for the cone or k_T algorithms given in [174, 175], although the leading terms for $\varepsilon\to 0$ are always the same. One can show that for arbitrary n

$$\begin{aligned}
I_{qq}^{(n)} &= C_F\left[-\frac{1}{\varepsilon}-\frac{3}{2}+\log(n)+\varepsilon\tilde{I}_{qq}^{(n)}\right] = I_{gq}^{(n)} \ , \\
I_{qg}^{(n)} &= \frac{1}{2}\left[\frac{2}{3}+\varepsilon\tilde{I}_{qg}^{(n)}\right] \ , \\
I_{gg}^{(n)} &= 2C_A\left[-\frac{1}{\varepsilon}-\frac{11}{6}+\log(n)+\varepsilon\tilde{I}_{gg}^{(n)}\right] \ ,
\end{aligned} \tag{2.38}$$

to which we will return later.

We now focus on the calculation of the $d\tilde{\sigma}_{j(k)}$. As described above, the mass limit relevant for this part may be obtained from Eq. (2.33) by substituting $\zeta\to z$ and division by z^2. Hence,

$$\left(m_{\mathrm{max}}^{J_{E_T}}\right)^2(z)=\frac{(p_T^{\mathrm{jet}})^2}{\beta}\frac{1}{z^2}\min\left(1-(1-z)^n,1-z^n\right) \ . \tag{2.39}$$

When using this mass limit, we observe an additional complication in the diagonal case compared to cone or k_T algorithms. Instead of terms $\propto(1-z)^{-1-2\varepsilon}$ we find the diagonal terms to be $\propto(1-z)^{-1-\varepsilon}(1-z^n)^{-\varepsilon}$. To make use of the relation (2.25), we observe that

$$(1-z^n)^{-\varepsilon} = n^{-\varepsilon}(1-z)^{-\varepsilon}\left[1+\mathcal{O}((1-z)^2)\right] \ . \tag{2.40}$$

This allows to proceed as in the diagonal cases for cone and k_T algorithms. Combining everything above, we obtain the following jet functions for J_{E_T} algorithms

$$\begin{aligned}
\mathcal{J}_q^{J_{E_T}}(z,\lambda,\mu_R) &= \delta(1-z) - \frac{\alpha_s(\mu_R)}{2\pi}\Bigg[2C_F(1+z^2)\left(\frac{\log(1-z)}{1-z}\right)_+ + P_{qq}(z)\log\left(\lambda^2\right) \\
&\qquad + \delta(1-z)I_q^{J_{E_T}} + \mathcal{I}_q^{J_{E_T}}(z) + C_F(1-z)\Bigg] \\
&\qquad - \frac{\alpha_s(\mu_R)}{2\pi}\Big[P_{gq}(z)\log\left(\lambda^2(1-z)^2\right) + C_F\, z\Big]\,, \\
\mathcal{J}_g^{J_{E_T}}(z,\lambda,\mu_R) &= \delta(1-z) - \frac{\alpha_s(\mu_R)}{2\pi}\Bigg[\frac{4C_A(1-z+z^2)^2}{z}\left(\frac{\log(1-z)}{1-z}\right)_+ \\
&\qquad + P_{gg}(z)\log\left(\lambda^2\right) + \delta(1-z)I_g^{J_{E_T}} + \mathcal{I}_g^{J_{E_T}}(z)\Bigg] \\
&\qquad - \frac{\alpha_s(\mu_R)}{2\pi}\,2N_f\Big[P_{qg}(z)\log\left(\lambda^2(1-z)^2\right) + z(1-z)\Big]\,,
\end{aligned} \tag{2.41}$$

with

$$\begin{aligned}
I_q^{J_{E_T},(n)} &= C_F\left(\tilde{I}_{qq}^{(n)} + \frac{\log^2 n}{2}\right)\,, \\
I_g^{J_{E_T},(n)} &= C_A\left(\tilde{I}_{gg}^{(n)} + \frac{\log^2 n}{2}\right) + \frac{N_f}{2}\tilde{I}_{qg}^{(n)}\,, \\
\mathcal{I}_q^{J_{E_T},(n)}(z) &= -\left[\frac{1+z^2}{(1-z)_+} + P_{gq}(z)\right]\Bigg[\left(\log(z)+\log(1-z)-\log(1-z^n)\right)\Theta\left(z>\frac{1}{2}\right) \\
&\qquad + \left(\log(1-z)+\log(z)-\log(1-(1-z)^n)\right)\Theta\left(z<\frac{1}{2}\right)\Bigg]\,, \\
\mathcal{I}_g^{J_{E_T},(n)}(z) &= -\left[2C_A\frac{(1-z+z^2)^2}{z(1-z)_+} + 2N_fP_{qg}(z)\right] \\
&\qquad \times\Bigg[\left(\log(z)+\log(1-z)-\log(1-z^n)\right)\Theta\left(z>\frac{1}{2}\right) \\
&\qquad + \left(\log(1-z)+\log(z)-\log(1-(1-z)^n)\right)\Theta\left(z<\frac{1}{2}\right)\Bigg]\,.
\end{aligned} \tag{2.42}$$

It is important to note, that double poles cancel in the calculation. Furthermore, the factor $n^{-\varepsilon}$ in (2.40) produces a term $C_j\delta(1-z)\log(n)$ which matches the terms $\propto \log(n)$ in the finite parts of $I_{qq}^{(n)}$, $I_{gg}^{(n)}$ in (2.38). Thus, these terms cancel as well in the difference $d\tilde{\sigma}_{jk} - d\tilde{\sigma}_{j(k)}$. Any remaining pole terms are independent of n and are removed by the subtraction of final-state collinear singularities in $d\hat{\sigma}_{ab}^{j(k)}$, as described in [174]. We have therefore shown that the jet cross section defined according to (1.107) is infrared-safe at NLO for arbitrary n. Moreover, the jet functions for J_{E_T} algorithms satisfy the momentum sum rule (2.30). Since we use the results for $n=1$ in Chap. 3, we list them explicitly:

$$\begin{aligned}
I_q^{J_{E_T}} &= C_F\left(-5+\frac{\pi^2}{2}-\frac{3}{2}\log 2\right) , \\
I_g^{J_{E_T}} &= C_A\left(-\frac{45}{8}+\frac{\pi^2}{2}-\frac{11}{6}\log 2\right)+\frac{N_f}{2}\left(\frac{23}{12}+\frac{2}{3}\log 2\right) , \\
\mathcal{I}_q^{J_{E_T}}(z) &= -\left[P_{qq}(z)+P_{gq}(z)\right]\left[\log(z)\Theta\left(z>\frac{1}{2}\right)+\log(1-z)\Theta\left(z<\frac{1}{2}\right)\right] , \\
\mathcal{I}_g^{J_{E_T}}(z) &= -\left[P_{gg}(z)+2N_f P_{qg}(z)\right]\left[\log(z)\Theta\left(z>\frac{1}{2}\right)+\log(1-z)\Theta\left(z<\frac{1}{2}\right)\right] .
\end{aligned} \tag{2.43}$$

Interestingly, we find

$$\begin{aligned}
I_j^{J_{E_T}} &= \frac{1}{2}\left(I_j^{\text{cone}}+I_j^{k_T}\right) , \\
\mathcal{I}_j^{J_{E_T}} &= \frac{1}{2}\left(\mathcal{I}_j^{\text{cone}}+\mathcal{I}_j^{k_T}\right) .
\end{aligned} \tag{2.44}$$

Note that we have dropped the superscript ($n=1$) here.

It is useful to compare the structure of the final result to that of the cross sections for the cone or k_T algorithms in the NJA. For the latter, one has for a given partonic channel

$$d\sigma_{ab\to\text{jet}X} = \mathcal{A}_{ab}\log(R^2)+\mathcal{B}_{ab}^{\text{algo}}+\mathcal{O}(R^2) , \tag{2.45}$$

where the $\mathcal{A}_{ab}$ are the same for both types of algorithms, but the $\mathcal{B}_{ab}^{\text{algo}}$ depend on the algorithm, i.e. $\mathcal{B}_{ab}^{\text{cone}} \neq \mathcal{B}_{ab}^{k_T}$. For the J_{E_T} algorithms defined by maximizing the function $J^{(n)}$ in Eq. (1.107) we instead have from (2.41) and (2.42)

$$d\sigma_{ab\to\text{jet}X} = \mathcal{A}_{ab}\log\left(\frac{1}{\beta}\right)+\mathcal{B}_{ab}^{(n)}+\mathcal{O}(1/\beta) , \tag{2.46}$$

where again the $\mathcal{A}_{ab}$ are the same as for the other algorithms and the $\mathcal{B}_{ab}^{(n)}$ are all different and also differ from $\mathcal{B}_{ab}^{\text{cone}}$ and $\mathcal{B}_{ab}^{k_T}$. In any case, one can see that there is a simple correspondence between logarithms of R^2 for the cone and k_T algorithms and logarithms of $1/\beta$ for the J_{E_T} ones. The implementation into the numerical code of [174, 175] is thus relatively straightforward.

2.3 Phenomenological Results

We now present a few phenomenological results for the NLO jet cross section for the new class of algorithms. For our studies we consider $p\bar{p}$ collisions at center-of-mass energy $\sqrt{S} = 1.96$ TeV at the Tevatron, and pp collisions at $\sqrt{S} = 7$ TeV at the LHC. For Tevatron we choose a jet rapidity interval $|\eta^{\text{jet}}| \leq 0.4$, while for the LHC we use two different bins in rapidity, $|\eta^{\text{jet}}| \leq 0.5$ and $2 \leq |\eta^{\text{jet}}| \leq 2.5$. We use the CTEQ6.6M parton distributions [207] and the renormalization/factorization scale $\mu = p_T^{\text{jet}}$ throughout. All our calculations presented here are carried out in the context of the NJA. We note that in Ref. [175] detailed comparisons of the NLO jet cross sections obtained within the NJA and obtained with a full NLO Monte-Carlo integration code, respectively, were performed, both for the cone and for the k_T algorithm. These comparisons showed that the NJA is very accurate for values $R = 0.4$ of the jet parameter, for the kinematics of interest in our present study. Moreover, *ratios* of cross sections obtained in the NJA typically match full NLO ones even better. We therefore always present our results for the new algorithms relative to the one for the k_T algorithm in the NJA with $R = 0.4$.

Figure 2.1 shows our results for Tevatron kinematics. The solid line is the result for the new algorithm with $n = 1$, using $\beta = 6.25$ which equals the value $1/R^2$ used for the baseline calculation of the cross section for the k_T algorithm. One can see that the result is relatively close to the one for the k_T algorithm in this case, indicating that the difference induced by the non-logarithmic pieces $\mathcal{B}_{ab}^{\text{algo}}$ in (2.45) is relatively small. To explore the dependence on

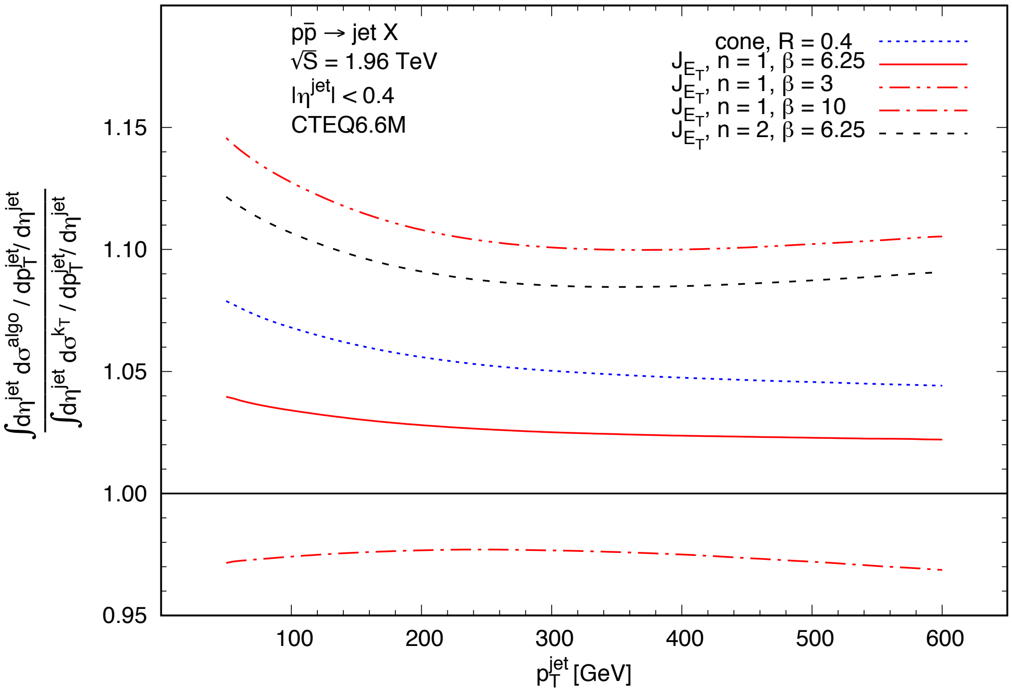

Figure 2.1: Comparison of jet cross sections in the NJA for Tevatron kinematics. All results are shown relative to the one for the k_T algorithm with $R = 0.4$.

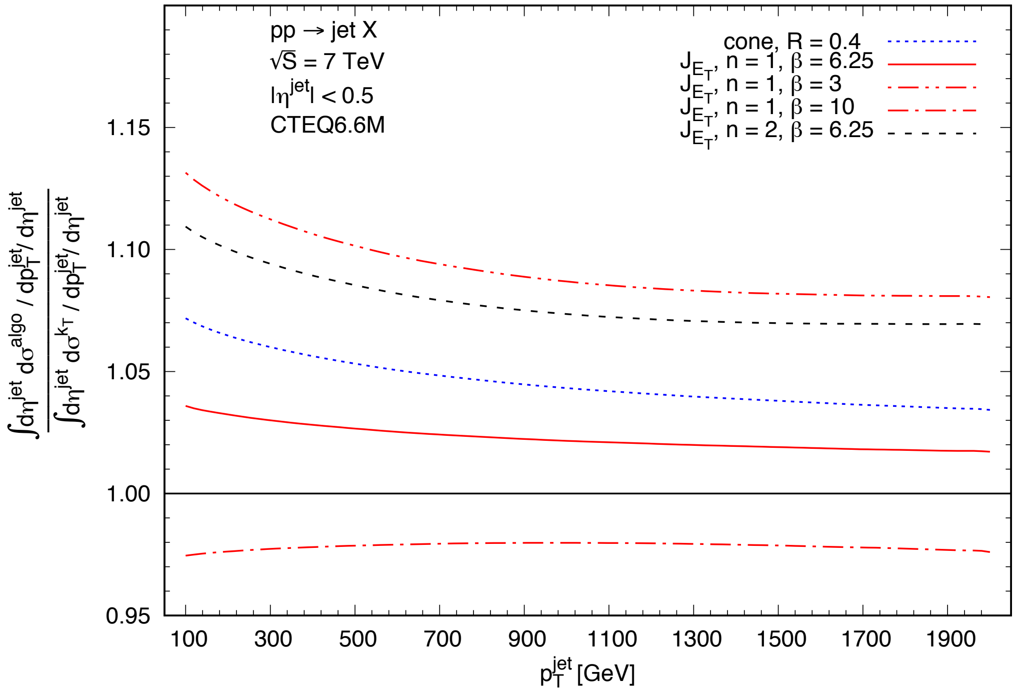

Figure 2.2: Same as Fig. 2.1 but for pp collisions at $\sqrt{S} = 7$ TeV.

β we also present results for $\beta = 3$ and $\beta = 10$ (dash-dotted lines), which are higher or lower, respectively, than the one for the k_T algorithm. Empirically, one finds that a value $\beta \approx 1.25/R^2$ leads to a ratio very close to unity. Such a finding is expected when the cross section has the form given in Eqs. (2.45). (We recall in this context that Ref. [190] observed that the cone and k_T algorithms lead to similar results when $R_{k_T} \approx 1.35\, R_{\rm cone}$). The dashed line in Fig. 2.1 shows the result for the J_{E_T} algorithm with $n = 2$ and $\beta = 6.25$. It is significantly higher (by about 10%) than the baseline one for the k_T algorithm. In fact, it is closer to that for the cone algorithm with $R = 0.4$, which is also shown in the figure by the dotted line.

In Fig. 2.2 we show our results for mid-rapidity jet production in pp collisions at the LHC. As one can see, all features found for Tevatron conditions carry over to this case as well. This remains essentially true also for jets produced at larger $|\eta^{\rm jet}|$, as shown by Fig. 2.3 for the case $2 \leq |\eta^{\rm jet}| \leq 2.5$.

2.4 Conclusions

We have presented a next-to-leading order calculation for single-inclusive jet production in hadronic collisions, using the recently introduced J_{E_T} algorithms to define jets. Our calculations have been performed analytically, assuming that the produced jets are rather collimated. We have found that all singular contributions arising at intermediate stages of the NLO calculation cancel in the final answer, which is a prerequisite for an infrared safe algorithm. Our numerical studies show that jets defined according to the J_{E_T} algorithms

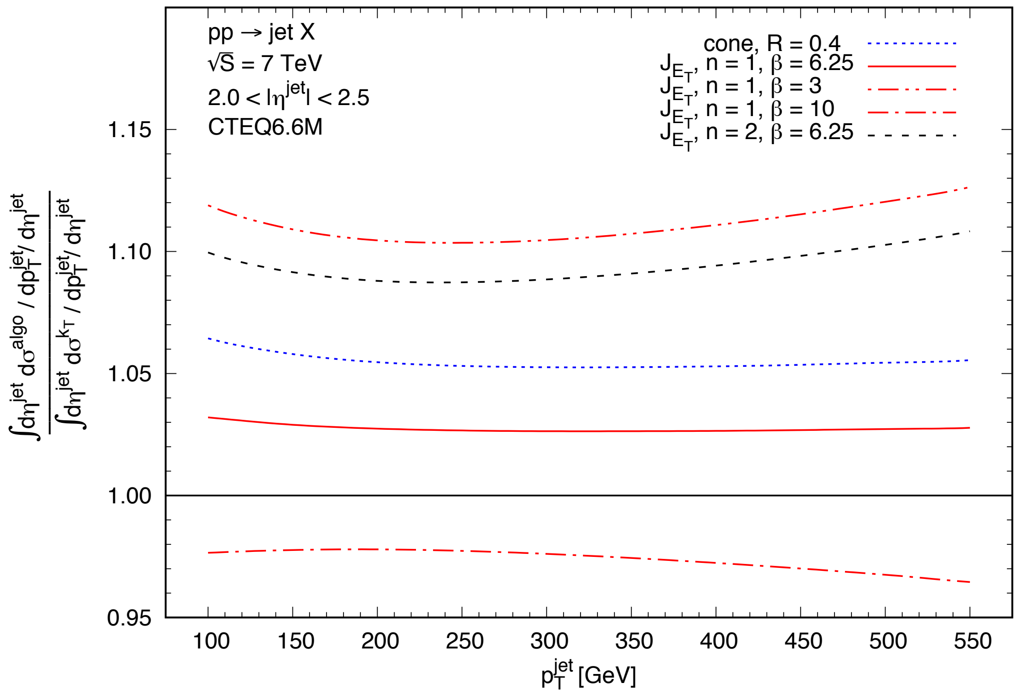

Figure 2.3: Same as Fig. 2.2 but for $2 \leq |\eta^{\rm jet}| \leq 2.5$.

have a cross section that is overall rather close to those for the more standard cone or k_T algorithms. While future work will need to decide whether the J_{E_T} algorithms offer any advantages over the standard ones in actual experimental jet studies, we think that our results are useful in assessing their theoretical status. Our analytical results will also be valuable for QCD resummation studies of jet production for the J_{E_T} algorithms, cf. [208].

Chapter 3

Hadron Fragmentation Inside Jets in Hadronic Collisions

In this chapter, which is based on our publication [197], we present an analytical next-to-leading order QCD calculation of the partonic cross sections for the process $pp \to (\mathrm{jet}\, h)X$, for which a specific hadron is observed inside a fully reconstructed jet. In order to obtain the analytical results, we assume the jet to be relatively narrow. We show that the results can be cast into a simple and systematic form based on suitable universal jet functions for the process. We confirm the validity of our calculation by comparing to previous results in the literature for which the next-to-leading order cross section was treated entirely numerically by Monte-Carlo integration techniques. We present phenomenological results for experiments at the LHC and at RHIC. These suggest that $pp \to (\mathrm{jet}\, h)X$ should enable very sensitive probes of fragmentation functions, especially of the one for gluons.

Final states produced at high transverse momentum (p_T), such as jets, single hadrons, or prompt photons, have long been regarded as sensitive and well-understood probes of short-distance QCD phenomena. Recently, a new “hybrid” type of high-p_T jet/hadron observable has been proposed and explored theoretically [35–39]. It is defined by an identified specific hadron found inside a fully reconstructed jet, giving rise to a same-side hadron-jet momentum correlation. This correlation may for example be described in terms of the variable $z_h \equiv p_T/p_T^{\mathrm{jet}}$, where p_T and p_T^{jet} are the transverse momenta of the hadron and the jet, respectively. The production of identified hadrons in jets was first considered for the case of e^+e^- annihilation [35–37] and subsequently also for pp scattering [38, 204–206]. Experimental studies have been pioneered in $p\bar{p} \to (\mathrm{jet}\, h)X$ at the Tevatron [209]. At the LHC, the ATLAS [40, 210–212], LHCb [41] and CMS [213] experiments have studied $pp \to (\mathrm{jet}\, h)X$, and measurements are being carried out by ALICE [214–216]. Measurements of the cross section (and, perhaps, spin asymmetries) should also be possible at RHIC.

There are several reasons why it is interesting to study the production of hadrons inside jets. Perhaps most importantly, the observable provides an alternative window on fragmentation functions [38]. The latter, denoted here by $D_c^h(z, \mu)$, describe the formation of a hadron h from a parent parton $c = q, \bar{q}, g$. The variable z is the fraction of the parton's momentum transferred to the hadron, and μ denotes the factorization scale at which the fragmentation function is probed. Usually, fragmentation functions for a hadron h are determined from the processes $e^+e^- \to hX$ or $ep \to ehX$, c.f. Sec. 1.3. The power of these processes lies in the fact that they essentially allow direct scans of the fragmentation functions as functions of z. The reason for this is that to lowest order (LO) in QCD, it turns out that z is identical to a kinematic (scaling) variable of the process. For instance, in $e^+e^- \to hX$ one has $z = 2p_h \cdot q/q^2$

to LO, where p_h is the momentum of the observed hadron and q the momentum of the virtual photon that is produced by the e^+e^- annihilation. NLO corrections dilute this direct "local" sensitivity only little. A drawback of $e^+e^- \to hX$ or $ep \to ehX$ is on the other hand that the gluon fragmentation function can be probed only indirectly by evolution or higher order corrections.

Being universal objects, the same fragmentation functions are also relevant for describing hadron production in pp-scattering. So far, one has been using the process $pp \to hX$ as a further source of information on the $D_c^h(z,\mu)$ [130–134]. Although this process does probe gluon fragmentation, its sensitivity to fragmentation functions is much less clear-cut than in the case of $e^+e^- \to hX$ or $ep \to ehX$. This is because for the single-inclusive process $pp \to hX$ the fragmentation functions arise in a more complex convolution with the partonic hard-scattering functions, which involves an integration over a typically rather wide range of z already at LO, where the dependence of cross section on the fragmentation functions schematically reads (see, for instance, [91] and Sec. 2.1.1)

$$d\sigma^{pp\to hX} \propto \sum_{a,b,c} \int_{z_c^{\min}}^{1} \frac{z_c}{z_c^2} \left[f_a \otimes f_b \otimes d\hat{\sigma}_{ab}^{c}(\hat{p}_T, \dots) \right] D_c(z_c, \mu) \,, \tag{3.1}$$

where $\hat{p}_T = p_T/z_c$ and $z_c^{\min} = \frac{2p_T}{\sqrt{S}} \cosh \eta$. Furthermore, f_a and f_b are the PDFs and $d\hat{\sigma}_{ab}^c$ are the corresponding partonic cross sections. Looking at the lower limit of the z_c integration for mid rapidities (i.e. $\cosh(\eta \approx 0) \approx 1$) and typical hadron momenta of the order of $p_T \approx 10$ GeV, we have for RHIC center of mass energies of $\sqrt{S} = 200$ GeV a lower limit of $z_c \approx 0.1$. For LHC energies, the lower limit becomes even smaller. Hence, the information on the z dependence of the $D_c^h(z,\mu)$ is smeared out and not readily available at a given fixed value of z.

The process $pp \to (\mathrm{jet}\, h)X$ allows to overcome this shortcoming. As it turns out, if one writes its cross section differential in the variable z_h introduced above, then to LO the hadron's fragmentation function is to be evaluated at $z = z_h$. This means that by selecting z_h one can "dial" the value at which the $D_c^h(z,\mu)$ are probed, similarly to what is available in $e^+e^- \to hX$ or $ep \to ehX$. Thanks to the fact that in pp scattering different weights are given to the various fragmentation functions than compared to $e^+e^- \to hX$ and $ep \to ehX$, it is clear that $pp \to (\mathrm{jet}\, h)X$ has the potential to provide complementary new information on the $D_c^h(z,\mu)$, especially on gluon fragmentation. Data for $pp \to (\mathrm{jet}\, h)X$ should thus become valuable input to future global QCD analyses of fragmentation functions. At the very least, they should enable novel tests of the universality of fragmentation functions. We note that similar opportunities are expected to arise when the hadron is produced on the "away-side" of the jet, that is, basically back-to-back with the jet [217], although the kinematics is somewhat more elaborate in this case.

The production of specific hadrons inside jets may also provide new insights into the structure of jets and the hadronization mechanism. Varying z_h and/or the hadron species, one can map out the abundances of specific hadrons in jets. Particle identification in jets becomes particularly interesting in a nuclear environment in AA scattering, where distributions of hadrons may shed further light on the phenomenon of "jet quenching". Knowledge of fragmentation functions in jet production and a good theoretical understanding of the process $pp \to (\mathrm{jet}\, h)X$ are also crucial for studies of the Collins effect [218–220], an important probe of spin phenomena in hadronic scattering [221].

In the present chapter, we perform a new next-to-leading order (NLO) calculation of $pp \to (\text{jet}\, h)X$. In contrast to the previous calculation [38] which was entirely based on a numerical Monte-Carlo integration approach, we will derive analytical results for the relevant partonic cross sections. Apart from providing independent NLO predictions in a numerically very efficient way, this offers several advantages. In the context of the analytical calculation, one can first of all explicitly check that the final-state collinear singularities have the structure required by the universality of fragmentation functions, meaning that the same fragmentation functions occur for $pp \to (\text{jet}\, h)X$ as for usual single-inclusive processes such as $pp \to hX$. We note that to our knowledge this has not yet been formally proven beyond NLO. Also, as we shall see, the NLO expressions show logarithmic enhancements at high z_h, which recur with increasing power at every order in perturbation theory, eventually requiring resummation to all orders. Having explicit analytical results is a prerequisite for such a resummation. In Ref. [37], considering the simpler color-singlet case of e^+e^--annihilation, such resummation calculations for large z_h were presented.

Technically, we will derive our results by assuming the jet to be relatively narrow, an approximation known as “Narrow Jet Approximation (NJA)”. This technique was used previously for NLO calculations of single-inclusive jet production in hadronic scattering, $pp \to \text{jet}\, X$ [174, 175, 193, 199, 200]; see also Chap. 2. The main idea is to start from NLO “inclusive-parton” cross sections $d\hat{\sigma}^c_{ab}$ for the processes $ab \to cX$, which are relevant for the cross section for $pp \to hX$. They are a priori not suitable for computing a jet cross section, which is evident from the fact that the $d\hat{\sigma}^c_{ab}$ require collinear subtraction of final-state collinear singularities, whereas a jet cross section is infrared-safe as far as the final state is concerned. Instead, it depends on the algorithm adopted to define the jet and thereby on a generic jet (size) parameter $\mathcal{R}$. As was shown in Refs. [174, 175, 193, 199, 200], at NLO one may nonetheless go rather straightforwardly from the single-inclusive parton cross sections to the jet ones, for any infrared-safe jet algorithm. The key is to properly account for the fact that at NLO two partons can fall into the same jet, so that the jet needs to be constructed from both. In fact, within the NJA, one can derive the translation between the $d\hat{\sigma}^c_{ab}$ and the partonic cross sections for jet production analytically. We note that the NJA formally corresponds to the limit $\mathcal{R} \to 0$, but turns out to be accurate even at values $\mathcal{R} \sim 0.4 - 0.7$ relevant for experiment. In the NJA, the structure of the NLO jet cross section is of the form $\mathcal{A} \log(R) + \mathcal{B}$; corrections to this are of $\mathcal{O}(\mathcal{R}^2)$ and are neglected. In this chapter, we apply the NJA to the case of $pp \to (\text{jet}\, h)X$, using it to derive the relevant NLO partonic cross sections. In the course of the explicit NLO calculation, we find that the partonic cross sections for $pp \to (\text{jet}\, h)X$ may be very compactly formulated in terms of the single-inclusive parton ones $d\hat{\sigma}^c_{ab}$, convoluted with appropriate perturbative “jet functions”. These functions are universal in the sense that they only depend on the type of the outgoing partons that fragment and/or produce the jet, but not on the underlying partonic hard-scattering function. On the basis of the jet functions, the NLO partonic cross sections for $pp \to (\text{jet}\, h)X$ take a very simple and systematic form. In fact, it turns out that for $pp \to (\text{jet}\, h)X$ the jet functions have a “two-tier” form, with a first jet function describing the formation of the jet and a second one describing the fragmentation of a parton inside the jet. We note that the concept of jet functions for formulating jet cross sections is not new but was introduced in the context of soft-collinear effective theories (SCET) [35–37, 201–203]. Recently, applications to $pp \to (\text{jet}\, h)X$ have been given as well [204–206]. Jet functions in a more general context of SCET or QCD resummation have been considered in Refs. [222] and [223], for example.

We also note that in Ref. [217] the NLO corrections for the case of away-side jet-hadron correlations were presented in the context of a Monte-Carlo integration code.
This chapter is organized as follows. In Sec. 3.1 we present our NLO calculation. In particular, that section contains our main new result, the formulation of $pp \to (\text{jet}\, h)X$ in terms of suitable jet functions. Section 3.2 presents phenomenological results for $pp \to (\text{jet}\, h)X$ for LHC and RHIC. We finally conclude our work in Sec. 3.3.

3.1 Associated Jet-plus-Hadron Production in the NJA

After having established a framework for inclusive jet production through the formulation of suitable jet functions in Chap. 2 we are prepared to tackle the case $H_1 H_2 \to (\text{jet}\, h)X$ where the hadron is observed inside a reconstructed jet and is part of the jet. Our strategy for performing an analytical NLO calculation will be to use the NJA and the same considerations as those that gave rise to Eq. (2.10). Subsequently, we will again phrase our results in a simple and rather general way in terms of suitable jet functions. Calculations involving final state jets always depend on an algorithm specifying the definition of a jet. The algorithm usually depends on a parameter $\mathcal{R}$. For the cone and (anti-)k_T algorithms $\mathcal{R}$ is just given by the usual jet size parameter R_{cone} and R_{k_T} introduced for these algorithms, while for the jet algorithm of [34, 194] we have $\mathcal{R} = 1/\sqrt{\beta}$ with β the "maximization" parameter defined for this algorithm. In the NJA we generally assume $\mathcal{R} \ll 1$ and neglect $\mathcal{O}(\mathcal{R}^2)$ contributions.
The cross section we are interested in is specified by the jet's transverse momentum p_T^{jet} and rapidity η^{jet}, and by the variable

$$z_h \equiv \frac{p_T}{p_T^{\text{jet}}}\,, \tag{3.2}$$

where as in section 2.1.1 p_T refers to the transverse momentum of the produced hadron. As we are working in the NJA, we consider collinear fragmentation of the hadron inside the jet. Thus, the observed hadron and the jet have the same rapidities, $\eta = \eta^{\text{jet}}$, since differences in rapidity are $\mathcal{O}(\mathcal{R}^2)$ effects and hence suppressed in the NJA.
The factorized jet-plus-hadron cross section is written as

$$\begin{aligned}\frac{d\sigma^{H_1 H_2 \to (\text{jet}\, h)X}}{dp_T^{\text{jet}} d\eta^{\text{jet}} dz_h} \;=\; & \frac{2p_T^{\text{jet}}}{S} \sum_{a,b,c} \int_{x_a^{\min}}^1 \frac{dx_a}{x_a} f_a^{H_1}(x_a, \mu_F) \int_{x_b^{\min}}^1 \frac{dx_b}{x_b} f_b^{H_2}(x_b, \mu_F) \\ & \times \int_{z_h}^1 \frac{dz_p}{z_p} \frac{d\hat{\sigma}_{ab}^{(\text{jet}\, c)}(\hat{s}, p_T^{\text{jet}}, \hat{\eta}, \mu_F, \mu_F', \mu_R, \mathcal{R}, z_p)}{v dv dw dz_p} D_c^h\left(\frac{z_h}{z_p}, \mu_F'\right)\,,\end{aligned} \tag{3.3}$$

where $x_a^{\min}$, $x_b^{\min}$, and $\hat{\eta} = \eta^{\text{jet}} - \frac{1}{2}\log(x_a/x_b)$ are as for the single-inclusive jet cross section, and where z_p is the partonic analog of z_h. In other words, the $d\hat{\sigma}_{ab}^{(\text{jet}\, c)}$ are the partonic cross sections for producing a final-state jet (subject to a specified jet algorithm), inside of which there is a parton c with transverse momentum $p_T^c = z_p p_T^{\text{jet}}$ that fragments into the observed hadron. The argument of the corresponding fragmentation functions is fixed by $p_T = z p_T^c$ and hence, using (3.2), is given by $z = z_h/z_p$. Thus the new partonic cross sections are in convolution with the fragmentation functions. Note that all other variables V, W and v, w have the same definitions as in the single-inclusive jet case; see Eq. (2.9).

At lowest order, there is only one parton forming the jet, and this parton also is the one that fragments into the observed hadron, implying $z_p = 1$. The partonic cross sections hence have the perturbative expansions

$$\frac{d\hat{\sigma}_{ab}^{(\text{jet}\,c)}}{dvdwdz_p} = \frac{d\hat{\sigma}_{ab}^{c,(0)}}{dv}\,\delta(1-w)\,\delta(1-z_p) + \frac{\alpha_s(\mu_R)}{\pi}\,\frac{d\hat{\sigma}_{ab}^{(\text{jet}\,c),(1)}}{dvdwdz_p} + \mathcal{O}(\alpha_s^2(\mu_R))\,, \tag{3.4}$$

with the same Born terms $d\hat{\sigma}_{ab}^{c,(0)}/dv$ as in (2.6).

In order to derive the NLO partonic cross sections $d\hat{\sigma}_{ab}^{(\text{jet}\,c),(1)}$, we revisit Eq. (2.10). Since we now "observe" a parton c in the final state (the fragmenting one), we must not sum over all possible final states, but rather consider only the contributions that contain parton c:

$$d\hat{\sigma}_{ab}^{c} - d\hat{\sigma}_{ab}^{c(d)} - d\hat{\sigma}_{ab}^{c(e)} + d\hat{\sigma}_{ab}^{cd} + d\hat{\sigma}_{ab}^{ce}\,. \tag{3.5}$$

However, for each term we now need to derive its proper dependence on z_p before combining all terms. For the terms $d\hat{\sigma}_{ab}^{c}$ and $d\hat{\sigma}_{ab}^{c(d)}, d\hat{\sigma}_{ab}^{c(e)}$ this is trivial since for all of these terms parton c alone produces the jet and also is the parton that fragments. As a result, all these terms simply acquire a factor $\delta(1-z_p)$. This becomes different for the pieces $d\hat{\sigma}_{ab}^{cd}, d\hat{\sigma}_{ab}^{ce}$. Following [174, 175, 193] and Chap. 2, in the NJA we may write the NLO contribution to any $d\hat{\sigma}_{ab}^{cd}$ as

$$\begin{aligned}\frac{d\hat{\sigma}_{ab}^{cd,(1)}}{dvdw} &= \frac{\alpha_s}{2\pi}\,\mathcal{N}_{ab\to K}(v,w,\varepsilon)\,\delta(1-w) \\ &\quad\times \int_0^1 dz_p\, z_p^{-\varepsilon}(1-z_p)^{-\varepsilon}\tilde{P}_{cK}^{<}(z_p)\int_0^{(m_{\text{J,max}}^{\text{algo}})^2(z_p)}\frac{dm_{\text{J}}^2}{m_{\text{J}}^2}\,m_{\text{J}}^{-2\varepsilon},\end{aligned} \tag{3.6}$$

where we have used dimensional regularization with $D = 4 - 2\varepsilon$ space-time dimensions. Equation (3.6) is similar to Eq. (2.14) and is derived from the fact that the leading contributions in the NJA come from a parton K splitting into partons c and d "almost" collinearly in the final state. The functions $\tilde{P}_{cK}^{<}$ are defined in Eq. (2.15). The argument of the splitting function is the fraction of the intermediate particle's momentum (equal to the jet momentum) transferred in the splitting. In the NJA it therefore coincides with our partonic variable z_p. In the second integral in (3.6) m_{J} is the invariant mass of the jet. As indicated, the upper limit of the jet mass integration $m_{\text{J,max}}^{\text{algo}}$ depends on the algorithm chosen to define the jet. We have [174, 175, 193]

$$(m_{\text{J,max}}^{\text{algo}})^2(z_p) = \begin{cases} (p_T^{\text{jet}}R)^2\,\min\left(\frac{z_p}{1-z_p},\frac{1-z_p}{z_p}\right) & \text{cone algorithm}\,, \\ (p_T^{\text{jet}}R)^2\,z_p(1-z_p) & (\text{anti}-)k_T\ \text{algorithm}\,, \\ \frac{(p_T^{\text{jet}})^2}{\beta}\,\min(z_p,1-z_p) & J_{E_T}\ \text{algorithm}\,. \end{cases} \tag{3.7}$$

To make the cross section $d\hat{\sigma}_{ab}^{cd,(1)}$ differential in z_p we now just need to drop the integration over z_p in (3.6). We next expand the resulting expression in ε. The m_{J}^2 integration produces a collinear singularity in $1/\varepsilon$. It also contributes a factor $(1-z_p)^{-\varepsilon}$ at large z_p which may be combined with the explicit factor $(1-z_p)^{-\varepsilon}$ in (3.6). In the presence of a diagonal splitting function in the integrand we hence arrive at a term $(1-z_p)^{-1-2\varepsilon}$, which may be expanded according to Eq. (2.25) in ε to give a further pole in $1/\varepsilon$ and "plus"-distributions in $(1-z_p)$. The double poles $1/\varepsilon^2$ arising in this way cancel against double poles in $d\hat{\sigma}_{ab}^{c(d)}, d\hat{\sigma}_{ab}^{c(e)}$. The remaining single poles are removed by collinear factorization into the fragmentation function for parton c. For non-diagonal splitting functions there are only single poles which are directly subtracted by factorization. We note that the original $d\hat{\sigma}_{ab}^{cd,(1)}$ is in fact needed both for the cross section with parton c fragmenting and also for the one where d fragments. This is reflected in the fact that the z_p-integral in (3.6) runs from 0 to 1, while for $d\hat{\sigma}_{ab}^{cd,(1)}$ the limit $z_p \to 0$ is never reached as long as $z_h > 0$. For parton d fragmenting, however, we need to use $d\hat{\sigma}_{ab}^{dc,(1)}$ which differs from $d\hat{\sigma}_{ab}^{cd,(1)}$ only by a change of the splitting function. In case of a quark splitting into a quark and a gluon, this change is from $\tilde{P}_{qq}^{<}(z)$ for an observed quark to $\tilde{P}_{gq}^{<}(z)$ for an observed gluon. Because of $\tilde{P}_{gq}^{<}(z) = \tilde{P}_{qq}^{<}(1-z)$ one precisely recovers the old expression for the inclusive-jet cross sections when all final states are summed over. Likewise, if a gluon splits into a $q\bar{q}$ or gg, the relevant splitting functions $\tilde{P}_{qg}^{<}(z)$, $\tilde{P}_{gg}^{<}(z)$ are by themselves symmetric under $z \leftrightarrow 1-z$.

From this discussion, and combining with Eqs. (3.4),(3.5), we obtain to NLO in the NJA:

$$\frac{d\hat{\sigma}_{ab}^{(\mathrm{jet}\,c)}}{dvdwdz_p} = \left[\frac{d\hat{\sigma}_{ab}^{c}}{dvdw} - \frac{d\hat{\sigma}_{ab}^{c(d)}}{dvdw} - \frac{d\hat{\sigma}_{ab}^{c(e)}}{dvdw}\right]\delta(1-z_p) + \frac{d\hat{\sigma}_{ab}^{cd}}{dvdwdz_p} + \frac{d\hat{\sigma}_{ab}^{ce}}{dvdwdz_p}\,. \tag{3.8}$$

Computing and inserting all ingredients of this expression, we find that the cross section may be cast into a form that again makes use of the *single-inclusive parton* production cross sections $d\hat{\sigma}_{ab}^{c}$, similar to the case of inclusive-jet production in Eq. (2.18):

$$\begin{aligned}\frac{d\sigma^{H_1H_2\to(\mathrm{jet}\,h)X}}{dp_T^{\mathrm{jet}}d\eta^{\mathrm{jet}}dz_h} &= \frac{2p_T^{\mathrm{jet}}}{S}\sum_{a,b,c}\int_{x_a^{\min}}^{1}\frac{dx_a}{x_a}f_a^{H_1}(x_a,\mu_F)\int_{x_b^{\min}}^{1}\frac{dx_b}{x_b}f_b^{H_2}(x_b,\mu_F)\\ &\times\int_{z_c^{\min}}^{1}\frac{dz_c}{z_c^2}\,\frac{d\hat{\sigma}_{ab}^{c}(\hat{s},\hat{p}_T,\hat{\eta},\mu_F,\mu_F',\mu_R)}{vdvdw}\\ &\times\sum_{c'}\int_{z_h}^{1}\frac{dz_p}{z_p}\,\mathcal{K}_{c\to c'}\left(z_c,z_p;\frac{\mathcal{R}p_T^{\mathrm{jet}}}{\mu_F'},\frac{\mathcal{R}p_T^{\mathrm{jet}}}{\mu_F''},\mu_R\right)D_{c'}^{h}\left(\frac{z_h}{z_p},\mu_F''\right)\,,\end{aligned} \tag{3.9}$$

where $x_a^{\min}, x_b^{\min}$ and $z_c^{\min}$ are as given in (2.3), with V and W defined in terms of jet transverse momentum and rapidity. Furthermore, as in (2.18) we have $\hat{p}_T = p_T^{\mathrm{jet}}/z_c$. The (jet algorithm dependent) functions $\mathcal{K}_{c\to c'}$ are new "semi-inclusive" jet functions that describe the production of a fragmenting parton c' inside a jet that results from a parton c produced in the hard scattering. For the "transition" $q \to q$ we find

$$\begin{aligned}\mathcal{K}_{q\to q}(z, z_p; \lambda, \kappa, \mu_R) &= \delta(1-z)\delta(1-z_p) + \frac{\alpha_s(\mu_R)}{2\pi}\Bigg[\\ -\delta(1-z_p)&\left\{2C_F(1+z^2)\left(\frac{\log(1-z)}{1-z}\right)_+ + P_{qq}(z)\log\left(\lambda^2\right) + C_F(1-z) + \tilde{\mathcal{I}}_{qq}^{\rm algo}(z)\right\} \\ +\delta(1-z)&\left\{2C_F(1+z_p^2)\left(\frac{\log(1-z_p)}{1-z_p}\right)_+ + P_{qq}(z_p)\log\left(\kappa^2\right) + C_F(1-z_p) + \mathcal{I}_{qq}^{\rm algo}(z_p)\right\}\Bigg],\end{aligned} \tag{3.10}$$

where $\mathcal{I}_{qq}^{\rm algo}(z_p)$ and $\tilde{\mathcal{I}}_{qq}^{\rm algo}(z)$ are functions that depend on the jet algorithm. For the other transitions we obtain

$$\begin{aligned}\mathcal{K}_{q\to g}^{\rm algo}(z, z_p; \lambda, \kappa, \mu_R) &= \frac{\alpha_s(\mu_R)}{2\pi}\Bigg[-\delta(1-z_p)\Big\{P_{gq}(z)\log\left(\lambda^2(1-z)^2\right) + C_F z + \tilde{\mathcal{I}}_{gq}^{\rm algo}(z)\Big\} \\ &+\delta(1-z)\Big\{P_{gq}(z_p)\log\left(\kappa^2(1-z_p)^2\right) + C_F z_p + \mathcal{I}_{gq}^{\rm algo}(z_p)\Big\}\Bigg],\end{aligned} \tag{3.11}$$

$$\begin{aligned}\mathcal{K}_{g\to g}^{\rm algo}(z, z_p; \lambda, \kappa, \mu_R) &= \delta(1-z)\delta(1-z_p) + \frac{\alpha_s(\mu_R)}{2\pi}\Bigg[\\ -\delta(1-z_p)&\left\{\frac{4C_A(1-z+z^2)^2}{z}\left(\frac{\log(1-z)}{1-z}\right)_+ + P_{gg}(z)\log\left(\lambda^2\right) + \tilde{\mathcal{I}}_{gg}^{\rm algo}(z)\right\} \\ +\delta(1-z)&\left\{\frac{4C_A(1-z_p+z_p^2)^2}{z_p}\left(\frac{\log(1-z_p)}{1-z_p}\right)_+ + P_{gg}(z_p)\log\left(\kappa^2\right) + \mathcal{I}_{gg}^{\rm algo}(z_p)\right\}\Bigg],\end{aligned} \tag{3.12}$$

$$\begin{aligned}\mathcal{K}_{g\to q}^{\rm algo}(z, z_p; \lambda, \kappa, \mu_R) &= \frac{\alpha_s(\mu_R)}{2\pi}\Bigg[\\ &-\delta(1-z_p)\Big\{P_{qg}(z)\log\left(\lambda^2(1-z)^2\right) + z(1-z) + \tilde{\mathcal{I}}_{qg}^{\rm algo}(z)\Big\} \\ &+\delta(1-z)\Big\{P_{qg}(z_p)\log\left(\kappa^2(1-z_p)^2\right) + z_p(1-z_p) + \mathcal{I}_{qg}^{\rm algo}(z_p)\Big\}\Bigg],\end{aligned} \tag{3.13}$$

where $\lambda = \mathcal{R}p_T^{\rm jet}/\mu_F'$, $\kappa = \mathcal{R}p_T^{\rm jet}/\mu_F''$. The algorithm dependent functions are given by

$$\mathcal{I}_{c'c}^{\rm algo}(z) = \begin{cases} 2P_{c'c}(z)\log\left(\frac{z}{1-z}\right)\Theta(z<1/2) & \text{cone algorithm}, \\ 2P_{c'c}(z)\log z & \text{(anti}-)k_T\text{ algorithm}, \\ P_{c'c}(z)\left[\log(z) + \log\left(\frac{z}{1-z}\right)\Theta(z<1/2)\right] & J_{E_T}\text{ algorithm}, \end{cases} \tag{3.14}$$

and

$$\tilde{\mathcal{I}}^{\text{algo}}_{c'c}(z) = \begin{cases} -2P_{c'c}(z)[\log(z)\Theta(z>1/2)+\log(1-z)\Theta(z<1/2)] & \text{cone algorithm}\,, \\ 0 & (\text{anti}-)k_T \text{ algorithm}\,, \\ -P_{c'c}(z)[\log(z)\Theta(z>1/2)+\log(1-z)\Theta(z<1/2)] & J_{E_T} \text{ algorithm}\,. \end{cases} \tag{3.15}$$

We note, that these results are consistent with Refs. [204–206] where calculations are performed within the framework of SCET. Again, similar to (2.44), we have

$$\begin{aligned} \mathcal{I}^{J_{E_T}}_{c'c}(z) &= \frac{1}{2}\left(\mathcal{I}^{\text{cone}}_{c'c} + \mathcal{I}^{k_T}_{c'c}\right)\,, \\ \tilde{\mathcal{I}}^{J_{E_T}}_{c'c}(z) &= \frac{1}{2}\left(\tilde{\mathcal{I}}^{\text{cone}}_{c'c} + \tilde{\mathcal{I}}^{k_T}_{c'c}\right)\,. \end{aligned} \tag{3.16}$$

As indicated, the $\mathcal{K}_{c\to c'}$ carry dependence on two (final-state) factorization scales, μ'_F and μ''_F (hidden in λ and κ). The former is the same as we encountered in the case of single-inclusive jets in Eqs. (2.18),(2.27). It was originally introduced in the collinear factorization for the single-inclusive parton cross sections, but now has to cancel exactly between the $d\hat{\sigma}^c_{ab}$ and the $\mathcal{K}_{c\to c'}$. As in the case of single-inclusive jets, the cancelation of dependence on μ'_F is just a result of the fact that we foremost define our observable by requiring a jet in the final state. In this sense, μ'_F is simply an artifact of the way we organize the calculation and is not actually present in the final answer. The scale μ''_F, on the other hand, arises because we now also require a hadron in the final state. Technically it arises when we subtract collinear singularities from the $d\hat{\sigma}^{cd,(1)}_{ab}$. The logarithms in μ''_F are thus just the standard scale logarithms that compensate the evolution of the fragmentation functions at this order. We also note that there are two sum rules that connect the inclusive and the semi-inclusive jet functions [35, 36]:

$$\begin{aligned} &\int_0^1 dz_p\, z_p\, [\mathcal{K}_{q\to q}(z,z_p;\lambda,\kappa,\mu_R) + \mathcal{K}_{q\to g}(z,z_p;\lambda,\kappa,\mu_R)] = \mathcal{J}_q(z,\lambda,\mu_R)\,, \\ &\int_0^1 dz_p\, z_p\, [\mathcal{K}_{g\to g}(z,z_p;\lambda,\kappa,\mu_R) + \mathcal{K}_{g\to q}(z,z_p;\lambda,\kappa,\mu_R)] = \mathcal{J}_g(z,\lambda,\mu_R)\,. \end{aligned} \tag{3.17}$$

Both are fulfilled by our expressions. Furthermore, $\int_0^1 dz_p\, \mathcal{K}_{q\to q}(z,z_p;\lambda,\kappa,\mu_R)$ reproduces the quark splitting contributions to $\mathcal{J}_q$, i.e. the first two lines in Eq. (2.27).

We may actually go one step further and decompose the functions $\mathcal{K}_{c\to c'}$ into products of jet functions that separate the dependence on z and z_p. We define two sets of functions:

$$\begin{aligned}
j_{q\to q}\left(z,\lambda,\mu_R\right) &\equiv \delta(1-z) - \frac{\alpha_s(\mu_R)}{2\pi}\left[2C_F(1+z^2)\left(\frac{\log(1-z)}{1-z}\right)_+ + P_{qq}(z)\log\left(\lambda^2\right)\right.\\
&\qquad\left. + \,\delta(1-z)I_q^{\rm algo} + C_F(1-z) + \tilde{\mathcal{I}}_{qq}^{\rm algo}(z)\right],\\
j_{q\to g}\left(z,\lambda,\mu_R\right) &\equiv -\frac{\alpha_s(\mu_R)}{2\pi}\left[P_{gq}(z)\log\left(\lambda^2(1-z)^2\right) + C_F z + \tilde{\mathcal{I}}_{gq}^{\rm algo}(z)\right],\\
j_{g\to g}\left(z,\lambda,\mu_R\right) &\equiv \delta(1-z) - \frac{\alpha_s(\mu_R)}{2\pi}\left[\frac{4C_A(1-z+z^2)^2}{z}\left(\frac{\log(1-z)}{1-z}\right)_+\right.\\
&\qquad\left. + \,P_{gg}(z)\log\left(\lambda^2\right) + \delta(1-z)I_g^{\rm algo} + \tilde{\mathcal{I}}_{gg}^{\rm algo}(z)\right],\\
j_{g\to q}\left(z,\lambda,\mu_R\right) &\equiv -\frac{\alpha_s(\mu_R)}{2\pi}\left[P_{qg}(z)\log\left(\lambda^2(1-z)^2\right) + z(1-z) + \tilde{\mathcal{I}}_{qg}^{\rm algo}(z)\right],
\end{aligned}\tag{3.18}$$

(where as before $\lambda = \mathcal{R}\,p_T^{\rm jet}/\mu'_F$), and

$$\begin{aligned}
\tilde{j}_{q\to q}\left(z_p,\kappa,\mu_R\right) &\equiv \delta(1-z_p) + \frac{\alpha_s(\mu_R)}{2\pi}\left[2C_F(1+z_p^2)\left(\frac{\log(1-z_p)}{1-z_p}\right)_+ + P_{qq}(z_p)\log\left(\kappa^2\right)\right.\\
&\qquad\left. + \,C_F(1-z_p) + \mathcal{I}_{qq}^{\rm algo}(z_p) + \delta(1-z_p)I_q^{\rm algo}\right],\\
\tilde{j}_{q\to g}\left(z_p,\kappa,\mu_R\right) &\equiv \frac{\alpha_s(\mu_R)}{2\pi}\left[P_{gq}(z_p)\log\left(\kappa^2(1-z_p)^2\right) + C_F z_p + \mathcal{I}_{gq}^{\rm algo}(z_p)\right],\\
\tilde{j}_{g\to g}\left(z_p,\kappa,\mu_R\right) &\equiv \delta(1-z_p) + \frac{\alpha_s(\mu_R)}{2\pi}\left[\frac{4C_A(1-z_p+z_p^2)^2}{z_p}\left(\frac{\log(1-z_p)}{1-z_p}\right)_+\right.\\
&\qquad\left. + \,P_{gg}(z_p)\log\left(\kappa^2\right) + \mathcal{I}_{gg}^{\rm algo}(z_p) + \delta(1-z_p)I_g^{\rm algo}\right],\\
\tilde{j}_{g\to q}\left(z_p,\kappa,\mu_R\right) &\equiv \frac{\alpha_s(\mu_R)}{2\pi}\left[P_{qg}(z_p)\log\left(\kappa^2(1-z_p)^2\right) + z_p(1-z_p) + \mathcal{I}_{qg}^{\rm algo}(z_p)\right],
\end{aligned}\tag{3.19}$$

where again $\kappa = \mathcal{R}\,p_T^{\rm jet}/\mu''_F$ and the $I_{q,g}^{\rm algo}$ are as given in Eqs. (2.28), (2.29) and (2.43) for the inclusive-jet case. To the order we are considering we then have

$$\mathcal{K}_{c\to c'}(z,z_p;\lambda,\kappa,\mu_R) \,=\, \sum_e j_{c\to e}(z,\lambda,\mu_R)\,\tilde{j}_{e\to c'}(z_p,\kappa,\mu_R)\;, \tag{3.20}$$

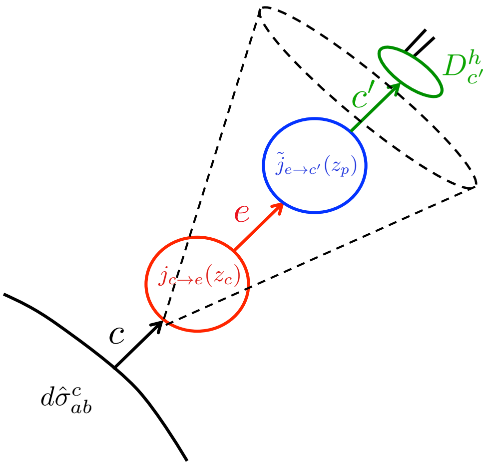

Figure 3.1: Sketch of the production of an observed hadron inside a jet, described in terms of the jet functions $j_{c\to e}$ and $\tilde{j}_{e\to c'}$ (see text).

and hence from (3.9)

$$\begin{aligned}\frac{d\sigma^{H_1H_2\to(\text{jet}\,h)X}}{dp_T^{\text{jet}}d\eta^{\text{jet}}dz_h} \;=\; & \frac{2p_T^{\text{jet}}}{S}\sum_{a,b,c}\int_{x_a^{\min}}^1\frac{dx_a}{x_a}f_a^{H_1}(x_a,\mu_F)\int_{x_b^{\min}}^1\frac{dx_b}{x_b}f_b^{H_2}(x_b,\mu_F)\\ & \times\int_{z_c^{\min}}^1\frac{dz_c}{z_c^2}\frac{d\hat{\sigma}^c_{ab}(\hat{s},\hat{p}_T,\hat{\eta},\mu_F,\mu'_F,\mu_R)}{vdvdw}\sum_e j_{c\to e}\left(z_c,\frac{\mathcal{R}\,p_T^{\text{jet}}}{\mu'_F},\mu_R\right)\\ & \times\sum_{c'}\int_{z_h}^1\frac{dz_p}{z_p}\tilde{j}_{e\to c'}\left(z_p,\frac{\mathcal{R}\,p_T^{\text{jet}}}{\mu''_F},\mu_R\right)D^h_{c'}\left(\frac{z_h}{z_p},\mu''_F\right).\end{aligned} \tag{3.21}$$

In other words, in the NJA the production of a jet with an observed hadron factorizes into the production cross section for parton c, a jet function $j_{c\to e}$ describing the formation of a jet "consisting" of parton e which has taken the fraction z_c of the parent parton's momentum, another jet function $\tilde{j}_{e\to c'}$ describing a "partonic fragmentation" of parton e to parton c' inside the jet, and finally a regular fragmentation function $D^h_{c'}$. This picture is sketched in Fig. 3.1. It is interesting to see that the structure of the first two lines of Eq. (3.21) is very similar to that of the inclusive-jet cross section (2.18) when formulated in terms of the jet functions $\mathcal{J}_c$. In fact, if we drop the last line and perform the sum over parton-type e, we will exactly arrive at (2.18), since

$$\begin{aligned} j_{q\to q}(z,\lambda,\mu_R)+j_{q\to g}(z,\lambda,\mu_R) &= \mathcal{J}_q(z,\lambda,\mu_R)\,,\\ 2N_f\,j_{g\to q}(z,\lambda,\mu_R)+j_{g\to g}(z,\lambda,\mu_R) &= \mathcal{J}_g(z,\lambda,\mu_R)\,.\end{aligned} \tag{3.22}$$

The last line of (3.21) thus describes the production of an identified hadron in the jet.

We note that at the level of our NLO computation we cannot prove the factorization in (3.21) to all orders. In fact, at $\mathcal{O}(\alpha_s)$ we can move terms between $j_{c\to e}$ and $\tilde{j}_{e\to c'}$. On the other hand, it seems very natural that the jet functions that we encountered in the single-inclusive jet case should play a role also in this case in the "first step" of the formation of the final state described by the $j_{c\to e}$. Also, our jet functions $\tilde{j}_{e\to c'}$ are identical to the corresponding functions found in the SCET study [37] of hadrons in jets produced in e^+e^--collisions, except for endpoint contributions $\propto \delta(1-z_p)$ that are necessarily different in the SCET formalism due to the presence of a soft function.

We finally note that the cross section (3.21) may also be expressed in terms of the hadron kinematics, using the relation

$$\frac{d\sigma^{H_1H_2\to(\mathrm{jet}\,h)X}}{dp_T d\eta dz_h}(p_T,\eta,z_h)=\frac{1}{z_h}\frac{d\sigma^{H_1H_2\to(\mathrm{jet}\,h)X}}{dp_T^{\mathrm{jet}}d\eta^{\mathrm{jet}}dz_h}\left(p_T^{\mathrm{jet}}=\frac{p_T}{z_h},\eta,z_h\right). \tag{3.23}$$

3.2 Phenomenological Results

We now present some phenomenological results for associated jet-plus-hadron production. First, we compare our analytical calculation in the NJA with the one of [38], where the NLO cross section was obtained numerically by Monte-Carlo integration techniques. As in that paper, we consider the case of charged hadrons produced in pp collisions at the LHC with center-of-mass energy $\sqrt{S}=8$ TeV. We define the jet by the anti-k_T algorithm with jet parameter $R=0.4$. The renormalization and initial-state factorization scales are set equal to the transverse momentum of the jet, $\mu_R=\mu_F=p_T^{\mathrm{jet}}$, while the final-state factorization scale is chosen as $\mu_F''=Rp_T^{\mathrm{jet}}$. The latter choice serves to sum logarithms of R to all orders [172, 224], although this only becomes necessary for jet sizes much smaller than $R=0.4$. As in [38] we use the CTEQ6.6M parton distributions [207] and the "de

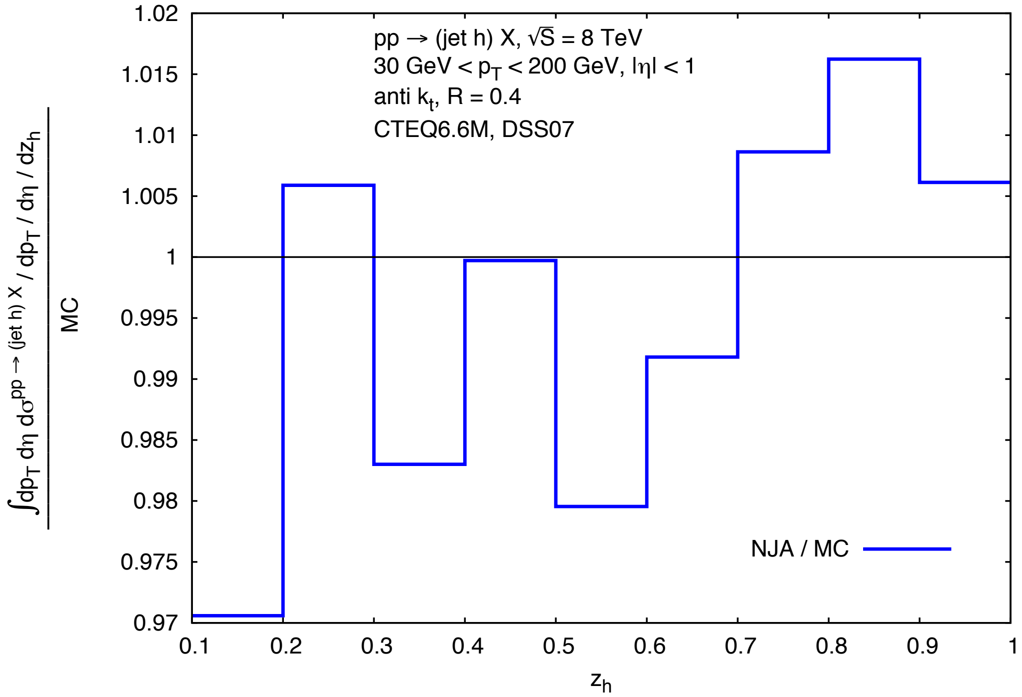

Figure 3.2: Comparison of our results in the NJA to the ones of [38] for LHC kinematics.

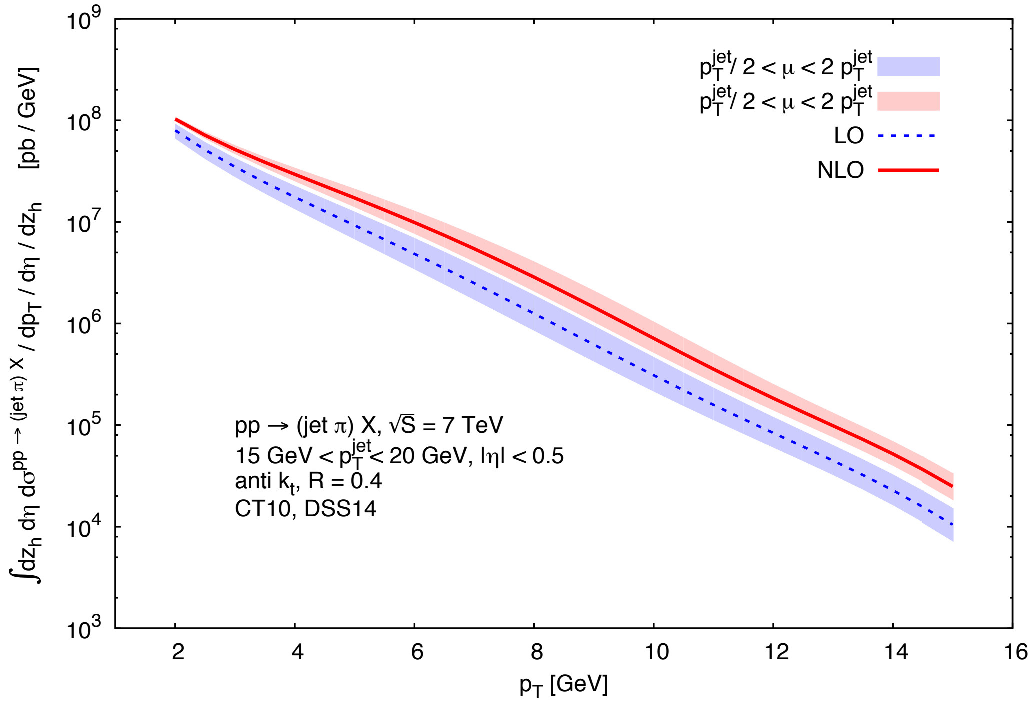

Figure 3.3: LO (dashed) and NLO (solid) cross sections for $pp \to (\text{jet}\,\pi)X$ for ALICE conditions, as functions of pion p_T. The bands show the scale dependence of the cross section for variations of the scale between $p_T^{\text{jet}}/2$ (upper end of bands) and $2p_T^{\text{jet}}$ (lower end of bands). The factorization and renormalization scales have all been set equal and varied simultaneously.

Florian-Sassot-Stratmann" (DSS07) fragmentation functions of Ref. [131]. Our results refer to (summed) charged hadrons, i.e. $h \equiv h^+ + h^-$.

In Fig. 3.2 we show the ratio of the cross section in the NJA with that obtained numerically in Ref. [38]. The ratio is shown as function of z_h, where the cross sections have been integrated over $|\eta| < 1$ and 30 GeV $< p_T <$ 200 GeV in hadron rapidity and transverse momentum. As one can see, the agreement of the two NLO calculations is very good. The deviations are smaller than 3% everywhere, which demonstrates the good accuracy of the NJA. We note that in [38] a closely related variable Z_h is considered, which is defined as

$$Z_h \equiv \frac{\vec{p}_T \cdot \vec{p}_T^{\,\text{jet}}}{|\vec{p}_T^{\,\text{jet}}|^2}\,. \tag{3.24}$$

This definition differs from (3.2) only by $\mathcal{O}(\mathcal{R}^2)$ corrections, which are anyway neglected in the NJA. In the limit $z_h \to 1$, the two definitions become equivalent. This explains why the ratio in Fig. 3.2 is even closer to unity for larger values of z_h. The excellent accuracy of the NJA observed in the figure is consistent with similar comparisons for the case of single-inclusive jet production in the NJA [174, 175].

Next, we show some results for the kinematics relevant for the ongoing studies in ALICE [215]. We consider pp collisions at $\sqrt{S} = 7$ TeV and fragmentation into charged pions ($\pi \equiv \pi^+ + \pi^-$). For the rapidity interval we choose $|\eta| < 0.5$ and we restrict the jet transverse momentum to

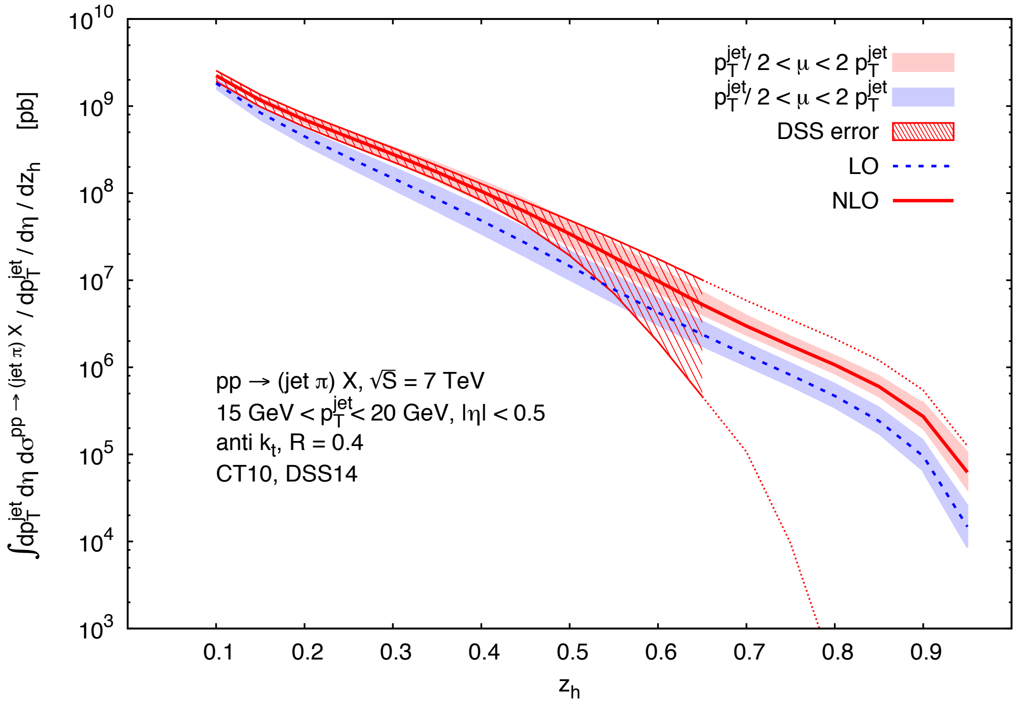

Figure 3.4: Same as in Fig. 3.3, but as function of z_h. As before the solid bands show the scale uncertainty. The hatched band displays the uncertainty of the cross section related to the fragmentation functions. This band is only reliable up to $z_h = 0.65$ and extrapolated beyond (see text).

15 GeV $< p_T^{\text{jet}} <$ 20 GeV. As before, the jet is defined by the anti-k_T algorithm with $R = 0.4$. We now use more modern sets for the parton distributions, CT10 [225], and fragmentation functions, DSS14 [132]. All scales are set equal to the transverse momentum of the jet, $\mu_R = \mu_F = \mu_F' = p_T^{\text{jet}} \equiv \mu$.

Figure 3.3 shows the LO (dashed) and NLO (solid) cross sections for associated jet-plus-pion production differential in the transverse momentum of the pion. Note that the variable z_h is determined as p_T/p_T^{jet} and hence is varied upon integration over p_T^{jet}. The bands show the changes of the cross sections when the scales are varied in the range $p_T^{\text{jet}}/2 < \mu < 2p_T^{\text{jet}}$. As one can see, the scale dependence of the cross sections improves somewhat when going from LO to NLO, although not as much as one would have hoped. This feature was also observed for single-inclusive hadron production in hadronic scattering [91]. For the same kinematical setup we also show the cross section differential in z_h, see Fig. 3.4. A fixed value of z_h implies that the hadron's transverse momentum varies as we integrate over p_T^{jet}. As discussed above, this arguably is the most interesting distribution for $pp \to (\text{jet}\,\pi)X$ since it allows direct scans of the fragmentation functions. Apart from the scale variation, we also show in the figure the uncertainty related to the fragmentation functions, which we compute using the Hessian error sets provided in the DSS14 set [132]. Note that the resulting uncertainty band is reliable only up to $z_h \approx 0.65$, beyond which there are presently hardly any hadron production data available for e^+e^- annihilation or ep scattering. We hence stop the main uncertainty band there and only sketch its possible extrapolation to higher z_h. It is clear

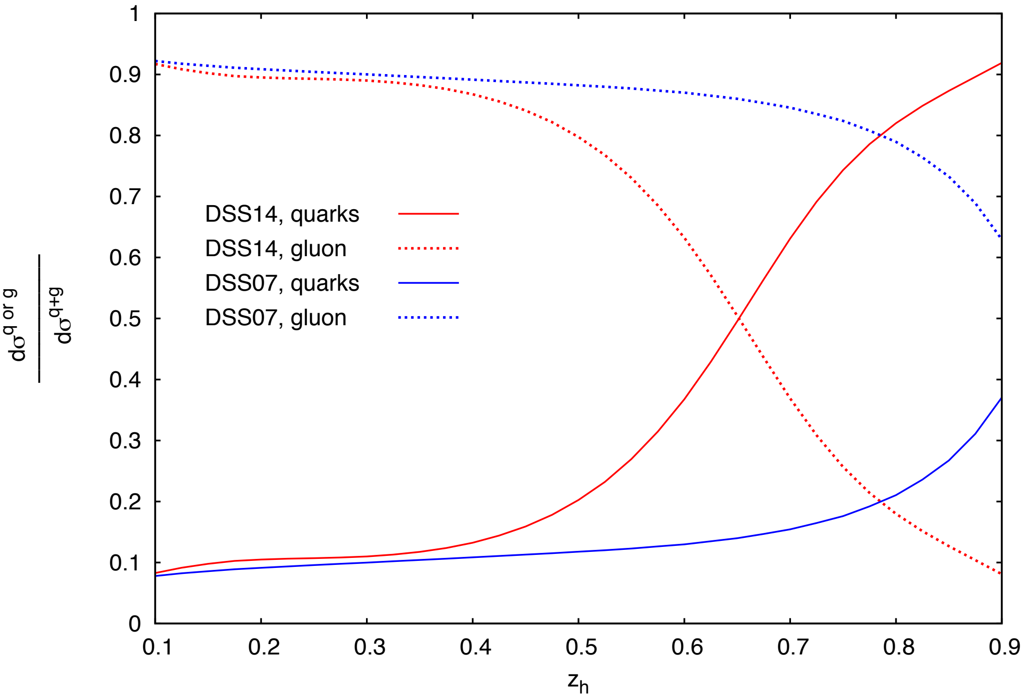

Figure 3.5: Normalized quark (solid) and gluon (dashed) contributions to the cross section differential in z_h for the kinematic conditions chosen for Fig. 3.4. We show results for DSS07 [130] and DSS14 [132] fragmentation functions.

from the figure that precise measurements of the cross section as a function of z_h have the potential to provide new information on fragmentation functions that is complementary to – and in some respects better than – that available from e^+e^- annihilation.

An interesting question is of course which of the fragmentation functions are primarily probed when the cross section for $pp \to (\text{jet}\,\pi)X$ is studied as a function of z_h. Depending on kinematics, different initial-states may dominate the contributions to the cross section, resulting also in different weights with which the fragmentation functions for the various parton species enter. Given how little information on gluon fragmentation is available from $e^+e^- \to hX$ and $ep \to ehX$, it is especially interesting to see how strongly the cross section for $pp \to (\text{jet}\,\pi)X$ depends on D_g^h. It is known that for LHC energies, channels with gluonic initial states (especially gg) typically make important contributions to cross sections. In order to explore whether this allows probes of D_g^h at the LHC, we investigate in Fig. 3.5 the relative contributions of quark/antiquark (summed over all flavors) and gluon fragmentation to the cross section for $pp \to (\text{jet}\,\pi)X$ at ALICE (as shown in the previous Fig. 3.4). We normalize the contributions to the full cross section, so that the quark and gluon contributions add up to unity. We use both the DSS07 and DSS14 sets. As one can see, for $z_h \lesssim 0.5$ the two sets give similar results and show that the cross section is strongly dominated by gluon fragmentation here. This is already interesting, since it implies that in this regime clean probes of D_g^h should be possible that should be much more sensitive than e^+e^- annihilation. Beyond $z_h = 0.5$, the two sets of fragmentation functions show very different behavior. For DSS07, gluon fragmentation continues to dominate all the way up to $z_h \sim 0.9$, whereas for DSS14

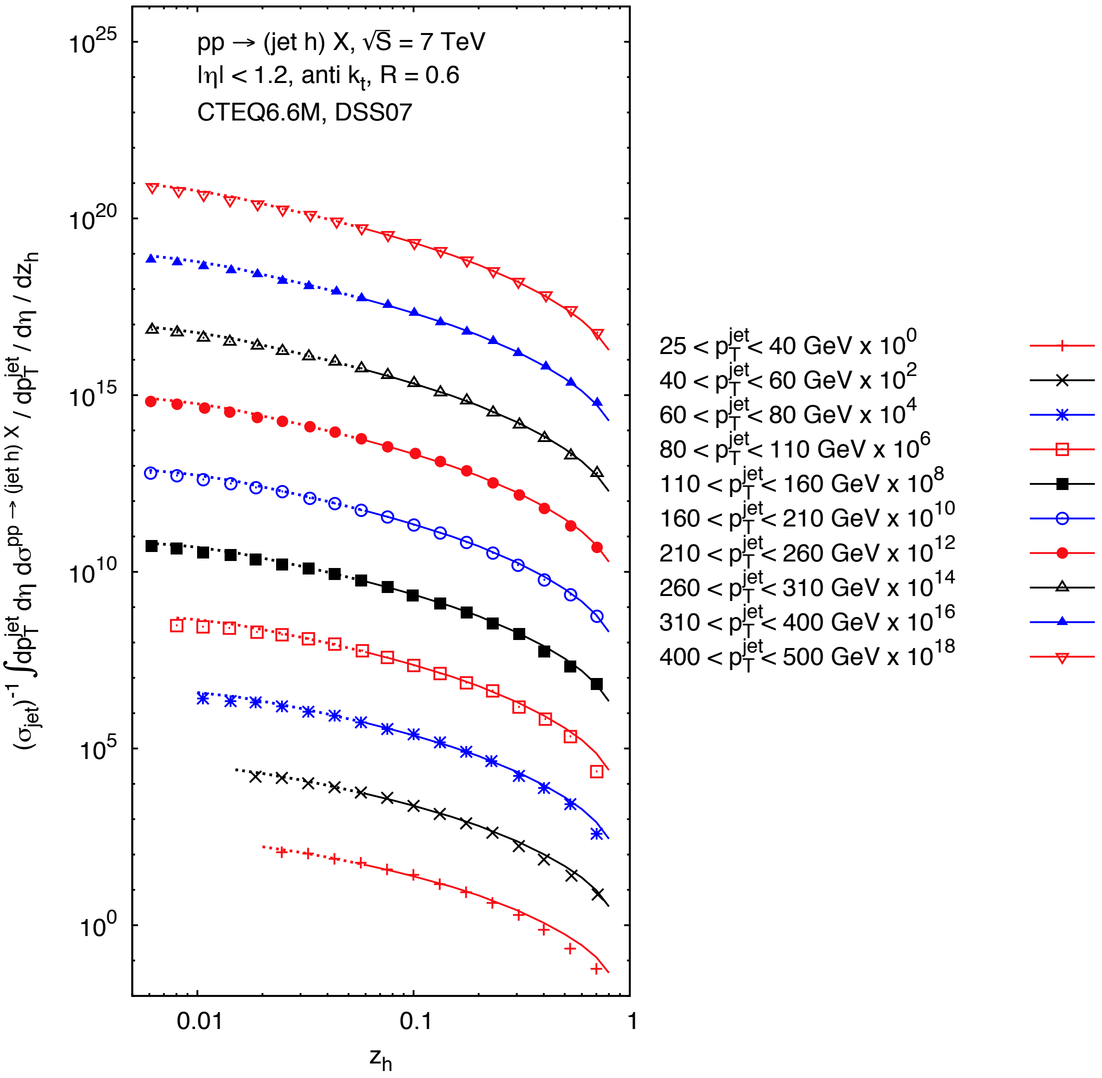

Figure 3.6: NLO cross section for $pp \to (\text{jet}\, h)X$ as function of z_h at $\sqrt{S} = 7$ TeV, compared to the ATLAS data [210] for charged hadron production in the leading jet. The cross section is normalized to the total jet rate. In the region outside the validity of the DSS07 set the theory curves are extrapolated and plotted as dotted lines.

the quarks take over at $z_h \sim 0.7$. We stress again that the uncertainties of the fragmentation functions become very large at such values of z, as we saw in the previous figure, and are in fact hard to quantify reliably. It is evident that information from $pp \to (\text{jet}\, \pi)X$ in this regime will be most valuable, regardless of whether quark or gluon fragmentation dominates. Detailed measurements for various bins in transverse momentum and rapidity will likely help in disentangling fragmenting quarks and gluons.

As mentioned above, measurements of charged hadrons produced in jets are already available from ATLAS [210] and CMS [213]. ATLAS has published measurements at $\sqrt{S} = 7$ TeV [210]

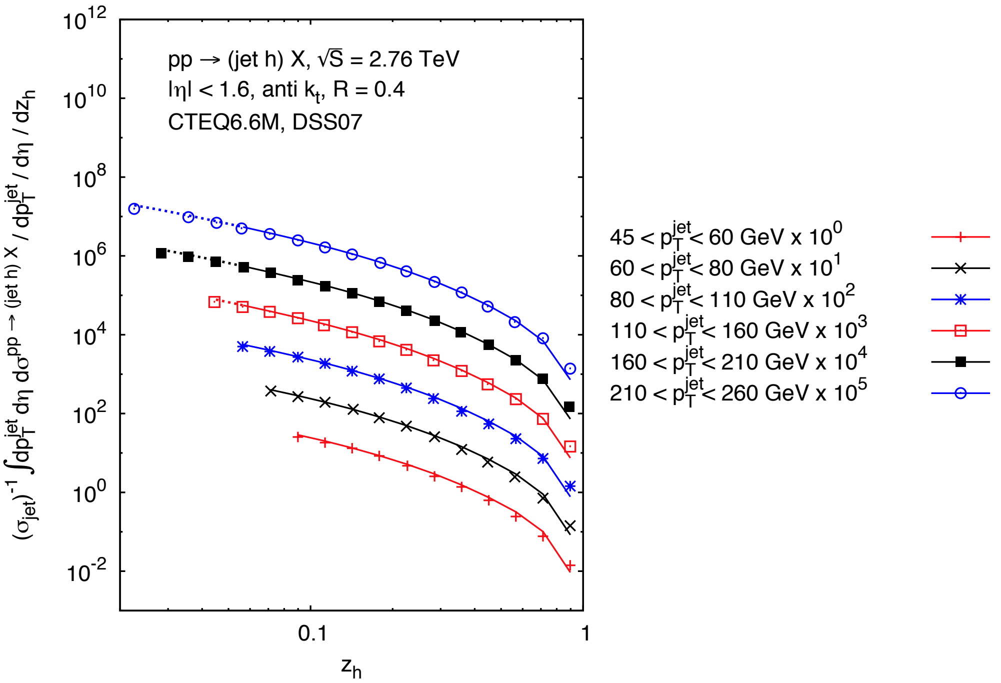

Figure 3.7: Same as Fig. 3.6 but at $\sqrt{S} = 2.76$ TeV, compared to the preliminary ATLAS data [211].

and presented preliminary data [211] also at $\sqrt{S} = 2.76$ TeV. The two analyses each use a slightly different definition of z_h which however both coincide with our z_h in the NJA limit. Figures 3.6 and 3.7 present comparisons of our NLO calculations to the ATLAS data for the two energies. We have now gone back to the DSS07 set, since unspecified charged-hadron fragmentation functions are not available in the more recent DSS14 set. As one can see, there is overall a very good agreement. Note that this agreement extends even down to values of $z_h < 0.05$, well outside the region of validity of the DSS sets. The figures clearly demonstrate the potential of the data to further pin down the charged-hadron fragmentation functions.

The CMS analysis [213] starts from a dijet sample and then studies charged-hadron production inside either the leading jet (which is required to have $p_T^{\mathrm{jet}} > 100$ GeV) or the subleading jet (with $p_T^{\mathrm{jet}} > 40$ GeV). As such, these conditions are different from the single-inclusive jet situation we consider in this work, and strictly speaking we cannot compare to the CMS data. On the other hand, it turns out that the CMS data for hadron production in the leading and the subleading jet are in remarkable agreement for $z_h \gtrsim 0.05$, when one normalizes each of them individually to the corresponding total (leading or subleading) jet event rate. This finding clearly indicates that fragmentation inside jets is really independent of the underlying event topology and happens in the same way in any jet. Therefore, the overall reservation notwithstanding, we show in Fig. 3.8 the comparison of the normalized one-jet rate differential in $\log(1/z_h)$ to the CMS data for hadron production in the leading jet. We show the theoretical curve down to $z_h \sim 0.1$. As one can see, the agreement with the data is very good in this regime. We have found that quark and gluon fragmentation contribute roughly in equal parts to the cross section.

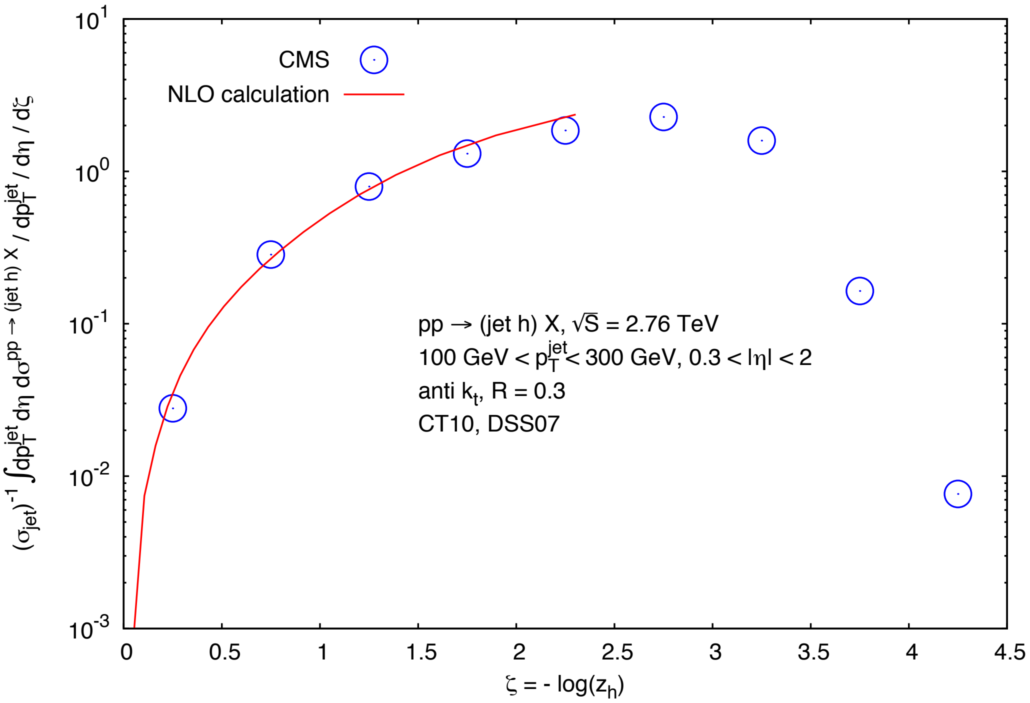

Figure 3.8: NLO cross section for $pp \to (\text{jet}\, h)X$ differential in $\zeta \equiv \log(1/z_h)$ at $\sqrt{S} = 2.76$ TeV, compared to the CMS data [213] for hadron production in the leading jet. The cross section is normalized to the total jet rate.

We finally note that measurements of $pp \to (\text{jet}\, \pi)X$ should readily be feasible at RHIC, especially in the STAR experiment where both inclusive jet [226] and pion cross sections [227, 228] have been measured. Figure 3.9 shows our NLO predictions as functions of z_h for pp collisions at $\sqrt{S} = 200$ GeV and $\sqrt{S} = 510$ GeV. For the former, we have integrated the jet transverse momentum over 5 GeV $< p_T^{\text{jet}} <$ 40 GeV, while for $\sqrt{S} = 510$ GeV we have used 10 GeV $< p_T^{\text{jet}} <$ 80 GeV. In both cases we integrate over $|\eta| < 1$. The jet is defined by the anti-k_T algorithm with $R = 0.6$. As before we use CT10 and DSS14 and set all scales equal to the jet transverse momentum.

3.3 Conclusions and Outlook

We have considered the process $pp \to (\text{jet}\, h)X$, for which a specific hadron is observed inside a fully reconstructed jet. Using the approximation of relatively narrow jets, we have performed an analytical next-to-leading order calculation of the partonic cross sections for this process. We have found that the NLO partonic cross sections may be systematically formulated in terms of simple jet functions for the process. These functions are universal; that is, they only depend on the types of partons producing the jet and fragmenting into the observed hadron. We note that in the process of computing the jet functions we needed to perform subtractions of the final-state collinear singularities. These take the same form as the corresponding subtractions in single-inclusive hadron production (without a reconstructed jet). This demonstrates that the fragmentation functions are universal to NLO in the sense

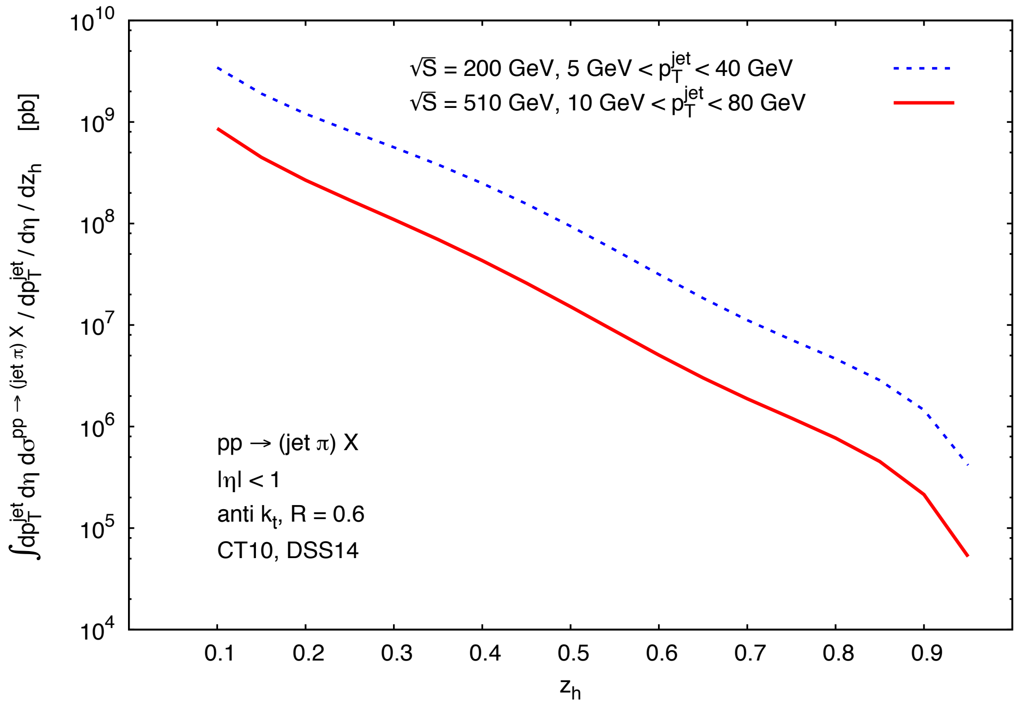

Figure 3.9: NLO cross section for $pp \to (\text{jet}\, h)X$ differential in z_h, for STAR kinematics with $\sqrt{S} = 200$ GeV (dashed) and $\sqrt{S} = 510$ GeV (solid).

that the same functions appear in $pp \to (\text{jet}\, h)X$ as in $pp \to hX$. Essentially, all effects of the fact that a jet is reconstructed along with the hadron factorize into a perturbatively computable factor, the jet function. The factorized structure in terms of jet functions we find at NLO suggests that this statement is true to all orders. Our finding is in line with the result of [37].

Our numerical results are in very good agreement with those obtained by Monte-Carlo integration techniques in [38]. We have presented phenomenological results for the NLO cross section for the kinematics relevant for forthcoming measurements at ALICE and for previous ones by ATLAS and CMS. These results show that $pp \to (\text{jet}\, h)X$ should enable very sensitive probes of fragmentation functions. In particular, the cross section differential in z_h probes the fragmentation functions almost "locally" at the momentum fraction z_h. The combination of fragmentation functions that is probed depends on the mix of initial-state parton distributions and hard-scattering functions that dominate. We find that, in contrast to the standard process $e^+e^- \to hX$ that is customarily used for extractions of fragmentation functions, the process $pp \to (\text{jet}\, h)X$ should offer detailed insights into gluon fragmentation. Also, information at very large z_h might become accessible, although here it may become necessary to perform resummations of large logarithmic terms in the jet functions. We note that at high z_h typical particle multiplicities in the jet a very low, so that power corrections and non-perturbative phenomena will become important here as well. As has been discussed in Ref. [229], hadronization corrections to inclusive-jet production may exhibit a scaling with $1/R$, making them especially relevant in the case of rather narrow jets. Although these corrections are at the same time suppressed by an inverse power of transverse momentum,

it will be an interesting and important task to investigate their structure in case of the hadron-plus-jet observable where two separate transverse momenta are present.
There are various other possible extensions of our work that we hope to address in the future. As is well known, hadron production in jets has important applications in studies of spin phenomena in QCD in terms of the Collins effect [221], where the azimuthal distribution of a hadron around the jet axis is considered. Studies of the effect in *pp* scattering [218–220] will require a detailed theoretical understanding of the process, to which we hope we have contributed in this thesis by computing the NLO corrections for the denominator of the spin asymmetry. We expect that our method based on jet functions is also applicable to the spin-dependent case. Finally, we mention that also photon fragmentation in jets could be interesting as a means to constrain the poorly known photon fragmentation functions (see [230] for related work on e^+e^- annihilation and *ep* scattering). We study this process in Chap. 5.

Chapter 4

Using Hadron-in-Jet Data in a Global Analysis of D^* FFs

In this chapter, which is based on our publication [231], we present a novel global QCD analysis of charged D^*-meson fragmentation functions at next-to-leading order accuracy. This is achieved by making use of the available data for single-inclusive D^*-meson production in electron-positron annihilation, hadron-hadron collisions, and, for the first time, in-jet fragmentation in proton-proton scattering. It is shown how to include all relevant processes efficiently and without approximations within the Mellin moment technique, specifically for the in-jet fragmentation cross section. The presented technical framework is generic and can be straightforwardly applied to future analyses of fragmentation functions for other hadron species, as soon as more in-jet fragmentation data become available. We choose to work within the Zero Mass Variable Flavor Number Scheme which is applicable for sufficiently high energies and transverse momenta. The obtained optimum set of parton-to-D^* fragmentation functions is accompanied by Hessian uncertainty sets which allow one to propagate hadronization uncertainties to other processes of interest.

Cross sections at collider experiments can often be reliably calculated within the framework of perturbative Quantum Chromodynamics (pQCD). The crucial foundation for such computations are so-called factorization theorems that allow for a systematic separation of perturbative and non-perturbative physics, see, for instance, Ref. [32]. Well-known examples for the latter are parton distribution functions (PDFs) that are, by now, rather tightly constrained by global QCD fits to data and are a crucial asset in all scattering processes with hadrons in the initial-state.

Whenever an observable involves detected hadrons in the final-state, the theoretical calculation requires another type of non-perturbative functions as input. These parton-to-hadron fragmentation functions (FFs) describe the non-perturbative transition of a parton produced in the hard-scattering event into the observed hadron. Like PDFs, these functions were shown to be universal but, in contrast to PDFs, they can only be extracted from data through global QCD analyses, see discussion at the end of Sec. 1.3.3. The knowledge of FFs for different hadron species and estimates of their uncertainties is therefore vital for precise theoretical calculations and, hence, has received quite some interest in the past; see, for instance, Ref. [111] for a recent review and Sec. 1.3 for a detailed discussion.

In this work, we consider the hadronization of quarks and gluons into heavy-flavored mesons, more specifically, charged D^*-mesons, that are of particular relevance in the era of the LHC. In general, the theoretical treatment of heavy quarks itself provides a unique laboratory to test pQCD. Correctly describing heavy flavor cross sections that have been measured both at

very high energies at the LHC and at various low energy experiments poses unique challenges to our understanding of QCD. Charm production cross sections are used, for example, to constrain the gluon PDF at small-x [232], and they play a vital role in cosmic-ray and neutrino astrophysics [233–236]. Another important area of research concerns the modification of heavy flavor yields in heavy-ion collisions [237, 238] where highly energetic partons can traverse the quark-gluon plasma thereby attaining valuable information about the properties of the QCD medium. For instance, the energy loss mechanisms, that allow for a quantitative description of in-medium effects, crucially depend on the underlying fragmentation process.
In pQCD calculations, the heavy quark mass m_Q introduces an additional large scale apart from some other hard scales characterizing the process, such as a measured transverse momentum p_T. These multi-scale problems carry additional theoretical challenges as compared to processes involving only light quarks and gluons. There are various approaches in the literature of how to deal with heavy quark masses in general and in the fragmentation process in particular. In the context of pp collisions relevant for LHC phenomenology the following schemes have been put forward and used in their various kinematic regimes of applicability.
In the Fixed Flavor Number Scheme (FFNS) [239–242], the heavy quark Q is not treated as an active parton in the proton but, instead, is solely produced extrinsically in the hard scattering. Logarithms of the ratio of the heavy quark mass m_Q and the hard scale of the process, p_T, are only taken into account in fixed order perturbation theory. Therefore, this scheme is applicable in the region $p_T \sim m_Q$. The Zero Mass Variable Flavor Number Scheme (ZMVFNS), on the other hand, is only applicable in the limit $p_T \gg m_Q$. Here, large logarithms of m_Q/p_T are resummed through DGLAP evolution equations to all orders. m_Q is set to zero in all partonic cross sections, and the heavy quark is treated as an active, massless parton in the proton.

In the context of fragmentation processes, the Fixed Order plus Next-to-Leading Logarithms prescription (FONLL) [243–246] as well as the General Mass Variable Flavor Number Scheme (GMVFNS) [247–253] are examples of unified frameworks to cover both the high p_T region, $p_T \gg m_Q$, and the low p_T tail, $p_T \lesssim m_Q$, similar to the ZMVFNS and FFNS, respectively. In the FONLL approach, the FFs of heavy-flavored mesons are separated into a perturbatively calculable parton-to-heavy quark $i \to Q$ contribution and a non-perturbative heavy quark-to-heavy meson $Q \to h$ piece that is fitted to data. This separation is possible as the heavy quark mass sets an additional scale in the perturbative regime. Instead, in the GMVFNS the entire parton-to-heavy meson FF is treated as a non-perturbative function and is extracted from the available data. We note that another scheme was developed recently in Ref. [254] within the framework of Soft Collinear Effective Theory (SCET).

Since we are primarily interested in LHC phenomenology in this work, in particular the impact of in-jet fragmentation data at $p_T \gg m_Q$, we choose to work in the ZMVFNS using purely non-perturbative FFs similar to the analyses of FFs for light hadron species. As will be discussed in detail below, the inclusive p_T-spectrum of charged D^*-mesons in pp collisions can be fairly well described in the ZMVFNS down to rather low values of about $p_T \sim 5\,\text{GeV}$ in spite of imposing a cut $p_T \geq 10\,\text{GeV}$ when fitting pp data.

Traditionally, the main reference process to determine FFs is semi-inclusive electron-positron annihilation (SIA), $e^+e^- \to hX$. Here, h denotes the detected hadron and X the unobserved final-state remnant. To the best of our knowledge, all the approaches to heavy quark fragmentation mentioned above rely only on SIA data to determine the relevant non-perturbative input following similar non-global fits of light hadron (pion, kaon) FFs [151, 255–257]. While quark-to-hadron FFs can be relatively well constrained from SIA data, it is, in particular, the gluon-to-hadron FF that is at best only very poorly constrained by SIA data alone. Therefore, global QCD analyses of light hadron FFs have also included vital proton-proton scattering data, $pp \to hX$, in order to better constrain the gluon FF. In addition, Semi-Inclusive Deep Inelastic Scattering (SIDIS), $\ell p \to \ell' hX$, data are needed to perform a quark-antiquark and quark flavor separation of FFs. Such global fits of light hadron FFs can be found in [130–132, 134, 258].

In this chapter, we will provide the first global QCD analysis of charmed-meson FFs following the framework outlined by the DSS group in [130–132, 134, 258] at next-to-leading order (NLO) accuracy using the Mellin moment technique [259]. We note that recently first efforts have been made to perform fits of light hadron FFs at next-to-next-to-leading order (NNLO) accuracy [117, 152], and also by including all-order resummations [116, 135]. So far, these efforts have been limited to SIA data only due to the lack of other single-inclusive particle production cross sections at NNLO accuracy; see, for example, [124] for the progress of an ongoing SIDIS calculation at NNLO. As has become customary for both PDF and FF analyses these days, we also present an attempt to estimate the remaining uncertainties of the extracted FF, for which we adopt the Hessian method [260, 261]. The Hessian uncertainty sets can be used to propagate hadronization uncertainties to any other processes of interest such as, for instance, high-p_T D^*-meson production in proton-nucleus collisions at the LHC or BNL-RHIC.

Besides the processes that are traditionally included in global analyses of FFs, like SIA and inclusive high-p_T hadron production in pp collisions, we also include for the first time in-jet fragmentation data from the LHC. Specifically, we include data for the "jet fragmentation function", $pp \to (\text{jet}\, h)X$, where a hadron is identified inside a jet. We consider the observable, where the longitudinal momentum distribution differential in $z_h = p_T/p_T^{\text{jet}}$ is measured, with p_T (p_T^{jet}) denoting the hadron (jet) transverse momentum. The fact that at leading order (LO) accuracy the in-jet observable is directly probing the $z = z_h$ dependence of FFs explains their potential relevance for analyses of FFs. In-jet fragmentation was pioneered in [35, 36, 262, 263] for exclusive jet samples. The extension to inclusive jet samples was developed in [38, 197] within standard pQCD at NLO accuracy, allowing for a direct comparison with data from the LHC. In Ref. [204] the result was re-derived within SCET. Thanks to the effective field theory treatment, the additional all-order resummation of single logarithms in the jet-size parameter $\alpha_s^n \ln^n R$ was achieved, yielding consistent results at NLO+NLL$_\text{R}$ accuracy. In this chapter we will work at NLO accuracy as a detailed study of the impact of NLO+NLL$_\text{R}$ corrections on fits of FFs is beyond the scope of this thesis.

In Ref. [264], it was found that the D^*-in-jet data from ATLAS [40] are not well described by existing fits of D^*-meson FFs [253] even though they give a good description of both SIA and inclusive pp data; see Ref. [265] for related work. This leads to the important question, which we address in detail in this work, if there is a real tension between the fitted data sets and the in-jet observable or if it is possible to accommodate all data sets in a combined, global fit. We note that apart from the D^*-in-jet data by ATLAS [40] there are also in-jet results available from the LHC for unidentified light charged hadrons [212, 266–268], mainly in heavy-ion collisions though, as well as for prompt and non-prompt J/ψ production in jets [41]. In this first exploratory study of the impact of in-jet data on fits of FFs we therefore limit ourselves to developing the necessary theoretical framework and to a global analysis

of parton-to-D^* FFs utilizing the ATLAS in-jet data. However, we wish to emphasize that the technical framework presented below is generic and can be straightforwardly applied to future analyses of fragmentation functions for other hadron species as soon as more in-jet fragmentation data become available.
Finally, we notice that various combined differential cross section data for charged D^* mesons obtained in deep-inelastic lepton-proton collisions are available from the H1 and ZEUS Collaborations [269]. Since the data extend down to relatively low values of transverse momentum and photon virtuality Q, they need to be described in a theoretical framework which keeps the full dependence on the charm quark mass [269]. Hence, these data cannot be included in our current global QCD analysis that is based on the ZMVFNS approximation.

The remainder of this chapter is organized as follows. In Section 4.1, we discuss the technical framework for all three processes that are included in our global QCD analysis, namely $e^+e^- \to D^*X$, $pp \to D^*X$, and $pp \to (\text{jet}\, D^*)X$, with particular emphasis on the latter. Note that throughout this chapter, D^* collectively denotes both charged mesons, i.e. D^{*+} and/or D^{*-}. Next, in Section 4.2, we briefly present the details of our analysis comprising the parametrization of the FFs at some input scale, the selection of experimental data and cuts imposed on the fit, the Mellin moment technique used throughout this chapter, and the Hessian uncertainty method. In Section 4.3, we present and discuss the results of our global analysis of parton-to-D^* FFs at NLO accuracy, and compare the results of the fit to the available data. In addition, we compare to the previous fit provided by Ref. [253]. In Section 4.4, we draw our conclusions and present a brief outlook.

4.1 Technical Framework

4.1.1 Single-inclusive e^+e^- Annihilation

The cross section for the single-inclusive annihilation process, $e^+e^- \to \gamma/Z \to hX$, as presented in Eq. (1.35), is usually normalized to the total hadronic cross section σ_{tot} and may be written schematically as

$$\frac{1}{\sigma_{\text{tot}}} \frac{d\sigma^{e^+e^- \to hX}}{dz} = \frac{\sigma_0}{\sigma_{\text{tot}}} \left[F_T^h(z, Q^2) + F_L^h(z, Q^2) \right] . \tag{4.1}$$

It is common to decompose the cross section (6.1) into a transverse (T) and longitudinal (L) part although this is of no practical relevance for D-meson production. We have introduced the scaling variable

$$z \equiv \frac{2P_h \cdot q}{Q^2} \overset{\text{c.m.s.}}{=} \frac{2E_h}{Q} , \tag{4.2}$$

where P_h and q are the four momenta of the observed hadron and time-like γ/Z boson, respectively. Moreover, $Q^2 \equiv q^2 = S$. As is indicated in Eq. (4.2), z reduces to the hadron's energy fraction in the center-of-mass system (c.m.s.) frame and is often also labeled as x_E [87]. The total cross section for $e^+e^- \to$ hadrons at NLO accuracy reads

$$\sigma_{\text{tot}} = \sum_q \hat{e}_q^2 \, \sigma_0 \left[1 + \frac{\alpha_s(Q^2)}{\pi} \right] , \tag{4.3}$$

where α and α_s are the electromagnetic and the strong coupling, respectively, and $\sigma_0 = 4\pi\alpha^2(Q^2)/S$. We denote the electroweak quark charges by $\hat{e}_q^2$, which may be found, for instance, in App. A of Ref. [83].

To make factorization explicit, the transverse and longitudinal time-like structure functions in Eq. (6.1) can be written as a convolution of perturbative coefficient functions $\mathbb{C}_i^k$, $i = q, \bar{q}, g$ [84, 270, 271], and non-perturbative FFs D_i^h, c.f. Eq. (1.45),

$$F_k^h(z, Q^2) = \sum_q \hat{e}_q^2 \Big\{ \Big[\mathbb{C}_q^k \otimes (D_q^h + D_{\bar{q}}^h)\Big](z, Q^2) + \Big[\mathbb{C}_g^k \otimes D_g^h\Big](z, Q^2)\Big\}, \tag{4.4}$$

where $k = T, L$. The standard convolution integral with respect to the first argument is denoted by the symbol $\otimes$ and given in Eq. (1.40).

As always, the notion of factorization as applied in Eq. (4.4) is only valid up to corrections proportional to inverse powers of the hard scale [87]. For a one-scale process like SIA, the hard scale should be chosen to be of $\mathcal{O}(Q)$ and Q itself should be at least of $\mathcal{O}$(few GeV). For simplicity, we have chosen the factorization and renormalization scales in Eq. (4.4) equal to the hard scale, i.e., $\mu_R = \mu_F \equiv Q$.

Kinematical effects related to the non-zero mass m_h of the produced hadron h are another source of corrections to the factorized framework where m_h is neglected throughout. Deviations of the data from theory are expected to show up at the lower end of the z-spectrum, as we shall see in the phenomenological section, and are more pronounced for heavier than for light mesons. One usually introduces a cut z_{min} in global analyses of FFs [130–132, 134, 151, 255–258] below which the data cannot be used and the theory outlined above is not valid. Such a cut also avoids the region in z where fixed-order evolution kernels receive large logarithmic corrections which otherwise can only be dealt with by all-order resummations, see, for instance, Ref. [116].

4.1.2 Single-inclusive D^* Production pp Collisions

The production of high-p_T hadrons in hadronic collisions offers valuable and complementary information compared to SIA data in global QCD analyses of FFs. The dominance of the $gg \to gX$ and $qg \to gX$ partonic subprocesses at not too large values of p_T gives access to the gluon-to-hadron fragmentation function, which is only very indirectly accessible in SIA through scaling violations and, hence, largely unconstrained.

In addition to data for the sum of charged D^* mesons, $D^{*+} + D^{*-} \equiv D^{*\pm}$, from ATLAS [272] and LHCb [273, 274], measurements of positively charged D^{*+} mesons are available from both the ALICE [275, 276] and CDF [277] collaborations. The latter sets of data offer new information on the charge separation of D^* meson FFs that is not available from SIA where only the sum $D^{*\pm}$ can be observed. It is also worth recalling that the Tevatron data from CDF [277] are taken in $p\bar{p}$ rather than pp collisions and that LHCb has the unique capability to perform measurements at different asymmetric, forward rapidity intervals [273, 274]. Both sets of data will add unique information to our global analysis.

The factorized cross section (2.1) for a given hadron p_T and pseudorapidity η may schematically be written as a convolution of appropriately combined PDFs, parton-to-hadron FFs, and partonic hard scattering cross sections:

$$\frac{d\sigma^{H_1 H_2 \to hX}}{dp_T d\eta} = \frac{2p_T}{S} \sum_{abc} f_a^{H_1} \otimes f_b^{H_2} \otimes d\hat{\sigma}_{ab}^c \otimes D_c^h \,. \tag{4.5}$$

Here, $f_a^{H_1}$ and $f_b^{H_2}$ denote the PDFs with flavor a and b in hadron H_1 and H_2, respectively, and D_c^h is the $c \to h$ FF. The sum in (4.5) is over all contributing partonic cross sections $ab \to cX$, denoted as $d\hat{\sigma}_{ab}^c$, which may be calculated as a perturbative series in α_s, starting at $\mathcal{O}(\alpha_s^2)$ which corresponds to the LO approximation. Hence, to perform a consistent NLO analysis of fragmentation functions, we include the $\mathcal{O}(\alpha_s^3)$ corrections which have been computed analytically in [91, 198]. As mentioned above, the factorized form given in Eq. (4.5) is again only valid up to power corrections that are suppressed by inverse powers of the hard scale, in this case p_T. Throughout this chapter, we choose the factorization and renormalization scales for this process to be equal to the transverse momentum of the observed hadron, i.e., $\mu = p_T$, but we will illustrate the residual dependence on μ in the phenomenological section below by varying μ by the conventional factor of two up and down.

One drawback of the single-inclusive high-p_T production process is that the information on the z dependence of the probed FFs is only accessible in integrated form through one of the convolution integrals in Eq. (4.5). The range of integration allowed by kinematical considerations for a given p_T and η of the observed hadron is rather broad (see discussion below Eq. (3.1)) and may reach well below the cut z_{min} mentioned above. However, it has been shown in Ref. [278] that one samples on average predominantly fairly large values of z in Eq. (4.5), $\langle z \rangle \simeq 0.4$ at mid rapidity and further increasing towards forward rapidities, and that z values below z_{min} are irrelevant for all practical purposes. Considering hadrons inside jets rather than single-inclusive hadron production allows one to sample z more directly, as we shall discuss in some detail next.

4.1.3 D^* Meson in-Jet Production

The inclusive production of identified hadrons inside a fully reconstructed jet $pp \to (\text{jet}\, h)X$, where the hadron is part of the jet, has been studied for pp collisions in Refs. [38, 197, 204] and Chap. 3. In [38], the NLO cross section was obtained using a Monte-Carlo (MC) phase space integrator. Instead, in Refs. [197, 204] analytical results were obtained using the approximation that the jet is sufficiently collimated. The NLO result of Chap. 3 was derived within the standard pQCD framework, whereas [204] employed methods within SCET for inclusive jet production [206, 279], which allows for the additional resummation of single logarithms of the jet size parameter R. We have demonstrated in Chap. 3 that at NLO accuracy, the analytical result of the cross section can be schematically written as $\mathcal{A} + \mathcal{B} \log R + \mathcal{O}(R^2)$. If the jet is sufficiently narrow, i.e., $R \ll 1$, power corrections of the order $\mathcal{O}(R^2)$ can be neglected. In studies for inclusive jet production [174, 175, 193, 280], it was found that this "narrow jet approximation" is valid even for relatively large values of R. For example, for $R = 0.7$ the agreement between the thus obtained analytical results and the full MC result at NLO is better than 5%. We have confirmed this observation for the in-jet production of hadrons in Fig. 3.2 by comparing to the full NLO MC calculation of [38].

In this chapter, we need the hadron-in-jet results for the anti-k_T jet algorithm [33]. Currently, the only available data set for $D^{*\pm}$ mesons within jets is provided by the ATLAS collaboration [40] for which the anti-k_T algorithm was used with a jet size parameter of $R = 0.6$. However, the results for cone [189] and J_{E_T} [34] jets have been presented in Chap. 3 as well. As it was discussed in detail in Chap. 3, the in-jet fragmentation provides a more direct access to the z-dependence of FFs than data on single-inclusive hadron production. At LO accuracy, the cross section is directly proportional to the FFs probed at the momentum fraction $z = z_h$, where

$$z_h \equiv \frac{p_T}{p_T^{\text{jet}}} \tag{4.6}$$

and p_T (p_T^{jet}) denotes the transverse momentum of the hadron (jet). The cross section (3.21) for the process $pp \to (\text{jet}\, h)X$ may equivalently be written as

$$\begin{aligned}\frac{d\sigma^{pp\to(\text{jet}\,h)X}}{dp_T^{\text{jet}} d\eta^{\text{jet}} dz_h} &= \frac{2p_T^{\text{jet}}}{S} \sum_{a,b,c} \int_{x_a^{\min}}^1 \frac{dx_a}{x_a} f_a(x_a,\mu) \int_{x_b^{\min}}^1 \frac{dx_b}{x_b} f_b(x_b,\mu) \\ &\quad \times \int_{z_c^{\min}}^1 \frac{dz_c}{z_c^2} \frac{d\hat{\sigma}_{ab}^c(\hat{s},\hat{p}_T,\hat{\eta},\mu)}{v dv dw}\, \mathcal{G}_c^h(z_c, z_h, \mu, R)\,, \end{aligned} \tag{4.7}$$

where, again, we have set the renormalization and factorization scales to be equal and collectively denoted them by μ. For this process, we choose $\mu = p_T^{\text{jet}}$ as our default choice of scale. The partonic cross sections $d\hat{\sigma}_{ab}^c$ are the same as they appear in the cross section for single-inclusive hadron production in Eq. (4.5). These hard functions depend on the jet partonic transverse momentum $\hat{p}_T = p_T^{\text{jet}}/z_c$, the partonic rapidity $\hat{\eta} = \eta^{\text{jet}} - \log(x_a/x_b)/2$ and the partonic c.m.s. energy squared $\hat{s} = x_a x_b S$ with $\sqrt{S}$ the hadronic c.m.s. energy. The integration limits are as given in (2.3), but with V and W defined in terms of jet transverse momentum and rapidity, i.e.

$$V \equiv 1 - \frac{p_T^{\text{jet}}}{\sqrt{S}}\, e^{-\eta^{\text{jet}}}\,, \quad W \equiv \frac{(p_T^{\text{jet}})^2}{SV(1-V)}\,, \tag{4.8}$$

The function $\mathcal{G}_c^h$ in Eq. (4.7) contains all the information on the production of the final-state jet and the identified hadron inside the jet and, hence, depends on the jet size parameter R. To NLO accuracy, $\mathcal{G}_c^h$ follows from (3.21) as

$$\mathcal{G}_c^h(z_c, z_h, \mu, R) = \sum_e j_{c\to e}(z_c, R, \mu) \sum_{c'} \int_{z_h}^1 \frac{dz_p}{z_p}\, \tilde{j}_{e\to c'}(z_p, R, \mu)\, D_{c'}^h\left(\frac{z_h}{z_p}, \mu\right). \tag{4.9}$$

The jet functions j and $\tilde{j}$ describe the formation of the jet and the partonic fragmentation, respectively, and may be found in Eqs. (3.18) and (3.19). Inserting Eq. (4.9) into Eq. (4.7), we may write the cross section as

$$\frac{d\sigma^{pp\to(\text{jet}\,h)X}}{dp_T^{\text{jet}} d\eta^{\text{jet}} dz_h} = \sum_{e,c'} \mathcal{E}_e \times \left[\tilde{j}_{e\to c'} \otimes D_{c'}^h\right](z_h) \tag{4.10}$$

where $\mathcal{E}_e$ contains all the sums and integrals over the PDFs, the partonic cross sections and the jet functions $j_{c\to e}$ and may be regarded as an "effective charge" weighting the different channels. The fragmentation functions appear in an actual convolution with the jet functions $\tilde{j}$ with respect to z_h, multiplied by these effective charges. Eq. (4.10) illustrates the structural similarity of the in-jet fragmentation cross section and SIA, enabling access to the z-dependence of the FFs. Due to the hadronic initial-state, the gluon fragmentation function already appears at LO accuracy, as it is the case for single-inclusive hadron production in pp collisions.

Typically, the hadron-in-jet production data are normalized to the inclusive jet cross section $pp \to \text{jet}X$. Hence, the actual experimental observable is given by

$$F(z_h, p_T^{\text{jet}}, \eta^{\text{jet}}) \equiv \frac{d\sigma^{pp\to(\text{jet}\,h)X}}{dp_T^{\text{jet}} d\eta^{\text{jet}} dz_h} \Big/ \frac{d\sigma^{pp\to\text{jet}\,X}}{dp_T^{\text{jet}} d\eta^{\text{jet}}} \,. \tag{4.11}$$

We found in Chap. 2 that the cross section for inclusive jet production may be written in a similar form as the single-inclusive hadron production cross section in Eq. (4.5), with only the fragmentation functions D_c^h replaced by perturbatively calculable jet functions J_c (see also [197, 279]), i.e.,

$$\frac{d\sigma^{H_1 H_2\to\text{jet}\,X}}{dp_T^{\text{jet}} d\eta^{\text{jet}}} = \frac{2p_T^{\text{jet}}}{S} \sum_{abc} f_a^{H_1} \otimes f_b^{H_2} \otimes d\hat{\sigma}_{ab}^c \otimes J_c \,. \tag{4.12}$$

Thus, we may use the numerically efficient codes of Refs. [174, 175, 193, 280] to compute the hadron-in-jet cross section observable (4.11) in our global analysis of D^* FFs.

4.2 Outline of the Analysis

4.2.1 Parametrization

As we choose to work in the ZMVFNS for our global analysis of D^* FFs, we closely follow the procedures for light hadron (pion and kaon) FFs as outlined in Refs. [117, 130–132, 134, 258]. However, due to the significantly smaller amount of data for D^* production, we adopt a slightly less flexible, more economical functional form to parametrize the non-perturbative parton-to-D^{*+} FFs at some initial scale μ_0 in the commonly adopted $\overline{\text{MS}}$ scheme:

$$D_i^{D^{*+}}(z, \mu_0^2) = \frac{N_i\, z^{\alpha_i}(1-z)^{\beta_i}}{B[2+\alpha_i, \beta_i+1]} \,. \tag{4.13}$$

We have tested that Eq. (4.13) nevertheless yields a very satisfactory description of the data, see also our results in Sec. 4.3 below. The much simpler functional form with significantly less parameters also has the additional benefit of greatly facilitating the fitting procedure and the determination of uncertainties with the Hessian method.

We choose our initial scale to be equal to the charm quark mass $\mu_0 = m_c$. As we adopt the CT14 set of NLO PDFs and determination of the strong coupling α_s [140] in all our calculations of hadronic cross sections and the scale evolution of FFs, we also use the heavy quark masses according to CT14, i.e., $m_c = 1.3\,\text{GeV}$ and $m_b = 4.75\,\text{GeV}$. Furthermore, we assume that at the initial scale μ_0 the FFs for all light quarks and antiquarks as well as for the anti-charm quark vanish, i.e.,

$$D_q^{D^{*+}}(z, \mu_0^2) = 0, \qquad \text{for } q = u, \bar{u}, d, \bar{d}, s, \bar{s}, \bar{c} \,, \tag{4.14}$$

which has no impact on the quality of the fit. In any case, none of these FFs can be reliably determined from the existing sets of data.

The bottom quark and antiquark FFs are included in the scale evolution above $\mu = m_b$, and, as non-perturbative input, we only parametrize the total bottom-to-D^{*+} fragmentation function $D_{b_{\text{tot}}}^{D^{*+}}(z, m_b^2) \equiv D_{b+\bar{b}}^{D^{*+}}(z, m_b^2)$. In total this leaves us with 9 non-zero parameters in

Eq. (4.13) for $i = g, c, b_{\text{tot}}$ which is further reduced to 8 actual parameters to be determined in our global analysis since it turns out that β_g is essentially unconstrained by data and has to be fixed.

As usual, the FFs for positively and negatively charged mesons are assumed to be related by charge conjugation, i.e.,

$$D_q^{D^{*-}}(z,\mu^2) = D_{\bar{q}}^{D^{*+}}(z,\mu^2) \tag{4.15}$$

for quarks and

$$D_g^{D^{*-}}(z,\mu^2) = D_g^{D^{*+}}(z,\mu^2) \tag{4.16}$$

for the gluon. This will be used to compute cross sections for all data sets which observe only the sum of charges $D^{*\pm}$.

Finally, the parametrization in Eq. (4.13) is normalized to the respective $N = 2$ Mellin moment by the denominator containing the Euler Beta function $B[a,b]$. Hence, the coefficients N_i constitute the contribution of $zD_i^{D^{*+}}$ to the energy-momentum sum rule (1.67).

4.2.2 Selection of Data Sets

Numerous experimental data exist for the three types of processes described in Sec. 4.1. Identified $D^{*\pm}$ mesons in e^+e^- collisions have been measured both by the ALEPH [281] and OPAL [282, 283] collaborations at LEP at a c.m.s. energy of $Q = M_Z$, the mass of the Z boson. Unfortunately, the results from the more recent OPAL analysis [283] are presented only in graphical form, and the corresponding numerical values are not anymore available [284]. Thus, we decide to use only the older set of OPAL data [282] with less statistics and somewhat larger uncertainties in our fit. Both collaborations also present bottom and charm flavor tagged data. Here, only the OPAL collaboration provides numerical values which we include in our global analysis.

Both data sets from ALEPH and OPAL are not corrected for the branching ratios of the decay channels used for the identification of the $D^{*\pm}$ mesons. To obtain properly normalized cross sections, we divide the data by the branching ratios B_1 and B_2 which are given by [64]

$$\begin{aligned} B_1(D^{*+} \to D^0\pi^+) &= (67.7 \pm 0.5)\%\,, \\ B_2(D^0 \to K^-\pi^+) &= (3.93 \pm 0.04)\%\,. \end{aligned} \tag{4.17}$$

The uncertainties of the branching rations, ΔB_1 and ΔB_2, are propagated into the systematic uncertainty of the SIA cross section data by adding them in quadrature, i.e.,

$$\Delta d\sigma^{\text{sys}} = \sqrt{\left(\frac{d\sigma \Delta B_1}{B_1^2 B_2}\right)^2 + \left(\frac{d\sigma \Delta B_2}{B_1 B_2^2}\right)^2 + \left(\frac{\Delta d\sigma}{B_1 B_2}\right)^2}\,. \tag{4.18}$$

Here, $\Delta d\sigma$ denotes the systematic error of the SIA data as provided by the ALEPH and OPAL experiments.

At lower c.m.s. energies, there are several measurements available around $Q \approx 30$ GeV [285–289]. However, these data sets are rather old, and they consist of only a few data points that have very large uncertainties. Therefore, these sets do not add any relevant additional constraints to our global analysis, and, for simplicity, we choose to not include them.

Finally, some e^+e^- experiments have measured $D^{*\pm}$ production just below the bottom threshold at around $Q \approx 10.5$ GeV. The most recent and precise data are from the BELLE collaboration [290]. However, as stated on the HEPDATA webpage, the "data for this record have been removed at the request of the authors due to an unrecoverable error in the measurement"; see [291]. Hence, we have to refrain from using this data set in our fit, which, potentially, could have been a very promising constraint from SIA in addition to the LEP data at $Q = M_Z$. We note that the previous analysis of D-meson FFs by the KKKS group [253], to which we compare later on, includes the BELLE data as they were not yet withdrawn at the time when their fit was performed. Furthermore, CLEO [292] and ARGUS [293] also provide data measured at similar c.m.s. energies as BELLE. However, both data sets are not corrected for initial-state radiation (ISR) effects. In addition, the ARGUS data points have very large uncertainties. The CLEO data have been included in the extractions of D^* FFs in Refs. [246, 253]. While Ref. [246] models the ISR effects based on data, the extraction of [253] includes ISR using certain approximations in the theory calculation of the cross section. However, both find noticeable tensions between the CLEO and ALEPH data. Since this may or may not be related to the treatment of ISR corrections, we choose not to include any of the low-energy SIA data in our analysis.

Data for inclusive $D^{*\pm}$ production in hadronic collisions are available from the CDF collaboration at the Tevatron [277] and from the ALICE [275, 276], ATLAS [272], and LHCb [273, 274] collaborations at the LHC. We utilize all of these data sets in our global QCD analysis, as they provide valuable constraints on the gluon fragmentation function. As was mentioned in Sec. 4.1.3, an important new asset of our analysis are the in-jet fragmentation data for which ATLAS has presented results for identified $D^{*\pm}$ mesons inside fully reconstructed jets [40].

To ensure the validity of the ZMVFNS approximation and the massless treatment of the D^* mesons in the factorized formalism used to describe fragmentation processes, we have to impose certain cuts on the above mentioned data sets. For SIA, we only use data in the interval $0.1 < z < 0.95$, i.e., $z_{\mathrm{min}} = 0.1$, which is sufficient for the LEP data taken at $Q = M_Z$. For all p_T-spectra of D^* mesons in hadronic collisions we select a very conservative cut of $p_T > p_T^{\mathrm{min}} = 10\,\mathrm{GeV}$ below which we exclude all data from the fit. Notice that this cut forces us to exclude the LHCb data sets from the 7 TeV run; we nevertheless show a comparison of our optimum fit to these data in Sec. 4.3. We are confident that our resulting set of FFs is not affected by our choice of p_T^{min} since we find that lowering the cut down to 5 GeV does not lead to any significant changes in both the quality of the fit and the obtained optimum fit parameters in Eq. (4.13). This also implies that our results can be reliably extrapolated down to p_T values of about 5 GeV, as we will also illustrate in some detail in Sec. 4.3.

4.2.3 Mellin Moment Technique

As mentioned above, we work entirely in complex Mellin N moment space in order to solve the scale evolution equations of the FFs, to compute the relevant SIA and pp cross sections discussed in Sec. 4.1, and to perform the actual fit and error analysis. The Mellin integral transform is well suited for these tasks as convolution integrals turn in ordinary products in Mellin N space (c.f. Eq. (1.80)) and the integro-differential evolution equations can be solved analytically. The resulting numerical codes for global QCD analyses are very efficient and fast. The pair of Mellin integral and inverse transforms of a function $f(z)$ and $f(N)$ are defined in Eqs. (1.78) and (1.79), respectively. In practice, one ends up having to compute only a limited number of moments along the contour $\mathcal{C}_N$ in order to numerically solve the integral in Eq. (1.79).

Our analysis is set up in the following way: for each data point we use the analytical "truncated" solution of the evolution equations at NLO accuracy in Mellin space, see, e.g., Refs. [116, 118, 124], to evolve the input FFs in (4.13) to the relevant scale. Next, the FFs are combined with appropriate N space expressions for the hard scattering subprocesses before the inverse transform in Eq. (1.79) is performed numerically to evaluate the quality of the fit, see the next subsection. More specifically, in case of SIA, see Sec. 4.1.1, this is achieved by taking the Mellin moments of Eq. (4.4) analytically, and all convolutions of FFs and coefficient functions turn schematically into

$$D(z) \otimes \mathbb{C}(z) = \frac{1}{2\pi i} \int_{\mathcal{C}_N} dN\, z^{-N}\, D(N)\, \mathbb{C}\,(N)\ . \tag{4.19}$$

Here, each coefficient function $\mathbb{C}(N)$ can be evaluated explicitly using the general definition in Eq. (1.78) and appropriate analytic continuations of harmonic sums to non-integer, complex N values, see, for instance, Ref. [116].

For the more complicated expressions in *pp* scattering discussed in Secs. 4.1.2 and 4.1.3, one has to invoke an intermediate step as it is no longer possible or too cumbersome to perform the Mellin transform of the hard scattering cross sections analytically. Instead, we follow the steps outlined in Refs. [130–132, 134, 258, 259] and first express the FFs that appear, e.g., in Eq. (4.5) in terms of their respective Mellin inverse, see Eq. (1.79). After some reordering, the inclusive hadron production cross section $H_1H_2 \to hX$ can be recasted as follows

$$\frac{d\sigma^{H_1H_2\to hX}}{dp_T d\eta} = \sum_c \frac{1}{2\pi i} \int_{\mathcal{C}_N} dN\, D_c^h(N) \times \left[\frac{2p_T}{S} \sum_{ab} f_a^{H_1} \otimes f_b^{H_2} \otimes d\hat{\sigma}_{ab}^c \otimes \tilde{D}_c^h\right]\ , \tag{4.20}$$

where $\tilde{D}_c^h(z) = z^{-N}$. The second part in squared brackets is independent of the FFs we are interested in, only needs to be evaluated once, and can be stored on a grid. In the end, for each data point one only has to perform the remaining contour integral in (4.20). This method is completely general and does not require any approximations such as K-factors, and is also employed for the in-jet fragmentation $pp \to (\text{jet}\, h)X$ in Sec. 4.1.3.

4.2.4 Fitting and the Hessian Uncertainty Method

We obtain the optimum values for the eight free fit parameters in Eq. (4.13) by a standard χ^2 minimization. We define the χ^2 for the M data sets included in the fit, each containing M_i data points that pass the selection cuts specified in Sec. 4.2.2, to be

$$\chi^2 = \sum_{i=1}^{M} \left[\frac{(1-\mathcal{N}_i)^2}{\Delta\mathcal{N}_i^2} + \sum_{j=1}^{M_i} \frac{(\mathcal{N}_i T_j - E_j)^2}{\Delta E_j^2}\right]\ , \tag{4.21}$$

where E_j is the experimental value for a given observable with uncertainty ΔE_j and T_j is the corresponding theory calculation. Furthermore, we have introduced normalization shifts $\mathcal{N}_i$ to account for this type of uncertainty whenever the normalization error $\Delta\mathcal{N}_i$ is stated by the experiments. The optimum normalization shifts $\mathcal{N}_i$ are computed analytically from the condition that they should minimize the χ^2. We note that we combine systematical and statistical uncertainties in quadrature in ΔE_j.

In order to estimate the uncertainties of the extracted FFs due to the experimental uncertainties ΔE_j and $\Delta\mathcal{N}_i$, we adopt the widely used iterative Hessian approach [260, 261] to explore the range of possible variations of the obtained optimum parameters in the vicinity of the minimum of the χ^2 function for a given tolerance $\Delta\chi^2$. To this end, we provide 16 eigenvector sets for our FFs that correspond to the + and − directions of the eigenvectors of the diagonalized Hessian matrix. These sets greatly facilitate the propagation of hadronization uncertainties to any observable of interest. In fact, the uncertainty of an observable $\mathcal{O}$ may be calculated straightforwardly as [260, 261]

$$\Delta\mathcal{O} = \frac{1}{2}\sqrt{\sum_{i=1}^{8}\left[\mathcal{O}_{+i} - \mathcal{O}_{-i}\right]^2}\,, \tag{4.22}$$

where $\mathcal{O}_{\pm i}$ denote the observable calculated with the plus or minus Hessian eigenvector set i, respectively.

Finally, we note that choosing the tolerance $\Delta\chi^2$ is to some extent arbitrary in the presence of non-Gaussian or unaccounted uncertainties accompanying any global fit of PDFs or FFs. We have made sure that our Hessian sets, computed with $\Delta\chi^2 = 4$, faithfully reflect the experimental uncertainties of the SIA data, as can be seen and will be discussed in the phenomenological section below. In this sense they correspond to uncertainties at the 68% confidence level in the z range that is constrained by data. Outside that range, the uncertainties are biased by the choice and flexibility of the selected functional form and assumptions made on the parameter space. In what follows, we will also briefly discuss additional, theoretical sources of uncertainties such as the choice and uncertainties of PDFs and from variations of the renormalization and factorization scales μ.

4.3 Results

4.3.1 Parton-to-D^{*+} Fragmentation Functions

In this section, we present the results of our global determination of the parton-to-D^{*+}-meson fragmentation functions and compare them to the previous fit of SIA data provided by Ref [253], which will be labeled "KKKS08". Note, that we use the public available numerical code from [294]. In Tab. 4.1, we list the numerical values of the parameters of our optimal fit at NLO accuracy, see Eq. (4.13). As already mentioned, the parameter β_g, which controls the $z \to 1$ behavior of the gluon FF, is basically unconstrained by data. For this reason, we decided to keep $\beta_g = 10$ fixed. Note that other choices, like $\beta_g = 5$ or 15 yield a total χ^2 which differs by less than one unit, which is well within our tolerance $\Delta\chi^2 = 4$. It is worth mentioning that in all fits with different values of β_g, the parameter α_g changes in such a way that the normalization N_g remains essentially the same. As can be seen from the normalizations N_i in Tab. 4.1, we find that the dominant contribution to D^{*+} mesons stems from valence charm quarks, $N_c = 0.179$, as is expected. The total bottom FF, $D_{b+\bar{b}}^{D^{*+}}$ contributes much less, and only a very small, though important, fraction of the gluon momentum is used to produce D^{*+} mesons. See the discussion of pp data below.

In Tab. 4.2 we list the data sets that pass the selection cuts on z and p_T as described in Sec. 4.2.2 above and are thus included in our fit. We show the number of data points that are fitted for each set along with the obtained individual χ^2 values. In addition, we

Table 4.1: Optimum parameters for our NLO FFs $D_i^{D^{*+}}(z,\mu_0)$ for positively charged D^{*+} mesons in the $\overline{\text{MS}}$ scheme at the input scale $\mu_0 = m_c = 1.3\,\text{GeV}$; cf. Eq. (4.13). The bottom FF refers to $\mu_0 = m_b = 4.75\,\text{GeV}$ and $\beta_g = 10$ was kept fixed, see text.

flavor i	N_i	α_i	β_i
c	0.179	7.286	2.495
$b+\bar{b}$	0.084	3.654	6.832
g	0.002	16.269	10

present the analytically obtained optimum normalization shifts $\mathcal{N}_i$ for each data set i. They contribute to the total χ^2 as specified in Eq. (4.21) and according to the quoted experimental normalization uncertainties $\Delta\mathcal{N}_i$; an entry $\mathcal{N}_i = 1$ in Tab. 4.2 indicates that normalization uncertainties are not provided by the experiment. As can be seen, 96 data points from 3 different types of processes, SIA, single-inclusive hadron production, and in-jet fragmentation in pp collisions are included in our global QCD analysis of FFs for D^{*+} mesons, yielding a χ^2 per degree of freedom of 1.17 for our best fit.

The so obtained FFs are shown for two representative scales $\mu^2 = 10\,\text{GeV}^2$ and $\mu^2 = M_Z^2$ in Fig. 4.1 and 4.2, respectively, along with our uncertainty estimates (shaded bands) based on the Hessian method with $\Delta\chi^2 = 4$, see Sec. 4.2.4.

As the gluon and the unfavored light quark contributions turn out to be very small compared to the dominant charm-to-D^{*+} FF, we show them again for the sake of better legibility in the top right panel of Fig. 4.1. Notice that we just show the total $u+\bar{u}$ FF as one example of the unfavored light quark and $\bar{c}$ FFs, which are all the same as they are generated solely by QCD evolution from a vanishing input distribution, see Sec. 4.2.1. This affects also the uncertainty estimates for these FFs which arise, again, just from evolution, i.e., mainly by propagating the uncertainties of the gluon FF. Hence, there is no direct access to the uncertainties of the unfavored light quark and $\bar{c}$ FFs, such that they have to be taken with a grain of salt. Since none of the presently available data sets is sensitive to the unfavored FFs into a D^{*+} meson, in contrast to the also small gluon FF, one is forced to make some assumption about them. In any case, light quarks are expected to fragment mainly into light mesons such as pions and kaons, and their contribution to D^* meson production should be small. Therefore, our choice of a vanishing input distribution for all unfavored FFs appears to be reasonable. We note that a similar assumption was made in the KKKS08 fit [253].

It is instructive to compare the results of our FFs into D^{*+} mesons to those obtained in the KKKS08 fit [253] that is based only on SIA data and includes the by now obsolete and withdrawn BELLE data. The KKKS08 results for $zD_i^{D^{*+}}(z,\mu^2)$ and the ratio to our FFs are shown as dashed lines in Figs. 4.1 and 4.2. As can be seen, one of the main differences is that our fit returns a significantly larger gluon contribution compared to KKKS08 at intermediate values of z which might be related to the fact that also the gluon FF starts from a vanishing input in the KKKS08 fit. However, both the inclusive high-p_T and, in particular, the in-jet fragmentation data, for the first time included in our global analysis, demand a non-zero gluon FF at our input scale in order to arrive at a satisfactory description of the data; see

Table 4.2: Data sets included in our global analysis, the corresponding optimum normalization shifts $\mathcal{N}_i$, and the individual χ^2 including the χ^2 penalty from the determination of the normalization shift if applicable.

experiment		data type	$\mathcal{N}_i$	#data in fit	χ^2
ALEPH [281]		incl.	0.991	17	31.0
OPAL [282]		incl.	1.000	9	6.5
		c tag	1.002	9	8.6
		b tag	1.002	9	5.6
ATLAS [272]		$D^{*\pm}$	1	5	13.8
ALICE [275]	$\sqrt{S} = 7$ TeV	D^{*+}	1.011	3	2.4
ALICE [276]	$\sqrt{S} = 2.76$ TeV	D^{*+}	1.000	1	0.3
CDF [277]		D^{*+}	1.017	2	1.1
LHCb [274]	$2 \leq \eta \leq 2.5$	$D^{*\pm}$	1	5	8.2
	$2.5 \leq \eta \leq 3$	$D^{*\pm}$	1	5	1.6
	$3 \leq \eta \leq 3.5$	$D^{*\pm}$	1	5	6.5
	$3.5 \leq \eta \leq 4$	$D^{*\pm}$	1	1	2.8
ATLAS [40]	$25 \leq \frac{p_T^{\text{jet}}}{\text{GeV}} \leq 30$	(jet $D^{*\pm}$)	1	5	5.5
	$30 \leq \frac{p_T^{\text{jet}}}{\text{GeV}} \leq 40$	(jet $D^{*\pm}$)	1	5	4.1
	$40 \leq \frac{p_T^{\text{jet}}}{\text{GeV}} \leq 50$	(jet $D^{*\pm}$)	1	5	2.4
	$50 \leq \frac{p_T^{\text{jet}}}{\text{GeV}} \leq 60$	(jet $D^{*\pm}$)	1	5	0.9
	$60 \leq \frac{p_T^{\text{jet}}}{\text{GeV}} \leq 70$	(jet $D^{*\pm}$)	1	5	1.6
TOTAL:				96	102.9

also the detailed comparisons to the inclusive and in-jet pp data below. One also notices, that the two valence charm FFs are somewhat shifted in z with respect to each other and that also the height of the peak is different. This is most likely caused by the different sets of SIA data included in our and the KKKS08 analyses. Also, the KKKS08 fit does not include any uncertainty estimates.

Finally, in Fig. 4.2, for $\mu = M_Z$, we also show the bottom-to-D^{*+} FF which starts to evolve from a non-zero input above the threshold $\mu_0 = m_b$, see Sec. 4.2.1. The total $b + \bar{b}$ FF turns out to be quite similar to the one obtained in the KKKS08 analysis. This is to be expected as the bottom FF is largely constrained by the bottom-tagged data of the OPAL collaboration which are included in both fits.

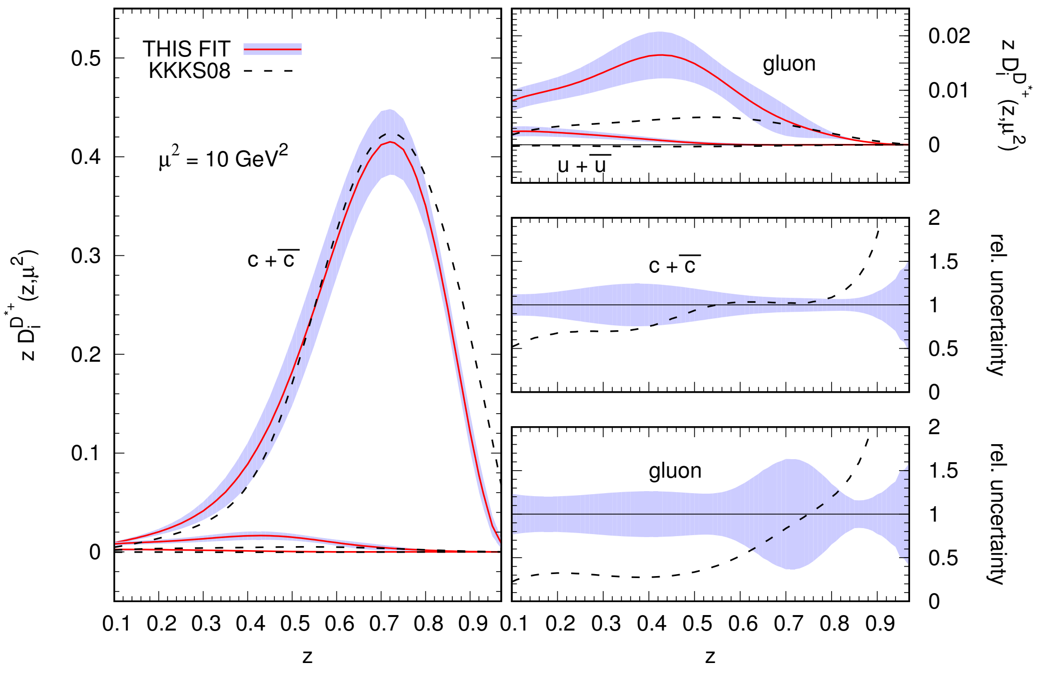

Figure 4.1: Left-hand-side: our FFs $zD_i^{D^{*+}}(z,\mu^2)$ at scale $\mu^2 = 10\,\mathrm{GeV}^2$ (solid lines) along with the obtained uncertainty estimates (shaded bands). The dashed lines refer to the results of KKKS08 fit [253]. Right-hand-side: to make the small gluon and $u + \bar{u}$ FFs better visible, they are shown again in the upper panel. The middle and lower panels give the ratios of our uncertainty estimates (shaded bands) and the KKKS08 fit relative to our best fit for the $c + \bar{c}$ and the gluon FF, respectively.

4.3.2 Detailed Comparison to Data

In this section we compare theoretical calculations based on the results of our global QCD analysis with the available data. Throughout, we shall also show uncertainty bands obtained with the Hessian sets for $\Delta\chi^2 = 4$ as discussed in Sec. 4.2.4. In addition, we perform all calculations with the FFs provided by Ref. [253]. Notice that [253] provides two sets of FFs which differ in the way they include finite charm quark and D^* meson mass effects. Since we work in the ZMVFNS, we choose, as in Figs. 4.1 and 4.2 above, the corresponding KKKS08 set of FFs without quark mass effects in order to arrive at a meaningful comparison with our results. However, according to [253], the KKKS analysis, some kinematic corrections due to the mass of the D^* meson have been retained in all their fits beyond the standard theoretical framework based on factorization, which might be the source of some of the differences we observe at small z.

We start with a study of the inclusive SIA data with identified $D^{*\pm}$ mesons. The upper panel of Fig. 4.3 shows the LEP data at $Q = M_Z$ from the ALEPH [281] and OPAL [282] collaboration along with the theory calculations for the SIA multiplicities at NLO accuracy as defined in Eq. (6.1). The solid and dashed lines are obtained with our best fit, labeled as

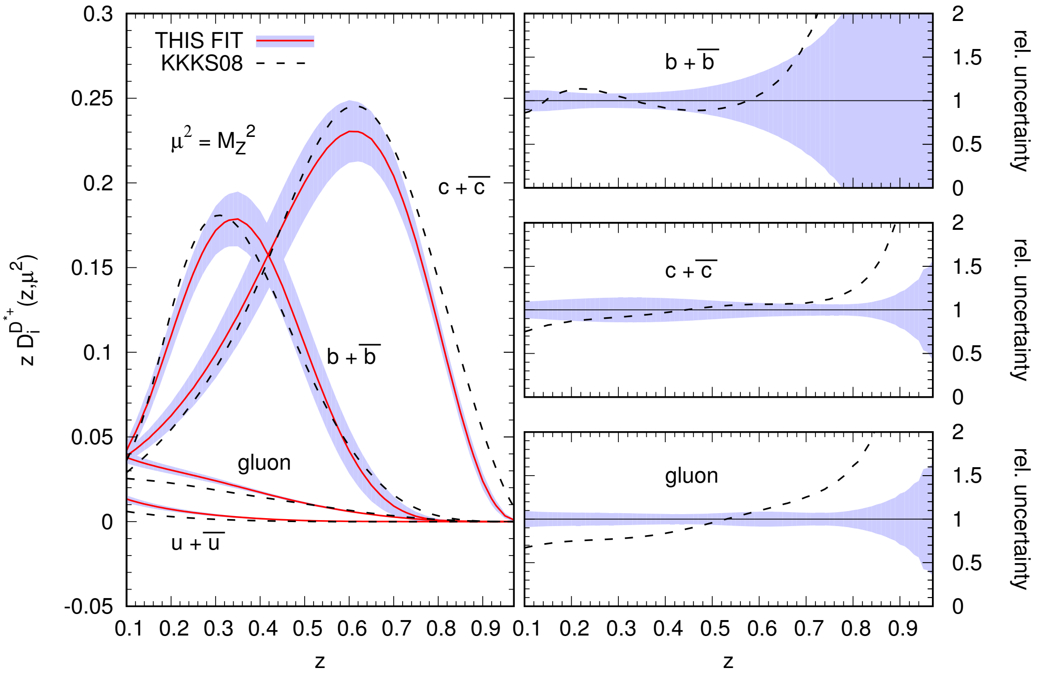

Figure 4.2: Similar to Fig. 4.1 but now for $\mu^2 = M_Z^2$ and including the total bottom FF. Here, the upper right panel shows the relative uncertainties and comparison to KKKS08 for the total $b + \bar{b}$ FF.

"THIS FIT" throughout this section, and the FFs of KKKS08. The ratio of data over theory, our relative uncertainty estimates, and the ratio between KKKS08 and our best fit are given in the lower panel of Fig. 4.3. The hatched regions with $z < z_{\text{min}} = 0.1$ and $z > 0.95$ are excluded from our fit as discussed in Sec. 4.2.2. The latter cut, which has no impact on the fit and in total only removes a single data point from our analysis, is imposed due to the presence of potentially large logarithms as $z \to 1$, which cannot be properly accounted for in a fixed-order calculation.

As can be already anticipated from the individual χ^2 values listed in Tab. 6.3, we find that our fit describes the inclusive SIA data very well, and our Hessian uncertainty estimates reflect the experimental uncertainties except for the data points with the lowest value of z in each data set. Both sets of FFs describe the data equally well in the intermediate z-region. Towards larger values of z, the KKKS08 FFs overshoot the LEP SIA data significantly, which might be related to some tension with the CLEO and the by now withdrawn BELLE data, that are both included in their fit. In the small-z region around our cut z_{min}, the KKKS08 fit agrees slightly better with the data which might indicate some signs of a breakdown of the massless framework which we pursue in our analysis. In addition, we note, that the fixed-order evolution of FFs becomes more and more unstable towards smaller values of z, see e.g. [116]. Eventually, this can result in unphysical negative values for the FFs and the cross sections. The onset of this pathological behavior depends of the fit parameters and might, in part, also be responsible for the KKKS08 results to start to drop. At smaller values of z than shown in Fig. 4.3, well below our cut z_{min}, even our, still rising SIA multiplicity

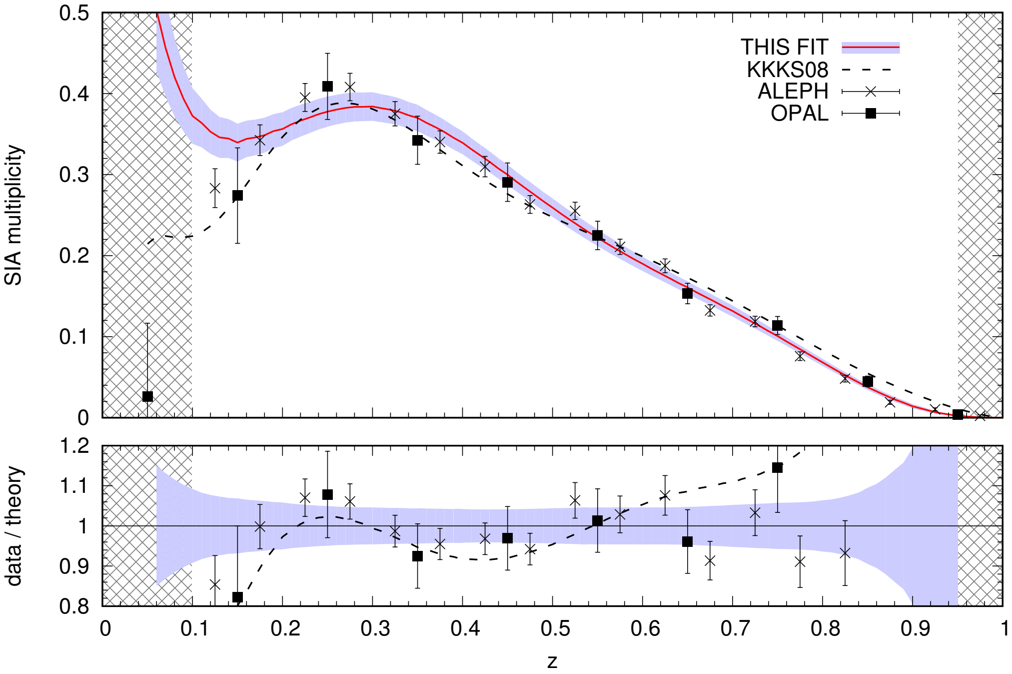

Figure 4.3: The SIA multiplicity data from LEP [281, 282] at $Q = M_Z$ are shown together with theory calculations using our best fit (solid lines) and FFs of KKKS08 (dashed lines). The shaded bands refer to our uncertainty estimates and the hatched areas are excluded from the fit, see text.

will start to drop and eventually reach unphysical, negative values.

In Fig. 4.4, we show the charm and bottom flavor-tagged data from OPAL [282] which are normalized to the total hadronic cross section. The bottom-tagged data are particularly instrumental in constraining the total bottom-to-D^{*+} FF in both our and the KKKS08 fit. As can be seen, both theoretical results describe the flavor-tagged data equally well, which have rather large uncertainties compared to the inclusive results shown in Fig. 4.3.

Following the order of processes as discussed in Sec. 4.1, we next consider the single-inclusive, high-p_T production of D^* mesons in hadronic collisions. Since we are working in the ZMVFNS, we are especially interested in data where the observed D^* meson has a transverse momentum p_T much larger than the charm quark or the D^* meson mass, i.e., $p_T \gg m_{D^*} \sim m_c \approx 2\,\text{GeV}$. As discussed in Sec. 4.2.2, we employ a rather stringent cut of $p_T > 10\,\text{GeV}$ in our global analysis. However, we will demonstrate that the so obtained FFs work unexpectedly well in describing single-inclusive D^* meson cross sections down to much smaller values of p_T around 5 GeV.

In this respect, the most relevant data set is the one presented by the ATLAS collaboration [272], shown in Fig. 4.5, which covers the range $3.5\,\text{GeV} < p_T < 100\,\text{GeV}$ at a pp c.m.s. energy of $\sqrt{S} = 7\,\text{TeV}$ integrated over the mid rapidity range $|\eta| < 2.1$. In the upper panel, a comparison of the ATLAS data with calculations at NLO accuracy is presented based on our best fit and KKKS08 $D^{*\pm}$ FFs and using Eq. (4.5); again, data in the hatched area, i.e., below our cut $p_T^{\text{min}} = 10\,\text{GeV}$, data are not included in our global analysis. The middle panel

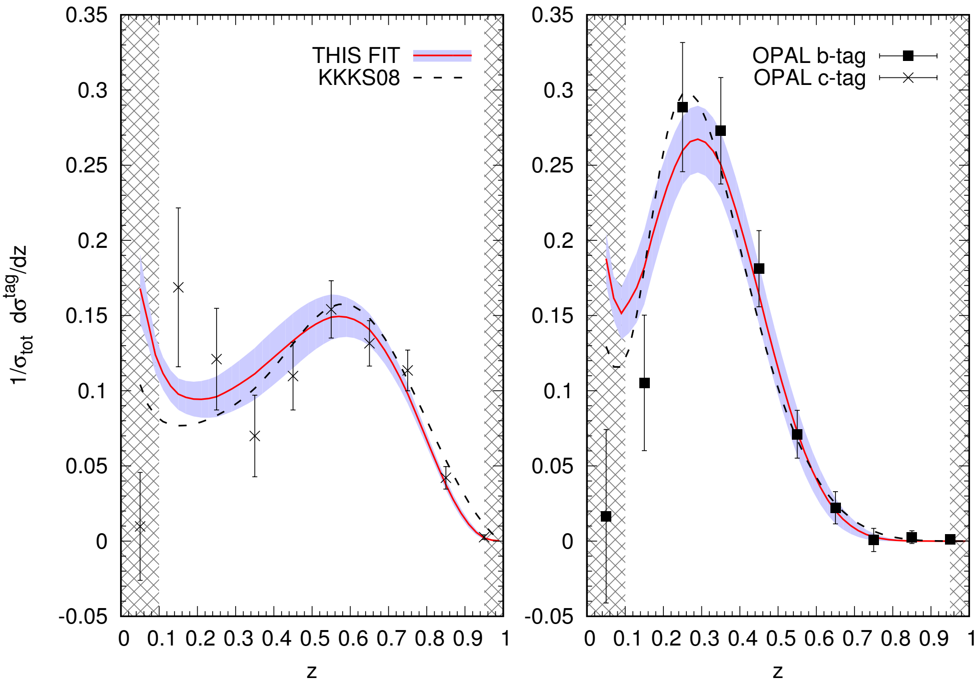

Figure 4.4: Charm (left panel) and bottom (right panel) tagged SIA multiplicities for charged $D^{*\pm}$ mesons from OPAL [282] at $Q = M_Z$ compared with theory calculations at NLO accuracy using our best fit (solid lines) and the KKKS08 FFs (dashed lines). The shaded bands refer to our uncertainty estimates based on the Hessian method. The hatched areas are excluded from our fit.

gives the ratios of the KKKS08 prediction and the ATLAS data with respect to our NLO calculation. In addition, it illustrates the uncertainty estimates (shaded bands) obtained from our Hessian sets of $D^{*\pm}$ FFs.

Both sets of FFs provide a satisfactory description of the data at NLO accuracy in the ZMVFNS even well below $p_T = 10\,\text{GeV}$. About 50% of the $D^{*\pm}$ mesons at $p_T \simeq 10\,\text{GeV}$ originate from gluon fragmentation which drops down to approximately 40% at the highest p_T measured by ATLAS. In view of the sizable differences between our and the KKKS08 gluon FF illustrated in Figs. 4.1 and 4.2, the similarity of the NLO cross sections is a remarkable result and indicates that the inclusive p_T spectra only constrain certain z-moments of the gluon FF rather than its detailed z shape. The differences between the two sets of FFs in Figs. 4.1 and 4.2, in particular, the gluon FF, will be much more pronounced when we turn to the in-jet fragmentation data below.

In the lower panel of Fig. 4.5, we show other important sources of theoretical uncertainties associated with a pQCD calculation of pp cross sections based on, e.g., Eq. (4.5). The outer shaded bands illustrates the ambiguities due to simultaneous variations of the factorization and renormalization scales in the range $p_T/2 < \mu < 2p_T$. As can be seen, in the p_T range used in our fit, this results in a roughly constant relative uncertainty of about 10%. The theoretical error related to PDF uncertainties are estimated with the Hessian sets provided by the CT14 collaboration [140]. They turn out to be smaller than QCD scale uncertainties

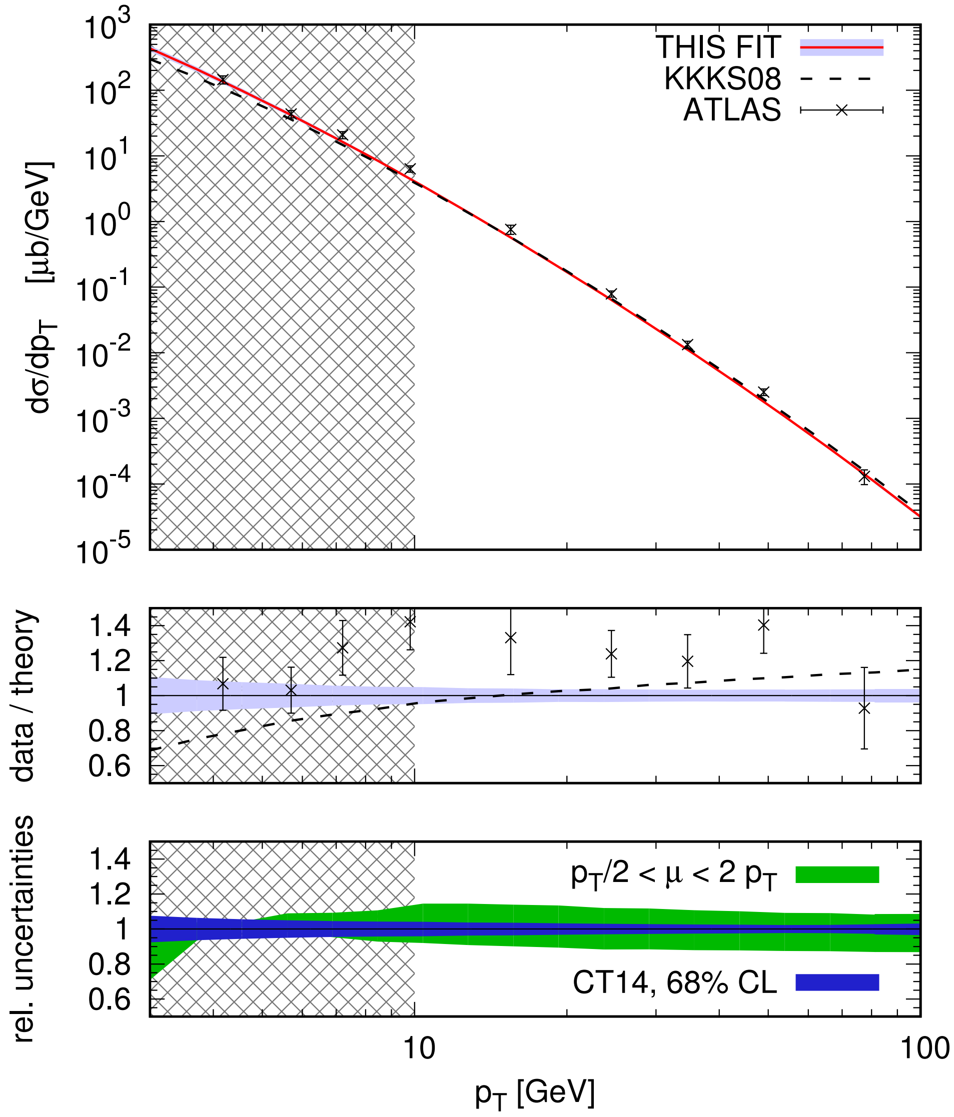

Figure 4.5: Upper panel: our NLO result (solid line) for the single-inclusive, high-p_T cross section for $D^{*\pm}$ meson production in pp collisions at $\sqrt{S} = 7\,\text{TeV}$ and integrated over rapidity $|\eta| < 2.1$ compared to data from the ATLAS collaboration [272] and a calculation using the KKKS08 FFs (dashed line). The middle panel shows the corresponding ratios to our result. The shaded bands refer to our uncertainty estimates based on the Hessian method. The lower panel illustrates relative theoretical uncertainties due to variations of the scale μ in Eq. (4.5) (outer shaded band) and the error estimate of the CT14 PDFs (inner shaded band) which we have rescaled to 68% C.L., see text. The hatched areas are excluded due to the cut $p_T > 10\,\text{GeV}$ imposed on our fit.

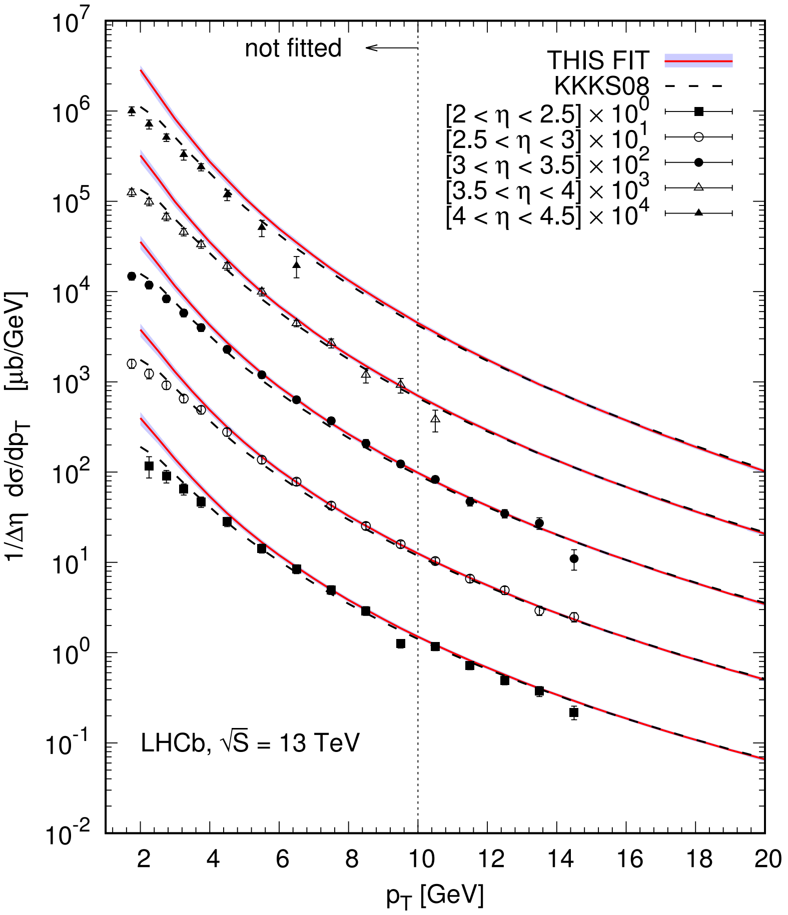

Figure 4.6: The p_T-spectra of $D^{*\pm}$ mesons at $\sqrt{S} = 13$ TeV for five different bins in rapidity, normalized to the width $\Delta\eta$ of each rapidity bin, as measured by LHCb [274]. To better delineate the data, each rapidity bin was multiplied with an increasing power of 10. The NLO calculations using our best fit and the KKKS08 FFs are shown as solid and dashed lines, respectively. As before, the shaded bands refer to our uncertainty estimates, and data below $p_T^{\min} = 10\,\text{GeV}$ are excluded from out fit.

and are at a level of about 5% as can be inferred from the inner shaded bands in the lower panel of Fig. 4.5. To be compatible with our estimates of the one-sigma uncertainties of the $D^{*\pm}$ FFs we follow Ref. [295] and rescale the available CT14 Hessian sets from the 90% to the 68% confidence level by a applying constant factor 1/1.645.

A large amount of data points for inclusive $D^{*\pm}$-meson production have been presented by the LHCb collaboration. They measured the single-inclusive $D^{*\pm}$ production cross section at forward rapidities η for two different c.m.s. energies, $\sqrt{S} = 7$ TeV [273] and 13 TeV [274]. For each c.m.s. energy, the data are presented in five bins of rapidity in the range from $\eta = 2$ up to $\eta = 4.5$. Compared to the mid rapidity data shown in Fig. 4.5, the LHCb data are limited to smaller values of p_T. Nevertheless, several data points from the $\sqrt{S} = 13\,\text{TeV}$ run [274]

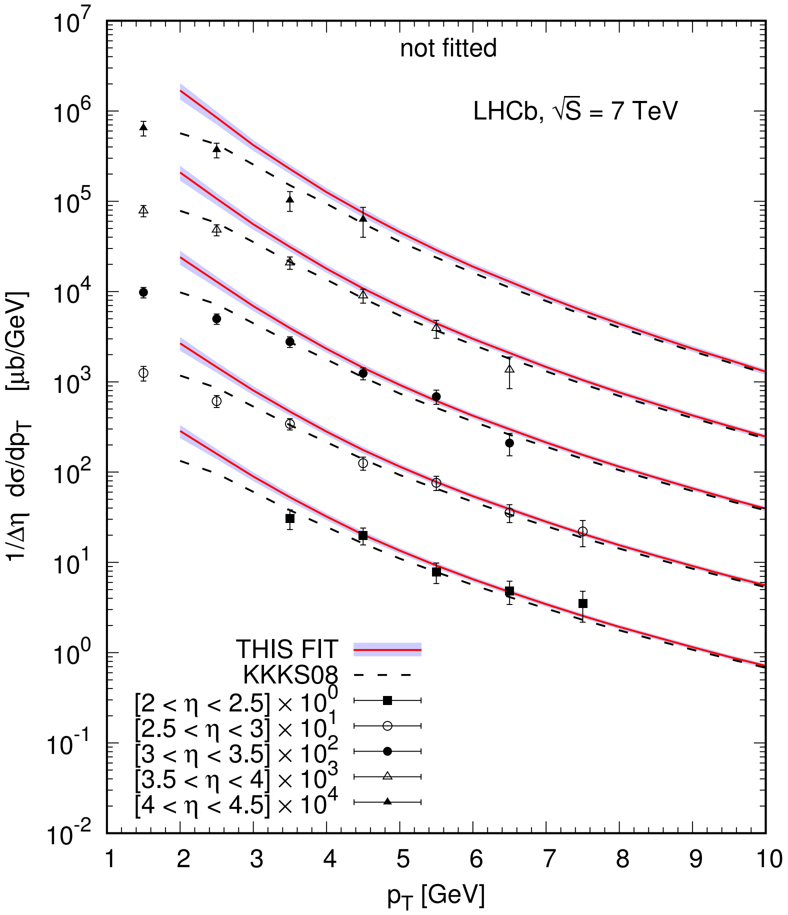

Figure 4.7: Same as Fig. 4.6 but now for $\sqrt{S} = 7$ TeV. Note, that all data points are below our cut on p_T.

are above our cut $p_T^{\text{min}} = 10\,\text{GeV}$ except for the most forward rapidity bin $4 < \eta < 4.5$ but, unfortunately, none of the data points taken at $\sqrt{S} = 7\,\text{TeV}$ [273] passes the cut. Both sets of data are shown in Figs. 4.6 and 4.7 and compared to the results of NLO calculations based on our and the KKKS08 set of FFs. We note that the more forward the rapidity interval, the more important is the role of gluon fragmentation in producing the observed $D^{*\pm}$ mesons, a feature that has already been observed for the production of lighter hadrons at the LHC [278]. For instance, at $\sqrt{S} = 7\,\text{TeV}$ around 80% of the $D^{*\pm}$ mesons at $p_T \simeq 5\,\text{GeV}$ originate from gluons. Since forward data also sample on average larger values of z [278], the LHCb data nicely complement the mid rapidity data by ATLAS.

As for the ATLAS data, both sets of FFs also give an equally good description of the LHCb data shown in Fig. 4.6 for $p_T > p_T^{\text{min}}$, as can be also inferred from Tab. 6.3, and they continue to follow the data well below our cut, down to about 5 GeV. Also the data taken at $\sqrt{S} = 7\,\text{TeV}$, that are not included in our fit, are well described down to $p_T \simeq 5\,\text{GeV}$ except for the most forward bin $4 < \eta < 4.5$. The KKKS08 FFs follow the trend of the data even further down to the lowest p_T values shown in Figs. 4.6 and 4.7; for the sake of applicability of pQCD, we refrain from showing comparisons to the LHCb data below $p_T = 2\,\text{GeV}$. This feature of the KKKS08 fit, which is unexpected in a ZMVFNS approach, might be due to the inclusion of finite hadron mass corrections in their fit of SIA data, that are, however, beyond the factorized framework outlined in Sec. 4.1 and adopted by us. It is also interesting to notice that there are some indications for a mild tension between the ATLAS and the LHCb data in our global fit. The ATLAS data alone would prefer a somewhat larger gluon-to-D^{*+} meson FF as can be inferred from the middle panel of Fig. 4.5. This would yield a significantly better fit of the ATLAS data in terms of χ^2 even when the in-jet fragmentation data, which we shall discuss next, are included in the fit. The latest, revised version of the LHCb data [274] does not tolerate, however, such an increased gluon FF in our global analysis.

We refrain from showing comparisons of our theoretical results with the ALICE and CDF data on single-inclusive, high-p_T D^{*+} meson production. As can be seen from Tab. 4.2, the few data points which pass our cut on p_T are very well reproduced by our fit. Again, adopting the KKKS08 set of FFs leads to a similar description of these data, assuming $D_i^{D^{*+}} = D_i^{D^{*\pm}}/2$.

Finally, we turn to data on in-jet production, which, in this paper, are considered for the first time in a global QCD analysis of FFs and, hence, represent the centerpiece of our phenomenological studies. The relevant QCD formalism to compute in-jet production in the standard factorized framework at NLO accuracy was sketched in Sec. 4.1.3. The main and novel asset of this process, as compared to single-inclusive hadron production in *pp* collisions, is the fact that in-jet data probe the parton-to-hadron FFs *locally* in the momentum fraction z in the LO approximation. Therefore, one anticipates a much improved sensitivity to the, in particular, z-dependence of the gluon FF also beyond LO accuracy than from single-inclusive probes. In the latter case, we have just found that two rather different gluon FFs, ours and the one from the KKKS08 fit, can result both in a good description of the existing data, cf. Figs. 4.5 and 4.6 above.

Specifically, for the in-jet production of $D^{*\pm}$ mesons, it was found in Ref. [264] that the cross section computed with the KKKS08 set of FFs falls significantly short of the corresponding yields observed by ATLAS [40]. The authors of Ref. [264] observed that by increasing the KKKS08 gluon FFs ad hoc by a z-independent factor of 2 would help to better describe the ATLAS data. However, such a modified gluon FF would then significantly overshoot the single-inclusive *pp* data for D^*-mesons. Clearly, to address this issue reliably and in detail, a simultaneous global QCD analysis of all relevant probes comprising SIA, and single-inclusive and in-jet production in proton-proton collisions is absolutely essential.

From Fig. 4.8 and Tab. 6.3 one can gather that our global fit yields an excellent description of the in-jet data by ATLAS in all five bins of the jet's transverse momentum without compromising the comparison to SIA or single-inclusive *pp* data. A corresponding calculation with the KKKS08 set of FFs falls short of the data for momentum fractions $z_h \lesssim 0.6$ of the $D^{*\pm}$ meson, as was already observed in Ref. [264]. In fact, the z-dependence of the NLO calculations with the two different sets of FFs very closely follow the corresponding dependence of the gluon-to-$D^{*\pm}$ FF illustrated for two different scales in Figs. 4.1 and 4.2. The main difference between our analysis and the KKKS08 extraction of FFs is that we allow for a non-zero gluon FF at our initial scale which appears to be necessary in order to achieve a good global fit of all data; recall that the KKKS08 analysis was based only on SIA data where some assumption about the gluon FF has to be made. The quark FFs, in particular,

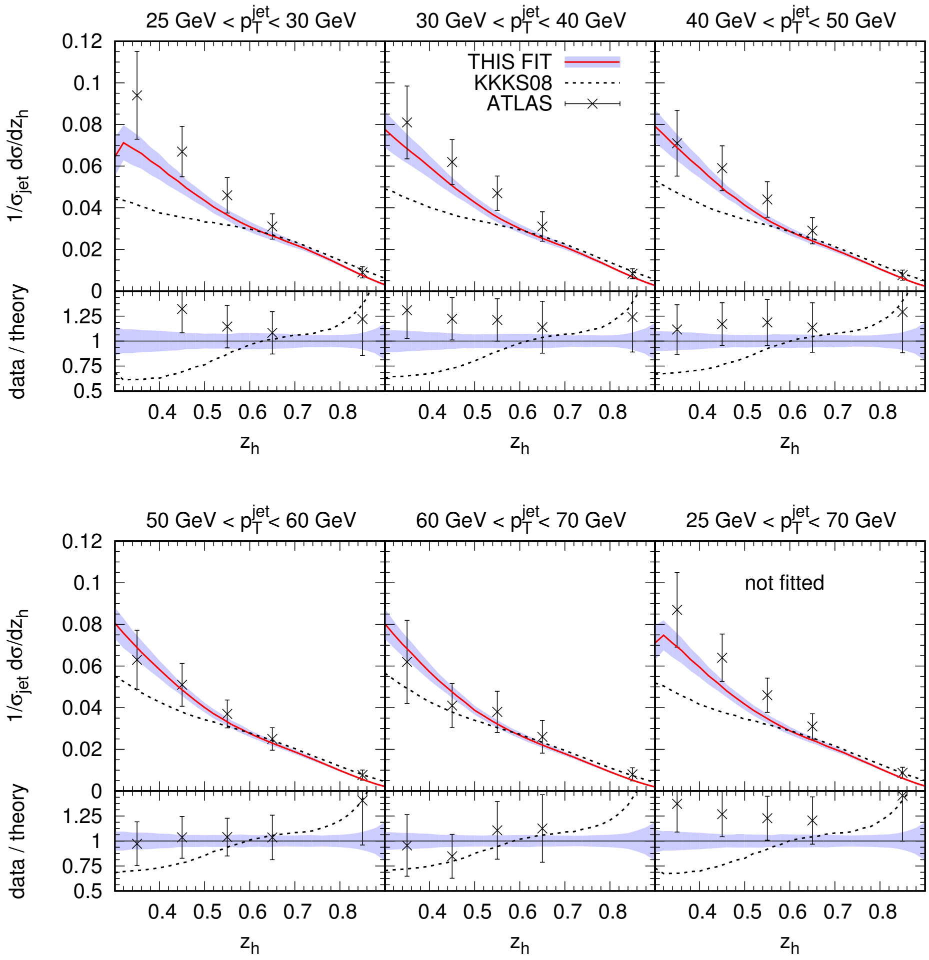

Figure 4.8: Data on in-jet-fragmentation into $D^{*\pm}$ mesons measured at $\sqrt{S} = 7$ TeV as a function of the momentum fraction z_h in five bins of p_T^{jet} integrated over rapidity $|\eta^{\text{jet}}| < 2.5$ as provided by ATLAS [40]. The combination of all p_T^{jet} bins (lower right) is only shown for comparison and is not included in our fit to avoid double-counting. In each panel, NLO results obtained with our best fit (solid lines) and the KKKS08 (dashed lines) FFs are shown. The shaded bands refer to uncertainty estimates based on our Hessian uncertainty sets. In the lower panels of each plot, the ratio of the data and the KKKS08 prediction with respect to our NLO result are given.

the charm FF, adjust accordingly in the fit but play only a very minor role in computations of pp cross sections in the p_T range currently covered by experiment. Finally, we note that theoretical uncertainties due to the choice of scale μ and from ambiguities in the adopted set of PDFs are of similar size as we have estimated for the single-inclusive data; cf. the lower panel of Fig. 4.5 and Ref. [197].

Our case study of $D^{*\pm}$ clearly reveals how powerful in-jet data can be in further constraining

FFs. Based on the framework developed and applied in this paper, in-jet data can be straightforwardly included in any future global fit of FFs once such data become available.

4.4 Conclusions and Outlook

We have presented the first global QCD analysis of fragmentation functions that makes use of in-jet data besides the usual sets of experimental results stemming from single-inclusive hadron production in electron-positron annihilation and proton-(anti)proton collisions. The necessary technical framework to incorporate in-jet fragmentation data consistently into a global fit at next-to-leading order accuracy was outlined in detail, and an implementation within the Mellin moment technique was given and henceforth adopted in all our phenomenological studies.

As a case study, we have analyzed available data for charged D^* mesons in terms of parton-to-D^{*+} meson fragmentation functions. An excellent global description of all the different processes included in the fit was achieved. In particular, the in-jet fragmentation data have been shown to be of great importance in pinning down the otherwise largely unconstrained momentum fraction dependence of the gluon fragmentation function. Compared to the only other previously available set of $D^{*\pm}$ fragmentation functions, that was based solely on electron-positron annihilation data, we obtain a rather different momentum dependence for the hadronization of gluons in order to describe the in-jet data.

In addition to our optimum fit, we have also, for the first time, estimated the uncertainties of charged D^* meson fragmentation functions. To this end, we have applied the Hessian method. The obtained Hessian sets provide a straightforward way to propagate our estimated uncertainties to any other process of interest. Apart from the experimental uncertainties that are incorporated in the Hessian sets, we have illustrated the importance of other, theoretical sources of ambiguities comprising the actual choice of renormalization and factorization scales and corresponding uncertainties of parton distribution functions which are needed in calculations of any hadronic collision process.

For the time being, we have adopted the ZMVFNS throughout our global analysis, i.e., we have imposed rather stringent cuts on the minimum transverse momentum of the D^* mesons for data to be included in our fit. We have demonstrated, however, that our fit gives a reasonable description of single-inclusive data from the LHC both at mid and forward rapidities even down to significantly smaller values of transverse momentum of about 5 GeV.

We believe that in-jet data will prove very valuable in the future in any upcoming analysis of fragmentation functions, in particular, in further constraining the detailed momentum dependence of the hadronization of gluons. The framework developed and applied in this chapter can be straightforwardly generalized to incorporate in-jet data in any future global fit of FFs once such data become available. We plan to extend our phenomenological studies to charged and neutral D mesons in the near future. Moreover, we plan to study in detail the impact of the resummation of logarithms of the jet size parameter R. By making use of the results for the in-jet fragmentation of hadrons derived within the SCET formalism, it is possible to extract fragmentation functions at a combined accuracy of NLO+$\mathrm{NLL_R}$.

Finally, we recall that fragmentation into photons is so far only rather poorly understood and constrained by data; see Sec. 1.3.4 for further details. Since we expect any upcoming photon-in-jet data to be very valuable in a new extraction of photon fragmentation functions, we extend the theoretical framework for the in-jet production of hadrons at next-to-leading order accuracy to include also photons in the next chapter, where we study the process $pp \to (\text{jet}\,\gamma)\,X$ in detail.

Chapter 5

Access to Photon FFs in Hadronic Jet Production

In this chapter, which is based on our publication [148], we argue that the process $pp \to (\text{jet}\gamma)X$, for which a photon is observed inside a fully reconstructed jet and is treated as part of the jet, offers new probes of the so far little known fragmentation functions for photons. We present a next-to-leading-order QCD calculation of the cross section for this process in the limit that the jet is relatively narrow. We also investigate the background resulting from the two-photon decay of neutral pions. We present numerical results relevant for possible measurements at the LHC and at RHIC. These suggest that $pp \to (\text{jet}\gamma)X$ should provide clean access to the photon fragmentation functions, provided an efficient suppression of the background is available in experiment.

The production of photons with high transverse momentum p_T in hadronic collisions is of fundamental importance in today's particle and nuclear physics. Foremost, it may serve as a tool for determining the gluon distributions of the scattering hadrons, thanks to the presence and dominance of the leading order (LO) Compton subprocess $qg \to \gamma q$. Photons also provide sensitive probes of the medium produced in collisions of heavy ions, being able to traverse and escape the medium with little attenuation. Finally, photon signals play an important role in studies of physics within and beyond the Standard Model, with the process $pp \to \gamma\gamma X$ through production and decay of a Higgs boson and the recent indication of a 750 GeV diphoton excess seen by the ATLAS [296] and CMS [297] collaborations at the LHC arguably being among the most well-known examples. Although the presumed "bump" in the 2015 data disappeared with more statistics in updated 2016 data [298, 299], the enormous interest by the community (hundreds of papers tried to give a possible explanation of this excess) demonstrated once again the importance of photon signals in the search for "new physics" beyond the Standard Model of particle physics.

When used in searches of new physics phenomena, photon "signal" processes are invariably affected by backgrounds from more mundane Standard Model sources. In view of this it is clear that a good quantitative theoretical understanding of photon production in high-energy hadronic collisions is crucial. For photons produced in a process characterized by a large momentum transfer, perturbative-QCD methods may be used.

Using the single-inclusive process $pp \to \gamma X$ as an example, QCD perturbation theory predicts the following schematic structure of the factorized cross section:

$$d\sigma = \sum_{a,b} f_a \otimes f_b \otimes \left[d\hat{\sigma}_{ab}^{\gamma} + \sum_c d\hat{\sigma}_{ab}^{c} \otimes D_c^{\gamma} \right] . \tag{5.1}$$

Here the sums run over all partons (quarks, antiquarks and gluons). The part involving the sum over partons c is the fragmentation component, while the other part is the direct one. Each part has its own partonic hard-scattering cross sections for producing either directly a photon, or a parton c that subsequently fragments into the photon as described by the fragmentation functions $D_c^\gamma \equiv D_c^\gamma(z,\mu)$, where z is the fraction of the parton's momentum picked up by the photon and μ the scale at which the fragmentation function is probed. Further details on photon FFs may be found in Sec. 1.3.4. Both the direct and the fragmentation parts involve parton distribution functions in the proton, denoted by f_a and f_b. The symbols $\otimes$ represent appropriate integrations over momentum fractions of the various participating partons.

Theoretical calculations of photon production cross sections in hadronic collisions thus rely on three ingredients:

(i) knowledge of parton distributions,

(ii) precision calculations of the partonic cross sections, and

(iii) parton-to-photon fragmentation functions.

The parton distribution functions of protons are by now very well known. A lot of work has gone into (ii) over the past three decades. For single-inclusive photon production, full next-to-leading order (NLO) computations of the partonic cross sections for the direct [162, 300–303] as well as for the fragmentation part [91, 198, 304] have been performed, and even all-order resummations of large logarithmic threshold corrections are available for both parts [93, 305–312].

Rather little is known, on the other hand, about the photon fragmentation functions. Some information is available from measurements at LEP [313], but with rather large uncertainties. Theoretical predictions [153–155, 314] for the photon fragmentation functions are compatible with these sparse data. Based on such sets of D_c^γ, one estimates that fragmentation photons contribute about 10-30% to the cross section for $pp \to \gamma X$ in the fixed-target regime [161]. At high-energy colliders, the fragmentation contribution is typically predicted to be only 10% or less [169]. The reason for this is that at colliders one introduces so-called isolation cuts. To isolate a photon candidate, one basically demands that the hadronic energy in a cone around the photon be limited to a certain value. Isolation suppresses the large background from $\pi^0 \to \gamma\gamma$ decay and also reduces the fragmentation contribution [169] since it basically confines it to very high values of the fragmentation variable z; see Sec. 1.3.4 for further information.

At any rate, the size of the fragmentation contribution arguably presents the largest uncertainty in predictions of photon production cross sections. In the present chapter, we propose a new promising method to experimentally access the D_c^γ in hadronic collisions. The idea is to identify a photon as part of a fully reconstructed jet. One measures the transverse momenta of the photon and the jet, p_T and p_T^{jet}, respectively. As we shall show, their ratio,

$$z_\gamma \equiv \frac{p_T}{p_T^{\text{jet}}}\,, \tag{5.2}$$

offers direct scans of the fragmentation functions $D_c^\gamma(z,\mu)$ in z. This is an advantage over the inclusive cross section $pp \to \gamma X$, which may also provide information on the photon fragmentation functions [160] but typically samples them over a broad region in z. This is similar to the discussion for the hadronic case, c.f. text below Eq. 3.1. We develop the formalism for the "same-side" photon-jet observable to NLO accuracy. Using the approximation of relatively narrow reconstructed jets, we are able to derive analytical results for the relevant NLO cross sections. In Chap. 3 (see also [37, 38, 197, 204, 264] for related work), we have already presented the corresponding NLO calculation for the process $pp \to (\text{jet}\, h)\, X$, where h denotes an identified hadron inside the jet, and demonstrated that this process opens a promising window on the determination of the parton-to-hadron fragmentation functions D_c^h. In the manner of speaking, we stepped through this promising window in Chap. 4 and used this process in an extraction of D^*-meson FFs. Indeed, we found that $pp \to (\text{jet}\, h)\, X$ helps in better understanding the FFs by adding complementary and new information compared to the traditionally used processes. Evidently, the background from $\pi^0 \to \gamma\gamma$ decay mentioned above will also be relevant in our case and hence will also be analyzed in this chapter.

We stress that the observable we have in mind is different from the "away-side" photon-jet correlations considered in Ref. [315] and provides a kinematically simpler and more direct access to the D_c^γ. In particular, in our case it is natural to divide the cross section for $pp \to (\text{jet}\gamma)X$ by the single-inclusive jet one for $pp \to \text{jet}X$, in which case many theoretical uncertainties related to the choice of parton distributions or (initial-state) factorization scale will cancel out. We also note that same-side photon-jet observables have been studied in the contexts of e^+e^- annihilation [230, 314] and ep collisions [316], where they were shown to provide access to the D_q^γ. However, the accuracy achievable in experiment is rather limited for these reactions, as the LEP results [313] show. More importantly, a drawback of these processes is that the gluon-to-photon fragmentation function can be probed only indirectly by evolution or higher-order corrections. This is different for the process $pp \to (\text{jet}\, \gamma)\, X$ which probes all photon fragmentation functions in the same hadronic environment as relevant for photon signals at colliders.

This chapter is organized as follows. In Sec. 5.1 we present our NLO calculation of $pp \to (\text{jet}\gamma)X$. We shall see that the results can be formulated in terms of simple photonic jet functions. Section 5.2 describes calculations of the pion decay background, taking into account basic experimental considerations concerning pion reconstruction. In Sec. 5.3 we present phenomenological results for $pp \to (\text{jet}\gamma)X$ relevant for collisions at RHIC and the LHC. Moreover, we demonstrate the potential of this process for providing valuable new information on parton-to-photon FFs in Sec. 5.4.

5.1 Same-side Jet-plus-Photon Production at NLO

We consider a high-p_T photon produced inside a jet. Our approach will be to consider the photon as part of the jet. To this end, we follow Ref. [230, 314] to cluster hadrons and photons "democratically" into mixed hadronic and electromagnetic jets, a procedure that may be applied to any of the commonly used jet algorithms [33, 34, 189–191, 194, 317]. In terms of a pQCD calculation it means that the photon is included as an additional parton. At lowest order in QCD, for $z_\gamma < 1$, there are only fragmentation contributions to the cross section for $pp \to (\text{jet}\, \gamma)\, X$. It is this feature that makes the cross section a powerful probe of the photon fragmentation functions. Our strategy for performing the NLO calculation is based on the techniques developed in Chap. 3 for the process $pp \to (\text{jet}\, h)\, X$. A key element of that study was the "narrow jet approximation (NJA)" [174] (see also Chap. 2 and

Ref. [318]), which assumes that the parameter $\mathcal{R}$ specifying the jet "opening" is relatively small. This allows for an analytical calculation of the NLO partonic cross sections. The NJA is accurate up to corrections of order $\mathcal{R}^2$. As was shown in Refs. [174], this is sufficient for essentially all jet opening parameters used in experiment.

In the language of Chap. 3, the NLO factorized cross section for $pp \to (\mathrm{jet}\,\gamma)\,X$ may be written as

$$\begin{aligned}\frac{d\sigma^{pp\to(\mathrm{jet}\,\gamma)X}}{dp_T^{\mathrm{jet}}\,d\eta^{\mathrm{jet}}dz_\gamma} &= \sum_{\substack{a,b,c\in\\ \{q,\bar{q},g,\gamma\}}} \int_{x_a^{\min}}^1 dx_a\, f_a(x_a,\mu_F) \int_{x_b^{\min}}^1 dx_b\, f_b(x_b,\mu_F) \\ &\times \int_{z_c^{\min}}^1 dz_c\, \frac{d\hat{\sigma}_{ab}^c(\hat{s},\hat{p}_T,\hat{\eta},\mu_F,\mu'_F,\mu_R)}{dp_T^{\mathrm{jet}}\,d\eta^{\mathrm{jet}}} \sum_{\substack{d\in\\ \{q,\bar{q},g,\gamma\}}} j_{c\to d}\left(z_c, \frac{\mathcal{R}\,p_T^{\mathrm{jet}}}{\mu'_F}\right) \\ &\times \sum_{\substack{c'\in\\ \{q,\bar{q},g,\gamma\}}} \int_{z_\gamma}^1 \frac{dz_p}{z_p}\, \tilde{j}_{d\to c'}\left(z_p, \frac{\mathcal{R}\,p_T^{\mathrm{jet}}}{\mu''_F}\right) \mathcal{D}_{c'}^{\gamma}\left(\frac{z_\gamma}{z_p},\mu''_F\right). \qquad (5.3)\end{aligned}$$

Apart from the variable z_γ defined in (5.2) the cross section is specified by the jet's transverse momentum p_T^{jet} and rapidity η^{jet}, the latter being equal to the photon rapidity η in the NJA. In Eq. (5.3) we have furthermore defined

$$\begin{aligned} x_a^{\min} &= \frac{p_T^{\mathrm{jet}}\mathrm{e}^{\eta^{\mathrm{jet}}}}{\sqrt{S}-p_T^{\mathrm{jet}}\mathrm{e}^{-\eta^{\mathrm{jet}}}}\,, \\ x_b^{\min} &= \frac{x_a p_T^{\mathrm{jet}}\mathrm{e}^{-\eta^{\mathrm{jet}}}}{x_a\sqrt{S}-p_T^{\mathrm{jet}}\mathrm{e}^{\eta^{\mathrm{jet}}}}\,, \\ z_c^{\min} &= \frac{p_T^{\mathrm{jet}}}{\sqrt{S}}\left(\frac{\mathrm{e}^{\eta^{\mathrm{jet}}}}{x_a}+\frac{\mathrm{e}^{-\eta^{\mathrm{jet}}}}{x_b}\right), \qquad (5.4)\end{aligned}$$

where $\sqrt{S}$ is the hadronic c.m.s. energy. The various partonic variables are $\hat{s}=x_a x_b S$, $\hat{p}_T = p_T^{\mathrm{jet}}/z_c$, $\hat{\eta}=\eta^{\mathrm{jet}}-\frac{1}{2}\log(x_a/x_b)$.

Equation (5.3) has been written in such a way that it includes both the direct and the fragmentation contributions. This is achieved by introducing the function

$$\mathcal{D}_{c'}^{\gamma}(z,\mu) \equiv \delta(1-z)\delta_{c'\gamma} + D_{c'}^{\gamma}(z,\mu)\,(1-\delta_{c'\gamma})\,, \qquad (5.5)$$

where the first part corresponds to the direct contribution and the second part to the fragmentation one. The partonic cross sections $d\hat{\sigma}_{ab}^c$ (with $c=\gamma,q,\bar{q},g$) in (5.3) are the usual NLO *single-inclusive photon/parton cross sections* as computed in Refs. [162, 300–303] and [91, 198, 304], respectively. Their perturbative expansions to NLO, but to lowest order in the electromagnetic coupling α, read

$$\begin{aligned} d\hat{\sigma}_{ab}^{\gamma} &= \alpha\alpha_s\left[d\hat{\sigma}_{ab}^{\gamma,(0)} + \frac{\alpha_s}{\pi}d\hat{\sigma}_{ab}^{\gamma,(1)} + \mathcal{O}(\alpha_s^2)\right], \\ d\hat{\sigma}_{ab}^{c\neq\gamma} &= \alpha_s^2\left[d\hat{\sigma}_{ab}^{c,(0)} + \frac{\alpha_s}{\pi}d\hat{\sigma}_{ab}^{c,(1)} + \mathcal{O}(\alpha_s^2)\right]. \qquad (5.6)\end{aligned}$$

Evidently, in order to compute the cross section for production of photons inside a jet, one needs corresponding partonic cross sections for this observable. These necessarily differ from the single-inclusive cross sections $d\hat{\sigma}^{\gamma}_{ab}, d\hat{\sigma}^{c}_{ab}$. As was shown in Chap. 3, it is relatively straightforward to convert the $d\hat{\sigma}^{\gamma}_{ab}, d\hat{\sigma}^{c}_{ab}$ into the cross sections that we need for same-side photon (or hadron) plus jet production. This is achieved by introducing suitable perturbative jet functions $j_{c\to d}$ and $\tilde{j}_{d\to c'}$. The former describe the formation of a jet "consisting" of parton d which has taken the fraction z_c of the parent parton's momentum, while the latter represent the "partonic fragmentation" of parton d to parton c' inside the jet, with momentum fraction z_p.

Before discussing the jet functions in more detail, we note that we have introduced several scales in Eq. (5.3): The renormalization scale μ_R, the initial-state factorization scale μ_F and two final-state factorization scales μ'_F and μ''_F, respectively. Of the latter two, μ'_F is an artifact of the way we organize our calculation, formulating the cross section in terms of *single-inclusive* parton cross sections. μ'_F was originally introduced in the mass factorization procedure for the $d\hat{\sigma}^{c}_{ab}$. Now, however, it cancels exactly between the $d\hat{\sigma}^{c}_{ab}$ and the jet functions $j_{c\to d}$ due to the fact that we foremost define our observable by requiring an infrared- and collinear safe jet in the final state. Hence, μ'_F is not present in the final result. The actual final-state factorization scale which survives in our final answer is μ''_F. This scale appears because we are asking for an observed photon in the final state as part of the jet. For details, see Chap. 3.

Throughout this chapter (and as anticipated in Eq. (5.6)), we will always work to lowest order $\mathcal{O}(\alpha)$ in the electromagnetic coupling α. This means that the initial partons a, b in Eq. (5.3) will never be photons in our calculations since the requirement that there also is a photon in the final state would make the corresponding contribution to the cross section $\mathcal{O}(\alpha^2)$. This holds true even for the photon fragmentation part since the fragmentation functions D^{γ}_{c} always provide an additional power of α. In order to specify the jet functions, it is therefore sufficient to just consider a fixed initial partonic state ab ($a, b \neq \gamma$) in Eq. (5.3) and disregard the parton distribution functions. Schematically, we then have the expression

$$\sum_{c,d,c'} d\hat{\sigma}^{c}_{ab} \otimes\, j_{c\to d} \otimes \tilde{j}_{d\to c'} \otimes \mathcal{D}^{\gamma}_{c'}\,. \tag{5.7}$$

The labels c, d, c' run over all QCD partons, but can also represent a photon. The jet functions with both $c \neq \gamma$ and $c' \neq \gamma$ contribute only to the fragmentation part. They are identical to those appearing in our calculation in Chap. 3 for hadron production inside jets, where they were given to NLO in Eqs. (3.18) and (3.19). To LO, they are all diagonal, $j_{q\to q} = j_{g\to g} = \delta(1-z_c)$ and $\tilde{j}_{q\to q} = \tilde{j}_{g\to g} = \delta(1-z_p)$. This shows that at this order the cross section for $pp \to (\text{jet}\,\gamma)\,X$ directly probes the photon fragmentation functions at value $z = z_\gamma$.

Starting at NLO, there is also a direct component of the cross section for photon-in-jet production. The corresponding contributions are always associated with either $c = \gamma$ or $c' = \gamma$. Being direct contributions, they always come with the piece $\propto \delta(1-z)$ in $\mathcal{D}^{\gamma}_{c'}$ in (5.5). We now discuss the various possibilities at $\mathcal{O}(\alpha)$:

(i) Case $c = c' = \gamma$: Here the expression in (5.7) becomes

$$\sum_{d} \underbrace{d\hat{\sigma}^{\gamma}_{ab}}_{\mathcal{O}(\alpha\alpha_s)} \otimes j_{\gamma\to d} \otimes \tilde{j}_{d\to\gamma} \otimes \underbrace{\mathcal{D}^{\gamma}_{\gamma}}_{\mathcal{O}(1)}\,. \tag{5.8}$$

As indicated, the partonic cross sections $d\hat{\sigma}^{\gamma}_{ab}$ start at order $\mathcal{O}(\alpha\alpha_s)$ (see Eq. (5.6)). Since all jet functions for $d \neq \gamma$ are of order $\mathcal{O}(\alpha)$, they would give rise to higher-order contributions in α. Hence, only $d = \gamma$ and $j_{\gamma\to\gamma} = \delta(1-z_c)$ and $\tilde{j}_{\gamma\to\gamma} = \delta(1-z_p)$ is possible at $\mathcal{O}(\alpha)$. Thus, this part gives precisely the direct part of the full NLO single-inclusive photon production cross section. However, because of the δ-functions from $\tilde{j}_{\gamma\to\gamma}$ and $\mathcal{D}^{\gamma}_{\gamma}$, the entire piece comes with a factor $\delta(1-z_\gamma)$, as is easily seen by insertion into Eq. (5.3). This in turn implies that for any measurement of the cross section carried out at $z_\gamma < 1$ this part of the cross section will not contribute. We note that the region $z_\gamma \to 1$ could be interesting when isolation cuts are imposed on the photon. In this region we have a photon carrying most of the jet's energy and accompanied by very little hadronic energy. For such studies at very high z_γ it may be preferred to integrate over a range of z_γ that includes the endpoint at $z_\gamma = 1$, in which case the contributions $\propto \delta(1-z_\gamma)$ will need to be kept.

In cases **(ii)** and **(iii)** we have $c = q$ and $c' = \gamma$ so that the expression in (5.7) becomes

$$\sum_d \underbrace{d\hat{\sigma}^{q}_{ab}}_{\mathcal{O}(\alpha_s^2)} \otimes j_{q\to d} \otimes \tilde{j}_{d\to\gamma} \otimes \underbrace{\mathcal{D}^{\gamma}_{\gamma}}_{\mathcal{O}(1)} \,. \tag{5.9}$$

To lowest order in α, we can then either have $d = \gamma$ or $d = q$ in Eq. (5.3). Thus we further distinguish:

(ii) Case $c = q, c' = \gamma, d = \gamma$: We have $\tilde{j}_{\gamma\to\gamma} = \delta(1-z_p)$ and, in the $\overline{\text{MS}}$ scheme,

$$j_{q\to\gamma}(z,\lambda) = -\frac{\alpha}{2\pi} e_q^2 \left[P_{\gamma q}(z) \log\left(\lambda^2 (1-z)^2\right) + z \right], \tag{5.10}$$

where e_q is the quark's fractional charge, and where

$$P_{\gamma q}(z) = \frac{1+(1-z)^2}{z} \,. \tag{5.11}$$

This contribution is again proportional to $\delta(1-z_\gamma)$ and does not contribute to measurements at $z_\gamma < 1$. However, this becomes different in

(iii) case $c = q, c' = \gamma, d = q$, where $j_{q\to q} = \delta(1-z_c)$ and, in the $\overline{\text{MS}}$ scheme and for the anti-k_t jet algorithm:

$$\tilde{j}^{\overline{\text{MS}}}_{q\to\gamma}(z,\lambda) = \frac{\alpha}{2\pi} e_q^2 \left[P_{\gamma q}(z) \log\left(\lambda^2 z^2 (1-z)^2\right) + z \right]. \tag{5.12}$$

The contribution associated with this jet function is, at this order, the *only* direct part of the cross section that is present at $z_\gamma < 1$. It is genuinely NLO, and its logarithmic dependence on the scale μ_F'' correctly compensates the scale dependence associated with the inhomogeneous piece [153–155, 314] in the evolution of the D^{γ}_{c}, c.f. Sec. 1.3.4.

The final possibility is

(iv) case $c = g, c' = \gamma$: Here we need to 'convert' a gluon exiting the hard scattering to an observed photon. This may happen through the combination $j_{g\to q}\,\tilde{j}_{q\to\gamma}$. The product of these functions is $\mathcal{O}(\alpha\alpha_s)$, which, when combined with the α_s^2 from the hard process is an order too high in α_s, that is, beyond NLO. The only contribution for $c = g$ arises when the photon is produced in fragmentation, as discussed above.

The NLO jet functions in the $\overline{\text{MS}}$ scheme are given as follows. First, for the jet functions j we find

$$\begin{aligned}
j_{\gamma\to\gamma}(z,\lambda) &= \delta(1-z)+\mathcal{O}(\alpha)\,,\\
j_{\gamma\to q}(z,\lambda) &= -\frac{\alpha e_q^2}{2\pi}\left[P_{q\gamma}(z)\log\left(\lambda^2(1-z)^2\right)+z(1-z)+\tilde{\mathcal{I}}^{\text{algo}}_{q\gamma}(z)\right]\,,\\
j_{q\to\gamma}(z,\lambda) &= -\frac{\alpha e_q^2}{2\pi}\left[P_{\gamma q}(z)\log\left(\lambda^2(1-z)^2\right)+z+\tilde{\mathcal{I}}^{\text{algo}}_{\gamma q}(z)\right]\,,\\
j_{\gamma\to g}(z,\lambda) &= \mathcal{O}(\alpha\alpha_s)\,,\\
j_{g\to\gamma}(z,\lambda) &= \mathcal{O}(\alpha\alpha_s)\,,\\
j_{(c\neq\gamma)\to(e\neq\gamma)}(z,\lambda) &= \delta(1-z)\delta_{ec}+\frac{\alpha_s}{2\pi}f_{c\to e}(z,\lambda)+\mathcal{O}(\alpha_s^2)+\mathcal{O}(\alpha\alpha_s)\,,
\end{aligned}\tag{5.13}$$

where the functions $\tilde{\mathcal{I}}^{\text{algo}}_{c'c}(z)$ are given in Eq. (3.15). The last line in Eq. (5.13) describes the "pure-QCD" type jet functions without any photonic contributions. They are shown only for the sake of completeness and listed explicitly in Eq. (3.18) from which the functions $f_{c\to e}(z,\lambda)$ may be read off easily.

The jet functions $\tilde{j}$ read

$$\begin{aligned}
\tilde{j}_{\gamma\to\gamma}(z,\lambda) &= \delta(1-z)+\mathcal{O}(\alpha)\,,\\
\tilde{j}_{\gamma\to q}(z,\lambda) &= \frac{\alpha e_q^2}{2\pi}\left[P_{q\gamma}(z)\log\left(\lambda^2(1-z)^2\right)+z(1-z)+\mathcal{I}^{\text{algo}}_{q\gamma}(z)\right]\,,\\
\tilde{j}_{q\to\gamma}(z,\lambda) &= \frac{\alpha e_q^2}{2\pi}\left[P_{\gamma q}(z)\log\left(\lambda^2(1-z)^2\right)+z+\mathcal{I}^{\text{algo}}_{\gamma q}(z)\right]\,,\\
\tilde{j}_{\gamma\to g}(z,\lambda) &= \mathcal{O}(\alpha\alpha_s)\,,\\
\tilde{j}_{g\to\gamma}(z,\lambda) &= \mathcal{O}(\alpha\alpha_s)\,,\\
\tilde{j}_{(e\neq\gamma)\to(c'\neq\gamma)}(z,\lambda) &= \delta(1-z)\delta_{ec'}+\frac{\alpha_s}{2\pi}\tilde{f}_{e\to c'}(z,\lambda)+\mathcal{O}(\alpha_s^2)+\mathcal{O}(\alpha\alpha_s)\,,
\end{aligned}\tag{5.14}$$

where the functions $\mathcal{I}^{\text{algo}}_{c'c}(z)$ are given in Eq. (3.14). Again, the last line in Eq.(5.14) describes the "pure-QCD" type jet functions given in Eq. (3.19) from which the functions $\tilde{f}_{e\to c'}(z,\lambda)$ may be read off easily.

From the above discussion, we conclude that as long as we stay at $z_\gamma < 1$ case **(iii)** generates the only non-vanishing direct contributions at $\mathcal{O}(\alpha)$ and NLO. We observe that the corresponding jet function in Eq. (5.12) shows a logarithmic divergence at $z\to 1$. A behavior of this type is quite familiar for NLO direct (pointlike) contributions in hadronic processes involving photons, where it is also exhibited by the corresponding photonic coefficient functions for space-like or time-like photon structure functions [145, 153]. This can become an issue, in principle, due to the fact that the coefficient functions appear directly in the structure function, potentially creating an unphysical divergent behavior of the structure function at high Bjorken-x. However, as was shown in Refs. [145, 153], for photon structure functions the situation may be remedied by adopting a factorization scheme different from the $\overline{\mathrm{MS}}$ scheme for the pointlike contribution. This scheme is known as DIS_γ scheme and will also be our choice in this chapter as it leads to an overall better perturbative stability. Using the results of [153] the scheme transformation is easily performed, and we find for the jet function in the DIS_γ scheme:

$$\begin{aligned}\tilde{j}^{\mathrm{DIS}_\gamma}_{q\to\gamma}(z,\lambda) &\equiv \tilde{j}^{\overline{\mathrm{MS}}}_{q\to\gamma}(z,\lambda) - \frac{\alpha}{2\pi}e_q^2\left[P_{\gamma q}(z)\log\Big(z^2(1-z)\Big) - 2\frac{1-z}{z}\right] \\ &= \frac{\alpha}{2\pi}e_q^2\,P_{\gamma q}(z)\left[\log\Big(\lambda^2(1-z)\Big)+1\right]. \end{aligned} \tag{5.15}$$

All other jet functions remain unaffected by the transformation. Interestingly, we find that even in the DIS_γ scheme a logarithmic term $\propto \log(1-z)$ remains in the jet function. The reason for this can be traced back to the fact that, compared to the inclusive structure function F_1^γ, the phase space for our photon-in-jet observable is different, being less inclusive and hence giving rise to two factors of $\propto \log(1-z)$ in the $\overline{\mathrm{MS}}$ scheme, only one of which is subtracted when transforming to the DIS_γ scheme. In any case, the remaining logarithm in (5.15) may be eliminated by a scale choice $(\mu_F'')^2 \propto (1-z_\gamma)$. As mentioned, the jet function in (5.15) refers to the anti-k_t jet algorithm. The results for other algorithms are given in Eq. (5.14) for the $\overline{\mathrm{MS}}$ scheme and may then be transformed to the DIS_γ scheme in the same fashion as above. All other jet functions are unaffected by that transformation.

For later reference, we finally note that the cross section (5.3) may also be expressed in terms of photon kinematics,

$$\frac{d\sigma^{pp\to(\mathrm{jet}\,\gamma)X}}{dp_T d\eta dz_\gamma}(p_T,\eta,z_\gamma) = \frac{1}{z_\gamma}\frac{d\sigma^{pp\to(\mathrm{jet}\,\gamma)X}}{dp_T^{\mathrm{jet}}d\eta^{\mathrm{jet}}dz_\gamma}\left(p_T^{\mathrm{jet}}=\frac{p_T}{z_\gamma},\eta,z_\gamma\right). \tag{5.16}$$

5.2 Pion Decay Background

Production of π^0 with the subsequent decay $\pi^0 \to \gamma\gamma$ (with a branching ratio of $\approx 98.8\%$ [319]) provides the largest source of unwanted background photons. There are two main components of this background [164, 320, 321]. First, at high pion transverse momentum, the two decay photons can become almost collinear and may not be resolved as two separate photons but rather as a single electromagnetic signal. We refer to this part of the background as "B1". It is sketched in Fig. 5.1b. Secondly, even when the two decay photons are well separated in angle, the decay may be very asymmetric in energy. It may happen that one of the decay photons is relatively soft, so that it is below the threshold for detection. In this case, only the high-energy decay photon will be seen and misinterpreted as a single prompt photon. This part of the background, denoted as "B2", is relevant toward lower transverse momentum, where the pion production cross section is large. We show a sketch of this kind of background in Fig. 5.1c.

Using the results from Chap. 3, it is relatively straightforward to estimate the sizes of B1 and B2. First, we consider the decay $\pi^0(P_\pi) \to \gamma(k_1)\gamma(k_2)$. From the axial anomaly prediction [322] in the chiral limit we have the decay matrix element

$$\mathcal{M} = \frac{ge^2}{4\pi^2 m_\pi}\varepsilon_{\mu\nu\rho\sigma}k_1^\rho k_2^\sigma \varepsilon_1^\mu \varepsilon_2^\nu\,, \tag{5.17}$$

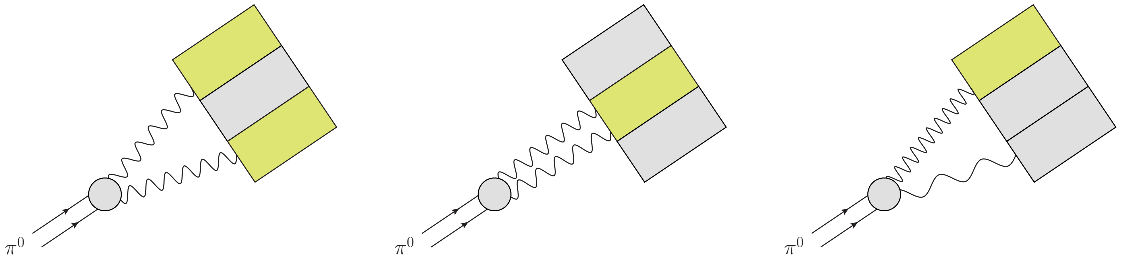

(a) No background **(b)** Background B1 **(c)** Background B2

Figure 5.1: Sketches of the different backgrounds discussed in the text. The incoming π^0 decays into two photons. The detector is schematically shown with three detector cells. The yellow cells observe a photon, while the grey cells detect nothing. Left: both decay photons are detected, hence this is not a background signal. Middle: collinear background B1. Right: background B2 where only the high energy photon is observed.

where ε_1 and ε_2 are the polarization vectors of the photons and the coupling is parametrized as $g = m_\pi/f_\pi$ with the pion decay constant f_π. From Eq. (5.17) we obtain a constant decay matrix element squared,

$$|\mathcal{M}|^2 = \frac{\alpha^2 m_\pi^2}{2 f_\pi^2 \pi^2}\,, \tag{5.18}$$

so that the normalized differential decay rate follows just from phase space considerations. For the decay rate we find

$$\begin{aligned} \Gamma &\equiv \frac{1}{2m_\pi}\int dPS_2\,|\mathcal{M}|^2 \\ &= \frac{1}{16\pi}\frac{|\mathcal{M}|^2}{m_\pi E_\pi \beta}\int_{E_\pi(1-\beta)/2}^{E_\pi(1+\beta)/2} dE_1\,, \end{aligned} \tag{5.19}$$

with the Lorentz factor $\beta = |\vec{P}_\pi|/E_\pi$. Thus, the normalized differential decay rate is given by

$$\frac{1}{\Gamma}\frac{d\Gamma}{dE_1} = \frac{1}{|\vec{P}_\pi|}\,, \tag{5.20}$$

where E_1 is the energy of one of the decay photons and $\vec{P}_\pi$ denotes the pion three-momentum in the hadronic c.m.s. As we are interested in the angular separation of the two photons, we relate E_1 to $\cos\theta_{12}$, where θ_{12} is the angle between the momenta of the two decay photons:

$$\cos\theta_{12} = 1 - \frac{m_\pi^2}{2E_1(E_\pi - E_1)}\,. \tag{5.21}$$

With the jacobian

$$\frac{dE_1}{d\cos\theta_{12}} = \frac{m_\pi^2}{2}\frac{1}{(1-\cos\theta_{12})^2}\left(\sqrt{E_\pi^2 - \frac{2m_\pi^2}{1-\cos\theta_{12}}}\right)^{-1}\,, \tag{5.22}$$

we then obtain
$$\frac{1}{\Gamma}\frac{d\Gamma}{d\cos\theta_{12}} = \frac{m_\pi^2}{|\vec{P}_\pi|}\frac{1}{(1-\cos\theta_{12})^2\sqrt{E_\pi^2 - \frac{2m_\pi^2}{1-\cos\theta_{12}}}}\,, \tag{5.23}$$
where E_π is the pion energy. For B1 we only need to impose the condition that θ_{12} be smaller than the angle the detector can resolve, so that the photons will be seen as a single electromagnetic signal. This happens when
$$1-\cos\theta_{12} \le \frac{\delta\phi^2+\delta\eta^2}{2\cosh^2\eta} \equiv \frac{\rho^2}{2\cosh^2\eta}\,, \tag{5.24}$$
where $\delta\phi$ and $\delta\eta$ are the detector resolutions in azimuthal angle and rapidity, respectively. To estimate B1 numerically, we simply have to integrate the normalized decay spectrum (5.23) subject to the constraint (5.24), i.e.
$$\int_{\cos\theta_{12}^{\min}}^{\cos\theta_{12}^{\max}} d\cos\theta_{12}\,\frac{1}{\Gamma}\frac{d\Gamma}{d\cos\theta_{12}} \;=\; \frac{1}{|\vec{P}_\pi|}\sqrt{E_\pi^2 - 4m_\pi^2\frac{\cosh^2\eta}{\rho^2}}\;\Theta\left(E_\pi^2 - 4m_\pi^2\frac{\cosh^2\eta}{\rho^2}\right)\,, \tag{5.25}$$
where $\cos\theta_{12}^{\min} \equiv 1-\rho^2/(2\cosh^2\eta)$, $\cos\theta_{12}^{\max} \equiv 1-2(1-\beta^2)$, and $\Theta(x)$ denotes the Heaviside function. Next, we multiply the result by the cross section for $pp \to (\mathrm{jet}\,\pi^0)\,X$ from our previous calculation in Chap. 3.

For B2, for which one of the two decay photons is not detected and the other photon has transverse momentum p_T, one needs to take into account that the decaying pion must have had a correspondingly higher transverse momentum or energy. This gives rise to a convoluted structure of the cross section for this part of the background. Denoting the energy threshold for photon detection by ε, we have
$$\frac{d\sigma^{\mathrm{B2}}}{d\eta^{\mathrm{jet}}dp_T^\gamma dz_\gamma} = \int_{p_T^\gamma}^{\infty}\frac{dp_T^\pi}{p_T^\pi}\,\frac{d\sigma^{(\mathrm{jet}\,\pi^0)}}{d\eta^{\mathrm{jet}}dp_T^\pi dz_\pi}\,\frac{1}{\Gamma}\frac{d\Gamma(x=p_T^\gamma/p_T^\pi)}{dx}\,, \tag{5.26}$$
where
$$\frac{1}{\Gamma}\frac{d\Gamma(x)}{dx} = \frac{2}{\beta}\Theta\left[\frac{1+\beta}{2}-x\right]\Theta\left[x-\max\left(1-\frac{\varepsilon}{E_\pi},\frac{1}{2}\left(1+\sqrt{1-\frac{4m_\pi^2\cosh^2\eta}{\rho^2E_\pi^2}}\right)\right)\right]\,. \tag{5.27}$$
We have introduced the variable x as the energy fraction of one photon with respect to the pion energy, $E_1 = xE_\pi$, and hence $E_2=(1-x)E_\pi$. Furthermore, p_T^π is the transverse momentum of the decaying pion and $z_\pi \equiv p_T^\pi/\hat{p}_T^{\mathrm{jet}}$ is defined in analogy to Eq. (5.2), with $\hat{p}_T^{\mathrm{jet}}$ the transverse momentum of the jet containing the pion. Clearly, we have $E_\pi = E_\gamma + E_2$ and hence $p_T^\gamma = xp_T^\pi$, since we assume that the other photon's energy, E_2, is not seen by the detector as it falls below the detector's energy threshold. A further consequence of this is that the photon with energy E_2 is not counted toward the jet energy. As a result, we have $p_T^{\mathrm{jet}} = x\hat{p}_T^{\mathrm{jet}}$. Combining these relations, we find that $z_\pi = z_\gamma$.

We now rewrite the integration in Eq. (5.26) in terms of the energy fraction x and use Eq. (5.16) to express everything in terms of the jet kinematics. Using $z_\pi = z_\gamma$ we finally arrive at
$$\frac{d\sigma^{\mathrm{B2}}}{dp_T^{\mathrm{jet}}d\eta^{\mathrm{jet}}dz_\gamma} = \int_0^1 dx\,\frac{d\sigma^{(\mathrm{jet}\,\pi^0)}}{d\hat{p}_T^{\mathrm{jet}}d\eta^{\mathrm{jet}}dz_\pi}\,\frac{1}{\Gamma}\frac{d\Gamma(x)}{dx}\,. \tag{5.28}$$

The integration limits in this equation are implemented implicitly in the definition of $\frac{1}{\Gamma}\frac{d\Gamma(x)}{dx}$ via Heaviside functions, see Eq. (5.27). They follow from the conditions that the decay be kinematically possible, that the unobserved decay photon must have energy below ε, and that the two photons have an opening angle larger than the detector resolution. Explicitly, one has

$$1 + \frac{m_\pi^2}{4E_\gamma^2} \le x^{-1} \le \min\left(1 + \frac{\varepsilon}{E_\gamma}, 1 + \frac{m_\pi^2}{\rho^2 p_T^2}\right) , \tag{5.29}$$

with $E_\gamma = p_T \cosh\eta$ the observed photon's energy.

To obtain a better understanding of the phase space for the two backgrounds and how they are connected, it is instructive to plot $\cos\theta_{12}$ as a function of E_1 according to Eq. (5.21). This is done in Fig. 5.2. Without any restrictions, the region underneath the solid line would be the available phase space for the two photon decay. If the pion could be reconstructed experimentally in this whole region, there would be no pion decay background. As described above, the experimental limitations lead to some regions where only one electromagnetic signal is seen. In the upper hatched region representing B1 the two photons are close together and cannot be seen as separate photons by the detector. In the shaded regions (B2) left and right, they are well separated in angle, but one of them has energy below threshold and is not seen either. The full background comes from the sum of these regions. Only in the the remaining part can both photons be seen and the parent pion be reconstructed. We note that Fig. 5.2 shows an idealized picture where we have chosen the pion energy and the parameters ρ and ε such that the main qualitative effects are well visible. If we were to

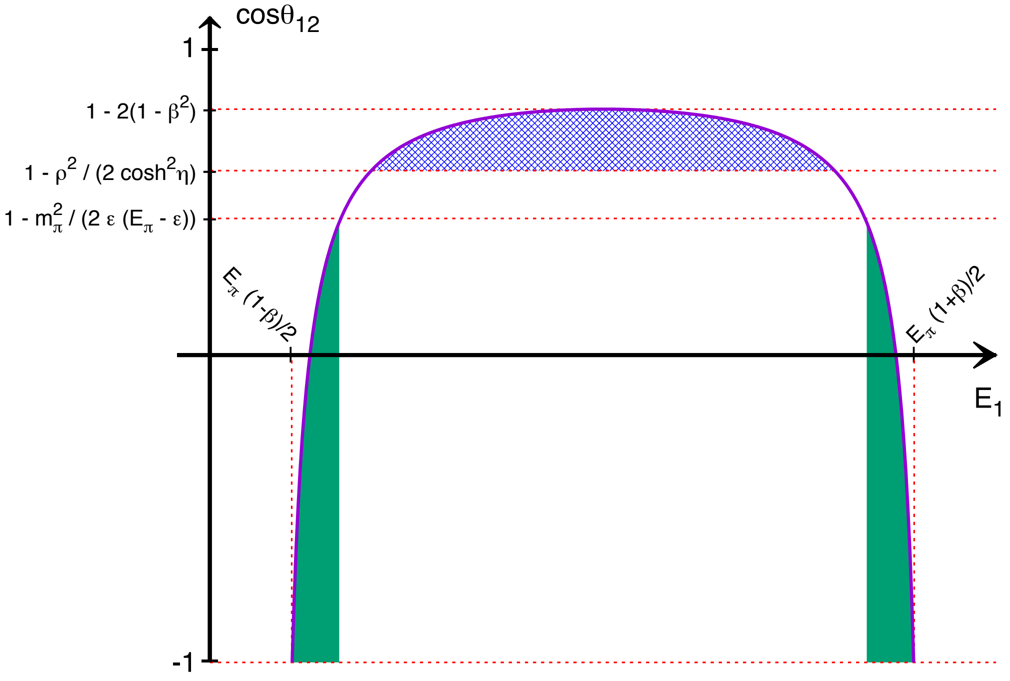

Figure 5.2: The cosine of the angle between the two photons, $\cos\theta_{12}$, as a function of the photon energy E_1, according to Eq. (5.21). The shaded areas correspond to B2 while the hatched one describes B1.

use more realistic values, the plot would look close to a rectangular function, with $\cos\theta_{12}$ very closely reaching unity at the upper end. The hatched and shaded areas would shrink in size, although they still make numerically very sizable contributions as we shall see in the next section. We also note that, depending on the kinematics, the areas of B1 and B2 may overlap. Hence, in the numerical calculation one has to carefully avoid double counting.

We finally emphasize that our calculations of the pion backgrounds are not limited to photon-in-jet production, but can also be applied to any other photon observable. Of course, one has to combine the decay results with the appropriate pion cross sections corresponding to the photon observable one is interested in. For example, to obtain a background estimation for single-inclusive photon production one would use a single-inclusive pion cross section and apply the expressions for B1 and B2.

5.3 Phenomenological Results

It is most interesting to consider the cross section differential in z_γ as it directly probes the z dependence of the D_c^γ. The upper part of Fig. 5.3 (solid line) shows the cross section for $pp \to (\text{jet}\,\gamma)\,X$ at $\sqrt{S} = 200$ GeV, corresponding to RHIC. In the lower part we show results for pp collisions at the LHC at $\sqrt{S} = 7$ TeV. We use the CT10 [225] parton distributions and the "Glück-Reya-Vogt" (GRV) photon fragmentation functions of Ref. [153]. The results

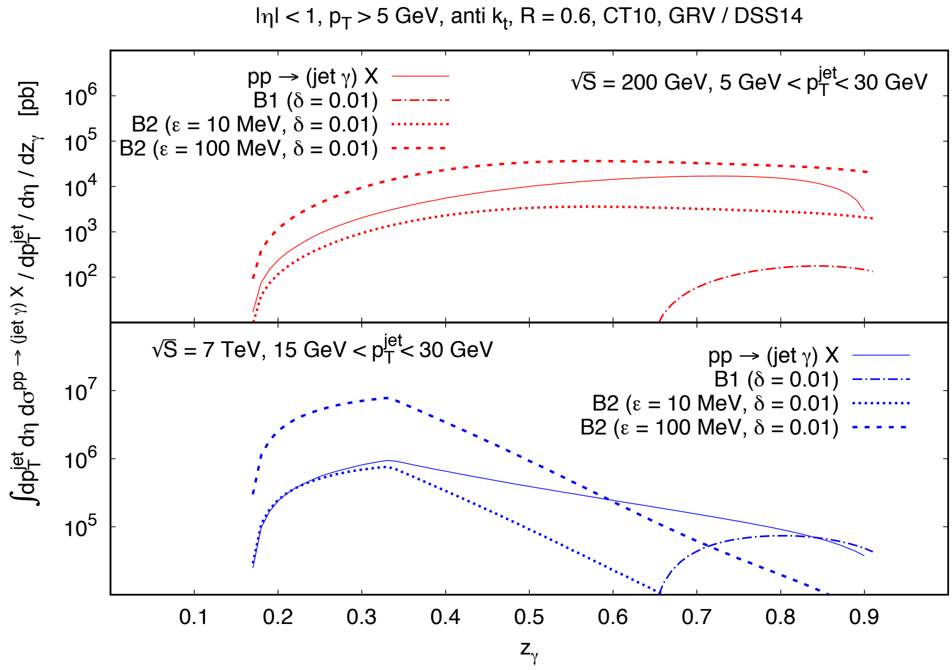

Figure 5.3: NLO cross section for $pp \to (\text{jet}\,\gamma)X$ at $\sqrt{S} = 200$ GeV as function of z_γ, for 5 GeV $< p_T^{\text{jet}} <$ 30 GeV (upper, solid), and at $\sqrt{S} = 7$ TeV for 15 GeV $< p_T^{\text{jet}} <$ 30 GeV (lower, solid). The other lines show in both cases the backgrounds B1 and B2 from π^0 decay, for various choices of the detection parameters.

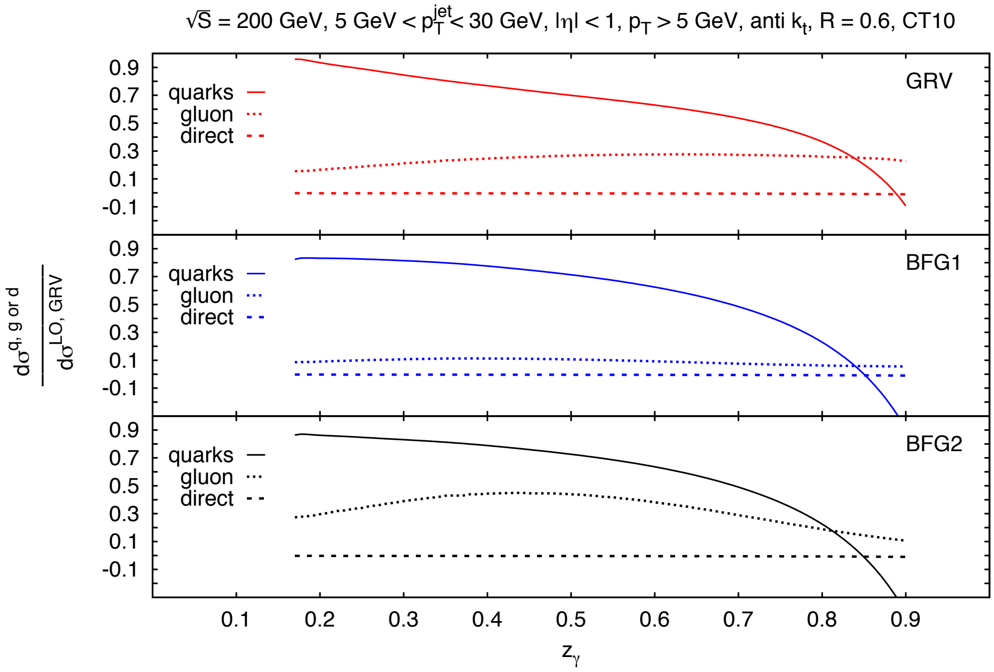

Figure 5.4: Normalized quark (solid) and gluon (dotted) fragmentation contributions together with the direct contribution (dashed) to the cross sections as functions of z_γ for 5 GeV $< p_T^{\text{jet}} <$ 30 GeV at $\sqrt{S} = 200$ GeV. We show results for the sets of fragmentation functions of Refs. [153, 154]. For purpose of clearer presentation, all results have been normalized to the LO cross section obtained for GRV fragmentation functions.

have been integrated over $|\eta^{\text{jet}}| < 1$ and over 5 GeV $< p_T^{\text{jet}} <$ 30 GeV for RHIC and 15 GeV $< p_T^{\text{jet}} <$ 30 GeV for the LHC. We also impose a cut $p_T > 5$ GeV on the photon transverse momentum, in order to make sure that we are in the perturbative regime. As it turns out, this cut also helps to suppress the pion decay background (for the LHC the cut causes the "edges" in the figure at $z_\gamma = 1/3$ where 5 GeV$/z_\gamma$ coincides with the lower limit of the p_T^{jet} integration). The jet is always defined by the anti-k_t algorithm with $R = 0.6$. We choose $\mu_R = \mu_F = p_T^{\text{jet}}$ for the renormalization and the initial state factorization scales. The final state factorization scale, on the other hand, is set to $\mu_F'' = p_T^{\text{jet}}\sqrt{1 - z_\gamma}$ (see also [37, 264]). Along with our value of R this choice helps to minimize the logarithm in Eq. (5.15) and hence the direct contribution to the cross section.

In addition to the cross sections we also show the estimated π^0 background in Fig. 5.3, separately for B1 and B2. Here we use the most recent set of pion fragmentation functions of [132]. We choose the detector resolutions $\delta\phi = \delta\eta \equiv \delta = 0.01$ in (5.24), which are typical values for the RHIC and LHC collider experiments. We furthermore assume two different values for the energy threshold for photon detection, $\varepsilon = 100$ MeV and $\varepsilon = 10$ MeV. We observe that for our choice of kinematics background B1 is small for $\delta\phi = \delta\eta = 0.01$, since the two photons start to be seen as a single one only when their combined transverse momentum exceeds ~ 20 GeV. One furthermore sees that background B2 remains below the

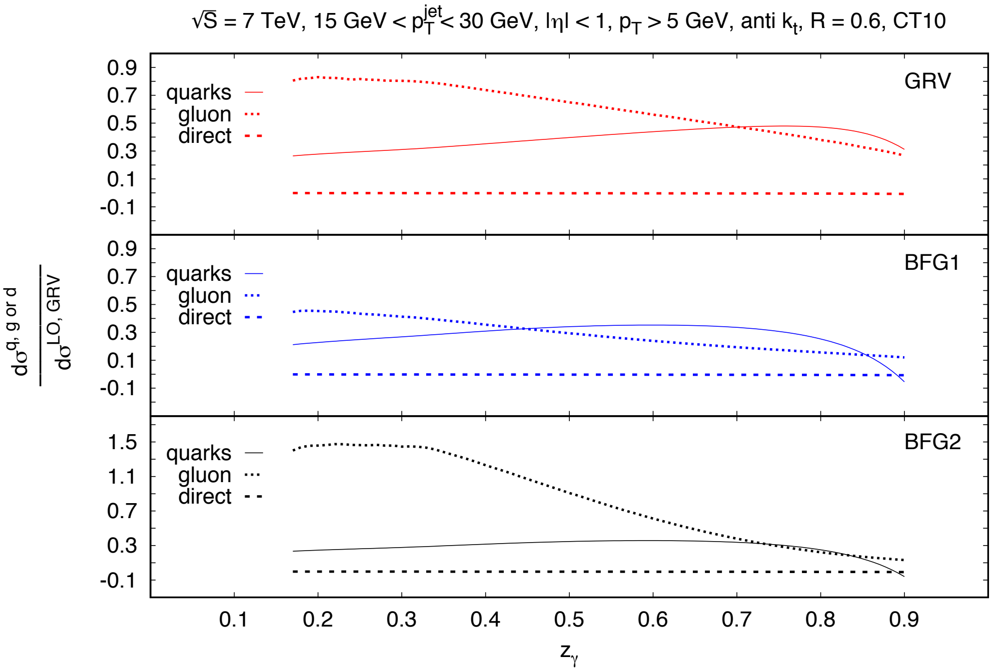

Figure 5.5: Same as Fig. 5.4 but for LHC kinematics, i.e. 15 GeV $< p_T^{\text{jet}} <$ 30 GeV at $\sqrt{S} = 7$ TeV.

photon cross section only for the relatively low threshold $\varepsilon = 10$ MeV. This evidently poses a challenge to experimental studies of photon-in-jet production.

Figure 5.4 analyzes the relative sizes of the contributions of quark/antiquark (summed over all flavors) and gluon fragmentation to the cross section, using the RHIC kinematical setup of Fig. 5.3. We have normalized all contributions to the LO cross section with GRV fragmentation functions. We show NLO results for three different sets of photon fragmentation functions: the GRV [153] one used so far, and the two sets of “Bourhis, Fontannaz, Guillet”, Ref. [154], which we refer to as “BFG1” and “BFG2” and properly transform to the DIS$_\gamma$ scheme. One can see that overall gluon fragmentation makes a sizable contribution to the photon cross section. The BFG2 set is characterized by an especially large gluon-to-photon fragmentation function, which becomes clearly visible in the figure. We also show the direct contribution based on Eq. (5.15) which, in the DIS$_\gamma$ scheme and for our choice of R and μ_F'', is tiny. The cross section for photons produced in jets thus offers a direct probe of photon fragmentation also at NLO. In Fig. 5.5 we show the same for LHC kinematics. The statements for RHIC remain essentially true also for the center of mass energy of $\sqrt{S} = 7$ TeV. However, the relative gluon contribution is much larger compared to RHIC energies which is mainly due to the dominance of the gluon PDF at LHC energies. Thus gluon channels are much enhanced at the LHC compared to colliders with a smaller center of mass energy.

5.4 Sensitivity to Parton-to-Photon FFs

As we have seen in Sec. 1.3.4, neither SIA nor inclusive photon production in *pp* collisions are able to provide detailed access to the fragmentation contribution. It is thus important to identify new observables that are able to yield new and complementary information on photon FFs. In this section, which is based on our publication [149], we demonstrate that the process studied in this chapter is indeed able to provide this information.

The main asset of the process $pp \to (\text{jet}\,\gamma)X$ is that at LO the cross section is *directly proportional* to the FFs probed at $z = z_\gamma$, as can be seen from the LO approximation of Eq. (5.3), which reads up to trivial factors

$$\left.\frac{d\sigma^{pp\to(\text{jet}\,\gamma)X}}{dp_T^{\text{jet}}\,d\eta^{\text{jet}}\,dz_\gamma}\right|_{\text{LO}} \propto \sum_{\substack{a,b,c\in\\ \{q,\bar{q},g,\gamma\}}} f_a \otimes f_b \otimes d\hat{\sigma}_{ab}^{c,\text{LO}} \times \Big[\delta(1-z_\gamma)\delta_{c\gamma} + D_c^\gamma(z_\gamma,\mu^2)(1-\delta_{c\gamma})\Big]\,. \quad (5.30)$$

The first part in the squared brackets of Eq. (5.30) is the direct part while the second one is the fragmentation contribution. Recall, that we impose $z_\gamma < 1$ to ensure that we have a hadronic jet around the photon. Hence, the direct part does not contribute at LO and only the fragmentation contribution remains. The various FFs are weighted by appropriate combinations of PDFs and partonic cross sections, which may be regarded as "effective charges". The structure of the cross section hence becomes similar to that for $e^+e^- \to \gamma X$, but with the essential difference that also gluon-to-photon fragmentation contributes at the lowest order.

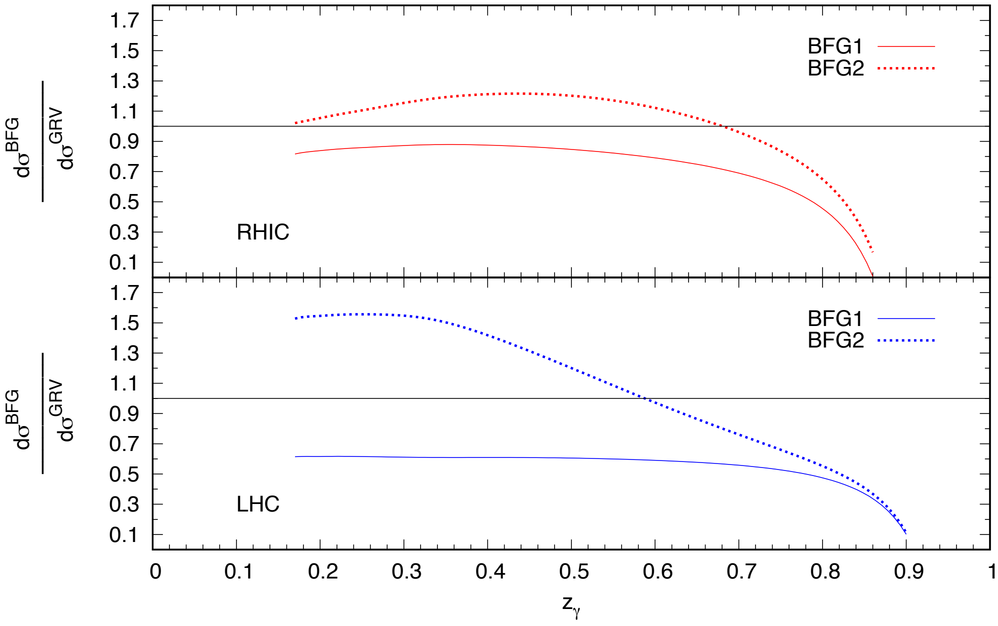

Figure 5.6: The ratio for cross sections computed with BFG sets with respect to GRV for the kinematical setups of Figs. 5.4 and 5.5.

In Fig. 5.6 we demonstrate the potential of the process $pp \to (\mathrm{jet}\,\gamma)X$ for providing valuable and new information on the photon FFs. We compare the full NLO cross sections for the different FF sets. We show the ratios of the cross sections computed with the BFG1 and BFG2 sets, relative to the cross section for the GRV FFs. The potential of this process becomes visible, especially for the LHC setup where we find differences among the cross sections of up to 50%. This is in stark contrast to what we saw for $pp \to \gamma X$ (see the lower part of Fig. 1.6), where over a large range in p_T the cross sections for the different FF sets differed by less than 10%. We are hence optimistic that experimental data for $pp \to (\mathrm{jet}\,\gamma)X$ would allow one to distinguish between the different FF sets.

5.5 Conclusions

We have proposed a method of accessing the elusive photon fragmentation functions in hadronic collisions at RHIC or the LHC. The idea is to identify photons produced inside fully reconstructed jets, with the photon treated as part of the jet. The variable $z_\gamma = p_T/p_T^{\mathrm{jet}}$ introduced in Eq. (5.2) allows to map out the z-dependence of the photon fragmentation functions. We have presented numerical results for the corresponding cross section that demonstrate the sensitivity to the fragmentation functions. We have also performed detailed estimates of the background from neutral-pion decay. These suggest that the measurement should be feasible provided a low photon detection threshold can be chosen. This will evidently present a significant challenge; on the other hand, there are likely further techniques available in experiment that allow to suppress the background, such as subtraction of the background using a measured pion-in-jet cross section. We are thus optimistic that clean measurements of the D_c^γ should become possible in pp collisions, enabling better theoretical control of collider observables involving high energy photons. We finally note that detailed future studies of the interplay of QCD radiation inside jets with photon production may also lead to new techniques for photon isolation.

Chapter 6

Fragmentation Functions Beyond Fixed Order Accuracy

In this chapter, which is based on our publication [116], we give a detailed account of the phenomenology of all-order resummations of logarithmically enhanced contributions at small momentum fraction of the observed hadron in semi-inclusive electron-positron annihilation and the time-like scale evolution of parton-to-hadron fragmentation functions. The formalism to perform resummations in Mellin moment space is briefly reviewed, and all relevant expressions up to next-to-next-to-leading logarithmic order are derived, including their explicit dependence on the factorization and renormalization scales. We discuss the details pertinent to a proper numerical implementation of the resummed results comprising an iterative solution to the time-like evolution equations, the matching to known fixed-order expressions, and the choice of the contour in the Mellin inverse transformation. First extractions of parton-to-pion fragmentation functions from semi-inclusive annihilation data are performed at different logarithmic orders of the resummations in order to estimate their phenomenological relevance. To this end, we compare our results to corresponding fits up to fixed, next-to-next-to-leading order accuracy and study the residual dependence on the factorization scale in each case.

As already mentioned in Sec. 1.3, the prime example for the determination of fragmentation functions (FFs) is single-inclusive electron-positron annihilation (SIA). Precise data on SIA [323–331], available at different $\sqrt{S}$, ranging from about 10 GeV up to the mass M_Z of the Z boson, reveal important experimental information on FFs that is routinely used in theoretical extractions, i.e., fits of FFs [117, 130–133, 151, 255–258]. Processes other than SIA are required, however, to gather the information needed to fully disentangle all the different FFs D_i^h for $i = u, \bar{u}, d, \bar{d}, \dots$ quark and antiquark flavors and the gluon. Specifically, data on semi-inclusive deep-inelastic scattering (SIDIS), $e^{\pm}p \to hX$, and the single-inclusive, high transverse momentum (p_T) production of hadrons in proton-proton collisions, $pp \to hX$, are utilized, which turn extractions of FFs into global QCD analyses [130–132, 258]. In Chap. 3, we have developed a proper theoretical framework in terms of FFs for a novel class of processes, where a hadron is observed inside a jet (see also [35–39, 197, 204]). It is expected that corresponding data will soon be included in global analyses of light hadrons, where they will provide additional constraints on, in particular, the gluon-to-hadron FF. For heavy D^*-mesons we have already included this process in the determination of the corresponding FFs in Chap. 4.

The ever increasing precision of all these probes sensitive to the hadronization of (anti-)quarks and gluons has to be matched by more and more refined theoretical calculations. One way of advancing QCD calculations is the computation of higher order corrections in the strong coupling α_s. Here, next-to-leading order (NLO) results are available throughout for all ingredients needed for a global QCD analysis of FFs as outlined above. Specifically, they comprise the partonic hard scattering cross sections for inclusive hadron production in SIA [86–88], SIDIS [83, 86–88, 332], and *pp* collisions [91, 198, 304] and the evolution kernels or time-like parton-to-parton splitting functions P_{ij}^T [28, 84, 270, 333–335], which govern the scale Q dependence of the FFs through a set of integro-differential evolution equations [101–105]. Such type of NLO global analyses of FFs represent the current state-of-the-art in this field. For instance, a recent extraction of parton-to-pion FFs D_i^π at NLO accuracy can be found in Ref. [132]. A special role in this context plays SIA, where fits of FFs can be carried out already at the next-to-next-leading order (NNLO) level thanks to the available SIA coefficient functions [84, 270, 271, 336] and kernels P_{ij}^T at NNLO [119–121]. This has not yet been achieved in the case of hadron production in SIDIS or in *pp* collisions. A first determination of parton-to-pion FFs from SIA data at NNLO accuracy has been performed recently in [117].

Another important avenue for systematic improvements in the theoretical analysis of data sensitive to FFs, which we pursue in this chapter, concerns large logarithms present in each fixed order of the perturbative series in α_s for both the evolution kernels P_{ij}^T and the process-dependent hard scattering coefficient functions. In this chapter we will deal with logarithms that become large in the limit of small momentum fractions z and, in this way, can spoil the convergence of the expansion in α_s even when the coupling is very small. As we shall see, two additional powers of $\log^{2k}(z)$ can arise in each fixed order α_s^k, which is numerically considerably more severe than in the space-like case relevant to deep-inelastic scattering (DIS) and the scale evolution of parton density functions (PDFs) and completely destabilizes the behavior of cross sections and FFs in the small-z regime.

To mitigate the singular small-z behavior imprinted by these logarithms, one needs to resum them to all orders in perturbation theory, a well-known procedure (see, for instance, [337–340]). Knowledge of the fixed-order results up to N^{m}LO determines, in principle, the first $m + 1$ "towers" of logarithms to all orders. Hence, thanks to the available NNLO results, small-z resummations have been pushed up to the first three towers of logarithms for SIA and the time-like splitting functions P_{ij}^T recently, which is termed the next-to-next-to-leading logarithmic (NNLL) approximation [42, 43]. Based on general considerations on the structure of all-order mass factorization, as proposed and utilized in Ref. [42, 43], we re-derive the resummed coefficient functions for SIA and the evolution kernels P_{ij}^T and compare them to the results available in the literature. Next, we shall extend these expressions by restoring their dependence on the factorization and renormalization scales μ_F and μ_R, respectively, which will allow us to estimate the theoretical uncertainties related to the choice of μ_F/Q. It is expected that the scale ambiguity will shrink the more higher order corrections are included. We note that large logarithms also appear in the limit $z \to 1$. Their phenomenological implications have been addressed in the case of SIA in Ref. [135, 341–345], and we shall not consider them in the present study focussing mainly on the small-z regime.

Resummations are most conveniently carried out in Mellin-N moment space, which also gives the best analytical insight into the solution of the coupled, matrix-valued scale evolution equations obeyed by the quark singlet and gluon FFs, c.f. Sec. 1.3.2. We shall discuss in some detail how we define a solution to these evolution equations beyond the fixed-order approximation, i.e., based on resumed kernels P_{ij}^T. We also explain how we match the resummed small-z expressions to a given fixed-order result defined for all z, thereby avoiding any double-counting of logarithms and also maintaining the validity of the momentum sum rule. We shall also address in our discussions the proper numerical implementation of the resummed expressions in Mellin-N space, in particular, the structure of singularities and the choice of the integration contour for the inverse Mellin transformation back to the physical z space. Already at fixed, NNLO accuracy this is known to be a non-trivial issue [117].

After all these technical preparations, we will present some phenomenological applications. So far, resummations in the context of FFs have been, to the best of our knowledge, exclusively studied for the first five integer N moments of the z-integrated hadron multiplicities, in particular, their scale evolution and the shift of the peak of the multiplicity distribution with energy (see, for instance, [337–340] and for recent studies of integrated hadron multiplicities, see, for example [346–350] and references therein). At fixed order, multiplicities are ill-defined due to the singularities induced by the small-z behavior. In the “modified leading logarithmic approximation” (MLLA) and beyond, i.e. upon including resummed expressions, these singularities are lifted, and one finds a rather satisfactory agreement with data, which can be used to determine, for instance, the strong coupling α_s in SIA [346–350].

In this chapter, we will apply resummations in the entire z range, i.e. for the first time, we extract FFs from SIA data with identified pions up to NNLO+NNLL accuracy, including a proper matching procedure. We shall investigate the phenomenological relevance of small-z resummations in achieving the best possible description of the SIA data. This will be done by comparing the outcome of a series of fits to data both at fixed order accuracy and by including up to three towers of small-z logarithms. We also compare the so obtained quark singlet and gluon FFs and estimate the residual theoretical uncertainty due to the choice of μ_F/Q in each case. An important phenomenological question that arises in this context is how low in z one can push the theoretical framework outlined above before neglected kinematic hadron mass corrections become relevant. Hadron mass effects in SIA have been investigated to some extent in [351] but, so far, there is no fully consistent way to properly include them in a general process [352], i.e., ultimately in a global analysis of FFs. Therefore, one needs to determine a lower value of z, largely on kinematical considerations, below which fits of FFs make no sense. We will discuss this issue as well in the phenomenological section of this chapter. In general, it turns out, that in the range of z where SIA data are available and where the framework can be applied, a fit at fixed, NNLO accuracy already captures most of the relevant small-z behavior needed to arrive at a successful description of the data, and resummations add only very little in a fit.

The remainder of this chapter is organized as follows: Section 6.1 comprises all relevant technical aspects. We start by briefly reviewing the fixed order results for semi-inclusive annihilation and catalogue the systematics of the small-z logarithms that appear in each order of perturbation theory. Next, we show how these logarithms can be resummed to all orders and compare to existing results in the literature. In Sec. 6.1.4 we provide the expressions containing logarithms of the factorization and renormalization scales to estimate the remaining theoretical uncertainties after resummation. The solution of the time-like evolution equations with resummed splitting functions in Mellin moment space is discussed in Sec. 6.1.5. Peculiarities important for a proper numerical implementation of the resummed expressions in N-space are raised in Sec. 6.1.6. In the second part of this chapter we discuss the phenomenological implications of small-z resummations for the extraction of fragmentation functions from data. In Sec. 6.2.1 we present and discuss various fits to semi-inclusive annihilation data at different fixed-orders in perturbation theory and levels of small-z resummations. Finally, in Sec. 6.2.2 we study the residual scale dependence with and without resummations of small-z logarithms. We conclude in Sec. 6.3.

6.1 Small-z Resummation for Semi-inclusive e^+e^- Annihilation

6.1.1 Fixed order SIA, FFs, and the Systematics of Small-z Logarithms

We consider the SIA process $e^+e^- \to \gamma/Z \to hX$, more specifically, cross sections as already defined in Eq. (1.35),

$$\frac{d\sigma^h}{dz} = \sum_{k=T,L} \frac{d\sigma^h_k}{dz} \,. \tag{6.1}$$

The parity-violating interference term of vector and axial-vector contributions, usually called "asymmetric" (A), is not present in (6.1) as we have already integrated over the scattering angle θ; see, e.g. [87]. Hence, only the transverse (T) and the longitudinal (L) parts remain and will be considered in what follows. The scaling variable z is defined in Eq. (4.2). Note, that experimental data are usually given in terms of hadron multiplicity distributions, which are equivalent to the cross sections as defined in Eq. (6.1) normalized by the total hadronic cross section σ_{tot} [84, 353–355], see Eq. (6.1).

The transverse and longitudinal cross sections in Eq. (6.1) may be written in a factorized form as [84, 336]

$$\begin{aligned} \frac{d\sigma^h_k}{dz} &= \sigma^{(0)}_{\text{tot}} \left[D^h_{\text{S}}(z,\mu^2) \otimes \mathbb{C}^{\text{S}}_{k,q}\left(z, \frac{Q^2}{\mu^2}\right) + D^h_g\left(z,\mu^2\right) \otimes \mathbb{C}^{\text{S}}_{k,g}\left(z,\frac{Q^2}{\mu^2}\right)\right] \\ &\quad + \sum_q \sigma^{(0)}_q \, D^h_{\text{NS},q}(z,\mu^2) \otimes \mathbb{C}^{\text{NS}}_{k,q}\left(z,\frac{Q^2}{\mu^2}\right) . \end{aligned} \tag{6.2}$$

For simplicity, we have chosen the factorization and renormalization scales equal, $\mu_R = \mu_F \equiv \mu$, and $\sigma^{(0)}_q = 3\sigma_0 \hat{e}^2_q$ is the total quark production cross section for a given flavor q at leading order (LO). $\sigma_0 = 4\pi\alpha^2/(3Q^2)$ denotes the lowest order QED cross section for the process $e^+e^- \to \mu^+\mu^-$ with α the electromagnetic coupling. The electroweak quark charges $\hat{e}_q$ can be found, e.g., in Ref. [84]. We also defined $\sigma^{(0)}_{\text{tot}} = \sum_q \sigma^{(0)}_q$. The symbol $\otimes$ denotes the standard convolution integral which defined in Eq. (1.41). With this notation, the transverse and longitudinal cross sections are related to the usual longitudinal and transverse structure functions [270] according to

$$\begin{aligned} F_k &\equiv \frac{1}{3\sigma_0}\frac{d\sigma^h_k}{dz} \\ &= \left(\sum_q \hat{e}^2_q\right) \left[D^h_{\text{S}}(z,\mu^2) \otimes \mathbb{C}^{\text{S}}_{k,q}\left(z,\frac{Q^2}{\mu^2}\right) + D^h_g\left(z,\mu^2\right) \otimes \mathbb{C}^{\text{S}}_{k,g}\left(z,\frac{Q^2}{\mu^2}\right)\right] \\ &\quad + \sum_q \hat{e}^2_q \, D^h_{\text{NS},q}(z,\mu^2) \otimes \mathbb{C}^{\text{NS}}_{k,q}\left(z,\frac{Q^2}{\mu^2}\right) \\ &= \sum_{l=q,\bar{q},g} D^h_l(z,\mu^2) \otimes \mathbb{C}_{k,l}\left(z,\frac{Q^2}{\mu^2}\right) . \end{aligned} \tag{6.3}$$

As usual, the factorized structure of Eq. (6.2) holds in the presence of a hard scale, i.e., of $\mathcal{O}$(few GeV), and up to corrections that are suppressed by inverse powers of the hard scale. SIA is a one-scale process, and the hard scale should be chosen to be of $\mathcal{O}(Q)$. The power corrections for SIA are much less well understood than in DIS, perhaps due to the lack of an operator product expansion in the time-like case. One source, which we will get back to later on, is of purely kinematic origin. Instead of the energy fraction z, SIA data are often given in terms of the hadron's three-momentum fraction in the c.m.s., $x_p = 2p/Q$, which leads to $1/Q^2$ corrections when converted back to proper scaling variable: $x_p = z - 2m_h^2/(zQ^2) + \mathcal{O}(1/Q^4)$ [87]. m_h is the produced hadron's mass and is neglected in the factorized formalism outlined above. Other sources of power corrections arise in the non-perturbative formation of a hadron from quarks or gluons and are expected to behave like $1/Q$ from model estimates [87].

The dependence of the FFs on the factorization scale μ may be calculated in pQCD and is described by the $2N_f + 1$ coupled integro-differential evolution equations [101–105] with N_f being the number of active quark flavors; see also Sec. (1.3.2). It is common to define certain linear combinations of quark and antiquark FFs that appear in SIA. The quark singlet (S) and nonsinglet (NS) FFs in Eq. (6.2) are given by

$$D_{\mathrm{S}}^h(z,\mu^2) = \frac{1}{N_f}\sum_q \left[D_q^h(z,\mu^2) + D_{\bar{q}}^h(z,\mu^2)\right] \tag{6.4}$$

and

$$D_{\mathrm{NS},q}^h(z,\mu^2) = D_q^h(z,\mu^2) + D_{\bar{q}}^h(z,\mu^2) - D_{\mathrm{S}}^h(z,\mu^2)\,, \tag{6.5}$$

respectively. The corresponding coefficient functions $i = \mathrm{S}, \mathrm{NS}$ in (6.2) can be calculated as a perturbative series in $a_s \equiv \alpha_s/4\pi$,

$$\mathbb{C}_{k,l}^i = \mathbb{C}_{k,l}^{i,(0)} + a_s\,\mathbb{C}_{k,l}^{i,(1)} + a_s^2\,\mathbb{C}_{k,l}^{i,(2)} + \mathcal{O}(a_s^3)\,, \tag{6.6}$$

where we have suppressed the arguments $(z, Q^2/\mu^2)$. Expressions for the $\mathbb{C}_{k,l}^i$ are available up to $\mathcal{O}(a_s^2)$ in Refs. [84, 270, 271], which is NNLO for the transverse coefficient functions but formally only next-to-leading accuracy (NLO) accuracy for the longitudinal coefficient functions as the latter start to be non-zero at $\mathcal{O}(a_s)$.

The fixed order results of the coefficient functions contain logarithms that become large for $z \to 1$ (large-z regime) and $z \to 0$ (small-z regime). Such large logarithms can potentially spoil the convergence of the perturbative expansion even for $a_s \ll 1$ and, hence, need to be taken into account to all orders in the strong coupling. The resummation of large-z logarithms in SIA has been addressed, for instance, in Refs. [135, 341–345]. The main focus of this chapter is on the so far very little explored small-z regime and its phenomenology. In contrast to the space-like DIS process with its single logarithmic enhancement, one finds a double logarithmic enhancement for the time-like SIA; see, e.g., [356] and references therein. For example, for the gluon sector in Eq. (6.2) one finds

$$\begin{aligned} \mathbb{C}_{T,g}^{S,(k)} &\propto a_s^k \frac{1}{z}\log^{2k-1-a}(z)\,, \\ \mathbb{C}_{L,g}^{S,(k)} &\propto a_s^k \frac{1}{z}\log^{2k-2-a}(z)\,, \end{aligned} \tag{6.7}$$

where $a = 0, 1$, and 2 corresponds to the leading logarithmic (LL), next-to-leading logarithmic (NLL), and NNLL contribution, respectively.
Furthermore, the same logarithmic behavior at small-z is found for the time-like splitting functions that govern the scale evolution of the FFs. For example, for the gluon-to-gluon and the quark-to-gluon splitting function, one finds

$$P_{gi}^{T,(k)} \propto a_s^{(k+1)} \frac{1}{z} \log^{2k-a}(z) \,, \tag{6.8}$$

where $i = q, g$, and k denotes the perturbative order starting from $k = 0$, i.e., LO. In order to obtain a reliable prediction from perturbative QCD in the small-z regime, these large logarithmic contributions, both in the coefficient functions and in the splitting functions, need to be resummed to all orders. The resulting expressions are available in the literature up to NNLL accuracy [42, 43] and we will re-derive them in the next subsections. Traditionally, and most conveniently, these calculations are carried out in the complex Mellin transform space. In general, the Mellin integral transform $f(N)$ of a function $f(z)$ was defined in Eq. (1.78). Hence, the Mellin transform of the small-z logarithms given in Eqs. (6.7) and (6.8) reads

$$\mathcal{M}\left[\frac{\log^{2k-1}(z)}{z}\right] = (-1)^k \frac{(2k-1)!}{\bar{N}^{2k}} \,, \tag{6.9}$$

where $\bar{N} \equiv N - 1$, i.e., they give rise to singularities at $N = 1$ in Mellin space.
The structure of the $1/\bar{N}$ divergences for all quantities relevant to a theoretical analysis of SIA up to NNLL accuracy is summarized schematically in Tables 6.1 and 6.2. Note that no LL contributions appear in the quark sector, neither for the splitting nor for the coefficient functions. Moreover, the LO and NLO small-z contributions to $\mathbb{C}^S_{T/L,q}$, P^T_{qq}, and P^T_{qg} are not contained in the generic structure summarized in Tables 6.1 and 6.2. Instead, these terms have to be extracted directly from the respective fixed order calculations. We would like to point out that there is no complete NNLO calculation (i.e., third order in a_s) for the longitudinal coefficient functions available at this time. Therefore, only the first

Table 6.1: The explicit $1/\bar{N}$ dependence of the coefficient functions $\mathbb{C}^S_{k,l} = \sum_n a_s^n \mathbb{C}^{S,(n)}_{k,l}$ at any given fixed order n of the perturbative expansion at the LL, NLL, and NNLL approximation. These generic structures are valid starting from $n = 1$ or $n = 2$ as indicated in the bottom row of the table. For smaller values of n, the correct $1/\bar{N}$ dependence must be extracted from the fixed order results; see text. Also, note that the entry for $\mathbb{C}^{S,(n)}_{L,g}$ at NNLL is obtained by $\mathcal{AC}$ relations; see text.

	$\mathbb{C}^{S,(n)}_{T,g}$	$\mathbb{C}^{S,(n)}_{T,q}$	$\mathbb{C}^{S,(n)}_{L,g}$	$\mathbb{C}^{S,(n)}_{L,q}$
LL	$\bar{N}^{-2n}$	–	$\bar{N}^{1-2n}$	–
NLL	$\bar{N}^{1-2n}$	$\bar{N}^{1-2n}$	$\bar{N}^{2-2n}$	$\bar{N}^{2-2n}$
NNLL	$\bar{N}^{2-2n}$	$\bar{N}^{2-2n}$	$\bar{N}^{3-2n}$	$\bar{N}^{3-2n}$
	$n \geq 1$	$n \geq 2$	$n \geq 1$	$n \geq 2$

Table 6.2: Same as Tab. 6.1 but for the splitting functions $P_{ij}^T = \sum_n a_s^{n+1} P_{ij}^{T,(n)}$.

	$P_{gg}^{T,(n)}$	$P_{gq}^{T,(n)}$	$P_{qq}^{T,(n)}$	$P_{qg}^{T,(n)}$
LL	$\bar{N}^{-1-2n}$	$\bar{N}^{-1-2n}$	–	–
NLL	$\bar{N}^{-2n}$	$\bar{N}^{-2n}$	$\bar{N}^{-2n}$	$\bar{N}^{-2n}$
NNLL	$\bar{N}^{1-2n}$	$\bar{N}^{1-2n}$	$\bar{N}^{1-2n}$	$\bar{N}^{1-2n}$
	$n \geq 0$	$n \geq 0$	$n \geq 2$	$n \geq 2$

two non-vanishing logarithmic contributions can be resummed for the time being. For this reason, the third entry for $\mathbb{C}_{L,g}^S$ in Tab. 6.1 has to be deduced using analytic continuation ($\mathcal{AC}$) relations between DIS and SIA; see Refs. [119–121, 357] for details.

6.1.2 The Idea of small-z Resummations

As already mentioned above, this chapter is dedicated to a specific class of double logarithms which are dominant for small momentum fractions z, so called "small-z logarithms". Large logarithmic contributions which spoil the the perturbative expansion are tamed by the techniques of resummation, where the logarithms are summed up to all orders in perturbation theory. Before presenting a systematic approach to resum small-z logarithms up to NNLL accuracy in the following Sec. 6.1.3, we start by looking into the LL case which can be understood in a quite instructive way from first principles. For the following discussion we closely follow Ref. [346].

The double logarithmic contribution to the cross section originates from configurations, where the unobserved part X consists of M soft gluons with momenta $k_1 \dots k_M$. Since they are part of the unobserved remainder, their phase space is fully integrated out. The cross section for the reaction $e^+e^- \to \gamma/Z \to q(p) + \bar{q}(\bar{p}) + g(k) + X$ can schematically be written as [346]

$$d\sigma(p, \bar{p}, k) = \sum_{M=0}^{\infty} d\sigma_{M+1}(p, \bar{p}, k, k_1, \dots, k_M)\,, \tag{6.10}$$

where $d\sigma_m(p, \bar{p}, k_1, \dots, k_m)$ denotes a cross section where m gluons with momenta $k_1 \dots k_m$ are produced in addition to the quark and anti-quark with momenta p and $\bar{p}$, respectively. Since the soft gluons are unobserved, the phase space integrations over the momenta k_α are implicitly understood in Eq. (6.10). It was shown in Ref. [358] that the double logarithms originate from strongly ordered kinematical configurations, i.e.

$$\begin{aligned} |\vec{k}| \ll |\vec{k}_1| \ll \cdots \ll |\vec{k}_M| \quad &\ll \quad \frac{Q}{2}\,, \\ \theta \ll \theta_1 \ll \cdots \ll \theta_M \quad &\ll \quad 1\,. \end{aligned} \tag{6.11}$$

In the eikonal approximation, the cross section for multiple soft gluon emission may be written as [359]

$$d\sigma_{M+1}(p, \bar{p}, k, k_1, \dots, k_M) \approx d\sigma^{\text{Born}}(p, \bar{p})\, dw_g(k)\, dw_g(k_1)\, \dots\, dw_q(k_M)\,. \tag{6.12}$$

The probability for the emission of a soft gluon from an initiation parton $I \in \{q, \bar{q}, g\}$ in the eikonal approximation for $n = 4 - 2\varepsilon$ dimensions reads [346, 359]

$$dw_I(k_\alpha) \equiv dw_I(\xi_\alpha, \zeta_\alpha) = \frac{\hat{\alpha}_s}{\pi} \left(\frac{\mu^2}{Q^2}\right)^{\varepsilon} \frac{(4\pi)^\varepsilon}{\Gamma(1-\varepsilon)} C_I \frac{d\xi_\alpha}{\xi_\alpha^{1+2\varepsilon}} \frac{d\zeta_\alpha}{\zeta_\alpha^{1+2\varepsilon}} \,. \tag{6.13}$$

The variables ξ_α and ζ_α follow from the usual Sudakov decomposition

$$k_\alpha = \xi_\alpha p + \zeta_\alpha \xi_\alpha \bar{p} + k_\alpha^\perp \,, \tag{6.14}$$

and hence are given by

$$\begin{aligned} \xi_\alpha &= \frac{\bar{p} \cdot k_\alpha}{\bar{p} \cdot p} \,, \\ \zeta_\alpha &= \frac{p \cdot k_\alpha}{\bar{p} \cdot k_\alpha} \,. \end{aligned} \tag{6.15}$$

Furthermore, in Eq. (6.13) we have introduced the mass scale μ (as usually done in dimensional regularization the keep to action dimensionless, see discussion below Eq. (1.29)) and the color factor C_I which depends on the parton species I and reads $C_q = C_{\bar{q}} = C_F$ and $C_g = C_A$ with $C_F = 4/3$ and $C_A = 3$ being the usual Casimir operators of $SU(3)$. Finally, $\hat{\alpha}_s$ denotes the unrenormalized coupling.

Following [346] we integrate out the unobserved degrees of freedom in Eq. (6.10) and normalize to the Born cross section. Moreover, we fix the momentum fraction ξ of the "observed" gluon to the experimentally measured momentum fraction z by replacing $dw_g(\xi, \zeta) \to dw_g(\xi', \zeta)\delta(\xi' - z)dz$ to obtain [346, 360]

$$\frac{1}{d\sigma^{\text{Born}}(p, \bar{p})} \frac{d\sigma(p, \bar{p}, z)}{dz} = \frac{C_F \, X \, z^{-1-2\varepsilon}}{C_A} \int_z^1 \frac{d\xi}{\xi} \, \xi \, G(\xi, X, \varepsilon) \,, \tag{6.16}$$

where after $\overline{\text{MS}}$ renormalization

$$X \equiv C_A \frac{\alpha_s(\mu_R^2)}{\pi} \left(\frac{\mu_R^2}{Q^2}\right)^{\varepsilon} \,. \tag{6.17}$$

Corrections of $\mathcal{O}(\varepsilon^2)$ and $\mathcal{O}(\alpha^2)$ to Eq. (6.17) give rise to contributions beyond LL accuracy and are not considered here. The function $G(\xi, X, \varepsilon)$ ist the probability for the inclusive emission of an observed gluon with momentum fraction ξ from an initiating gluon. It contains all the phase space integrations over the $d\xi_\alpha$ and $d\zeta_\alpha$ for the unobserved soft gluons. The integration limits respect the constraint dictated by Eq. (6.11), i.e. strongly ordered angles and momenta of the soft gluons. The explicit expression is rather lengthly and may be found in Ref. [346]. Since resummations are conveniently carried out in Mellin-N space, we only need the Mellin transform of G with respect to ξ, which is given by [346]

$$G(N, X, \varepsilon) \equiv \int_0^1 d\xi \, \xi^{N-1} \, G(\xi, X, \varepsilon) = \sum_{k=0}^{\infty} \left(-\frac{X}{2\varepsilon^2}\right)^k \frac{1}{k!} \frac{1}{\Pi_{p=1}^k \left(\frac{N}{2\varepsilon} - p\right)} \,. \tag{6.18}$$

Equation (6.18) is divergent for $\varepsilon \to 0$. This is not surprising, since we are looking at a quantity containing collinear divergencies. However, we can use the method of factorization described in Sec. 1.2 to express the function G in terms of a finite coefficient function C and a time-like transition function Γ which contains all the $1/\varepsilon$ poles. This factorized expression schematically reads [28, 346]

$$G(N, X, \varepsilon) = C\left(N, \alpha_s(Q^2), \varepsilon\right) \Gamma\left(N, \alpha_s(Q^2), \varepsilon\right) , \tag{6.19}$$

where, for simplicity, we have chosen the renormalization and factorization scales $\mu_R = \mu_F = Q$. This also implies $X = C_A\, \alpha_s(Q^2)/\pi$. Ideally, one would determine the finite coefficient functions by expanding Eq. (6.18) in ε, which apparently seems not be possible [346]. However, it was found in [346] that the function G satisfies the differential equation

$$\frac{\ddot{G} - \frac{\bar{N}}{2\varepsilon}\dot{G}}{G} = \frac{X}{2\varepsilon^2} , \tag{6.20}$$

where for a function $f(X)$ we have defined

$$\dot{f}(X) \equiv X \frac{df}{dX} . \tag{6.21}$$

We now insert Eq. (6.19) into (6.20) and use the relation [346]

$$\dot{\Gamma} = -\frac{P_{gg}^T}{\varepsilon}\Gamma , \tag{6.22}$$

to obtain

$$\frac{1}{\varepsilon^2}\left[\left(P_{gg}^T\right)^2 + \frac{\bar{N}\, P_{gg}^T}{2}\right] - \frac{1}{\varepsilon}\left[\left(2P_{gg}^T + \frac{\bar{N}}{2}\right)\frac{\dot{C}}{C} + \dot{P}_{gg}^T\right] + \frac{\ddot{C}}{C} = \frac{X}{2\varepsilon^2} . \tag{6.23}$$

We now compare the coefficients of ε^{-2} on both sides of Eq. (6.23), which yields a simple equation for P_{gg}^T with the solution [346]

$$P_{gg}^T = -\frac{1}{4}\left(\bar{N} - \sqrt{\bar{N}^2 + 8C_A \frac{\alpha_s}{\pi}}\right) , \tag{6.24}$$

which is nothing but the resummed gluon-gluon splitting function at LL accuracy. This result is consistent with the result available in literature [337–340, 358]. The comparison of the ε^{-1} coefficients in Eq. (6.23) yields [346]

$$\frac{\partial C}{\partial P_{gg}^T} = -\frac{1}{2}\frac{C}{P_{gg}^T + \frac{\bar{N}}{4}} , \tag{6.25}$$

and hence

$$C = \frac{A(\bar{N})}{\sqrt{P_{gg}^T + \frac{\bar{N}}{4}}} . \tag{6.26}$$

To determine the integration constant $A(\bar{N})$ one has to use the known result for the coefficient function from fixed order perturbation theory, i.e. $C(N, 0) = 1$, which gives $A(\bar{N}) = \sqrt{\bar{N}}/2$ [346]. Thus, we find for the resummed coefficient function at LL accuracy

$$C(N, \alpha_s) = \frac{1}{\left(1 + 8C_A \frac{\alpha_s}{\pi}\frac{1}{\bar{N}^2}\right)^{\frac{1}{4}}} . \tag{6.27}$$

Note that, for simplicity, we have only considered the inclusive production of an "observed" gluon in the discussion above. In the complete calculation [346], where also the inclusive production of a quark is considered, the factorized formula (6.19) consists of two components, one for the quark and the other for the gluon part. Moreover, the transition function becomes a 2 × 2 matrix. We refrain from showing any details here, since the aim of this section is to present the main idea of small-z resummations. In the following Sec. 6.1.3 we summarize the main result of Ref. [42] which is a systematic approach for small-z resummations up to NNLL accuracy, based on the ideas as presented above.

6.1.3 Small-z Resummations up to NNLL

The resummation of the first three towers of small-z logarithms, summarized in Tables 6.1 and 6.2, was performed recently in Refs. [42, 43] in a formalism based on all-order mass factorization relations and the general structure of unfactorized structure functions in SIA. Explicit analytical results can be found for the choice $\mu = Q$. The corresponding LL and NLL expressions are known for quite some time [337–340, 358] and have been derived by other means. We have adopted the same framework based on mass factorization as in [42, 43] and re-derived all results from scratch up to NNLL accuracy. We are in perfect agreement with all of their expressions except for some obvious, minor typographical errors [1]. In this section, we will concisely summarize the main aspects of the calculation as we will extend the obtained results to a general choice of scale $\mu \neq Q$ in the next subsection.

One starts from the unfactorized structure functions using dimensional regularization. In our case, we choose to work in $d = 4 - 2\varepsilon$ dimensions. The unfactorized partonic structure functions can be written as

$$\hat{\mathcal{F}}_{k,l}(N, a_s, \varepsilon) = \sum_{i=q,g} C_{k,i}(N, a_s, \varepsilon)\Gamma_{il}(N, a_s, \varepsilon)\,, \tag{6.28}$$

with $k = L, T$ and $l = q, g$. We have introduced the d-dimensional coefficient functions $C_{k,l}$, which contain only positive powers in ε,

$$C_{k,l}(N, a_s, \varepsilon) = \delta_{kT}\delta_{l,q} + \sum_{i=1}^{\infty} a_s^i \sum_{j=0}^{\infty} \varepsilon^j c_{k,l}^{(i,j)}(N)\,, \tag{6.29}$$

whereas the transition functions Γ_{ij} include all IR/mass singularities, which are manifest in $1/\varepsilon$ poles, i.e., they contain all negative powers of ε. The transition functions are calculable order by order in a_s by solving the equation

$$\beta_d(a_s)\frac{\partial \Gamma_{ik}}{\partial a_s}\Gamma_{kj}^{-1} = P_{ij}^T\,. \tag{6.30}$$

Here, $\beta_d(a_s) = -\varepsilon\, a_s - a_s^2 \sum_{i=0}^{\infty} \beta_i a_s^i$ denotes the d-dimensional beta function of QCD. Eq. (6.30) can be derived from the time-like evolution equations (as shown in Eq. (1.86))

---

[1] We noticed the following typographical errors in Ref. [42] which should be corrected as follows:

Eq. (2.12): $\left(\frac{67}{9}C_A - 4\zeta_2\right) \to \left(\frac{67}{9} - 4\zeta_2\right)$

Eq. (3.18) 1st line, last term: $-\frac{38}{9}C_A^2 C_F n_f \to -\frac{38}{9}C_A C_F^2 n_f$

Eq. (4.8) 2st line, last term: $-\frac{47}{9}C_F n_f^2 \to -\frac{47}{9}C_F^2 n_f$

Eq. (5.5) denominator: $9(N-1)^{2n-2} \to 9(N-1)^{2n-3}$

and its solution reads

$$\begin{aligned}\mathbf{\Gamma} \;=\;& \mathbb{1} - a_s \frac{\boldsymbol{P}^{T,(0)}}{\varepsilon} \\ & + a_s^2 \Big[\frac{1}{2\varepsilon^2}(\boldsymbol{P}^{T,(0)} + \beta_0)\boldsymbol{P}^{T,(0)} - \frac{1}{2\varepsilon}\boldsymbol{P}^{T,(1)} \Big] \\ & + a_s^3 \Big[-\frac{1}{6\varepsilon^3}(\boldsymbol{P}^{T,(0)} + \beta_0)(\boldsymbol{P}^{T,(0)} + 2\beta_0)\boldsymbol{P}^{T,(0)} \\ & \qquad + \frac{1}{6\varepsilon^2}\Big\{ (\boldsymbol{P}^{T,(0)} + 2\beta_0)\boldsymbol{P}^{T,(1)} + (\boldsymbol{P}^{T,(1)} + \beta_1)2\boldsymbol{P}^{T,(0)} \Big\} \\ & \qquad - \frac{1}{3\varepsilon}\boldsymbol{P}^{T,(2)} \Big] \\ & + \mathcal{O}(a_s^4) \end{aligned} \tag{6.31}$$

where

$$\boldsymbol{P}^T \equiv \sum_{i=0}^{\infty} a_s^{i+1} \boldsymbol{P}^{T,(i)} \equiv \sum_{i=0}^{\infty} a_s^{i+1} \begin{pmatrix} P_{qq}^{T,(i)} & P_{gq}^{T,(i)} \\ P_{qg}^{T,(i)} & P_{gg}^{T,(i)} \end{pmatrix} \tag{6.32}$$

is the 2 × 2 matrix that contains the time-like singlet splitting functions. Throughout this work, we use bold face characters to denote 2 × 2 matrices. Since we are interested only in the small-z regime, we take the small-$\bar{N}$ limit of the known coefficient and splitting functions in Eq. (6.28).

Alternatively, one can express the unfactorized partonic structure functions in Eq. (6.28) as a series in a_s,

$$\hat{\mathcal{F}}_{k,l}(N, a_s, \varepsilon) = \sum_n a_s^n \hat{\mathcal{F}}_{k,l}^{(n)}(N, a_s, \varepsilon)\,. \tag{6.33}$$

The key ingredient to achieve the resummations of the leading small-$\bar{N}$ contributions, which is the main result of [42], is the observation that the $\mathcal{O}(a_s^n)$ contribution in Eq. (6.33) may be written as

$$\hat{\mathcal{F}}_{k,l}^{(n)}(N, a_s, \varepsilon) = \varepsilon^{\delta_{kL}+\delta_{lq}+1-2n} \sum_{i=0}^{n-1-\delta_{lq}} \frac{1}{\bar{N} - 2(n-i)\varepsilon} \left(A_{k,l}^{(i,n)} + \varepsilon B_{k,l}^{(i,n)} + \varepsilon^2 C_{k,l}^{(i,n)} + \dots \right). \tag{6.34}$$

Each of the coefficients A, B, and C is associated with a different logarithmic accuracy of the resummation, i.e., LL, NLL, and NNLL, respectively.

By equating Eqs. (6.28) and (6.33), one obtains a system of equations which may be solved recursively order by order in a_s. The small-z (small-$\bar{N}$) limits of the fixed order results are needed here as initial conditions for the first recursion. Since these results are only known up to NNLO accuracy, resummations are limited for the time being to the first three towers listed in Tables 6.1 and 6.2. At each order n, this procedure then yields expressions for $c_{k,l}^{(n,m)}$, $P_{ij}^{T,(n-1)}$, $A_{k,l}^{(m,n)}$, $B_{k,l}^{(m,n)}$, and $C_{k,l}^{(m,n)}$.

Note that up to NNLL accuracy only β_0 is needed in Eq. (6.31). All terms proportional $\beta_{i\geq 1}$ will generate subleading contributions and, hence, can be discarded. For instance, when initiating the recursive solution, $\boldsymbol{P}^{T,(0)}$ and $\boldsymbol{P}^{T,(1)}$ are known from fixed order calculations, and $\boldsymbol{P}^{T,(2)}$, that appears at $\mathcal{O}(a_s^3)$ in Eq. (6.31), is the unknown function that is being determined. The NNLL contribution for, say, $P_{gg}^{T,\,(2)}$ is $\propto 1/\bar{N}^2$, cf. Table 6.2, whereas the highest inverse power of $\bar{N}$ in the term $\beta_1 P_{gg}^{T,\,(0)}$ appearing in the curly brackets of Eq. (6.31) is $\propto 1/\bar{N}$ and, thus, beyond NNLL accuracy.

After solving the system of equations algebraically using MATHEMATICA [361], we find expressions for $c_{k,l}^{(n,0)}$, and $P_{ij}^{T,(n)}$. Since the coefficient functions and the splitting functions both have a perturbative expansion in a_s,

$$P_{ij}^{T} = \sum_{n=0}^{\infty} a_s^{n+1} P_{ij}^{T,\,(n)} \tag{6.35}$$

and

$$\mathbb{C}_{k,l}^{\mathrm{S}} = \sum_{n=0}^{\infty} a_s^{n} c_{k,l}^{(n,0)} \tag{6.36}$$

one can eventually deduce a closed expression for resummed splitting functions and coefficient functions as listed in [43]. As mentioned above, we fully agree with these results up to the typographical errors listed in the footnote.

6.1.4 Resummed Scale Dependence

All calculations presented so far, including Refs. [42, 43], have been performed by identifying, for simplicity, the renormalization and factorization scales with the hard scale Q, i.e., by setting $\mu_F = \mu_R = \mu = Q$. However, it is well known that the resummation procedure should not only yield more stable results but should also lead to a better control of the residual dependence on the unphysical scales μ_F and μ_R that arises solely from the truncation of the perturbative series. Hence, for our subsequent studies of the phenomenological impact of the small-z resummations on the extraction of FFs from SIA data it is imperative to separate the dependence on the artificial scales μ_F and μ_R from the hard scale Q in the resummed expressions. This is the goal of this section. In what follows, we reinstate the scale dependence with two different, independent methods. We find full agreement between the two approaches.

Firstly, we consider a renormalization group approach; see also Ref. [362]. The dependence of the coefficient functions on the factorization scale μ_F can be expressed as

$$\mathbb{C}_{k,l}^{\mathrm{S}}(N, a_s, L_M) = \sum_{i=0}^{\infty} a_s^{i} \left(c_{k,l}^{(i)}(N) + \sum_{m=1}^{i} \tilde{c}_{k,l}^{(i,m)}(N) L_M^{m} \right) , \tag{6.37}$$

with $L_M \equiv \log \frac{Q^2}{\mu_F^2}$. The coefficients $c_{k,l}^{(i)} \equiv \tilde{c}_{k,l}^{(i,0)}$ are the finite (i.e., ε independent) coefficients as given in Eq. (6.29). The $\tilde{c}_{k,l}^{(i,m)}$ can be calculated order by order in a_s by solving a set of renormalization group equations (RGEs). These equations can be obtained by requiring that $\frac{d}{d\log\mu_F^2} F_k \overset{!}{=} 0$, where $F_k \equiv \sum_l \mathbb{C}_{k,l} D_l$ (see Eq. (6.3) for the definition of these structure functions in z space), which leads to

$$\left[\left\{ \frac{\partial}{\partial \log \mu_F^2} + \beta(a_s) \frac{\partial}{\partial a_s} \right\} \delta_{lm} + P_{lm}^{T}(N) \right] \mathbb{C}_{k,m}^{\mathrm{S}}(N, a_s, L_M) = 0\,. \tag{6.38}$$

Here, the sum over $m = q, g$ is left implicit. For the sake of better readability, we drop the arguments of all functions for now. From (6.38), the following recursive formula can be obtained

$$\tilde{c}_{k,l}^{(i,m)} = \frac{1}{m} \sum_{w=m-1}^{i-1} \tilde{c}_{k,j}^{(w,m-1)} \left(P_{lj}^{T,\,(i-w-1)} - w\beta_{i-w-1}\delta_{jl} \right) . \tag{6.39}$$

Again, the sum over $j = q, g$ is implicitly understood. Up to NNLO accuracy, we obtain the same results as given in [84].

If one now plugs in the small-$\bar{N}$ results for the splitting and coefficient functions, one can compute the coefficients $\tilde{c}_{k,l}^{(n,m)}$ up to any order n and identify the leading three towers of $1/\bar{N}$ in Eq. (6.37), i.e., the LL, NLL, and NNLL contributions. At order n we find at LL accuracy

$$\mathbb{C}_{k,g}^{\mathrm{S,LL},(n)} = c_{k,g}^{\mathrm{LL},(n)} . \tag{6.40}$$

Thus, no improvement of the scale dependence is achieved by a LL resummation (recall that resummation in the quark sector only starts at NLL accuracy). The full L_M dependence is given by the fixed-order expressions, which have to be matched to the resummed result for all practical purposes. As usual, the matching of a resummed observable T^{res} to its N$^\kappa$LO fixed-order expression $T^{\mathrm{N}^\kappa\mathrm{LO}}$ is performed according to the prescription schematically given by

$$T^{\mathrm{matched}} = T^{\mathrm{N}^\kappa\mathrm{LO}} + T^{\mathrm{res}} - T^{\mathrm{res}}|_{\mathcal{O}(a_s^\kappa)} . \tag{6.41}$$

Here, $T^{\mathrm{res}}|_{\mathcal{O}(a_s^\kappa)}$ denotes the expansion in a_s of T^{res} up to order $\mathcal{O}(a_s^\kappa)$.

Likewise, at NLL accuracy one obtains the following results

$$\mathbb{C}_{T,g}^{\mathrm{S,NLL},(n)} = c_{T,g}^{\mathrm{NLL},(n)} + L_M \left\{ P_{gq}^{T\,\mathrm{LL},(n-1)} + \sum_{j=0}^{n-2} c_{T,g}^{\mathrm{LL},(n-1-j)} P_{gg}^{T\,\mathrm{LL},(j)} \right\} , \tag{6.42}$$

$$\mathbb{C}_{L,g}^{\mathrm{S,NLL},(n)} = c_{L,g}^{\mathrm{NLL},(n)} + L_M \sum_{j=0}^{n-2} c_{L,g}^{\mathrm{LL},(n-1-j)} P_{gg}^{T\,\mathrm{LL},(j)} \tag{6.43}$$

and

$$\mathbb{C}_{T,q}^{\mathrm{S,NLL},(n)} = c_{T,q}^{\mathrm{NLL},(n)} , \tag{6.44}$$

$$\mathbb{C}_{L,q}^{\mathrm{S,NLL},(n)} = c_{L,q}^{\mathrm{NLL},(n)} . \tag{6.45}$$

The scale dependent terms $\propto L_M$ enter here for the first time in the gluonic sector, Eqs (6.42) and (6.43), and are expressed in terms of LL quantities. Due to the fact that the quark coefficient functions are subleading, they still do not carry any scale dependence at NLL.

Finally, at NNLL accuracy one finds

$$\begin{aligned}
\mathbb{C}_{T,g}^{\mathrm{S,NNLL},(n)} &= c_{T,g}^{\mathrm{NNLL},(n)} \\
&\quad + L_M \Bigg\{ P_{gq}^{T\,\mathrm{NLL},(n-1)} - (n-1)\beta_0 c_{T,g}^{\mathrm{LL},(n-1)} + \sum_{j=0}^{n-3} c_{T,q}^{\mathrm{NLL},(n-1-j)} P_{gq}^{T\,\mathrm{LL},(j)} \\
&\qquad + \sum_{j=0}^{n-2} \left(c_{T,g}^{\mathrm{LL},(n-1-j)} P_{gg}^{T\,\mathrm{NLL},(j)} + c_{T,g}^{\mathrm{NLL},(n-1-j)} P_{gg}^{T\,\mathrm{LL},(j)} \right) \Bigg\} \\
&\quad + \frac{L_M^2}{2} \Bigg[\sum_{j=0}^{n-2} P_{gq}^{T\,\mathrm{LL},(n-2-j)} P_{gg}^{T\,\mathrm{LL},(j)} \\
&\qquad + \sum_{i=0}^{n-3} \sum_{j=0}^{n-2-i} c_{T,g}^{\mathrm{LL},(n-2-i-j)} P_{gg}^{T\,\mathrm{LL},(i)} P_{gg}^{T\,\mathrm{LL},(j)} \Bigg] , \qquad (6.46)
\end{aligned}$$

$$\begin{aligned}
\mathbb{C}_{L,g}^{\mathrm{S,NNLL},(n)} &= c_{L,g}^{\mathrm{NNLL},(n)} \\
&\quad + L_M \Bigg\{ -(n-1)\beta_0 c_{L,g}^{\mathrm{LL},(n-1)} \\
&\qquad + \sum_{j=0}^{n-2} \left(c_{L,g}^{\mathrm{LL},(n-1-j)} P_{gg}^{T\,\mathrm{NLL},(j)} + c_{L,g}^{\mathrm{NLL},(n-1-j)} P_{gg}^{T\,\mathrm{LL},(j)} \right) \\
&\qquad + \sum_{j=0}^{n-2} c_{L,q}^{\mathrm{NLL},(n-1-j)} P_{gq}^{T\,\mathrm{LL},(j)} \Bigg\} \\
&\quad + \frac{L_M^2}{2} \sum_{i=0}^{n-3} \sum_{j=0}^{n-3-i} c_{L,g}^{\mathrm{LL},(n-2-i-j)} P_{gg}^{T\,\mathrm{LL},(i)} P_{gg}^{T\,\mathrm{LL},(j)} , \qquad (6.47)
\end{aligned}$$

$$\begin{aligned}
\mathbb{C}_{T,q}^{\mathrm{S,NNLL},(n)} &= c_{T,q}^{\mathrm{NNLL},(n)} \\
&\quad + L_M \Bigg\{ P_{qq}^{T\,\mathrm{NLL},(n-1)} (1-\delta_{n,2}) + \sum_{j=0, j\neq 1}^{n-1} c_{T,g}^{\mathrm{LL},(n-1-j)} P_{qg}^{T\,\mathrm{NLL},(j)} \Bigg\} ,
\end{aligned} \qquad (6.48)$$

and

$$\mathbb{C}_{L,q}^{\mathrm{S,NNLL},(n)} = c_{L,q}^{\mathrm{NNLL},(n)} + L_M \sum_{j=0, j\neq 1}^{n-2} c_{L,g}^{\mathrm{LL},(n-1-j)} P_{qg}^{T\,\mathrm{NLL},(j)} . \qquad (6.49)$$

It should be noticed that by the subscripts LL, NLL, and NNLL in Eqs. (6.40) and (6.42)-(6.49), we denote *only* those contributions in $1/\bar{N}$ specific to the tower at LL, NLL, or NNLL accuracy, respectively. This means, for instance, that the full next-to-next-to-leading logarithmic expression at some given order n in the a_s perturbative expansion of $\mathbb{C}_{k,l}^{\mathrm{S}}$ in Eq.(6.37) will be always given by the *sum* of the individual LL, NLL, and NNLL contributions. As one may expect from the fixed-order results, the scale dependence at N^mLL is expressed entirely in terms of the resummed expressions at N^kLL with $k < m$. Since the resummed results are known up to NNLL accuracy, we may, in principle, extend our calculations to fully predict the scale dependent terms at N^3LL. These findings are consistent with the scale dependence of fixed-order cross sections. Finally, for all practical purposes, as we shall see below, it is numerically adequate to have explicit results for each tower up to sufficiently high order in n, say, $n = 20$, in lieu of a closed analytical expression for the resummed series as was provided for the case $\mu = Q$ in Refs. [42, 43].

We may now reintroduce the renormalization scale dependence as well by following the straightforward steps outlined in Ref. [84]. In practice, this amounts to replacing all couplings a_s in the expressions given above according to

$$a_s(\mu_F^2) = a_s(\mu_R^2)\left(1 + a_s(\mu_R^2)\beta_0 \log\frac{\mu_R^2}{\mu_F^2} + \mathcal{O}(a_s^2)\right) . \tag{6.50}$$

In a second step one needs to re-expand all results in terms of $a_s(\mu_R^2)$ which leads to additional logarithms of the type $L_R \equiv \log(\mu_R^2/\mu_F^2)$. In our phenomenological studies below we will study, however, only the case $\mu_F = \mu_R \neq Q$ and, hence, we do not pursue the L_R dependence any further.

The second approach we adopt to recover the scale dependence of the SIA coefficient functions obtained in Sec. 6.1.3 is based on the all-order mass factorization procedure. After removing the ultraviolet (UV) singularities from the bare partonic structure functions $\hat{\mathcal{F}}_{k,l}$ (which have been computed directly from Feynman diagrams) by a suitable renormalization procedure, the remaining final-state collinear/mass singularities have to be removed by mass factorization

$$\tilde{\mathcal{F}}_{k,l} = \mathbb{C}_{k,i} \otimes \tilde{\Gamma}_{li} \, . \tag{6.51}$$

Here, all singularities are absorbed into the transition functions $\tilde{\Gamma}_{li}$ while the coefficient functions $\mathbb{C}_{k,i}$ are finite. We have labeled the quantities in Eq. (6.51) with a tilde to show that they contain the full dependence on all scales.

We may thus proceed in the following way: first, we "dress" the transition functions and partonic structure functions in Eq. (6.28) with the appropriate scale dependence, i.e., we substitute $a_s \to a_s \cdot (\mu_F^2/\mu^2)^{-\varepsilon}$ in the Γ_{ij} and $a_s \to a_s \cdot (Q^2/\mu^2)^{-\varepsilon}$ in the $\hat{\mathcal{F}}_{k,l}$, where the mass parameter μ stems from adopting dimensional regularization. As a next step, we go back to the unrenormalized expressions, where we assume that the renormalization was performed at the scale μ_F^2 and Q^2, respectively. Afterwards, we perform renormalization again, but now at a different scale μ_R^2. Schematically, this amounts to

$$\tilde{\Gamma}_{ij} = R_{\mu^2}^{\mu_R^2}\left[(R_{\mu^2}^{\mu_F^2})^{-1}\left[\Gamma_{ij}(a_s \to a_s \cdot (\mu_F^2/\mu^2)^{-\varepsilon})\right]\right] \tag{6.52}$$

and

$$\tilde{\mathcal{F}}_{k,l} = R_{\mu^2}^{\mu_R^2}\left[(R_{\mu^2}^{Q^2})^{-1}\left[\mathcal{F}_{k,l}(a_s \to a_s \cdot (Q^2/\mu^2)^{-\varepsilon})\right]\right] . \tag{6.53}$$

Here, we are using the following notation: with $R_{\mu^2}^{\mu_R^2}[\hat{f}(\hat{a}_s)] = f[a_s(\mu_R^2)]$ we denote the renormalization of a bare quantity $\hat{f}(\hat{a}_s)$ which, as indicated, depends on the unrenormalized, bare coupling $\hat{a}_s$. This procedure yields a renormalized quantity $f[a_s(\mu_R^2)]$, which now depends on the physical coupling $a_s(\mu_R^2)$. The renormalization procedure $R_{\mu^2}^{\mu_R^2}$ is performed by replacing the bare coupling with

$$\hat{a}_s = a_s(\mu_R^2) Z(\mu_R^2, \mu^2)\,, \tag{6.54}$$

where we have introduced the renormalization constant

$$Z(\mu_R^2, \mu^2) \equiv \left[1 - a_s(\mu_R^2) \cdot \left(\frac{\mu_R^2}{\mu^2}\right)^{-\varepsilon} \frac{\beta_0}{\varepsilon} + \mathcal{O}(a_s^2)\right]. \tag{6.55}$$

Analogously, $(R_{\mu^2}^{\mu_R^2})^{-1}[f[a_s(\mu_R^2)]] = \hat{f}(\hat{a}_s)$ performs the inverse operation, i.e., it translates the renormalized quantity $f(a_s(\mu_R^2))$ back to the corresponding bare quantity $\hat{f}(\hat{a}_s)$. This is achieved by replacing the renormalized coupling with

$$a_s(\mu_R^2) = \hat{a}_s \hat{Z}(\mu_R^2, \mu^2)\,, \tag{6.56}$$

where the "inverse" renormalization constant reads

$$\hat{Z}(\mu_R^2, \mu^2) \equiv \left[1 + \hat{a}_s \cdot \left(\frac{\mu_R^2}{\mu^2}\right)^{-\varepsilon} \frac{\beta_0}{\varepsilon} + \mathcal{O}(\hat{a}_s^2)\right]. \tag{6.57}$$

The latter can be obtained from Eq. (6.55) by a series reversion. After substituting Eqs. (6.52) and (6.53) into Eq. (6.51) one can solve the latter equation for the coefficients $\mathbb{C}_{k,i}$, which now exhibit the full dependence on μ_R and μ_F.

In order to generate the renormalization constant Z in Eq. (6.55) at each order n in an expansion in a_s with the maximal precision available at this time (i.e., up to terms proportional to β_i, $i \leq 2$), we adopt renormalization group techniques (see, for instance, [69]). The general form of the renormalization constant reads

$$Z = 1 + \sum_{k=1}^{\infty} a_s^k \sum_{l=1}^{k} \frac{f_{k,l}}{\varepsilon^l} \tag{6.58}$$

and may also be written as

$$Z = 1 + \sum_{l=1}^{\infty} \frac{g_l(a_s)}{\varepsilon^l} \tag{6.59}$$

where $g_l(a_s) = \sum_{k=l}^{\infty} a_s^k f_{k,l}$ is a power series in a_s with l being the lowest power. Using the RGE it is possible to derive a recursive formula for this power series,

$$g'_{k+1}(a_s) = g'_1(a_s) \frac{d(a_s g_k(a_s))}{da_s}\,. \tag{6.60}$$

Here the prime denotes a derivative with respect to a_s. Hence, we obtain $g_{k+1}(a_s)$ by integration of Eq. (6.60). From the expression of the renormalization constant up to a_s^3, see, for example Ref. [363], we obtain as initial conditions

$$f_{1,1} = -\beta_0, \qquad f_{2,1} = -\frac{\beta_1}{2}, \qquad f_{3,1} = -\frac{\beta_2}{3}\,. \tag{6.61}$$

As already stated above, only terms proportional to β_0 are relevant up to NNLL accuracy.

6.1.5 Solution to the time-like Evolution Equation with a resummed Kernel

The dependence of the gluon and N_f quark and antiquark FFs on the factorization scale μ_F is governed by a set of $2N_f + 1$ RGEs. We have extensively discussed the methods and strategies used in the fixed-order approach in Sec. 1.3.2. Here, we extend the technical framework to solve Eq. (1.68) in Mellin moment space to the resummed case.

Instead of the fixed-order expressions defined in Eq. (1.69), we shall consider the resummed results for the splitting functions $P_{jl}^{T\ \mathrm{N}^{\kappa}\mathrm{LL}}$ as discussed in Sec. 6.1.3 and listed in Ref. [42, 43]. They obey a similar expansion in a_s as in Eq.(1.69), which reads

$$P_{ji}^{T\ \mathrm{N}^{\kappa}\mathrm{LL}} = \sum_{n=0}^{\infty} a_s^{n+1} P_{ji}^{T\ \mathrm{N}^{\kappa}\mathrm{LL},(n)} \,, \tag{6.62}$$

where each term $P_{ji}^{T\ \mathrm{N}^{\kappa}\mathrm{LL},(n)}$ in (6.62) is, in principle, known up to NNLL accuracy, i.e., for $\kappa = 0$, 1, and 2.

The simplest way of extending the fixed-order framework outlined in Sec. 1.3.2 to the resummed case is to take the *iterated solution* which we have introduced in that section. However, instead of setting contributions beyond the fixed order to zero, we use the resummed expressions. One can define a N^{m}LO+N$^\kappa$LL resummed “matched solution” by defining the k-th term of the splitting matrix which appears in Eq. (1.82) as follows:

$$\widetilde{\boldsymbol{P}}^{T,(k)} \equiv \begin{cases} \widetilde{\boldsymbol{P}}^{T\ \mathrm{FO},(k)} & k \leq m\,, \\ \widetilde{\boldsymbol{P}}^{T\ \mathrm{N}^{\kappa}\mathrm{LL},(k)} & k > m\,. \end{cases} \tag{6.63}$$

In other words, the full fixed-order expressions $\widetilde{\boldsymbol{P}}^{T\ \mathrm{FO},(k)}$ for $k \leq m$ are kept in $\boldsymbol{R}_k$, whereas we use the resummed expressions for $k > m$. This iterated and matched solution is the one implemented in our numerical code and will be used in Sec. 6.2 for all our phenomenological studies. For the range of z-values covered by the actual data sets considered in this chapter, only the terms up to $k = 20$ are indeed numerically relevant as we shall discuss further in Sec. 6.1.6. However, when evolving the FFs in scale with such an extended iterative solution, one finds that momentum conservation is broken to some extent due to missing sub-leading terms in the evolution kernels.

In fact, total momentum conservation for FFs is expressed by the sum rules for combinations of splitting functions, see, e.g. Ref. [104].

$$\begin{aligned} \int_0^1 dx\, x \left(P_{qq}^T(x) + P_{gq}^T(x)\right) &= 0\,, \\ \int_0^1 dx\, x \left(P_{gg}^T(x) + P_{qg}^T(x)\right) &= 0\,. \end{aligned} \tag{6.64}$$

In terms of Mellin moments, these relations read

$$P_{qq}^T(N=2) + P_{gq}^T(N=2) = 0\,, \tag{6.65}$$

$$P_{gg}^T(N=2) + P_{qg}^T(N=2) = 0\,. \tag{6.66}$$

These sum rules are satisfied, i.e., built into the kernels, at any given fixed order.

In the case of the iterated and matched solution we use in our numerical implementation, the sum rules in Eqs. (6.65) and (6.66) deviate from zero only about a few ‰ which is perfectly tolerable. We note, that in calculations of the SIA cross section, we also adopt the matching procedure for the relevant resummed coefficient functions as specified in Eq. (6.41).

However, when evaluating the sum rules without matching, the sums in (6.65) and (6.66) yield the approximate values 0.05 and 0.1, respectively, which is, of course, not acceptable.

We would like to point out that a NLO *truncated* + resummed solution has been proposed in Ref. [356]. Its extension to NNLO accuracy and the numerical comparison with its *iterated* counterpart as discussed above is not pursued in this chapter but will be subject to future work.

Given that the logarithmic contributions to the NS splitting function are subleading up to the NNLL accuracy considered in this chapter, see Ref. [43], no small-z effects have to be considered. The usual fixed-order NS evolution equations and kernels should be used instead.

6.1.6 Numerical Implementation

In this section, we will review how to adapt the numerical implementation of the fixed-order results up to NNLO accuracy, as discussed in Ref. [117] to include also the small-z resummations as discussed above.

Following the discussions on the iterated solution in Sec. 6.1.5, we start with assessing the order k in $\boldsymbol{P}^{T\ \mathrm{N}^{\kappa}\mathrm{LL},(k)}$ that is necessary to capture the behavior of fully resummed series down to values of z relevant for phenomenological studies of SIA data in terms of scale-dependent FFs. To this end, we study the convergence of the series expansion of the resummed expressions when evaluated up to a certain order k. This is achieved by first expanding the resummed splitting functions in Mellin N space and then using an appropriate numerical Mellin inversion, see below, to compare the expanded result with the fully resummed splitting functions in z-space given in [42, 43]. A typical example, the gluon-to-gluon splitting function, is shown in Fig. 6.1. As can be seen, $k = 20$ in the expansion is accurate at a level of less than 0.3‰ differences down to values of $z \approx 10^{-5}$. This is more than sufficient for all phenomenological studies as SIA data only extend down to about $z = 10^{-3}$ as we shall discuss later.

However, the splitting functions enter the scale evolution of the FFs in a highly non-trivial way, cf. Eqs. (1.81) and (1.82), such that this convergence property does not directly imply that the effects of truncating the expansion at $\mathcal{O}(k = 20)$ are also negligible in the solution of the evolution equations. To explore this further, we recall that the N-space version of Eq. (1.68) reads

$$\frac{\partial}{\partial \ln \mu^2} D_i^h(N, \mu^2) = \sum_j \widetilde{P}_{ji}^T(N, \mu^2) \cdot D_j^h\left(N, \mu^2\right) , \tag{6.67}$$

where $\widetilde{P}_{ji}^T$ is the ij-entry of the 2×2 singlet matrix in (1.83). One can solve this equation numerically with the fully resummed kernels, assuming some initial set of FFs, and compare the resulting, evolved distributions with the corresponding FFs obtained from the iterative solution of Eq. (1.84) at $\mathcal{O}(k = 20)$ defined in Sec. 6.1.5. Again, we find that the two results agree at a level of a few per mill for $z \gtrsim 10^{-5}$, i.e., after transforming the evolved FFs from N to z-space.

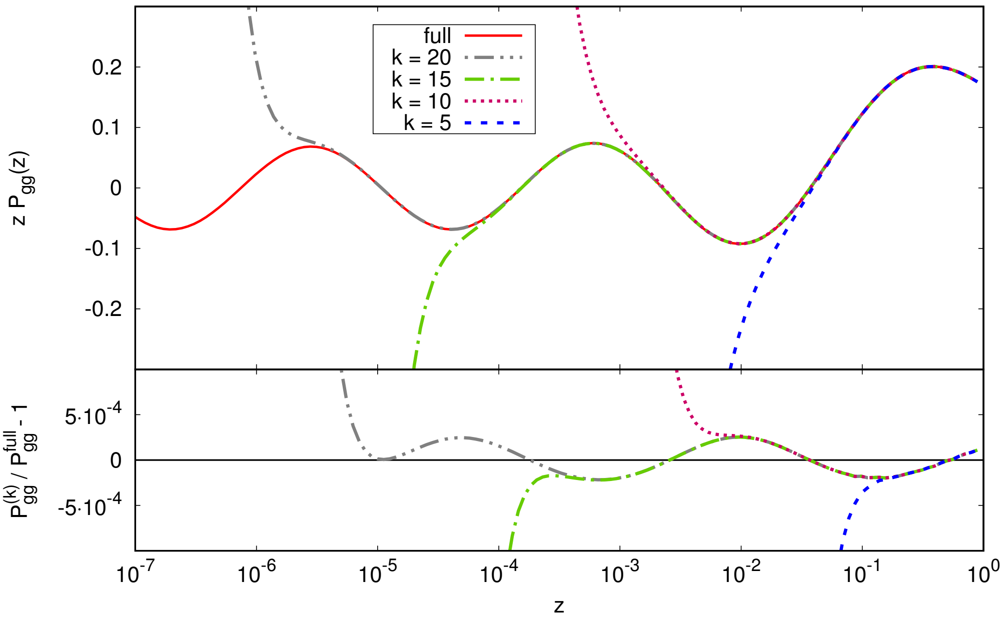

Figure 6.1: Upper panel: expansion of the splitting function $P_{gg}(z)$ times z at NNLL accuracy for different upper values of k compared to the fully resummed expression of Ref. [42, 43]. Lower panel: deviation of the full and $\mathcal{O}(k)$ expanded results. All functions are evaluated at $Q^2 = 110\,\mathrm{GeV}^2$ and $N_f = 5$ active flavors.

In general, the Mellin inversion of a function $f(N)$ was defined in Eq. (1.79) and reads

$$f(z) = \frac{1}{2\pi i}\int_{\mathcal{C}_N} dN\, z^{-N}\, f(N)\,, \tag{6.68}$$

where the contour $\mathcal{C}_N$ in the complex plane is usually taken parallel to the imaginary axis with all singularities of the function $f(N)$ to its left. For practical purposes, i.e. faster numerical convergence, one chooses a deformed contour instead, which can be parametrized in terms of a real variable t, an angle φ, and a real constant c as $N(t) = c + te^{i\varphi}$; see Fig. 6.2 for an illustration of the chosen path and Ref. [118] for further details.

In order to properly choose the contour parameters c and φ, we proceed as in Ref. [117] and analyze the pole structure of the evolution kernels $\mathcal{K}^T_{ij}$. They are defined as the entries of the 2×2 time-like evolution matrix in

$$\boldsymbol{D}^h(N, a_s) = \begin{pmatrix} \mathcal{K}^T_{11}(a_s, a_0, N) & \mathcal{K}^T_{12}(a_s, a_0, N) \\ \mathcal{K}^T_{21}(a_s, a_0, N) & \mathcal{K}^T_{22}(a_s, a_0, N) \end{pmatrix} \boldsymbol{D}^h(N, a_0)\,, \tag{6.69}$$

i.e. they encompass all the evolution matrices $\boldsymbol{U}_k$ on the right-hand-side of Eq. (1.84).

In complete analogy to what was found in Ref. [356] in the space-like case, the fully resummed time-like splitting functions exhibit additional singularities as compared to the fixed order expressions. Their location in the complex plane away from the real axis depends on the value

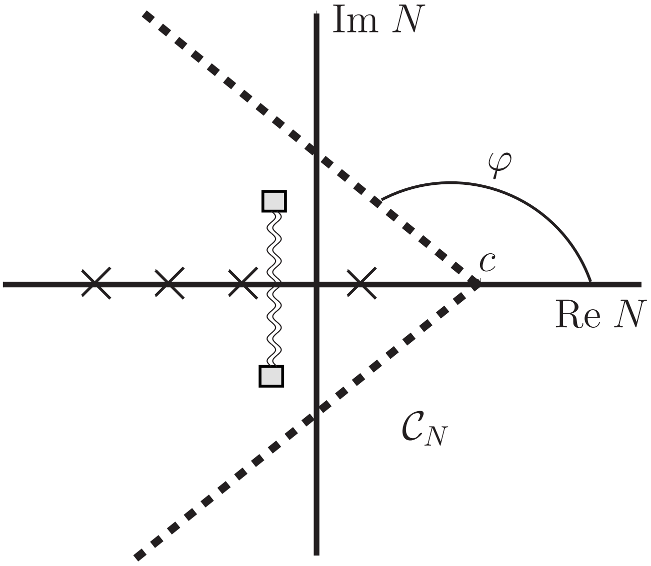

Figure 6.2: The dashed line represents the standard contour $\mathcal{C}_N$ in the complex N plane for the inverse Mellin transformation (6.70). The poles of the integrand along the real axis are schematically represented by crosses, whereas the poles lying in the complex plane away from the real axis are represented by squares. The branch cut is illustrated by the wiggly line.

of a_s. More specifically, if we consider, for instance, P_{gg}^{T} at NLL [43], one can identify terms proportional to $\left(\sqrt{1+32C_A a_s(\mu)/(N-1)^2}\right)^{-1}$ which lead to poles at $N = 1 \pm i\sqrt{32C_A a_s(\mu)}$ that are connected by a branch cut. If we had chosen to directly solve Eq. (6.67) numerically with the fully resummed splitting functions, the appropriate choice of contour for the Mellin inversion in Fig. 6.2 would have to be μ dependent as the position of these poles, denoted by the squares, depends on $a_s(\mu)$.

In the iterative solution, which we adopt throughout, only the expanded splitting functions $\boldsymbol{P}^{T\ \mathrm{N}^{\kappa}\mathrm{LL},(k)}$ enter the $\mathcal{K}_{ij}^{T}$ in Eq. (6.69). Therefore, the evolution is not affected by the singularities present in the fully resummed kernels, and a unique, μ-independent choice of the contour parameters c and φ is still possible. In our numerical code, we take $c = 4$ and $\varphi = 3/4\,\pi$. This choice also tames numerical instabilities generated, in particular, by large cancellations caused by the oscillatory behavior in the vicinity of the $N = 1$ pole. This is visualized in the upper panel of Fig. 6.3. Here, we show the real part of the singlet evolution kernel $\mathrm{Re}\{\mathcal{K}_{12}^{T}\}$ defined in Eq. (6.69) at NLO+NNLL accuracy and $Q^2 = 110\,\mathrm{GeV}^2$. The numerical instabilities are well recognizable near the $N = 1$ pole.

Finally, in order to perform a fit of FFs based on SIA data one has to compute the multiplicities as defined in Eq. (6.2). As was mentioned above, in order to arrive at a fast but reliable numerical implementation of the fitting procedure, we choose to evaluate the SIA cross section also in Mellin moment space and, then, perform a numerical inverse transformation to

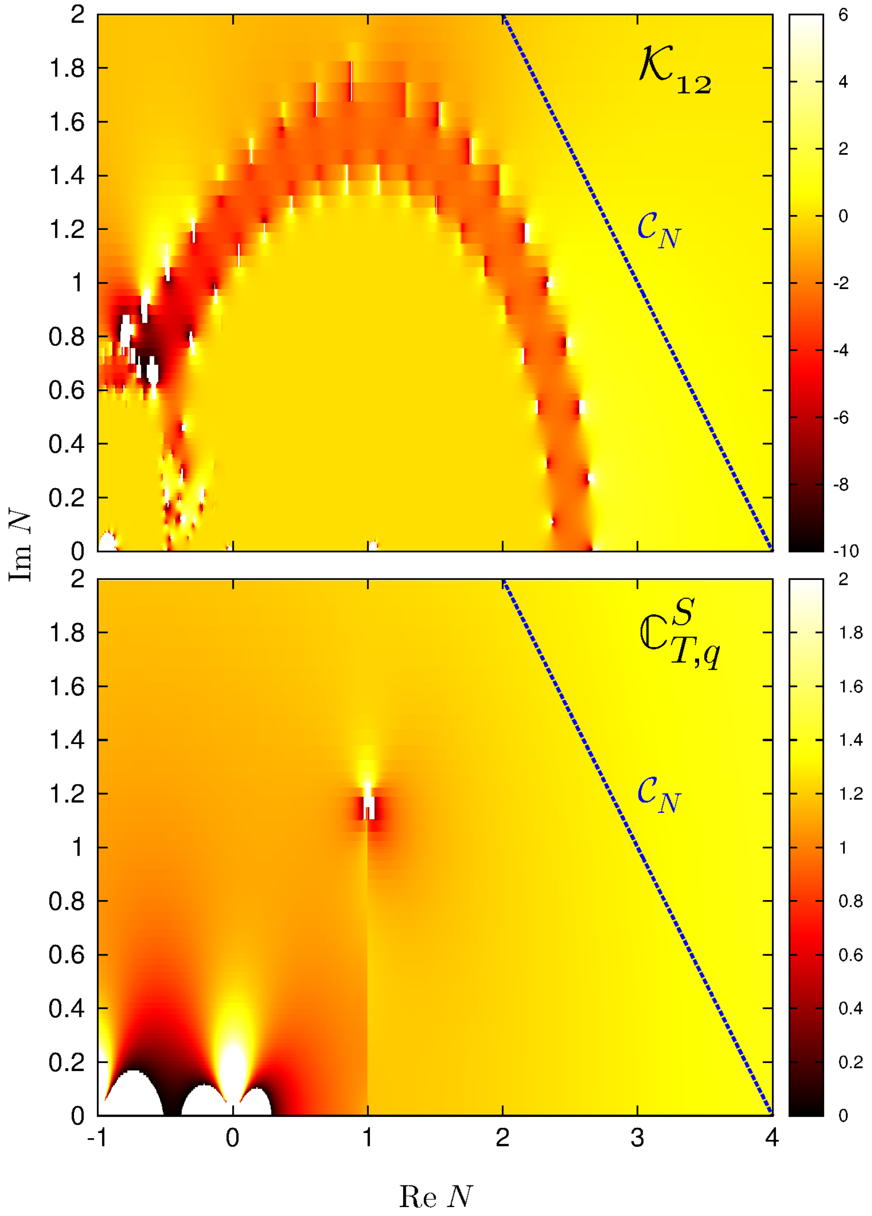

Figure 6.3: Upper panel: real part of $\mathcal{K}_{12}$ in Eq. (6.69) in a portion of the complex N plane. Lower panel: as above but for the coefficient function $\mathbb{C}^S_{T,q}(N)$. Both quantities are computed at NLO+NNLL accuracy for $Q^2 = 110\,\text{GeV}^2$. The line corresponds to the contour $\mathcal{C}_N$ in (6.70).

z-space. Schematically, one has to compute integrals of the form

$$D(z) \otimes \mathbb{C}(z) = \frac{1}{2\pi i} \int_{\mathcal{C}_N} dN\, z^{-N}\, D(N)\, \mathbb{C}\,(N)\ , \tag{6.70}$$

where the FFs $D(N)$ are given by Eq. (1.84); for brevity, we have omitted any dependence on the scale μ and the parton flavor. In principle, while performing the Mellin inversion, one has to deal with the same kind of a_s-dependent singularities in the fully resummed resummed coefficient functions, cf. Ref. [43], that we have just encountered in the resummed splitting functions. In the lower panel of Fig. 6.3, we show the real part of the coefficient function $\mathbb{C}^S_{T,q}(N)$ for which the pole structure and the branch cut are again well recognizable. However, for the typical scales relevant for a phenomenological analysis ($\mu = 10.5 - 91.2$ GeV; see Sec. 6.2), our choice of contour $\mathcal{C}_N$ is nevertheless applicable since the position of the singularities does not change considerably in this range of energies.

6.2 Phenomenological Applications

In the literature, small-z resummations have been exploited to exclusively study the fixed $N = 1$ moment of integrated hadron multiplicities in SIA, in particular, their scale evolution and the shift of the peak of the multiplicity distribution with energy [346–350]. In this section, we will extend these studies to the entire z-range and present a first phenomenological analysis of SIA data with identified pions in terms of FFs up to NNLO+NNLL accuracy. More specifically, we use the same data sets as in a recent fixed-order fit of parton-to-pion FFs at NNLO accuracy [117]. In Sec. 6.2.1 we perform various fits to SIA data with and without making use of small-z resummations to quantify their phenomenological relevance. The impact of small-z resummations on the residual dependence on the factorization scale is studied in Sec. 6.2.2.

6.2.1 Fits to SIA Data and the Relevance of Resummations

To set up the framework for fitting SIA data with identified pions, we closely follow the procedures outlined in Refs. [117, 130–132, 258]. Thus, we adopt the same flexible functional form

$$D_i^{\pi^+}(z, \mu_0^2) = \frac{N_i\, z^{\alpha_i} (1-z)^{\beta_i} [1 + \gamma_i (1-z)^{\delta_i}]}{B[2+\alpha_i, \beta_i + 1] + \gamma_i B[2 + \alpha_i, \beta_i + \delta_i + 1]} \tag{6.71}$$

to parametrize the non-perturbative FFs for charged pions at some initial scale μ_0 in the commonly adopted $\overline{\text{MS}}$ scheme. Other than in Refs. [117, 130–132, 258], we choose, however, $\mu_0 = 10.54$ GeV, which is equivalent to the lowest c.m.s. energy $\sqrt{S}$ of the the data sets relevant for the fit. This choice is made to avoid any potential bias in our comparison of fixed-order and resummed extractions of FFs from starting the scale evolution at some lowish, hadronic scale $\mathcal{O}(1\,\text{GeV})$ where non-perturbative corrections, i.e., power corrections, might be still of some relevance. The Euler Beta function $B[a, b]$ in the denominator of (6.71) is introduced to normalize the parameter N_i for each flavor i to its contribution to the energy-momentum sum rule.

As can be inferred from Eq. (6.2), SIA is only sensitive to certain combinations of FFs, namely the sum of quarks and anti-quarks, $q_i + \bar{q}_i$, for a given flavor i and the gluon D^h_g. Therefore, in all our fits, we only consider FFs for these flavor combinations, i.e., $u+\bar{u}$, $d+\bar{d}$, $s+\bar{s}$, $c+\bar{c}$, $b+\bar{b}$, and g, each parametrized by the ansatz in (6.71). The treatment of heavy flavor FFs, i.e., charm and bottom quark and antiquark, proceeds in the same, non-perturbative input scheme (NPIS) used in Ref. [117] and in the global analyses of [130–132, 258]. More specifically, non-perturbative input distributions $D^h_{c+\bar{c},b+\bar{b}}(z,m^2_{c,b})$, are introduced as soon as the scale in the evolution crosses the value of the heavy quark pole mass $m_{c,b}$, for which we use $m_c = 1.4\,\mathrm{GeV}$ and $m_b = 4.75\,\mathrm{GeV}$, respectively. At the same time, the number of active flavors is increased by one, $N_f \to N_f + 1$, in all expressions each time a flavor threshold is crossed. Since we use $\mu_0 = 10.54$ GeV $> m_b$, this never actually happens in the present fit. The parameters of $D^h_{c+\bar{c},b+\bar{b}}(z,m^2_{c,b})$ are determined by the fit to data according to the Eq. (6.71). We note that a general-mass variable flavor number scheme for treating the heavy quark-to-light hadron FFs has been recently put forward in Ref. [364]. Since this scheme, as well as other matching prescriptions [365], are only available up to NLO accuracy, we refrain from using them in our phenomenological analyses.

Rather than fitting the initial value of the strong coupling at some reference scale in order to solve the RGE governing its running, we adopt the following boundary conditions $\alpha_s(M_Z) =$ 0.135, 0.120, and 0.118 at LO, NLO, and NNLO accuracy, respectively, from the recent MMHT global analysis of PDFs [141]. When we turn on small-z resummations at a given logarithmic order N^{m}LL in our fit, we keep the α_s value as appropriate for the underlying, fixed-order calculation to which the resummed results are matched. For instance, in a fit at NLO+NNLL accuracy, we use the α_s value at NLO.

In the present chapter, we are mainly interested in a comparison of fixed-order fits with corresponding analyses including small-z resummations to determine the phenomenological impact of the latter. We make the following selection of data to be included in our fits. First of all, as in Ref. [117], we limit ourselves to SIA with identified pions since these data are the most precise ones available so far. They span a c.m.s. energy range from $\sqrt{S} \simeq 10.5\,\mathrm{GeV}$ at the b-factories at SLAC and KEK to $\sqrt{S} = M_Z \simeq 91.2\,\mathrm{GeV}$ at the CERN-LEP. The second, more important selection cut concerns the lower value in z accepted in the fit. Traditionally, fits of FFs introduce a minimum value z_{min} of the energy fraction z in the analyses below which all SIA data are discarded and FFs should not be used in other processes. This rather ad hoc cut is mainly motivated by kinematic considerations, more specifically, by the finite hadron mass or other power corrections which are neglected in the factorized framework [87]. Hadron mass effects in SIA have been investigated to some extent in [351] but there is no systematic way to properly include them in a general process [352], i.e., ultimately in a global analysis of FFs. In case of pion FFs, one usually sets $z_{\mathrm{min}} = 0.1$ [130, 132] or $z_{\mathrm{min}} = 0.075$ [117].

The two main assets one expects from small-z resummations, and which we want to investigate, are an improved scale dependence and an extended range towards lower values of z in which data can be successfully described. For this reason, we have systematically explored to which extent one can lower the cut z_{min} in a fit to SIA data once resummations as outlined in Sec. 6.1 are included. It turns out, that for the LEP data, taken at the highest c.m.s. energy of $\sqrt{S} = 91.2$ GeV, we can extend the z-range of our analyses from $0.075 < z < 0.95$ used in the NNLO fit [117] to $0.01 < z < 0.95$. Unfortunately, any further extension to even lower values of z is hampered by the fact that two of the data sets from LEP, the ones from ALEPH [329] and OPAL [331], appear to be mutually inconsistent below $z \simeq 0.01$, see

Fig. 6.4. Including these data at lower z, always lets the fits, i.e., the minimization in the multi-dimensional parameter space defined by Eq. (6.71), go astray and the convergence is very poor.

For the relevant data sets at lower c.m.s. energies, TPC [325–327] ($\sqrt{S} = 29$ GeV), BELLE [323] ($\sqrt{S} = 10.52$ GeV), and BABAR [324] ($\sqrt{S} = 10.54$ GeV), the above mentioned problems related to the finite hadron mass arise at small values of z. A straightforward, often used criterion to assess the relevance of hadron mass effects is to compare the scaling variable z, i.e. the hadron's energy fraction $z = 2\,E_h/Q$ in a c.m.s. frame, with the corresponding three-momentum fraction x_p which is often used in experiments. Since they are related by $x_p = z - 2m_h^2/(zQ^2) + \mathcal{O}(1/Q^4)$ [87], i.e., they coincide in the massless limit, any deviation of the two variables gives a measure of potentially important power corrections. To determine the cut $z_{\min}$ for a given data set, we demand that z and x_p are numerically similar at a level of 10 to at most 15%. The BELLE data are limited to the range $z > 0.2$ [323], where z and x_p differ by less than 1%. BABAR data are available for $z \gtrsim 0.05$, which translates in a maximum difference of the two variables of about 14%. Concerning the TPC data, we had to place a lower cut $z_{\min} = 0.02$ to arrive at a converged fit, which corresponds to a difference of approximately 11% between z and x_p. After imposing these cuts, the total amount of data points taken into account in our fits is 436. We note that, in general, the interplay between small-z resummations and the various sources of power corrections poses a highly non-trivial problem which deserves to be studied further in some dedicated future work.

It is also worth mentioning that with the lowered kinematic cut $z_{\min}$, we achieve a better convergence of our fits with our choice of a larger initial scale $\mu_0 = 10.54$ GeV in Eq. (6.71). Starting the scale evolution from a lower value $\mu_0 = \mathcal{O}(1)$ GeV, like in the NNLO analysis of Ref. [117], leads, in general, to less satisfactory fits in terms of their total χ^2 value which is used to judge the quality of the fits. This could relate to the fact that other types of power corrections have to be considered as well when evolving from such a low energy scale in order to be able to describe the shape of the differential pion multiplicities, cf. Fig. 6.4, measured in experiment. To corroborate this hypothesis is well beyond the scope of this thesis. In any case, our choice of μ_0 is certainly in a region where the standard perturbative framework can be safely applied and meaningful conclusions on the impact of small-z resummations in SIA can be drawn. We emphasize that the choice of μ_0 is solely due to technical rather than conceptional reasons. As the evolution equations are, in principle, forward-backward symmetric, the actual choice of μ_0 should not matter in a fit. Our functional form (6.71) is presumably not flexible enough to obtain an equally good description of the data if the initial scale is chosen well below 10 GeV, which manifests itself in larger values of χ^2 and poor convergence of the fits. The main results and conclusions of this chapter are, however, not affected by the actual choice of μ_0.

Turning back to the choice of our flexible ansatz for the FFs, it is well known that fits based solely on SIA data are not able to constrain all of the free parameters in Eq. (6.71) for each of the flavors i. As was shown in the global analysis of SIA, SIDIS, and pp data in [132], charge conjugation and isospin symmetry are well satisfied for pions. Therefore, we impose the constraint $D^{\pi^\pm}_{u+\bar{u}} = D^{\pi^\pm}_{d+\bar{d}}$. We further limit the parameter space associated with the large-z region by setting $\delta_{g,s+\bar{s},c+\bar{c}} = 0$ and $\gamma_{g,s+\bar{s},c+\bar{c}} = 0$. Note that in contrast to Ref. [117], we are now able to keep β_g as a free parameter in the fits.

The remaining 19 free parameters are then determined by a standard χ^2 minimization pro-

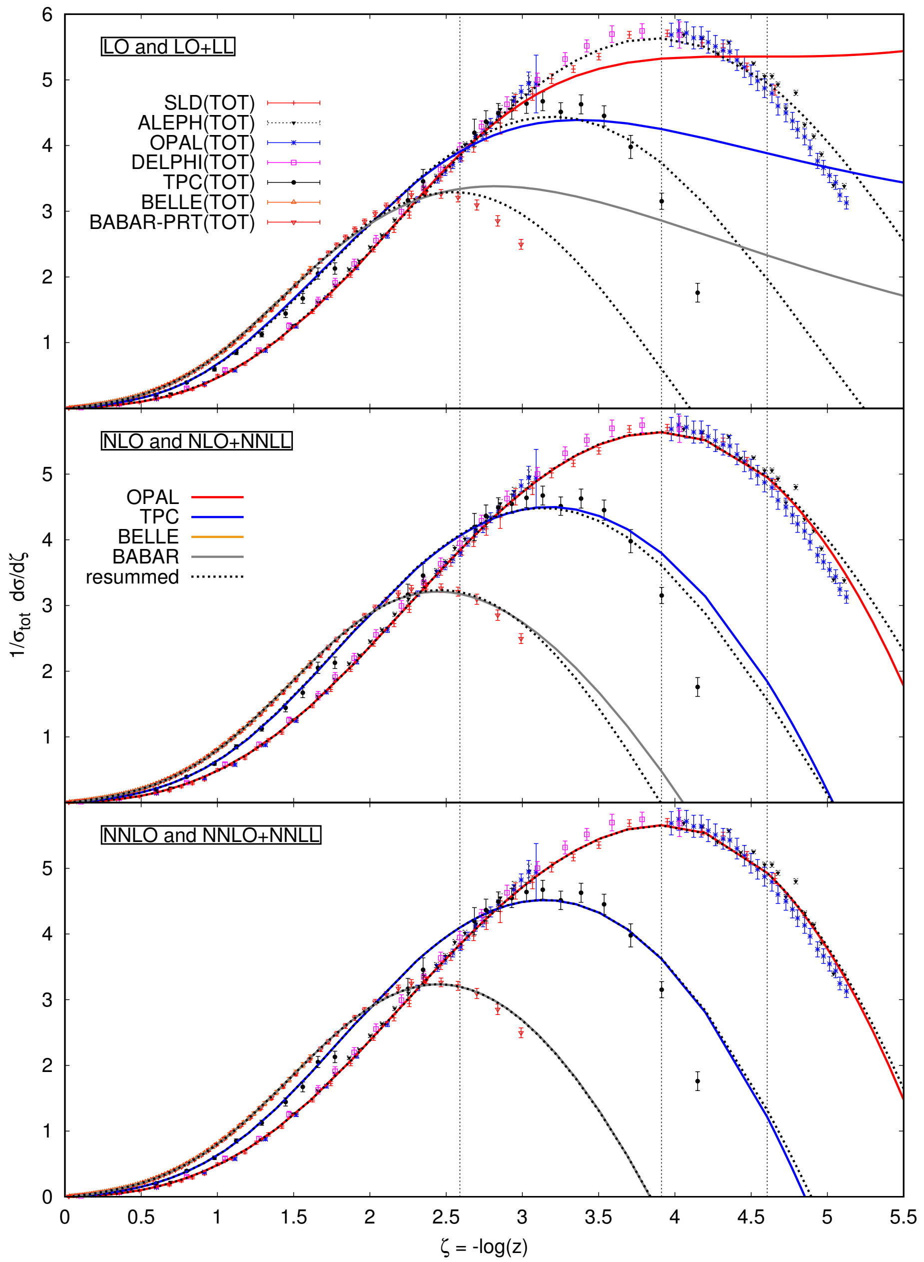

Figure 6.4: Pion multiplicity data [323–331] included in the analyses as a function of $\zeta = \log(1/z)$ compared to the results of various fits without (solid lines) and with (dotted lines) small-z resummations. All curves refer to the central choice of scale $\mu = Q$. The top, middle, and lower panel shows the results at LO and LO+LL, NLO and NLO+NNLL, and NNLO and NNLO+NNLL accuracy, respectively. The vertical dotted lines illustrate, from left to right, the lower cuts $z_{\min} = 0.075$ adopted in [117], and $z_{\min} = 0.02$ and 0.01 used in all our fits for the TPC data and otherwise, respectively.

Table 6.3: The obtained χ^2-values, the "penalties" from normalization shifts, and the χ^2/dof for the fits at fixed order and resummed accuracy as described in the text.

accuracy	χ^2	norm shift	χ^2/dof
LO	1260.78	29.02	2.89
NLO	354.10	10.93	0.81
NNLO	330.08	8.87	0.76
LO+LL	405.54	9.83	0.93
NLO+NNLL	352.28	11.27	0.81
NNLO+NNLL	329.96	8.77	0.76

cedure as described in Sec. 4.2.4. The optimal normalization shifts for each data set are computed analytically. They contribute to the total χ^2 according to the quoted experimental normalization uncertainties; see, e.g., Eq. (4.21) for further details. The resulting χ^2-values, the corresponding "penalties" from the normalization shifts, and the χ^2 per degree of freedom (dof) are listed in Tab. 6.3 for a variety of fits with a central choice of scale $\mu = Q$. Results are given both for fits at fixed order (LO, NLO, and NNLO) accuracy and for selected corresponding fits obtained with small-z resummations. Here, all cross sections are always matched to the fixed order results according to the procedures described in Sec. 6.1.4 and Sec. 6.1.5. More specifically, we choose the logarithmic order in such a way that we do not resum logarithmic contributions which are not present in the fixed-order result. For this reason, we match the LO calculation only with the LL resummation as the only logarithmic contribution at LO is of LL accuracy; cf. Tabs. 6.1 and 6.2. Using the same reasoning, we match NLO with the NNLL resummed results. Finally, at NNLO accuracy five towers of small-z logarithms are present. However, the most accurate resummed result currently available is at NNLL accuracy which includes the first three towers. Thus, we can match NNLO only with NNLL.

It should be stressed that the results for the fixed-order fits are not directly comparable to the ones given in Ref. [117] since we use more data points at lower values of z, a slightly different set of fit parameters, and a different initial scale μ_0. However, the main aspects of these fits remain the same and can be read off directly from Tab. 6.3: a LO fit is not able to describe the experimental results adequately. The NLO fit already gives an acceptable result, which is further improved upon including NNLO corrections. Compared to the corresponding fixed-order results, the fits including also all-order resummations of small-z logarithms exhibit, perhaps somewhat surprisingly, only a slightly better total χ^2, except for the LO+LL fit, where resummation leads to a significant improvement in its quality. The small differences in χ^2 between fits at NNLO and NNLO+NNLL accuracy are not significant. Hence, we must conclude that in the z-range covered by the experimental results, NNLO expressions already capture most of the relevant features to yield a satisfactory fit to the SIA data with identified pions.

The same conclusions can be reached from Fig. 6.4, where we compare the used inclusive pion multiplicity data in SIA with the theoretical cross sections at different levels of fixed- and logarithmic-order obtained from the fits listed in Tab. 6.3. The theoretical curves are

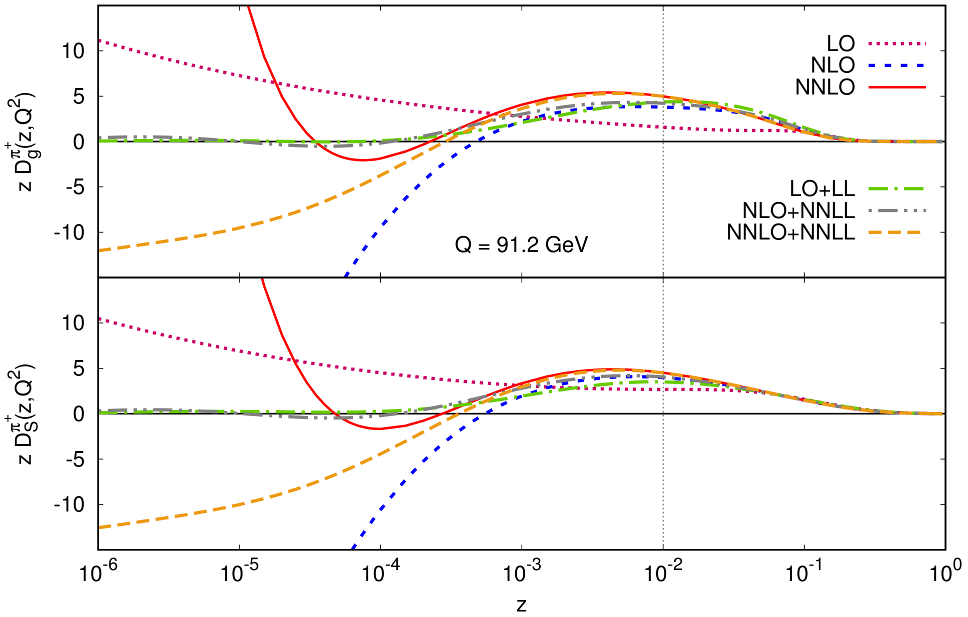

Figure 6.5: z times the obtained gluon (upper panel) and singlet (lower panel) FFs as a function of z, evaluated at $Q = 91.2$ GeV for the different fits listed in Tab. 6.3. The singlet is shown for $N_f = 5$ active flavors. The fitted z-range, $z > 0.01$, is to the right of the dotted vertical line.

corrected for the optimum normalization shifts computed for each set of data. For the sake of readability, we only show a single curve for the different experiments at $\sqrt{S} = M_Z$ which is corrected for the normalization shift obtained for the OPAL data. The individual normalization shifts for the other sets are, however, quite similar. We refrain from showing the less precise flavor-tagged data which are, nevertheless, also part of the fit. The vertical dotted lines in Fig. 6.4 indicate the lower cuts in z applied for the data sets at different c.m.s. energies as discussed above. The leftmost line (corresponding to $z_{\rm min} = 0.075$) is the cut used in the NNLO analysis in Ref. [117]. Both, the data and the calculated multiplicities are shown as a function of $\zeta \equiv -\log z$.

In Fig. 6.5, we plot z times the gluon and singlet FFs for positively charged pions, $D_g^{\pi^+}(z,Q^2)$ and $D_S^{\pi^+}(z,Q^2)$, respectively, resulting from our fits given in Tab. 6.3. The FFs are computed at $Q = M_Z = 91.2\,\text{GeV}$ and in a range of z shown extending well below the $z_{\rm min} = 0.01$ cut above which they are constrained by data. We would like to point out that the resummed (and matched) results for which we have full control over all logarithmic powers (i.e. for LO+LL and NLO+NNLL) are well behaved at small-z and show the expected oscillatory behavior with z which they inherit from the resummed splitting functions through evolution. The latter behave like different combinations of Bessel functions when the Mellin inverse back to z-space is taken; for more details see Ref. [43]. The singlet and gluon FFs at NNLO+NNLL accuracy still diverge for $z \to 0$ (i.e. they turn to large negative values in the z-range shown in Fig. 6.5) since we do not have control over all five logarithmic powers that appear in a fixed-order result at NNLO; cf. Tabs. 6.1 and 6.2. However, the resummation of the three leading towers of logarithms, considerably tames the small-z singularities as compared to the corresponding result obtained at NNLO.

Finally, to further quantify the impact of small-z resummations in the range of z relevant for phenomenology, Fig. 6.6 shows the K-factors at scale $Q = 91.2\,\text{GeV}$ for the pion multiplicities (6.2) obtained in our fits. Schematically, they are defined as

$$K \equiv \frac{\mathbb{C}^{\text{FO + Res}} \otimes D^{\text{FO + Res}}}{\mathbb{C}^{\text{FO}} \otimes D^{\text{FO}}} \,. \tag{6.72}$$

Here, $\mathbb{C}^{\text{FO}}$ and $\mathbb{C}^{\text{FO+Res}}$ denote the fixed-order coefficient functions at LO, NLO, and NNLO accuracy and the corresponding resummed and matched coefficient functions, respectively. Likewise, D^{FO} and $D^{\text{FO+Res}}$ are the FFs evolved with splitting functions at fixed order and resummed, matched accuracy, respectively. In order to assess the relevance of the small-z resummations independent of the details of the non-perturbative input for the FFs at scale μ_0, we adopt the same FFs for both calculating the numerator and the denominator. In each computation of K, we select the set of FFs obtained from the corresponding fixed-order fit and the different logarithmic orders of the resummations are chosen as discussed and given in Tab. 6.3.

By comparing the results for the K-factors at LO+LL, NLO+NNLL, and NNLO+NNLL

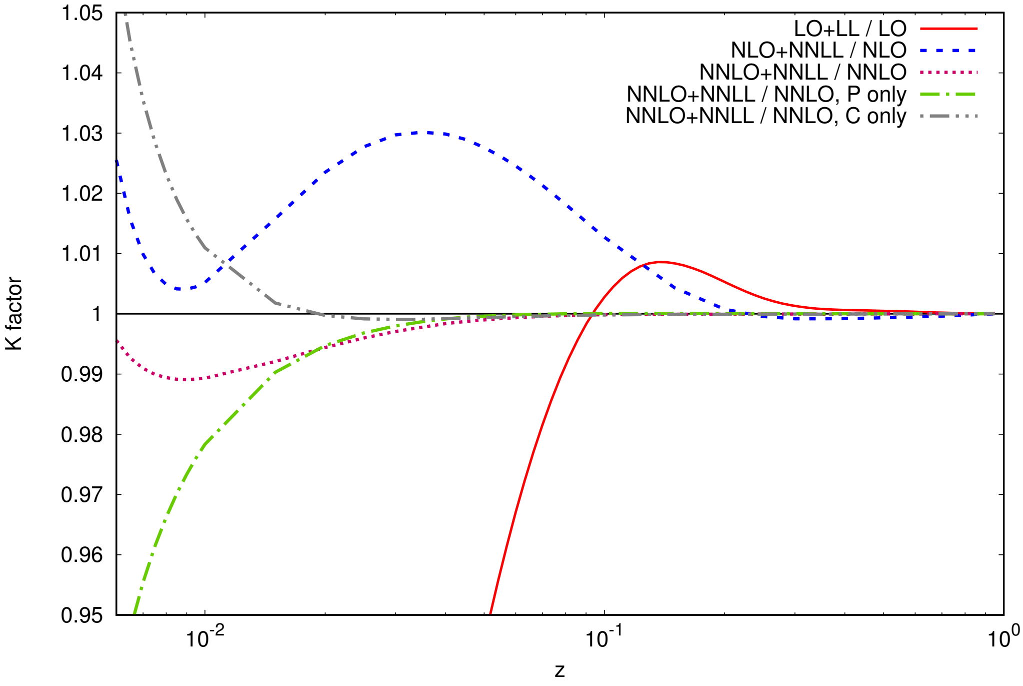

Figure 6.6: K-factors as defined in Eq. (6.72) at LO+LL, NLO+NNLL, and NNLO+NNLL accuracy at $Q = 91.2$ GeV in the range of z relevant for phenomenology. In addition, we show NNLO+NNLL results where the resummations are only performed either for the coefficient functions (”C only”) or for the splitting functions (”P only”).

accuracy, it can be inferred that the corrections due to the small-z resummations start to become appreciable at a level of a few percent already below $z \simeq 0.1$. As one might expect, resummations are gradually less important when the perturbative accuracy of the corresponding fixed-order baseline is increased, i.e., the NNLO result already captures most of the small-z dynamics relevant for phenomenology whereas the differences between LO and LO+LL are still sizable. This explains the pattern of χ^2 values we have observed in Tab. 6.3. In addition, Fig. 6.6 also gives the K-factor at NNLO+NNLL accuracy where the small-z resummations are only performed either for the coefficient functions (labeled as "C only") *or* for the splitting functions ("P only"). By comparing these results with the full K-factor at NNLO+NNLL accuracy, one can easily notice, that there are very large cancellations among the two.

6.2.2 Scale Dependence

In this section, the remaining scale dependence of the resummed expressions is studied and compared to the corresponding fixed-order results. The scale-dependent terms are implemented according to the discussions in Sec. 6.1.4. As usual, we use the iterated solution with up to $n = 20$ terms in the perturbative expansion.

As was already observed in the NNLO analysis of Ref. [117], the dependence on the factorization scale μ_F in SIA is gradually reduced the more higher order corrections are considered in the perturbative expansion. This is in line with the expectation that all artificial scales, μ_F and μ_R, should cancel in an all-order result, i.e. if the series is truncated at order m, the remaining dependence on, say, μ_F should be of order a_s^{m+1}. Following this reasoning, we do expect a further reduction of the scale dependence upon including small-z resummations on top of a given fixed-order calculation; see Sec. 6.1.4.

Usually, the scale dependence is studied by varying the scale μ_F by a factor of two or four around its default (central) value, $\mu_F = Q$ in case of SIA. Therefore, we introduce the parameter $\xi \equiv \mu_F^2/Q^2$; note that in this chapter we keep $\mu_F = \mu_R$ as is commonly done. Hence, $\xi = 1$ corresponds to the standard choice of scale $\mu_F = Q$. The conventional way of showing the dependence of a quantity T, like the pion multiplicity (6.2), on ξ is to plot the ratio $T(\xi)/T(\xi = 1)$ for various values of ξ; in our analyses, we will use $\xi = 2$ and $\xi = 0.5$.

However, we find that the oscillatory behavior of the resummed splitting and coefficient functions causes the SIA multiplicities to become an oscillatory function as well, which for certain small values of z, well below the cut $z_{\min}$ down to which we fit FFs to data, eventually becomes negative. Therefore, it is not feasible to utilize the common ratio plots to investigate the resummed scale dependence. Instead, we decide to study the *width* of the scale variation Δ_T for a quantity T, defined as

$$\begin{aligned} \Delta_T(z) \equiv\ & \max[T_{\xi=1}(z), T_{\xi=2}(z), T_{\xi=0.5}(z)] \\ & - \min[T_{\xi=1}(z), T_{\xi=2}(z), T_{\xi=0.5}(z)] \end{aligned} \tag{6.73}$$

in the range $\xi = [0.5, 2]$ as a measure of the residual dependence on μ_F.

In Fig. 6.7, we show $\Delta_{\mathrm{SIA}}(z)$ for the pion multiplicities (6.2) at $Q = 10.54\,\mathrm{GeV}$ for the two fixed-order fits (NLO and NNLO accuracy) as well as for resummed and matched fit at NNLO+NNLL. The main plot, which covers the z-range down to 10^{-7}, clearly demonstrates that the band Δ_{SIA} is, on average, considerably more narrow for the NNLO+NNLL resummed cross section than for the fixed-order results, according to the expectation. From the middle inset in Fig. 6.7, which shows z values relevant for experiments, i.e. $z \gtrsim 10^{-3}$, one can infer that the band Δ_{SIA} is roughly of the same size for all calculations and resummations do not lead to any improvement in the scale dependence in this range. The small inset zooms into the range $z > 0.01$, where a similar conclusion can be reached.

In order to fully understand this behavior, one perhaps would have to include the yet missing N^{4}LL corrections, which would allow one to resum all five logarithmic towers present at NNLO accuracy. The observed result might be due to these missing subleading terms or it could be related to some intricate details in the structure of the perturbative series in the time-like case at small-z.

In any case, one can safely conclude that in the z-region relevant for phenomenology of SIA, the residual scale dependence of the resummed result does not differ from the fixed order calculation at NNLO accuracy. The latter is therefore entirely sufficient for extractions of FFs from SIA data as resummations neither improve the quality of the fit, cf. Sec. 6.2.1 nor do they reduce theoretical uncertainties. Nonetheless, it important to demonstrate from a theoretical point of view that, on average, resummation does achieve smaller scale uncertainties, although for values of z that are well outside the range of currently available data. It should be also kept in mind that the study of the $N = 1$ moment of multiplicities, though not studied in this thesis, would not be possible without invoking small-z resummations as fixed-order results are singular.

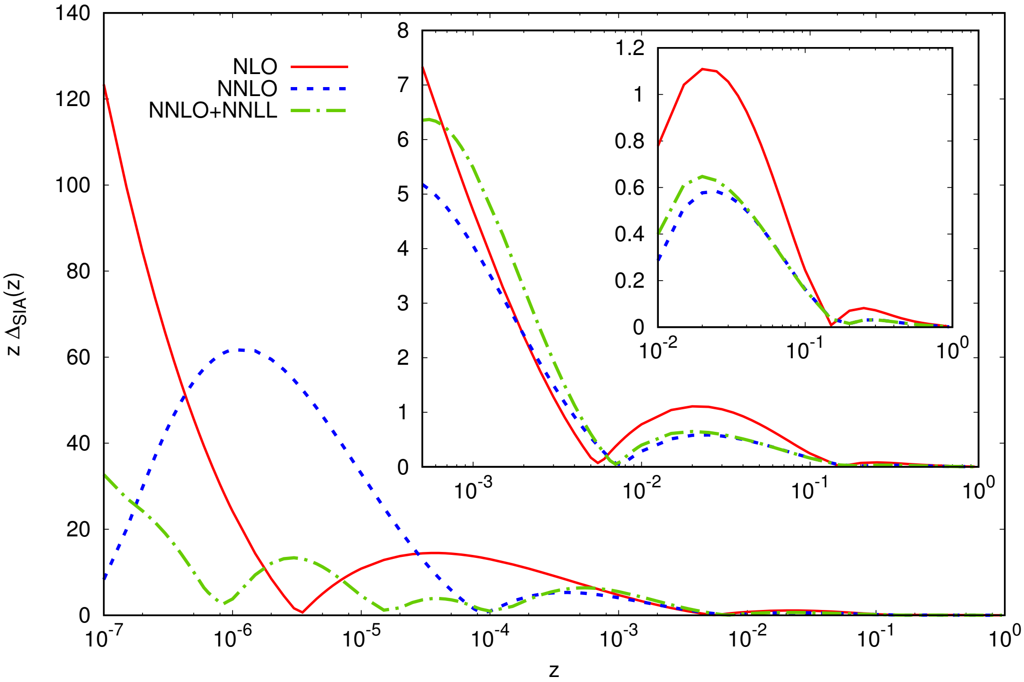

Figure 6.7: z times the width of the scale band Δ_{SIA} defined in (6.73) for for three different ranges of z at NLO, NNLO and NNLO+NNLL accuracy. All results for the SIA pion multiplicities are obtained for $Q = 10.54\,\mathrm{GeV}$; see text.

6.3 Conclusions and Outlook

We have presented a detailed phenomenological analysis of small-z resummations in semi-inclusive annihilation, the time-like scale evolution of fragmentation functions, and their determination from data.

After detailing the systematics of the enhanced contributions at small momentum fractions of the observed hadron for both coefficient and splitting functions, we have reviewed how to resum them to all orders in perturbation theory up to next-to-next-to-leading logarithmic accuracy. The approach used in this chapter was proposed in the literature and is based on general considerations concerning all-order mass factorization. Our results agree with those presented in the literature, and we have extended them to allow for variations in the factorization and renormalization scales away from their default values.

Next, we have shown how to properly implement the resummed expressions in Mellin moment space and how to set up a solution to the coupled, matrix-valued singlet evolution equations. The non-singlet sector is subleading and not affected by the presently available logarithmic order. For all practical purposes we advocate an iterated solution for the scale evolution of fragmentation functions, and we have shown that keeping twenty terms in the expansion of the resummed expressions is sufficient for all applications. We have also discussed how to match the resummed towers of logarithms for both the coefficient and the evolution kernels to the known fixed-order expressions. Numerical subtleties in complex Mellin moment space related to finding a proper choice of contour for the inverse transformation despite the more complicated structure of singularities of the resummed evolution kernels and coefficient functions have been addressed as well.

In the second part of this chapter, a first analysis of semi-inclusive annihilation data with an identified pion in terms of parton-to-pion fragmentation functions and in the presence of resummations was presented. To this end, various fits at different fixed-orders in perturbation theory and levels of small-z resummations were compared in order to study and quantify the phenomenological impact of the latter. It turned out that for both the quality of the fit to data and the reduction of theoretical uncertainties due to the choice of the factorization scale, resummations provide only litte improvements with respect to an analysis performed at fixed, next-to-next-to-leading order accuracy. At values of the hadron's momentum well outside the range of phenomenological interest, we did observe, however, a significant improvement in the scale dependence of the inclusive pion cross section in the presence of resummations.

Possible future applications of resummations comprise revisiting the analyses of the first moment of hadron multiplicities available in the literature. Here, resummations are indispensable for obtaining a finite theoretical result. So far, the main focus was on the energy dependence of the peak of the multiplicity distribution, its width, and a determination of the strong coupling. It might be a valuable exercise to merge the available data on the first moment and the relevant theoretical formalism with the extraction of the full momentum dependence of fragmentation functions as described in this chapter to further our knowledge of the non-perturbative hadronization process.

As was pointed out in this chapter, a better understanding of the interplay of resummations and other sources of potentially large corrections in the region of small momentum fractions is another important avenue of future studies for time-like processes. One, if not the most important source of power corrections is the hadron mass, which is neglected in the factorized framework adopted for any analysis of fragmentation functions. At variance with the phenomenology of parton distributions functions, where one can access and theoretically describe the physics of very small momentum fractions, hadron mass corrections prevent that in the time-like case. In fact, they become an inevitable part and severely restrict the range of applicability of fragmentation functions and the theoretical tools such as resummations. In addition, resummations can and have been studied for large fractions of the hadron's momentum. With more and more precise data becoming available in this kinematical regime, it would be very valuable to incorporate also these type of large logarithms into the analysis framework for fragmentation functions at some point in the future.

Final Conclusions and Outlook

In this thesis, we have presented several calculations for important processes in the era of high energy particle colliders. We hope that our results will help to better understand the nature of hadronic physics, especially the fragmentation process, in the near future.

We have presented a new way of formulating the partonic cross sections for inclusive jet production in hadronic collisions. We followed the calculations in literature and used the narrow jet approximation to obtain analytical results. However, by close inspection of the results and a change of variables, we have obtained an elegant and convenient formulation of the partonic cross sections in terms of appropriate inclusive jet functions. The cross section in terms of jet functions has a very similar structure to the cross section for inclusive hadron production. Only the fragmentation functions are replaced by the jet functions. We have shown how to calculate these jet functions in perturbation theory for any infrared safe jet definition. Hence, our formulation allows for a relatively straightforward implementation of new jet algorithms, which we have demonstrated by performing a first NLO calculation for a rather new jet algorithm proposed in 2014.

Next, we have extended this framework to the semi-inclusive process where an identified hadron is observed inside a fully reconstructed jet. We have demonstrated that the analytical formulation of the partonic cross sections in terms of jet functions takes a two-tire form with two different kinds of semi-inclusive jet functions. One kind is responsible for the formation of the jet while the other kind parametrizes the formation of a parton inside the jet. The so obtained partonic cross sections for an "observed" parton within the jet are eventually convoluted with the non-perturbative fragmentation functions. This structure is very similar to SIA and we have demonstrated that hadron-in-jet production indeed shows the same benefits as SIA regarding the extraction of FFs from experimental data. Especially, direct access to the z-dependence of FFs is possible as the LO cross section is directly proportional to the FFs probed at $z = z_h \equiv p_T^h/p_T^{\text{jet}}$. Hence, by choosing certain values for p_T^{jet} and p_T^h it is possible to "dial" the value at which the FFs are probed. Moreover, thanks to the hadronic initial state, the gluon FF is accessible already at LO. We have utilized this feature to perform a global NLO analysis of D^*-meson FFs where we have, for the first time, included recent data for D^*-in-jet production. Our set of D^* fragmentation functions is competitive with other FFs available in literature regarding the description of SIA and $pp \to hX$ data. However, our FFs yield a much more satisfactory description of the hadron-in-jet data.

Additionally, we have studied two topics closely related to the work summarized above. We have presented analytical NLO results for photon-in-jet production which show the same potential for future extractions of photon-FFs as the hadron-in-jet cross section does for hadronic FFs. Finally, we have addressed the small-z region of FFs, where we have included NNLL resummed results for the time-like evolution kernel and the coefficient functions of SIA. However, we found that for the phenomenological description of SIA data already NNLO results are sufficient.

There are several possible extensions of this work for the near future. Quite some work on extractions of FFs is waiting. Regarding the potential of the in-jet fragmentation data to pin down the z-dependence of FFs, it is obvious that this process should also be included in future extractions of light hadron FFs as soon as the corresponding data are available by the experiments. Moreover, a new extraction of photon FFs could be performed in the near future, including recent PHENIX data for inclusive photon production and, if available, also photon-in-jet data. Additionally, we plan to extend our analysis of charmed meson FFs by performing fits for D^+ and D^0 fragmentation functions. However, since corresponding hadron-in-jet data are not available yet, we have to restrict said analysis to SIA and $pp \to hX$. Furthermore, we aim for a detailed comparison of our extracted D^* FFs with an extraction where the hadron-in-jet cross section is calculated within the framework of SCET. This framework allows for a resummation of the logarithmic dependence on the jet size parameter to all orders in perturbation theory. It will be very interesting to figure out whether the available D^*-in-jet data are precise enough and the jet size is small enough to distinguish between the different theoretical frameworks.

Less phenomenological extensions of this work are possible as well. Hadron-in-jet production is not only important for the extraction of FFs. As is well known, hadron production in jets has important applications in studies of spin phenomena in QCD in terms of the Collins effect, where the azimuthal distribution of a hadron around the jet axis is considered. With our calculation, we have contributed the denominator of this spin asymmetry. Since we expect that our method based on jet functions is also applicable to the spin-dependent case, one could also calculate the numerator to complete the theoretical description of the spin asymmetry. Moreover, the fixed order NLO results for the semi-inclusive jet functions show logarithmic enhancement for $z_h \to 1$. Such types of logarithms, which usually originate from soft gluon radiation, could be addressed by resummation techniques.

In general, large logarithms for $z \to 1$ are also present in the time-like evolution kernels and coefficient functions of SIA. Thus, the next step would be to extend our studies on the small-z behavior of FFs and to include the large-z resummed expressions as well. Therefore, it would be necessary to find a consistent formulation to include both, small- and large-z resummed results. Regarding the large amount of precise BELLE data in the large-z region, it would be very interesting to investigate the relevance of these resummations.

Acknowledgements

First of all, I would like to thank Prof. Dr. Werner Vogelsang for giving me the opportunity to write my PhD thesis on such interesting topics in his working group. I am very grateful for his continuous support and many interesting and helpful discussions. Moreover, I am very thankful for the opportunity to attend so many interesting and joyful workshops and conferences all around the world.

I am very grateful to Dr. Marco Stratmann for his advice, numerous helpful and interesting discussions, and the coffee supply. It has been a great pleasure working together.

Special thanks to my collaborators on research projects during this PhD: Prof. Dr. Asmita Mukherjee, Dr. Felix Ringer, Dr. Ivan Vitev and Daniele Anderle.
I am thankful to all the people in the seventh floor of the physics building for creating such a nice atmosphere, especially Prof. Dr. Thomas Gutsche, Prof. Dr. Barbara Jäger, Dr. Lukas Salfelder, Dr. Marc Schlegel, Felix Heckhorn, Patriz Hinderer, Matthias Kesenheimer, Martin Lambertsen, Julius Steiglechner, Marina Walt.

Furthermore, I want to thank Sabine Werner and Ingrid Estiry for their help with all the administrative stuff.

I would like to thank Tobias Jammer and Alexander Tietzsch for helpful comments on parts of this work.

Last but not least, I would like to thank my family, friends and my wife Ann-Katrin for their enormous support during this thesis.

Bibliography

[1] J.J. Thomson. *Philosophical Magazine Series 5*, 44(269):293–316, 1897.

[2] H. Geiger and E. Mardsen. *Proc. Roy. Soc. 1909 A*, 82:495–500, 1909.

[3] E. Rutherford. *Phil. Mag. Ser.6*, 21:669–688, 1911.

[4] E. Rutherford. *Phil. Mag. Ser.6*, 37:536–587, 1919.

[5] J. Chadwick. *Nature*, 129:312, 1932.

[6] J. Chadwick. *Proc. Roy. Soc. Lond.*, A136(830):692–708, 1932.

[7] P. A. R. Ade et al. *Astron. Astrophys.*, 594:A13, 2016.

[8] P. A. R. Ade et al. *Astron. Astrophys.*, 594:A14, 2016.

[9] C. L. Bennett et al. *Astrophys. J. Suppl.*, 208:20, 2013.

[10] David J. Gross and Frank Wilczek. *Phys.Rev.Lett.*, 30:1343–1346, 1973.

[11] H. David Politzer. *Phys.Rev.Lett.*, 30:1346–1349, 1973.

[12] Elliott D. Bloom et al. *Phys. Rev. Lett.*, 23:930–934, 1969.

[13] Martin Breidenbach, Jerome I. Friedman, Henry W. Kendall, Elliott D. Bloom, D. H. Coward, H. C. DeStaebler, J. Drees, Luke W. Mo, and Richard E. Taylor. *Phys. Rev. Lett.*, 23:935–939, 1969.

[14] R. Brandelik et al. *Phys. Lett.*, B86:243–249, 1979.

[15] D. P. Barber et al. *Phys. Rev. Lett.*, 43:830, 1979.

[16] Christoph Berger et al. *Phys. Lett.*, B86:418–425, 1979.

[17] G. Arnison et al. *Phys. Lett.*, 122B:103–116, 1983.

[18] M. Banner et al. *Phys. Lett.*, 122B:476–485, 1983.

[19] G. Arnison et al. *Phys. Lett.*, 126B:398–410, 1983.

[20] P. Bagnaia et al. *Phys. Lett.*, B129:130–140, 1983.

[21] F. Abe et al. *Phys. Rev. Lett.*, 74:2626–2631, 1995.

[22] S. Abachi et al. *Phys. Rev. Lett.*, 74:2422–2426, 1995.

[23] Stephen B. Libby and George F. Sterman. *Phys. Rev.*, D18:3252, 1978.

[24] R. Keith Ellis, Howard Georgi, Marie Machacek, H. David Politzer, and Graham G. Ross. *Phys. Lett.*, B78:281–284, 1978.

[25] R. Keith Ellis, Howard Georgi, Marie Machacek, H. David Politzer, and Graham G. Ross. *Nucl. Phys.*, B152:285–329, 1979.

[26] D. Amati, R. Petronzio, and G. Veneziano. *Nucl. Phys.*, B140:54–72, 1978.

[27] D. Amati, R. Petronzio, and G. Veneziano. *Nucl. Phys.*, B146:29–49, 1978.

[28] G. Curci, W. Furmanski, and R. Petronzio. *Nucl. Phys.*, B175:27–92, 1980.

[29] John C. Collins, Davison E. Soper, and George F. Sterman. *Phys. Lett.*, B134:263, 1984.

[30] John C. Collins, Davison E. Soper, and George F. Sterman. *Nucl. Phys.*, B261:104–142, 1985.

[31] John C. Collins and Davison E. Soper. *Ann. Rev. Nucl. Part. Sci.*, 37:383–409, 1987.

[32] John C. Collins, Davison E. Soper, and George F. Sterman. *Adv. Ser. Direct. High Energy Phys.*, 5:1–91, 1989.

[33] Matteo Cacciari, Gavin P. Salam, and Gregory Soyez. *JHEP*, 0804:063, 2008.

[34] Howard Georgi. `arXiv:1408.1161`, 2014.

[35] Massimiliano Procura and Iain W. Stewart. *Phys. Rev.*, D81:074009, 2010. [Erratum: Phys. Rev.D83,039902(2011)].

[36] Ambar Jain, Massimiliano Procura, and Wouter J. Waalewijn. *JHEP*, 05:035, 2011.

[37] Massimiliano Procura and Wouter J. Waalewijn. *Phys. Rev.*, D85:114041, 2012.

[38] Francois Arleo, Michel Fontannaz, Jean-Philippe Guillet, and Chi Linh Nguyen. *JHEP*, 04:147, 2014.

[39] Mathias Ritzmann and Wouter J. Waalewijn. *Phys. Rev.*, D90(5):054029, 2014.

[40] Georges Aad et al. *Phys. Rev.*, D85:052005, 2012.

[41] Roel Aaij et al. *Phys. Rev. Lett.*, 118(19):192001, 2017.

[42] A. Vogt. *JHEP*, 10:025, 2011.

[43] C. H. Kom, A. Vogt, and K. Yeats. *JHEP*, 10:033, 2012.

[44] Murray Gell-Mann. Report Number: CTSL-20, TID-12608, 1961.

[45] Yuval Ne'eman. *Nucl. Phys.*, 26:222–229, 1961.

[46] Murray Gell-Mann. *Phys. Lett.*, 8:214–215, 1964.

[47] G. Zweig. Report Number: CERN-TH-401, 1964.

[48] V. E. Barnes et al. *Phys. Rev. Lett.*, 12:204–206, 1964.

[49] O. W. Greenberg. *Phys. Rev. Lett.*, 13:598–602, 1964.

[50] Chen-Ning Yang and Robert L. Mills. *Phys.Rev.*, 96:191–195, 1954.

[51] H. Fritzsch, Murray Gell-Mann, and H. Leutwyler. *Phys. Lett.*, B47:365–368, 1973.

[52] R. Keith Ellis, W. James Stirling, and B. R. Webber. *QCD and collider physics.* 1996.

[53] Francis Halzen and Alan D. Martin. *Quarks and leptons: an introductory course in modern particle physics.* 1984.

[54] Michael Edward Peskin and Daniel V. Schroeder. *An introduction to quantum field theory.* 1999.

[55] Murray Gell-Mann. *Phys.Rev.*, 125:1067–1084, 1962.

[56] R.P. Feynman. *Rev.Mod.Phys.*, 20:367–387, 1948.

[57] R.P. Feynman and A.R. Hibbs. *Quantum mechanics and path integrals.* 1965.

[58] E. S. Abers and B. W. Lee. *Phys. Rept.*, 9:1–141, 1973.

[59] L.D. Faddeev and V.N. Popov. *Phys.Lett.*, B25:29–30, 1967.

[60] George Leibbrandt. *Rev. Mod. Phys.*, 59:1067, 1987.

[61] O. V. Tarasov, A. A. Vladimirov, and A. Yu. Zharkov. *Phys. Lett.*, B93:429–432, 1980.

[62] S. A. Larin and J. A. M. Vermaseren. *Phys. Lett.*, B303:334–336, 1993.

[63] T. van Ritbergen, J. A. M. Vermaseren, and S. A. Larin. *Phys. Lett.*, B400:379–384, 1997.

[64] C. Patrignani et al. *Chin. Phys.*, C40(10):100001, 2016.

[65] M. Beneke. *Phys. Rept.*, 317:1–142, 1999.

[66] Carola Friederike Berger. PhD thesis, SUNY, Stony Brook, 2003.

[67] B. L. Ioffe. *Prog. Part. Nucl. Phys.*, 56:232–277, 2006.

[68] H. Lehmann, K. Symanzik, and W. Zimmermann. *Nuovo Cim.*, 1:205–225, 1955.

[69] Werner Vogelsang. Skript zur Vorlesung Quantenfeldtheorie und Elementarteilchenphysik, 2012-2014.

[70] Gerard 't Hooft and M.J.G. Veltman. *Nucl.Phys.*, B44:189–213, 1972.

[71] C.G. Bollini and J.J. Giambiagi. *Nuovo Cim.*, B12:20–25, 1972.

[72] J.F. Ashmore. *Lett.Nuovo Cim.*, 4:289–290, 1972.

[73] G.M. Cicuta and E. Montaldi. *Lett.Nuovo Cim.*, 4:329–332, 1972.

[74] Gerard 't Hooft. *Nucl.Phys.*, B61:455–468, 1973.

[75] Steven Weinberg. *Phys.Rev.*, D8:3497–3509, 1973.

[76] William A. Bardeen, A. J. Buras, D. W. Duke, and T. Muta. *Phys. Rev.*, D18:3998, 1978.

[77] T. Muta. *World Sci. Lect. Notes Phys.*, 5:1–409, 1987.

[78] P. Pascual and R. Tarrach. *Lect. Notes Phys.*, 194:1–277, 1984.

[79] Zoltan Kunszt and Davison E. Soper. *Phys. Rev.*, D46:192–221, 1992.

[80] Davison E. Soper. In *The Strong interaction, from hadrons to partons: Proceedings, 24th SLAC Summer Institute on Particle Physics (SSI 96)*, pages 15–42, 1996.

[81] T. Kinoshita. *J.Math.Phys.*, 3:650–677, 1962.

[82] T.D. Lee and M. Nauenberg. *Phys.Rev.*, 133:B1549–B1562, 1964.

[83] D. de Florian, M. Stratmann, and W. Vogelsang. *Phys. Rev.*, D57:5811–5824, 1998.

[84] P. J. Rijken and W. L. van Neerven. *Nucl. Phys.*, B487:233–282, 1997.

[85] R. Baier and K. Fey. *Z. Phys.*, C2:339–349, 1979.

[86] Guido Altarelli, R. Keith Ellis, G. Martinelli, and So-Young Pi. *Nucl. Phys.*, B160:301–329, 1979.

[87] P. Nason and B. R. Webber. *Nucl. Phys.*, B421:473–517, 1994. [Erratum: Nucl. Phys.B480,755(1996)].

[88] W. Furmanski and R. Petronzio. *Z. Phys.*, C11:293, 1982.

[89] E. B. Zijlstra and W. L. van Neerven. *Nucl. Phys.*, B383:525–574, 1992.

[90] E. B. Zijlstra and W. L. van Neerven. *Phys. Lett.*, B297:377–384, 1992.

[91] B. Jager, A. Schafer, M. Stratmann, and W. Vogelsang. *Phys. Rev.*, D67:054005, 2003.

[92] Nikolaos Kidonakis, Gianluca Oderda, and George F. Sterman. *Nucl. Phys.*, B525:299–332, 1998.

[93] Eric Laenen, Gianluca Oderda, and George F. Sterman. *Phys. Lett.*, B438:173–183, 1998.

[94] R. Sassot. Talk given at QCD-N'16 in Bilbao, 2016.

[95] R.P. Feynman. *Photon-Hadron Interactions.* 1998.

[96] R. D. Field and R. P. Feynman. *Nucl. Phys.*, B136:1, 1978.

[97] R. D. Field and R. P. Feynman. *Phys. Rev.*, D15:2590–2616, 1977.

[98] Howard Georgi and H. David Politzer. *Nucl. Phys.*, B136:445–460, 1978.

[99] J. F. Owens. *Phys. Lett.*, B76:85–88, 1978.

[100] Tsuneo Uematsu. *Phys. Lett.*, B79:97–102, 1978.

[101] V. N. Gribov and L. N. Lipatov. *Sov. J. Nucl. Phys.*, 15:438–450, 1972. [Yad. Fiz.15,781(1972)].

[102] V. N. Gribov and L. N. Lipatov. *Sov. J. Nucl. Phys.*, 15:675–684, 1972. [Yad. Fiz.15,1218(1972)].

[103] L. N. Lipatov. *Sov. J. Nucl. Phys.*, 20:94–102, 1975. [Yad. Fiz.20,181(1974)].

[104] Guido Altarelli and G. Parisi. *Nucl. Phys.*, B126:298–318, 1977.

[105] Yuri L. Dokshitzer. *Sov. Phys. JETP*, 46:641–653, 1977. [Zh. Eksp. Teor. Fiz.73,1216(1977)].

[106] Davison E. Soper. *Phys. Rev.*, D15:1141, 1977.

[107] Davison E. Soper. *Phys. Rev. Lett.*, 43:1847, 1979.

[108] John C. Collins and Davison E. Soper. *Nucl. Phys.*, B194:445–492, 1982.

[109] R. L. Jaffe. *Nucl. Phys.*, B229:205–230, 1983.

[110] John Collins. *Foundations of perturbative QCD.* 2011.

[111] Andreas Metz and Anselm Vossen. *Prog. Part. Nucl. Phys.*, 91:136–202, 2016.

[112] P. J. Mulders and R. D. Tangerman. *Nucl. Phys.*, B461:197–237, 1996. [Erratum: Nucl. Phys.B484,538(1997)].

[113] Daniel Boer, R. Jakob, and P. J. Mulders. *Nucl. Phys.*, B504:345–380, 1997.

[114] P. J. Mulders and J. Rodrigues. *Phys. Rev.*, D63:094021, 2001.

[115] S. Meissner, A. Metz, and D. Pitonyak. *Phys. Lett.*, B690:296–303, 2010.

[116] Daniele P. Anderle, Tom Kaufmann, Marco Stratmann, and Felix Ringer. *Phys. Rev.*, D95(5): 054003, 2017.

[117] Daniele P. Anderle, Felix Ringer, and Marco Stratmann. *Phys. Rev.*, D92(11):114017, 2015.

[118] A. Vogt. *Comput. Phys. Commun.*, 170:65–92, 2005.

[119] A. Mitov, S. Moch, and A. Vogt. *Phys. Lett.*, B638:61–67, 2006.

[120] S. Moch and A. Vogt. *Phys. Lett.*, B659:290–296, 2008.

[121] A. A. Almasy, S. Moch, and A. Vogt. *Nucl. Phys.*, B854:133–152, 2012.

[122] Oleksandr Gituliar and Sven Moch. *Acta Phys. Polon.*, B46(7):1279–1289, 2015.

[123] Stefano Catani, Michelangelo L. Mangano, Paolo Nason, and Luca Trentadue. *Nucl. Phys.*, B478:273–310, 1996.

[124] Daniele Anderle, Daniel de Florian, and Yamila Rotstein Habarnau. *Phys. Rev.*, D95(3):034027, 2017.

[125] A. Vogt. Talk given at the Seminar “Aktuelle Themen der Theoretischen Hochenergiephysik” in Tübingen, 2015.

[126] George F. Sterman. *An Introduction to quantum field theory.* 1993.

[127] P. Chiappetta, Mario Greco, J. P. Guillet, S. Rolli, and M. Werlen. *Nucl. Phys.*, B412:3–38, 1994.

[128] J. Binnewies, Bernd A. Kniehl, and G. Kramer. *Phys. Rev.*, D53:3573–3581, 1996.

[129] D. de Florian, M. Stratmann, and W. Vogelsang. *Phys. Rev. Lett.*, 81:530–533, 1998.

[130] Daniel de Florian, Rodolfo Sassot, and Marco Stratmann. *Phys. Rev.*, D75:114010, 2007.

[131] Daniel de Florian, Rodolfo Sassot, and Marco Stratmann. *Phys. Rev.*, D76:074033, 2007.

[132] Daniel de Florian, R. Sassot, Manuel Epele, Roger J. Hernández-Pinto, and Marco Stratmann. *Phys. Rev.*, D91(1):014035, 2015.

[133] S. Albino, B. A. Kniehl, and G. Kramer. *Nucl. Phys.*, B803:42–104, 2008.

[134] D. de Florian, M. Epele, R. J. Hernandez-Pinto, R. Sassot, and M. Stratmann. *Phys. Rev.*, D95(9):094019, 2017.

[135] Daniele P. Anderle, Felix Ringer, and Werner Vogelsang. *Phys. Rev.*, D87(3):034014, 2013.

[136] Daniele P. Anderle, Felix Ringer, and Werner Vogelsang. *Phys. Rev.*, D87:094021, 2013.

[137] Patriz Hinderer, Felix Ringer, George F. Sterman, and Werner Vogelsang. *Phys. Rev.*, D91(1): 014016, 2015.

[138] S. Moch, J. A. M. Vermaseren, and A. Vogt. *Nucl. Phys.*, B688:101–134, 2004.

[139] A. Vogt, S. Moch, and J. A. M. Vermaseren. *Nucl. Phys.*, B691:129–181, 2004.

[140] Sayipjamal Dulat, Tie-Jiun Hou, Jun Gao, Marco Guzzi, Joey Huston, Pavel Nadolsky, Jon Pumplin, Carl Schmidt, Daniel Stump, and C. P. Yuan. *Phys. Rev.*, D93(3):033006, 2016.

[141] L. A. Harland-Lang, A. D. Martin, P. Motylinski, and R. S. Thorne. *Eur. Phys. J.*, C75(5): 204, 2015.

[142] Richard D. Ball et al. *JHEP*, 04:040, 2015.

[143] Xiangdong Ji. *Phys. Rev. Lett.*, 110:262002, 2013.

[144] Yan-Qing Ma and Jian-Wei Qiu. `arXiv:1404.6860`, 2014.

[145] M. Gluck, E. Reya, and A. Vogt. *Phys. Rev.*, D45:3986–3994, 1992.

[146] M. Gluck, E. Reya, and A. Vogt. *Phys. Rev.*, D46:1973–1979, 1992.

[147] A. D. Martin and M. G. Ryskin. *Eur. Phys. J.*, C74:3040, 2014.

[148] Tom Kaufmann, Asmita Mukherjee, and Werner Vogelsang. *Phys. Rev.*, D93(11):114021, 2016.

[149] Tom Kaufmann, Asmita Mukherjee, and Werner Vogelsang. To appear in: Proceedings, PHOTON 2017.

[150] J. F. Owens. *Rev. Mod. Phys.*, 59:465, 1987.

[151] Nobuo Sato, J. J. Ethier, W. Melnitchouk, M. Hirai, S. Kumano, and A. Accardi. *Phys. Rev.*, D94(11):114004, 2016.

[152] Valerio Bertone, Stefano Carrazza, Nathan P. Hartland, Emanuele R. Nocera, and Juan Rojo. 2017.

[153] M. Gluck, E. Reya, and A. Vogt. *Phys. Rev.*, D48:116, 1993. [Erratum: Phys. Rev.D51,1427(1995)].

[154] L. Bourhis, M. Fontannaz, and J. P. Guillet. *Eur. Phys. J.*, C2:529–537, 1998.

[155] P. Aurenche, P. Chiappetta, M. Fontannaz, J. P. Guillet, and E. Pilon. *Nucl. Phys.*, B399: 34–62, 1993.

[156] K. Ackerstaff et al. *Eur. Phys. J.*, C2:39–48, 1998.

[157] D. Buskulic et al. *Z. Phys.*, C69:379–392, 1996.

[158] S. Abachi et al. *Phys. Rev.*, D40:706, 1989.

[159] Tomas Jezo, Michael Klasen, and Florian König. *JHEP*, 11:033, 2016.

[160] Michael Klasen and F. König. *Eur. Phys. J.*, C74(8):3009, 2014.

[161] W. Vogelsang and A. Vogt. *Nucl. Phys.*, B453:334–354, 1995.

[162] L. E. Gordon and W. Vogelsang. *Phys. Rev.*, D48:3136–3159, 1993.

[163] S. S. Adler et al. *Phys. Rev. Lett.*, 98:012002, 2007.

[164] A. Adare et al. *Phys. Rev.*, D86:072008, 2012.

[165] A. Adare et al. *Phys. Rev.*, C87:054907, 2013.

[166] P. Aurenche, M. Fontannaz, J. Ph. Guillet, Bernd A. Kniehl, E. Pilon, and M. Werlen. *Eur. Phys. J.*, C9:107–119, 1999.

[167] Patrick Aurenche, Michel Fontannaz, Jean-Philippe Guillet, Eric Pilon, and Monique Werlen. *Phys. Rev.*, D73:094007, 2006.

[168] David d'Enterria and Juan Rojo. *Nucl. Phys.*, B860:311–338, 2012.

[169] M. Gluck, L. E. Gordon, E. Reya, and W. Vogelsang. *Phys. Rev. Lett.*, 73:388–391, 1994.

[170] S. Catani, M. Fontannaz, J. P. Guillet, and E. Pilon. *JHEP*, 05:028, 2002.

[171] L. E. Gordon and W. Vogelsang. *Phys. Rev.*, D52:58–67, 1995.

[172] S. Catani, M. Fontannaz, J. Ph. Guillet, and E. Pilon. *JHEP*, 09:007, 2013.

[173] W.T. Giele, E.W. Nigel Glover, and David A. Kosower. *Phys.Rev.*, D52:1486–1499, 1995.

[174] B. Jager, M. Stratmann, and W. Vogelsang. *Phys. Rev.*, D70:034010, 2004.

[175] Asmita Mukherjee and Werner Vogelsang. *Phys. Rev.*, D86:094009, 2012.

[176] W.T. Giele, E.W. Nigel Glover, and J. Yu. *Phys.Rev.*, D53:120–130, 1996.

[177] T. Affolder et al. *Phys.Rev.Lett.*, 88:042001, 2002.

[178] V.M. Abazov et al. *Phys.Rev.*, D80:111107, 2009.

[179] Bogdan Malaescu and Pavel Starovoitov. *Eur.Phys.J.*, C72:2041, 2012.

[180] Georges Aad et al. *JHEP*, 1301:029, 2013.

[181] Serguei Chatrchyan et al. *Phys.Rev.*, D87:114015, 2013.

[182] John E. Huth et al. Toward a standardization of jet definitions. In *1990 DPF Summer Study on High-energy Physics: Research Directions for the Decade (Snowmass 90)*, pages 0134–136, 1990.

[183] Gerald C. Blazey et al. Run II jet physics. In *QCD and weak boson physics in Run II*, pages 47–77, 2000.

[184] Gregory Soyez. *Nucl.Phys.Proc.Suppl.*, 191:131–140, 2009.

[185] S.G. Salesch. PhD thesis, 1993.

[186] M. H. Seymour. *Nucl. Phys.*, B513:269–300, 1998.

[187] R. Akers et al. *Z. Phys.*, C63:197–212, 1994.

[188] Bora Isildak. PhD thesis, Bogazici U., 2011.

[189] Gavin P. Salam and Gregory Soyez. *JHEP*, 0705:086, 2007.

[190] S. Catani, Yuri L. Dokshitzer, M.H. Seymour, and B.R. Webber. *Nucl.Phys.*, B406:187–224, 1993.

[191] Stephen D. Ellis and Davison E. Soper. *Phys.Rev.*, D48:3160–3166, 1993.

[192] Yuri L. Dokshitzer, G.D. Leder, S. Moretti, and B.R. Webber. *JHEP*, 9708:001, 1997.

[193] Tom Kaufmann, Asmita Mukherjee, and Werner Vogelsang. *Phys. Rev.*, D91(3):034001, 2015.

[194] Yang Bai, Zhenyu Han, and Ran Lu. *JHEP*, 03:102, 2015.

[195] Shao-Feng Ge. *JHEP*, 05:066, 2015.

[196] Iain W. Stewart, Frank J. Tackmann, and Wouter J. Waalewijn. *Phys. Rev. Lett.*, 105:092002, 2010.

[197] Tom Kaufmann, Asmita Mukherjee, and Werner Vogelsang. *Phys. Rev.*, D92(5):054015, 2015.

[198] F. Aversa, P. Chiappetta, Mario Greco, and J. P. Guillet. *Nucl. Phys.*, B327:105, 1989.

[199] F. Aversa, L. Gonzales, Mario Greco, P. Chiappetta, and J. P. Guillet. *Z. Phys.*, C49:459–466, 1991.

[200] J. P. Guillet. *Z. Phys.*, C51:587–598, 1991.

[201] Stephen D. Ellis, Christopher K. Vermilion, Jonathan R. Walsh, Andrew Hornig, and Christopher Lee. *JHEP*, 11:101, 2010.

[202] Christian W. Bauer, Andrew Hornig, and Frank J. Tackmann. *Phys. Rev.*, D79:114013, 2009.

[203] Wouter J. Waalewijn. *Phys. Rev.*, D86:094030, 2012.

[204] Zhong-Bo Kang, Felix Ringer, and Ivan Vitev. *JHEP*, 11:155, 2016.

[205] Zhong-Bo Kang, Felix Ringer, and Wouter J. Waalewijn. `arXiv:1705.05375`, 2017.

[206] Lin Dai, Chul Kim, and Adam K. Leibovich. *Phys. Rev.*, D94(11):114023, 2016.

[207] Pavel M. Nadolsky, Hung-Liang Lai, Qing-Hong Cao, Joey Huston, Jon Pumplin, Daniel Stump, Wu-Ki Tung, and C. P. Yuan. *Phys. Rev.*, D78:013004, 2008.

[208] Daniel de Florian, Patriz Hinderer, Asmita Mukherjee, Felix Ringer, and Werner Vogelsang. *Phys. Rev. Lett.*, 112:082001, 2014.

[209] F. Abe et al. *Phys. Rev. Lett.*, 65:968–971, 1990.

[210] Georges Aad et al. *Eur. Phys. J.*, C71:1795, 2011.

[211] The ATLAS collaboration. Report Number: ATLAS-CONF-2015-022, 2015.

[212] The ATLAS collaboration. Report Number: ATLAS-CONF-2017-004, 2017.

[213] Serguei Chatrchyan et al. *JHEP*, 10:087, 2012.

[214] Xianguo Lu. *Nucl. Phys.*, A931:428–432, 2014.

[215] Benjamin Andreas Hess. In *Proceedings, 2nd Conference on Large Hadron Collider Physics Conference (LHCP 2014)*, 2014.

[216] Benjamin Andreas Hess. PhD thesis, Tubingen U., 2015-06-10.

[217] Daniel de Florian. *Phys. Rev.*, D79:114014, 2009.

[218] Feng Yuan. *Phys. Rev.*, D77:074019, 2008.

[219] Feng Yuan. *Phys. Lett.*, B666:44–47, 2008.

[220] Umberto D'Alesio, Francesco Murgia, and Cristian Pisano. *Phys. Rev.*, D83:034021, 2011.

[221] John C. Collins. *Nucl. Phys.*, B396:161–182, 1993.

[222] Christian W. Bauer and Aneesh V. Manohar. *Phys. Rev.*, D70:034024, 2004.

[223] G. P. Korchemsky and G. Marchesini. *Nucl. Phys.*, B406:225–258, 1993.

[224] Mrinal Dasgupta, Frédéric Dreyer, Gavin P. Salam, and Gregory Soyez. *JHEP*, 04:039, 2015.

[225] Hung-Liang Lai, Marco Guzzi, Joey Huston, Zhao Li, Pavel M. Nadolsky, Jon Pumplin, and C. P. Yuan. *Phys. Rev.*, D82:074024, 2010.

[226] B. I. Abelev et al. *Phys. Rev. Lett.*, 97:252001, 2006.

[227] B. I. Abelev et al. *Phys. Rev.*, D80:111108, 2009.

[228] G. Agakishiev et al. *Phys. Rev. Lett.*, 108:072302, 2012.

[229] Mrinal Dasgupta, Lorenzo Magnea, and Gavin P. Salam. *JHEP*, 02:055, 2008.

[230] E. W. Nigel Glover and A. G. Morgan. *Z. Phys.*, C62:311–322, 1994.

[231] Daniele P. Anderle, Tom Kaufmann, Marco Stratmann, Felix Ringer, and Ivan Vitev. *Phys. Rev.*, D96(3):034028, 2017.

[232] Rhorry Gauld, Juan Rojo, Luca Rottoli, and Jim Talbert. *JHEP*, 11:009, 2015.

[233] M. V. Garzelli, S. Moch, and G. Sigl. *JHEP*, 10:115, 2015.

[234] Atri Bhattacharya, Rikard Enberg, Mary Hall Reno, Ina Sarcevic, and Anna Stasto. *JHEP*, 06:110, 2015.

[235] Rhorry Gauld, Juan Rojo, Luca Rottoli, Subir Sarkar, and Jim Talbert. *JHEP*, 02:130, 2016.

[236] M. Benzke, M. V. Garzelli, B. Kniehl, G. Kramer, S. Moch, and G. Sigl. `arXiv:1705.10386`, 2017.

[237] Zhong-Bo Kang, Felix Ringer, and Ivan Vitev. *JHEP*, 03:146, 2017.

[238] A. Andronic et al. *Eur. Phys. J.*, C76(3):107, 2016.

[239] W. Beenakker, H. Kuijf, W. L. van Neerven, and J. Smith. *Phys. Rev.*, D40:54–82, 1989.

[240] P. Nason, S. Dawson, and R. Keith Ellis. *Nucl. Phys.*, B327:49–92, 1989. [Erratum: Nucl. Phys.B335,260(1990)].

[241] W. Beenakker, W. L. van Neerven, R. Meng, G. A. Schuler, and J. Smith. *Nucl. Phys.*, B351: 507–560, 1991.

[242] Michelangelo L. Mangano, Paolo Nason, and Giovanni Ridolfi. *Nucl. Phys.*, B373:295–345, 1992.

[243] Matteo Cacciari and Mario Greco. *Nucl. Phys.*, B421:530–544, 1994.

[244] Matteo Cacciari, Mario Greco, and Paolo Nason. *JHEP*, 05:007, 1998.

[245] Matteo Cacciari, Stefano Frixione, and Paolo Nason. *JHEP*, 03:006, 2001.

[246] Matteo Cacciari, Paolo Nason, and Carlo Oleari. *JHEP*, 04:006, 2006.

[247] J. Binnewies, Bernd A. Kniehl, and G. Kramer. *Phys. Rev.*, D58:014014, 1998.

[248] Bernd A. Kniehl and Gustav Kramer. *Phys. Rev.*, D74:037502, 2006.

[249] B. A. Kniehl, G. Kramer, I. Schienbein, and H. Spiesberger. *Phys. Rev.*, D71:014018, 2005.

[250] B. A. Kniehl, G. Kramer, I. Schienbein, and H. Spiesberger. *Eur. Phys. J.*, C41:199–212, 2005.

[251] B. A. Kniehl, G. Kramer, I. Schienbein, and H. Spiesberger. *Eur. Phys. J.*, C72:2082, 2012.

[252] B. A. Kniehl, G. Kramer, I. Schienbein, and H. Spiesberger. *Eur. Phys. J.*, C75(3):140, 2015.

[253] T. Kneesch, B. A. Kniehl, G. Kramer, and I. Schienbein. *Nucl. Phys.*, B799:34–59, 2008.

[254] Michael Fickinger, Sean Fleming, Chul Kim, and Emanuele Mereghetti. *JHEP*, 11:095, 2016.

[255] S. Kretzer. *Phys. Rev.*, D62:054001, 2000.

[256] S. Albino, B. A. Kniehl, and G. Kramer. *Nucl. Phys.*, B725:181–206, 2005.

[257] M. Hirai, S. Kumano, T. H. Nagai, and K. Sudoh. *Phys. Rev.*, D75:094009, 2007.

[258] Manuel Epele, Romina Llubaroff, Rodolfo Sassot, and Marco Stratmann. *Phys. Rev.*, D86: 074028, 2012.

[259] Marco Stratmann and Werner Vogelsang. *Phys. Rev.*, D64:114007, 2001.

[260] J. Pumplin, D. R. Stump, and W. K. Tung. *Phys. Rev.*, D65:014011, 2001.

[261] J. Pumplin, D. Stump, R. Brock, D. Casey, J. Huston, J. Kalk, H. L. Lai, and W. K. Tung. *Phys. Rev.*, D65:014013, 2001.

[262] Ambar Jain, Massimiliano Procura, and Wouter J. Waalewijn. *JHEP*, 04:132, 2012.

[263] Christian W. Bauer and Emanuele Mereghetti. *JHEP*, 04:051, 2014.

[264] Yang-Ting Chien, Zhong-Bo Kang, Felix Ringer, Ivan Vitev, and Hongxi Xing. *JHEP*, 05:125, 2016.

[265] Reggie Bain, Lin Dai, Andrew Hornig, Adam K. Leibovich, Yiannis Makris, and Thomas Mehen. *JHEP*, 06:121, 2016.

[266] Georges Aad et al. *Phys. Lett.*, B739:320–342, 2014.

[267] B. Abelev et al. *JHEP*, 03:013, 2014.

[268] Serguei Chatrchyan et al. *Phys. Rev.*, C90(2):024908, 2014.

[269] H. Abramowicz et al. *JHEP*, 09:149, 2015.

[270] P. J. Rijken and W. L. van Neerven. *Phys. Lett.*, B386:422–428, 1996.

[271] Alexander Mitov and Sven-Olaf Moch. *Nucl. Phys.*, B751:18–52, 2006.

[272] Georges Aad et al. *Nucl. Phys.*, B907:717–763, 2016.

[273] R Aaij et al. *Nucl. Phys.*, B871:1–20, 2013.

[274] Roel Aaij et al. *JHEP*, 03:159, 2016. [Erratum: JHEP05,074(2017)].

[275] B. Abelev et al. *JHEP*, 01:128, 2012.

[276] Betty Abelev et al. *JHEP*, 07:191, 2012.

[277] D. Acosta et al. *Phys. Rev. Lett.*, 91:241804, 2003.

[278] Rodolfo Sassot, Pia Zurita, and Marco Stratmann. *Phys. Rev.*, D82:074011, 2010.

[279] Zhong-Bo Kang, Felix Ringer, and Ivan Vitev. *JHEP*, 10:125, 2016.

[280] F. Aversa, Mario Greco, P. Chiappetta, and J. P. Guillet. *Z. Phys.*, C46:253, 1990.

[281] R. Barate et al. *Eur. Phys. J.*, C16:597–611, 2000.

[282] R. Akers et al. *Z. Phys.*, C67:27–44, 1995.

[283] K. Ackerstaff et al. *Eur. Phys. J.*, C1:439–459, 1998.

[284] S. Söldner-Rembold. *Private communications.*

[285] J. M. Yelton et al. *Phys. Rev. Lett.*, 49:430, 1982.

[286] Philip S. Baringer et al. *Phys. Lett.*, B206:551–556, 1988.

[287] W. Bartel et al. *Phys. Lett.*, 146B:121–125, 1984.

[288] H. Aihara et al. *Phys. Rev.*, D34:1945, 1986.

[289] W. Braunschweig et al. *Z. Phys.*, C44:365, 1989.

[290] R. Seuster et al. *Phys. Rev.*, D73:032002, 2006.

[291] Concerning the withdrawal of the BELLE data, see: `http://durpdg.dur.ac.uk/view/ins686014`.

[292] M. Artuso et al. *Phys. Rev.*, D70:112001, 2004.

[293] H. Albrecht et al. *Z. Phys.*, C52:353–360, 1991.

[294] The KKKS08 code we use was downloaded from `http://lapth.cnrs.fr/ffgenerator/`.

[295] G. Watt. *JHEP*, 09:069, 2011.

[296] The ATLAS collaboration. Report Number: ATLAS-CONF-2015-081, 2015.

[297] CMS Collaboration. Report Number: CMS-PAS-EXO-15-004, 2015.

[298] The ATLAS collaboration. Report Number: ATLAS-CONF-2016-059, 2016.

[299] CMS Collaboration. Report Number: CMS-PAS-EXO-16-027, 2016.

[300] P. Aurenche, A. Douiri, R. Baier, M. Fontannaz, and D. Schiff. *Phys. Lett.*, B140:87–92, 1984.

[301] P. Aurenche, R. Baier, M. Fontannaz, and D. Schiff. *Nucl. Phys.*, B297:661–696, 1988.

[302] H. Baer, J. Ohnemus, and J. F. Owens. *Phys. Rev.*, D42:61–71, 1990.

[303] L. E. Gordon and W. Vogelsang. *Phys. Rev.*, D50:1901–1916, 1994.

[304] Daniel de Florian. *Phys. Rev.*, D67:054004, 2003.

[305] Stefano Catani, Michelangelo L. Mangano, and Paolo Nason. *JHEP*, 07:024, 1998.

[306] Stefano Catani, Michelangelo L. Mangano, Paolo Nason, Carlo Oleari, and Werner Vogelsang. *JHEP*, 03:025, 1999.

[307] Nikolaos Kidonakis and J. F. Owens. *Phys. Rev.*, D61:094004, 2000.

[308] George F. Sterman and Werner Vogelsang. *JHEP*, 02:016, 2001.

[309] Eric Laenen, George F. Sterman, and Werner Vogelsang. *Phys. Rev. Lett.*, 84:4296–4299, 2000.

[310] Paolo Bolzoni, Stefano Forte, and Giovanni Ridolfi. *Nucl. Phys.*, B731:85–108, 2005.

[311] Daniel de Florian and Werner Vogelsang. *Phys. Rev.*, D72:014014, 2005.

[312] Thomas Becher and Matthew D. Schwartz. *JHEP*, 02:040, 2010.

[313] D. Buskulic et al. *Z. Phys.*, C69:365–378, 1996.

[314] A. Gehrmann-De Ridder, T. Gehrmann, and E. W. Nigel Glover. *Phys. Lett.*, B414:354–361, 1997.

[315] Z. Belghobsi, M. Fontannaz, J. Ph. Guillet, G. Heinrich, E. Pilon, and M. Werlen. *Phys. Rev.*, D79:114024, 2009.

[316] A. Gehrmann-De Ridder, T. Gehrmann, and E. Poulsen. *Eur. Phys. J.*, C47:395–411, 2006.

[317] Jesse Thaler. *Phys. Rev.*, D92(7):074001, 2015.

[318] Mrinal Dasgupta, Frédéric A. Dreyer, Gavin P. Salam, and Gregory Soyez. *JHEP*, 06:057, 2016.

[319] K. A. Olive et al. *Chin. Phys.*, C38:090001, 2014.

[320] Y. Akiba. *Private communications.*

[321] C. Gagliardi. *Private communications.*

[322] J. Wess and B. Zumino. *Phys. Lett.*, 37B:95–97, 1971.

[323] M. Leitgab et al. *Phys. Rev. Lett.*, 111:062002, 2013.

[324] J. P. Lees et al. *Phys. Rev.*, D88:032011, 2013.

[325] H. Aihara et al. *Phys. Lett.*, B184:299–304, 1987.

[326] H. Aihara et al. *Phys. Rev. Lett.*, 61:1263, 1988.

[327] Xing-Qi Lu. PhD thesis, Johns Hopkins U., 1986.

[328] K. Abe et al. *Phys. Rev.*, D59:052001, 1999.

[329] D. Buskulic et al. *Z. Phys.*, C66:355–366, 1995.

[330] P. Abreu et al. *Eur. Phys. J.*, C5:585–620, 1998.

[331] R. Akers et al. *Z. Phys.*, C63:181–196, 1994.

[332] Dirk Graudenz. *Nucl. Phys.*, B432:351–376, 1994.

[333] W. Furmanski and R. Petronzio. *Phys. Lett.*, B97:437–442, 1980.

[334] L. Baulieu, E. G. Floratos, and C. Kounnas. *Nucl. Phys.*, B166:321–339, 1980.

[335] M. Stratmann and W. Vogelsang. *Nucl. Phys.*, B496:41–65, 1997.

[336] J. Blumlein and V. Ravindran. *Nucl. Phys.*, B749:1–24, 2006.

[337] Alfred H. Mueller. *Phys. Lett.*, B104:161–164, 1981.

[338] Alfred H. Mueller. *Nucl. Phys.*, B213:85–108, 1983.

[339] Alfred H. Mueller. *Nucl. Phys.*, B241:141–154, 1984.

[340] Alfred H. Mueller. *Nucl. Phys.*, B228:351–364, 1983.

[341] Matteo Cacciari and Stefano Catani. *Nucl. Phys.*, B617:253–290, 2001.

[342] J. Blumlein and V. Ravindran. *Phys. Lett.*, B640:40–47, 2006.

[343] S. Moch and A. Vogt. *Phys. Lett.*, B680:239–246, 2009.

[344] A. Vogt. *Phys. Lett.*, B691:77–81, 2010.

[345] A. A. Almasy, N. A. Lo Presti, and A. Vogt. *JHEP*, 01:028, 2016.

[346] S. Albino, P. Bolzoni, B. A. Kniehl, and A. Kotikov. *Nucl. Phys.*, B851:86–103, 2011.

[347] P. Bolzoni, B. A. Kniehl, and A. V. Kotikov. *Phys. Rev. Lett.*, 109:242002, 2012.

[348] Paolo Bolzoni, Bernd A. Kniehl, and Anatoly V. Kotikov. *Nucl. Phys.*, B875:18–44, 2013.

[349] Redamy Perez-Ramos and David d'Enterria. *JHEP*, 08:068, 2014.

[350] David d'Enterria and Redamy Pérez-Ramos. In *Proceedings, 50th Rencontres de Moriond, QCD and high energy interactions*, page 117, 2015.

[351] Alberto Accardi, Daniele P. Anderle, and Felix Ringer. *Phys. Rev.*, D91(3):034008, 2015.

[352] Ekaterina Christova and Elliot Leader. *Phys. Rev.*, D94(9):096001, 2016.

[353] K. G. Chetyrkin, A. L. Kataev, and F. V. Tkachov. *Phys. Lett.*, B85:277–279, 1979.

[354] Michael Dine and J. R. Sapirstein. *Phys. Rev. Lett.*, 43:668, 1979.

[355] William Celmaster and Richard J. Gonsalves. *Phys. Rev. Lett.*, 44:560, 1980.

[356] Johannes Blumlein and Andreas Vogt. *Phys. Rev.*, D58:014020, 1998.

[357] J. Blumlein, V. Ravindran, and W. L. van Neerven. *Nucl. Phys.*, B586:349–381, 2000.

[358] A. Bassetto, M. Ciafaloni, G. Marchesini, and Alfred H. Mueller. *Nucl. Phys.*, B207:189–204, 1982.

[359] A. Bassetto, M. Ciafaloni, and G. Marchesini. *Phys. Rept.*, 100:201–272, 1983.

[360] Daniele Paolo Anderle. PhD thesis, Tubingen U., 2017.

[361] Wolfram Research Inc. *Mathematica 10.0*, 2014.

[362] W. L. van Neerven and A. Vogt. *Nucl. Phys.*, B588:345–373, 2000.

[363] S. Moch, J. A. M. Vermaseren, and A. Vogt. *JHEP*, 08:049, 2005.

[364] M. Epele, C. A. Garcia Canal, and R. Sassot. *Phys. Rev.*, D94(3):034037, 2016.

[365] Matteo Cacciari, Paolo Nason, and Carlo Oleari. *JHEP*, 10:034, 2005.